UNIVERSITY OF Southampton
School of Chemistry

Controlled Electrodeposition of Metal Nanocentres For Catalysis

by Hartini Haji Mohd. Yasin

A thesis submitted for the degree of

Doctor of Philosophy

November 2010

UNIVERSITY OF SOUTHAMPTON

ABSTRACT

FACULTY OF NATURAL AND ENVIRONMENTAL SCIENCES
SCHOOL OF CHEMISTRY

Doctor of Philosophy

Controlled Electrodeposition of Metal Nanocentres For Catalysis

by Hartini Haji Mohd Yasin

In this research, electrodeposition was used with the aim of preparing surfaces with controlled dispersion and uniform small centre size to enhance the catalytic performance. Nanoparticle catalyst centres are designed to minimize the amount of expensive metal components loaded onto a cheaper substrate but with optimum catalytic activity. The electrodeposition of platinum and gold nanocentres have been investigated by varying the deposition parameters in hydrogen hexachloroplatinate(IV) acid and hydrogen tetrachloroaurate(III) hydrate respectively. Various substrates such as microdisc, microband and microwire electrodes were used for the study of controlled electrodeposition. Their smaller surface area provides a better tool for the study of nucleation and growth of nuclei. The effect of mass transport was studied with microdisc and rotating disc electrodes.

The mechanism for the reduction of hydrogen hexachloroplatinate(IV) in hydrochloric acid was investigated. Voltammograms show two reduction waves and both waves lead to the deposition of platinum(0). At high overpotential, the reaction becomes diffusion controlled. No dissolution of platinum is observed on the reverse scan. In contrast, the reduction of hydrogen tetrachloroaurate(III) hydrate in acidic media produces a simple mass transfer controlled three-electron reduction wave with a stripping peak of gold observed on the backward scan.

Several approaches, such as cyclic voltammetry, single potential step and double-pulse potential step deposition were used to electrodeposit platinum and gold nanocentres. Isolated and hemispherical nanocentres of platinum and gold were successfully electrodeposited onto carbon surfaces. In contrast, the electrodeposition of platinum onto a gold substrate quickly leads to complete layers when observed with a scanning electron microscope. The platinum and gold nanocentres were characterized by means of cyclic voltammetry in acid solution, scanning electron microscopy (SEM) and energy dispersive X-ray spectroscopy (EDXS).

The electrodeposition of platinum from a lyotropic liquid crystalline mixture, specifically from a micellar solution, produced platinum deposits with higher specific catalyst area than those deposited in aqueous solution. The nanostructured

platinum was not observable with the scanning electron microscope, even at high magnification; however the presence of nanostructured platinum was confirmed by cyclic voltammetry in sulphuric acid. On gold electrodes, the nanostructured platinum showed good catalytic response for hydrogen evolution and oxygen reduction reactions.

This study has shown that a surface with small centres and high nuclei number density could be produced by electrodeposition at high overpotentials. A smooth surface with small centres deposited at low charge density will produce low roughness factor, and this makes it difficult to be confirmed with cyclic voltammetry in sulphuric acid. In addition, small centres of less than 50 nm cannot be observed using scanning electron microscopy. However, small centres are believed to be present on the surface as they lead to the centres observed at higher charge densities when deposited at very negative potentials.

DECLARATION OF AUTHORSHIP

I, ***Hartini Haji Mohd Yasin*** declare that the thesis entitled ***Controlled Electrodeposition of Metal Nanocentres For Catalysis***

and the work presented in the thesis are both my own, and have been generated by me as the result of my own original research. I confirm that:

- this work was done wholly or mainly while in candidature for a research degree at this University;
- where any part of this thesis has previously been submitted for a degree or any other qualification at this University or any other institution, this has been clearly stated;
- where I have consulted the published work of others, this is always clearly attributed;
- where I have quoted from the work of others, the source is always given. With the exception of such quotations, this thesis is entirely my own work;
- I have acknowledged all main sources of help;
- where the thesis is based on work done by myself jointly with others, I have made clear exactly what was done by others and what I have contributed myself;
- parts of this work have been published as:
    - H. M. Yasin, G. Denuault, D. Pletcher, ***Journal of Electroanalytical Chemistry***, 633 (2009) 327.

Signed: ……..

Date:…….

ACKNOWLEDGEMENTS

Syukur Alhamdulilah, thank you to ***Allah*** for giving me patience and enthusiasm in achieving my wish to continue my study in the field I like most.

I would like to express my sincere gratitude to my co-supervisors, ***Professor Derek Pletcher*** and ***Dr. Guy Denuault*** for their supervision, guidance, constant support and encouragement throughout my electrochemical studies in Southampton. Without their motivation and encouragement, I would not be able to finish this thesis.

Special thanks to my beloved parents, ***Haji Mohd Yasin Bin Haji Tengah*** and ***Hajah Masnah Binti Dato Paduka Haji Abdul Wahab***, for their prayers, encouragement and having confidence in whatever I do. I would like to thank my siblings, ***Masyati***, ***Dr. Haji Mohd Yusni***, ***Dr. Harliza***, ***Dr. Nur Azri*** and ***Nur Qutrul A'ini*** for their motivation and moral support throughout the year. With this accomplishment, I hope I can make them proud.

I also like to acknowledge the financial support received from ***the Brunei Government*** throughout the period of this work, and the help and understanding of staff at the ***In-service Training Department, Brunei High Commissioner*** and ***the University of Brunei Darussalam.***

Thank you to all my group mates; ***Laila***, ***Kelly***, ***Mohammad Aziz***, ***Ihsin***, ***Alicja*** and ***Jacek*** for being supportive in any kinds of discussions, compromising with sharing equipments and also the cooperation given in managing the lab in order to make it a welcoming place to do work. Also I should not forget to mention those who have left the group; ***Clélia***, ***Maria*** and ***Jin*** for all their help, moral support and advice throughout this project. I also would like to thank the ***Bartlett*** and ***Russell*** groups;

Thomas, ***Magda***, ***David***, ***Maciej***, ***Ahmet***, ***Rob***, ***Mohammad Ghanem***, ***Summet***, ***Prabalini*** and ***Gael*** for the friendship and the helping hands offered when needed. And not forgetting ***Alistair*** for the SEM training and providing me tips in using the SEM, and also the indirect involvement of the glassblowers in my research (especially in the fabrication of the microelectrodes).

Finally, thank you to my friends, ***Sharina***, ***Faizah***, ***Dr. Ena Kartina***, ***Hajah Sarawati*** and ***Haji Muhd Arpan*** for their understanding and time in listening when I need a friend to talk to. Not forgetting, ***Dr Hajah Noor Maya*** and family for their kindness and great companion whenever I feel homesick. And to those friends back home who I did not mention, my big thank you!!

TABLE OF CONTENTS

List of symbols

Symbols	*Description*	*units*
A	Area of electrode	cm^2
A_{geo}	Geometric area of electrode	cm^2
$A_{electroactive}$	Electroactive area of electrode	cm^2
c^{∞}	Bulk concentration	M or mol cm^{-3}
D	Diffusion coefficient	$cm^2\ s^{-1}$
E	Applied potential	V
E_e	Equilibrium potential versus reference electrode	V
E_e^o	Formal potential versus reference electrode	V
$E_{½}$	Half-wave potential	V
F	Faraday constant	96485 C mol^{-1}
j	Current density	mA cm^{-2}
j_o	Exchange current denisty	mA cm^{-2}
k	Rate constant for a chemical reaction	s^{-1}
k_m	Mass transfer coefficient	cm s^{-1}
m	Number of moles of product formed	mol
M_{Pt}	Molecular weight of platinum	195.08 g mol^{-1}
n	Number of electrons	-
q	Charge density	C cm^{-2}
Q	Charge	C
Q_{ads}	Hydrogen adsorption charge	µC
Q_{mono}	Charge density for a monolayer	210 µC cm^{-2}
r	Radius of electrode	cm or µm
R	Gas constant	8.314 J K^{-1} mol^{-1}
R_f	Roughness factor	-
R_u	Uncompensated resistance	Ω
S	Specific catalyst area	$m^2\ g^{-1}$
t	Time	s
T	Temperetaure	K
W	Metal loadings	µg cm^{-2}
α	Transfer coefficient	-
η	Overpotential	V
ρ_{Pt}	Density of platinum	21.45 g cm^{-3}
ω	Rotation rate of a rotating disc electrode	rpm

Abbreviations

I_1	Cubic phase
H_1	Hexagonal phase
H_2	Inverse hexagonal phase
L_1	Micellar solution
L_α	Lamellar phase
L_2	Inverse lamellar phase
V_1	Bicontinuous cubic phase
SCE	Saturated calomel electrode
SEM	Scanning electron microscope
EDXS	Energy dispersive X-ray spectroscopy

Chapter 1

1 Introduction

1.1. Small metal centres

There is now considerable interest in the study of nanostructured particles deposited onto an inert substrate to enhance catalytic activity [1-3]. It is believed that smaller particles with dimensions in the range of 1 to 10 nm have more edge sites, thus increasing the catalytic activity of the material compared to the macrostructure of metal deposits [1]. During the past decade, nanoparticles of different metals such as Pt [2-6], Pd [7-10], Ru [11, 12] and Au [13-17] have been used in the preparation of electrodes for many electrochemical applications.

The electrocatalytic properties of nanoparticles differ considerably from that of the bulk metal [1, 18]. The increase in the catalytic activity of the metal deposits may be identified by either an increase in current density at a fixed potential or a decrease in the overpotential during electrolysis at fixed current density [19]. Nanoparticle catalysts are designed to minimize the amount of expensive metal components loaded onto a cheaper substrate but with optimum performance of catalytic activity. The particle size, shape and dispersion play a very important role in determining their catalytic activity [20-24]. Thus, it is necessary to control the size of particles

within a narrow size distribution, in order to optimize the catalytic activity and at the same time, reduce the cost of the final material.

1.1.1. Applications of small centres

In recent years, nanoparticles have been extensively investigated due to their practical applications in diverse fields, such as optical and electronic nanodevices, catalysts, and sensors in biomedical applications [16, 25].

Wang et. al. reported that gold nanoparticles on indium tin oxide (ITO) have higher catalytic capability for biosensors [26]. In recent studies, nanostructured Pd/Au(111) and Pt/Au(111) surfaces showed an increase in catalytic activity as the amount of catalyst material decreases, with respect to hydrogen oxidation reaction and hydrogen evolution reaction [7, 9]. Moreover, gold nanoparticles were found to have an extraordinary electrocatalytic activity for oxidation of carbon monoxide [20], the catalytic hydrogenation of unsaturated alcohols and aldehydes and epoxydation of alkenes [13, 14]. For the same reactions, the bulk Au electrodes showed a lesser or even no electrocatalytic activity [20].

Platinum is well-known as a very good catalyst in fuel cells [1, 27, 28] for oxygen reduction [29-31] and the oxidation of hydrogen, carbon monoxide and methanol [32]. The platinum-based catalysts in the oxygen reduction reaction have been widely studied [32-34]. Generally, platinum nanoparticles are invariably required in the fuel cell electrodes in order to catalyse the cathode reactions [29-31]. The direct methanol fuel cell (DMFC) has significant advantages for electronic portable devices and automobile applications. However, the high cost of the Pt and Pt alloy electrocatalyst is a crucial problem. Thus, there has been an extensive investigation of the fabrication of electrode surfaces with high platinum utilization for energy conversion in fuel cells and lower amount of precious metal in electrocatalyst, in order to reduce the overall cost of fuel cells [4, 35].

The purpose of electrocatalysis is to design surfaces that provide alternative pathways for the reaction of interest to occur at high current densities at low overpotential [19]. An increase in current density can be achieved by using a high electroactive area of electrode, as well as choosing a higher catalytic activity electrode material. Thus, a high electroactive geometric area can be prepared by dispersing small centres on an inert substrate [19] or implementing rough, porous or other high area surfaces [36].

1.1.2. Effects of small size centres and distribution

The catalytic performance of metal particles greatly depends on the particle size, shape and dispersion of the metal catalyst [21, 37-41]. As the size of nanoparticles is reduced, the ratio of surface area to volume increases [2].

Small gold catalysts of diameter less than 10 nm in size have shown extraordinary high activity towards carbon monoxide oxidation [20, 37, 42-44]. The catalytic activity decreases sharply as the particle size increases and almost no activity is observed for gold nanoparticles with diameter greater than 10 nm [42, 45]. ***El-Deab et. al.*** reported Au nanoparticles electrodeposited on Au electrodes have shown higher reduction and decomposition rates of hydrogen peroxide [22, 46]. The increase in oxygen reduction reaction activity has also been observed on Au nanoparticles deposited on a boron-doped diamond support [47-49] as well as on Au electrodes [46] as compared with bulk polycrystalline gold in acid solution. ***Yagi et. al.*** discovered that an increase in current efficiency for the $4e^{-}$ reduction and a lower overpotential for oxygen reduction was observed, when small Au particles of diameter greater than 2 nm were used [49]. ***El-Deab et. al.*** [50] also showed that the electrodeposition of gold nanoparticles in the presence of iodide ions in the gold plating bath solution produced a high particle density with narrow particle size distribution range (10-40 nm). However, it was found to have less specific surface area than the nanoparticles produced in the presence of cysteine. Thus, the activity of

the electrode towards the oxygen reduction reactions was lower. Figure 1 illustrates the morphology of gold nanoparticles produced on highly oriented pyrolytic graphite (HOPG) from a gold plating bath solution, as well as with the addition of either cysteine or iodide ions. The shape and size of the gold nanoparticles were shown to be sensitive to the additive even though they were electrodeposited onto the same substrate.

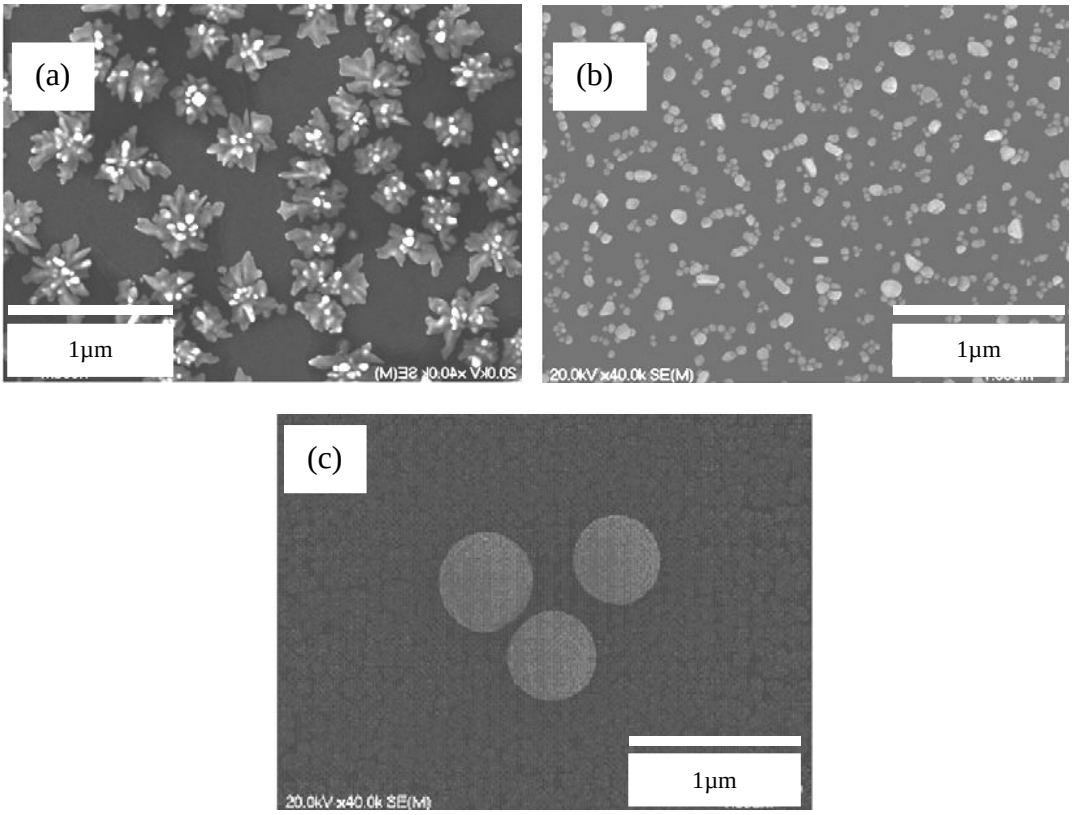

Figure 1. SEM images of Au nanoparticles electrodeposited on untreated HOPG substrate from a solution containing 1 mM Na[$AuCl_4$] and 0.5 M H_2SO_4 **(a)** *absence of any organic additives and with the presence of* **(b)** *0.1 mM iodide ions and* **(c)** *0.1 mM cysteine. (Reproduced from Ref.* ***[51]****).*

On the other hand, some research groups claim the dependency of gold particle size depends on the investigated reaction. ***Guerin et. al.*** [52] have shown that the oxygen reduction activity in acid media decreases rapidly as the Au particle decreases below

~3.0 nm diameter and the activity is independent of the particle size above this critical particle diameter. The oxygen reduction activity has been investigated with Au nanoparticles both on carbon and TiO_x substrates. ***Guan et. al.*** demonstrated that gold nanoparticles of intermediate size (about 6 nm diameter) exhibit better catalytic performance than smaller or larger particles for the dehydrogenation of ethanol [53].

The catalytic activity of Pt for the electrochemical reduction of oxygen [54, 55] as well as methanol oxidation [3, 56] is strongly dependent on the particle size and the surface orientation of Pt nanoparticles. The specific activity of Pt on carbon for the oxygen electroreduction is widely known for its 'size effect' [40, 54, 55]. ***Watanabe et. al.*** and ***Yahikozawa et. al.*** [24, 57] have reported that the specific activity of the catalyst decreases with a decreasing catalyst particle size. They suggested that as the surface area of the Pt particles is reduced, sintering occurs more rapidly [58], or a reduction in intercrystallite distance occurs [24, 57]. ***Watanabe et. al.*** [24] also concluded that maximum catalytic activity can be achieved when the separations of the platinum crystallites on a carbon substrate is less than 20 nm. However, ***Higuchi et al.*** [59] found that the area-specific activity for the oxygen reduction reaction was not influenced by the Pt-loading level on carbon black from 19.2 to 63.2 wt% even at an optimised dispersion state. ***Satter et. al.*** reported that the maximum activity of Pt was at about 3 to 5 nm [60].

The catalytic rate for the electrooxidation of carbon monoxide monolayer decreases with decreasing particles size and higher overpotential is required to oxidise carbon monoxide [3, 61, 62]. Porous platinum nanoflowers have shown higher catalytic activity for the oxidation of methanol when compared to platinum nanoparticles [63]. Figure 2 shows the Pt nanoflowers and Pt nanoparticles electrodeposited onto indium tin oxide from hexachloroplatinate(IV) in sulphuric acid and potassium chloride solution respectively. ***Kolics*** reported that the sulphuric acid anions (HSO_4^- or SO_4^{2-}) preferentially adsorb on certain Pt surface planes [64], thereby inhibit further growth. This leads to anisotropic growth of the deposited metal hence, the surface area of the platinum increases.

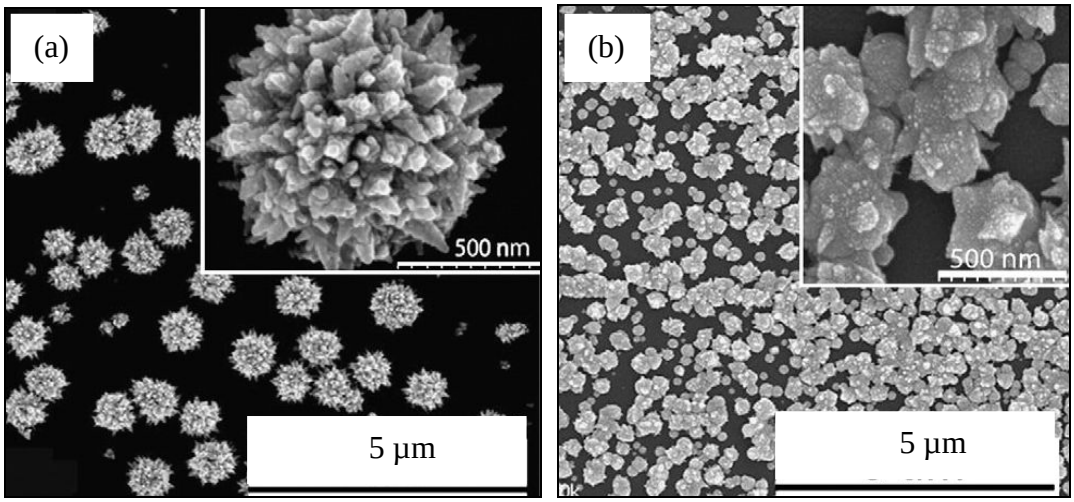

Figure 2. SEM images of platinum nanostructures on indium tin oxide from solution containing 3 mM H_2PtCl_6 in **(a)** *0.5 M H_2SO_4 (dep_{time} = 1000 s) and* **(b)** *0.1 M KCl (dep_{time} = 2000 s). (Reproduced from Ref.* ***[63]****).*

In recent studies, ***Song et. al.*** [65] reported that gold-platinum (Au-Pt) hybrid nanoparticles have been successfully electrodeposited onto indium tin oxide surfaces from a solution containing both $AuCl_4^-$ and $PtCl_6^{2-}$. The cauliflower-shaped structure of the Au-Pt nanoparticles exhibit alloy properties with a predominant (111) orientation, thus showed electrocatalytic activity for nitrite oxidation and oxygen reduction.

The composition of the plating bath and/or with the addition of organic components can influence the structure and distribution of the metal deposits. In addition, it was reported that the activity of such supported particles also depends on the nature of the electrocatalyst support material [66, 67] as well as the method of preparation [22, 68].

1.1.3. Effects of substrate

The support helps to provide a high surface area to stabilize highly dispersed, nanosized particles. The nature of the substrate influences the nucleation and growth kinetics of the deposited metals. Hence the substrate influences the size and morphology of the metal crytallites, and thereby their electrocatalytic activity [1, 69, 70]. Moreover, the design and role of the support also determines the activity and life time of the nanoparticles in various applications.

There has been a growing interest in implementing metal nanoparticle-modified electrodes in many electrochemical applications due to their extraordinary catalytic properties over bulk metal electrodes [20-22, 46, 71]. Nanostructured palladium and platinum films on gold substrates showed very sharp peaks in the hydrogen region in acidic medium [71]. Moreover, ***El-Deab et. al.*** observed that Au nanoparticles electrodeposited on Au electrodes showed excellent activity for the oxygen reduction in acidic medium [22, 46].

The nature of the substrate and the preparation of the electrode greatly influence the resulting Au nanoparticles size, shape and crystallographic orientation [50, 72], hence control the activity of supported catalysts of gold nanoparticles [42]. Gold nanoparticles on different carbon substrates, for instance, glassy carbon [51, 72], highly oriented pyrolytic graphite (HOPG) [50, 51] and boron-doped diamond (BDD) [47, 49, 73] have been implemented in order to study the catalytic activity in oxygen reduction reaction. In addition, ***Commotti et. al.*** [42] has reported that the activity of gold nanoparticles changes when using different metal oxide supports even with identical particle sizes. ***Ye et. al.*** [74] demonstrated that gold flowerlike nanostructures have been observed on modified indium tin oxide (ITO) after coating with biopolymer-polydopamine. However, the electrodeposited gold on bare indium tin oxide only developed into quasi-spherical shape even after similar deposition time. ***Tian et. al.*** [75] has also reported that the modified ITO substrate with polypyrrole helps to adhere more platinum nanoparticles onto the substrate, hence

affecting the size, shape and number density of the nanoparticles (as shown in Figure 3).

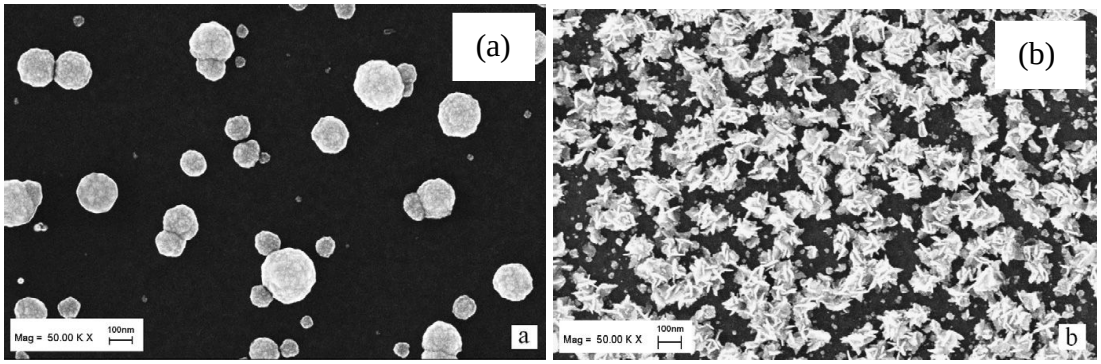

Figure 3. SEM images of the platinum nanostructures deposited on **(a)** *a bare indium tin oxide (ITO) and* **(b)** *modified ITO with polypyrrole film. (Reproduced from Ref.* ***[75]****).*

Duarte et al. [76] discovered that the platinum deposited on glassy carbon shows different size and morphology than when using graphite fibres as the substrate. This was suggested to be attributable to the geometry and the properties of the carbonaceous supports. Moreover, ***Lin Cai*** [69] reported that the platinum deposited onto vitreous carbon exhibited no activity towards methanol oxidation, but, on the other hand, small deposits of platinum on gold were unusually active. Figure 4 shows the SEM images of electrodeposited platinum on glassy carbon and gold electrode at high overvoltage. ***Plyasova et. al.*** [77] observed that platinum on gold forms a continuous layer as the primary nucleation sites are higher on gold support when compared to glassy carbon. In addition, ***Bennett et. al.*** [78] reported that the deposition of platinum on diamond is favourable compared to glassy carbon, as the microstructure and morphology of diamond influence the nucleation and growth of platinum. In recent years, platinum deposited onto titanium oxide [79] and boron-doped diamond electrodes [80] have shown high specific area. These electrodes

increase the catalytic activity for oxygen reduction [79] and the oxidation of hydrogen, carbon monoxide and methanol [80].

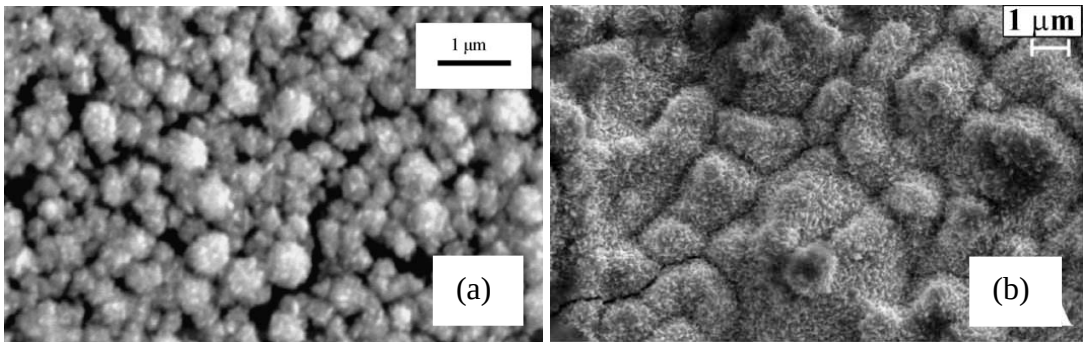

Figure 4. SEM images of platinum electrodeposited at -0.285 V vs. SCE on **(a)** *GC and* **(b)** *Au electrode. (Reproduced from Ref.* ***[77]****).*

Numerous studies attempting to fabricate electrodes with minimal platinum usage have been widely reported. Platinum-based catalysts have been widely studied, they exhibit better electrocatalytic activity than the bulk metal [33, 34]. ***Markovic et. al.*** [81, 82] reported $Pt_3Ni(111)$ surface has shown the highest catalytic activity for oxygen reduction reaction so far. The specific activity is 10 times higher than Pt(111) and 90 times higher than the carbon-supported Pt catalysts. Implementing Pt alloys with other metals or supported metal nanoparticles helps to reduce the amount of platinum electrocatalysts in oxygen reduction reaction without losing the catalytic activity. ***Paulus et. al.*** [83, 84] and ***Mukerjee et. al.*** [85, 86] reported an increase in the catalytic responses for oxygen reduction reaction in low temperature polymer electrolyte fuel cells (PEFCs) when using Pt-Co and Pt-Ni alloys when compared to supported Pt catalysts. In such bimetallic systems, the catalytic activity of platinum nanoparticles can be changed through electronic and/or geometric effects [87, 88]. It has been observed that Pt-alloy metal nanoparticles dispersed on supports such as carbon, aluminium oxide, or titanium oxide [89] have a strong impact on the performance of a polymer electrolyte membrane fuel cells (PEMFC) [90, 91]. Hence,

further reduction of the Pt content with enhanced catalytic activity can be achieved with optimized catalytic architecture and support.

Hence, the catalytic performance of the nanoparticle-based electrodes is generally found to depend on the particle size and the nature of the support. Several studies report that methods of preparation [20, 22, 68] also influence the catalytic activity and this will be further discussed in the next subsection.

1.1.4. Various methods of preparation

Most methods of preparation of metal nanocentres lead to a distribution of sizes. The nuclei centre dimensions reported mainly refer to the mean diameters rather than the actual nuclei size. The electrocatalytic activity is strongly influenced by the particle size, shape, support, but also the distribution of the particles.

Different approaches have been employed to prepare nanostructured metals. The Pt supported on carbon substrate can be prepared by impregnation [92, 93], ion exchange [94] and colloidal method [95]. Some techniques such as sol-gel [96, 97], deposition-precipitation [98], coprecipitation [38], sputter deposition [47, 49, 52, 99] and dip-coating techniques have been used in the preparation of gold nanoparticles. Other fabrication methods of different metal nanoparticles include the conventional chemical deposition [6], chemical reduction [100], chemical vapour deposition on highly ordered pyrolytic graphite [101] and electrochemical deposition [48, 51, 71-73, 102] and templated electrodeposition in liquid crystals [103-105]. The conventional techniques either by impregnation, adsorption, or ion-exchange methods typically require post-synthesis treatment. These treatments often lead to uncontrolled growth of metal particle size and shape. Moreover, aggregation and/or sintering of metal particles occur at high temperatures. Of all these methods,

electrodeposition is probably the most explored means to produce dispersed metal particles and it is an easy and fast procedure for the fabrication of nanoparticles [22].

Although electrodeposition has not found general utility for the preparation of catalysts, it has been proved to be successful in producing electrode surfaces with controllable size and morphology of the nanosized particles by adjusting the electrochemical parameters [106-108]. ***Lu*** [109] reported that more uniform platinum particles with less aggregation on highly oriented pyrolitic graphite are formed by increasing the deposition overpotential. However, ***Thompson et. al***. [110] reported that it had been a problem in maintaining the small particle size when using electrodeposition. It was suggested that further platinum reduction took place on the initial sites of platinum deposits.

There are different approaches for electrodeposition, such as cyclic voltammetry [111, 112], potential step deposition [77, 113] and double-pulse deposition [76, 108]. The potential step deposition or chronoamperometry provides a tool to control the amount of metal deposited, the number of metallic sites and their size. Double pulse deposition has also been applied to produce high particle density and more uniform particle dispersions [114, 115]. Most studies consider electrodeposited centres greater than 20 nm. Different shapes of metal nanoparticles, for instance spheres, rods and triangles have been successfully synthesised by electrodeposition [116]. The electrochemical deposition presents the advantage that materials deposited onto a conducting substrate provide an excellent electrical contact without requiring post treatment.

Electrochemical deposition in a lyotropic liquid crystalline phase provides a template for nanofabrication. This enables the formation of three-dimensional nanomaterials possessing high specific surface area, well-defined and highly regular porous nanoarchitectures on the scale of 2 – 10 nm [104, 117]. It also provides good mechanical and electrochemical stability [104]. The method involves

electrodeposition of the metal through the structure provided by the liquid crystalline template. Thus, the metal electrodeposited onto the available conductive substrate to produce ordered metal architectures. The porous nanostructure of the resulting material is actually a cast of the structure of the liquid crystalline phase used in the synthesis.

Attard et. al. [104] first reported the preparation of mesoporous platinum powders (***H_1***-ePt) by implementing a 'true liquid crystal template technique' via the reduction of hexachloroplatinic acid (HCPA). In recent years, the electrodeposition of metals, such as platinum, palladium, cobalt and silver, has been carried out in lyotropic liquid crystalline plating mixtures to produce well-defined periodic nanostructured materials [104, 105, 118-129]. ***Kijima et. al.*** [130] demonstrated that the noble metals (platinum, palladium and silver) nanotubes prepared by applying mixed surfactant template and the reduction of metal salts. In this research, small platinum centres have been fabricated via potential step using direct lyotropic liquid crystalline template with the aim to form distributed platinum centres. The next sections describe key aspects of the preparation and characterisation of the liquid crystals solutions used for this work.

1.2. Lyotropic liquid crystals (LLC)

Lyotropic liquid crystalline phases are formed when sufficient concentrations of surfactants are mixed with water. A mesoporous structure is produced when the amphiphillic group of non-ionic surfactants begin to self-assemble in the mixture, forming nanoscale moulds into which a solid material can be deposited. The concentration of surfactant and temperature greatly influence the surface area, the regularity of the nanostructure and the surface morphology of the deposited metal. Moreover, the choice of surfactant molecule also determines the size of the pores. However, when the surfactant concentration is less than that required for the

formation of a liquid crystal phase, micellar solutions are formed. Then nonstructured material are obtained [131] and this synthesis has been used in the preparation of metal colloids [132].

Poly(oxyethylene) surfactants have been used to prepare mesoporous platinum [118]. ***Attard et. al.*** also showed that it was possible to produce electrochemically either nanostructured hexagonal (***H_1***-ePt) or cubic (***V_1***-ePt) modified electrodes. The size and thickness of the mesoporosity could be controlled by varying the deposition conditions of lyotropic liquid crystalline plating mixtures [104, 105, 119, 133, 134]. It has also been demonstrated that various metals have been successfully employed in synthesizing mesoporous material using lyotropic liquid crystal [122, 123, 125].

1.2.1. Formation of liquid crystals

The lyotropic liquid crystal phases are formed by dissolution of the amphiphilic molecules in a polar solvent, commonly water [135]. Amphiphilic molecules (or surfactants) are characterised by the presence of a polar hydrophilic head group and non-polar hydrophobic tail made up of a long hydrocarbon chain in the same molecule [136]. The solvation energy is important for the formation of lyotropic liquid crystalline phases [137]. Moreover, the presence of water provides crucial interactions in order to stabilise the lyotropic structure [135]. Figure 5 shows the schematic diagram of an amphiphilic octaethyleneglycol monohexadecyl ether ($C_{16}EO_8$), containing the hydrophilic polyethylene oxide head group and hydrophobic alkyl tail. The surfactant $C_{16}EO_8$ is mainly used in this research.

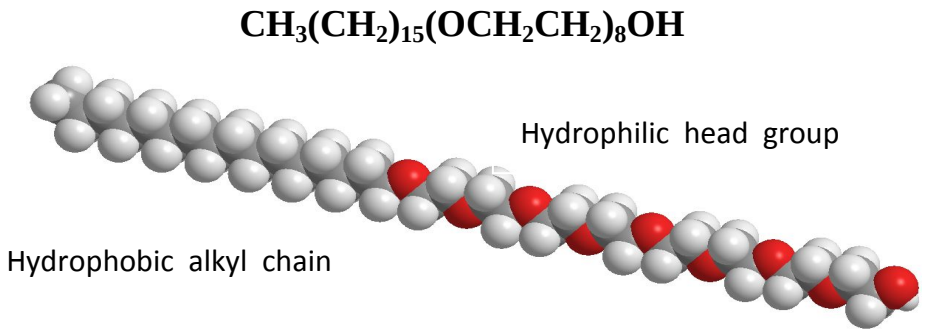

Figure 5. Schematic diagram of octaethyleneglycol monohexadecyl ether ($C_{16}EO_8$) showing the hydrophilic head group and hydrophobic alkyl tail.

At very dilute concentrations of surfactant, the molecules dissolve and distribute. As the concentration increases, the molecules begin to aggregate into micelles and form a micellar solution. The micellar solution behaves as an isotropic fluid [138]. Micelles are stable in water and can only be formed when the surfactant solubility is equal to or greater than the critical micelle concentration [139]. The formation of micelle arises from the hydrophobic effect, that is the interaction between nonpolar solutes and water [140]. A spherical micelle unit is formed, with the hydrocarbon chains shielded away from water and the hydrophilic heads arranged closely to the aqueous solvent (see Figure 6). The micellar solution is usually denoted by $\boldsymbol{L_1}$ phase [135]. As the surfactant concentration increases, different liquid crystalline phases (hexagonal, cubic, or lamellar mesophases) are formed, depending upon the temperature and concentration of the surfactant. In the next subsection, these crystalline phases will be discussed briefly.

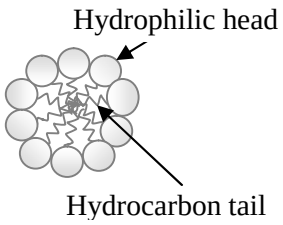

Figure 6. Structure of micelle formed by amphiphilic molecules.

1.2.2. Phases of lyotropic liquid crystals

The phase of the lyotropic liquid crystals are determined by the concentration of amphiphiles in water. The physical properties of lyotropic liquid crystalline systems are generally determined by the structures and shapes of micelles in these lyotropic mesophases. Spherical, rod and bilayer micelles occur under different mixture conditions. There are three different types of lyotropic liquid crystal phase structures, namely cubic (either $\boldsymbol{I_1}$ or $\boldsymbol{V_1}$), hexagonal ($\boldsymbol{H_1}$) and lamellar ($\boldsymbol{L_\alpha}$) phases [135-138].

1.2.2.1. Hexagonal phase

The hexagonal phase (indicated as $\boldsymbol{H_1}$) consists of micellar cylinders of infinite length packed in a hexagonal manner (see Figure 7(a)). The hexagonal liquid crystalline mixture is very viscous. The spacing between micellar cylinders depends on the amount of water and surfactant in the mixture. The continuous region between cylinders varies between 1 and 5 nm [138, 141].

There are two different hexagonal phase, a normal hexagonal ($\boldsymbol{H_1}$) and reversed hexagonal phase (denoted as $\boldsymbol{H_2}$). The inverse structures of the hexagonal liquid crystalline phase are formed as the concentration of the surfactant in water is increased. The reversed hexagonal phase is much rarer than the hexagonal phase and it occupies a smaller region of the phase diagrams. In the reverse hexagonal phase, the micellar cylinders are inverted, thus the non-polar hydrocarbon chain occupy the spaces between the hexagonally packed water cylinders (see Figure 7(c)). The non-polar hydrocarbon tails in the spaces overlap, hence the cylinders are arranged much closer than the hexagonal phase. The water is contained within the cylindrical reversed micelles which have a typical diameter of 1 to 2 nm [136, 138]. Thus, most of the research papers reported the implementation of the normal hexagonal phase for the liquid crystalline template. Both phases have anisotropic structures, thus this

liquid crystal phase exhibits birefringence. They have fan-like optical textures when observed under polarizing light microscope [141].

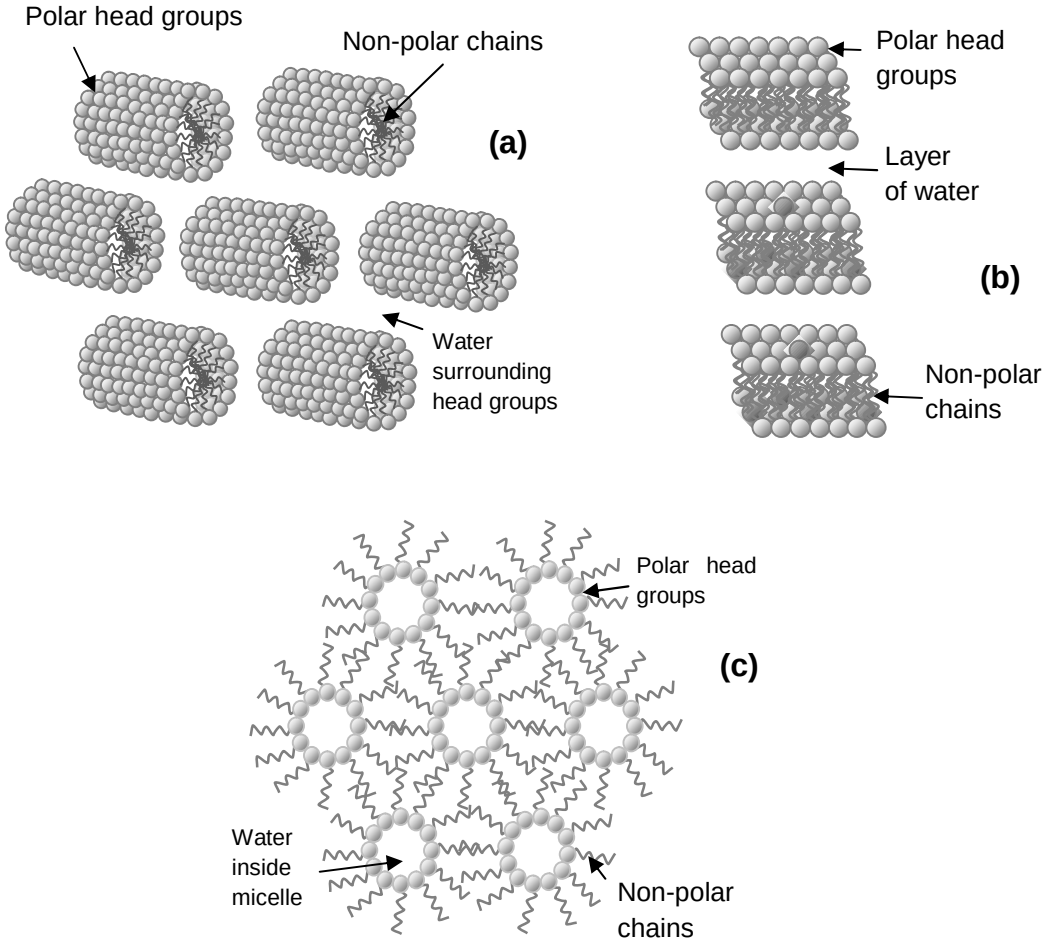

Figure 7. ***(a)*** *Hexagonal phase (H_1)* ***(b)*** *lamellar phase (L_α)* ***(c)*** *Cross-section of inverse hexagonal phase (H_2) of lyotropic liquid crystals.*

1.2.2.2. Lamellar phase

The lamellar phase (also called "neat" phase) is usually produced when the amount of surfactant is more than 50 % by weight in water [138]. Figure 7(b) shows the amphiphilic molecules arranged in double layers, in such a way that water exists between the polar heads of adjacent layers and the hydrocarbon tails are in a non-

polar environment [136]. The lamellar phase (indicated as $\boldsymbol{L}_{\alpha}$) is less viscous than the hexagonal phase despite the mixture contains less amount of water. The lamellar phase is anisotropic, therefore it is birefringent [137]. When observed under polarizing light microscope, it is readily identified from its characteristic optical texture, distinctive from the hexagonal phase.

1.2.2.3. Cubic phase

There are two different forms of cubic phases [139, 142]. At compositions between a micellar solution ($\boldsymbol{L_1}$) and the hexagonal ($\boldsymbol{H_1}$) phase, the micelles still retain their spherical shape but are organised in either a face-centred cubic or body-centered cubic arrangement (labelled $\boldsymbol{I_1}$) [135]. A bicontinuous cubic phase (labelled $\boldsymbol{V_1}$) exists between lamellar ($\boldsymbol{L}_{\alpha}$) and hexagonal ($\boldsymbol{H_1}$) phases [139, 142] and consists of large water continuous channelled networks ($\boldsymbol{V_1}$) [138, 141]. Figure 8 shows the structure of the face-centred and bicontinuous cubic phases. The cubic liquid crystalline phases are optically isotropic when examined under optical polarising microscope and therefore non-birefringent [137].

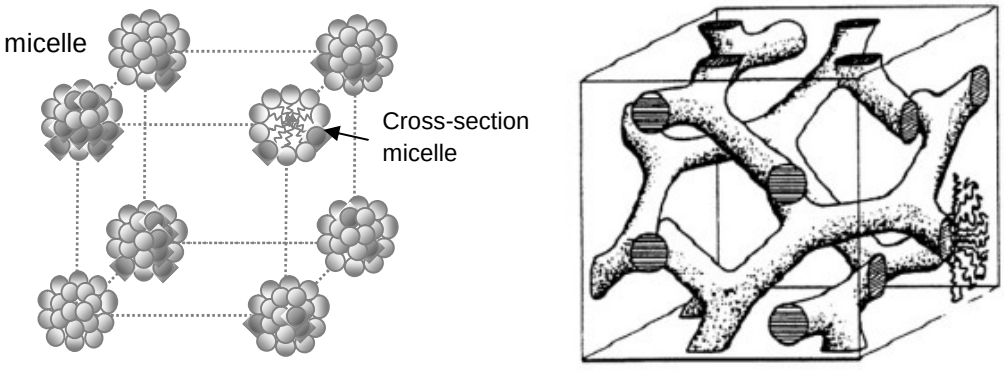

Figure 8. Structures of micelles formed in cubic (I_1) and bicontinuous cubic (V_1) network.

1.2.3. Phase diagrams of the octaethylenegylcol monohexadecyl ether in water

The typical phase diagram of octaethyleneglycol monohexadecyl ether ($C_{16}EO_8$) indicating different liquid crystalline phases is shown in Figure 9. At a certain concentration, the lyotropic liquid crystal phase can be controlled by changing the temperature. However, the addition of hexachloroplatinic acid to the surfactant mixture will change the phase boundaries of the binary system. A pseudobinary phase diagram of octaethyleneglycol monohexadecyl ether ($C_{16}EO_8$) and water with fixed 1.92 M hexachloroplatinic acid has been reported (as shown in Figure 10) [143]. With the presence of the hexachloroplatinic acid into the system, there is an increase in temperature range over which the ***I₁***, ***H₁*** and ***V₁*** phases were found to be stable [143]. The liquid crystalline nature of ternary mixtures of hexachloroplatinic acid, surfactant and water was confirmed by polarized light optical microscopy.

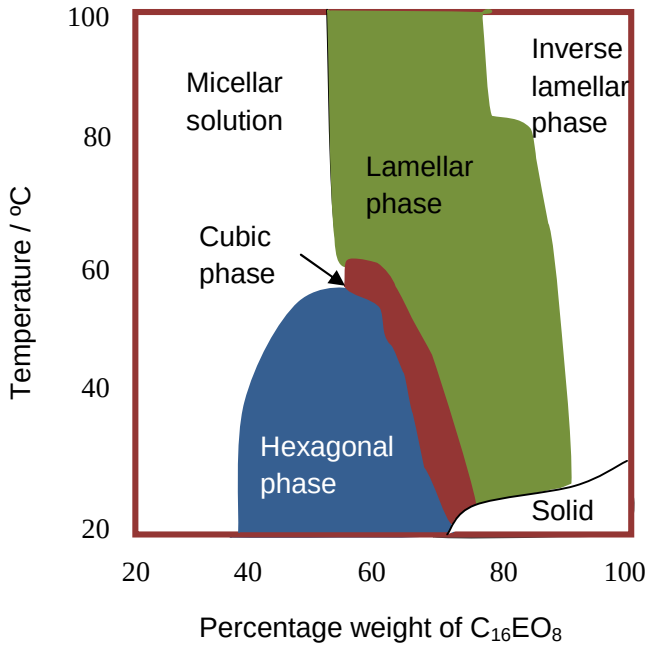

Figure 9. Typical phase diagram of octaethyleneglycol monohexadecyl ether *($C_{16}EO_8$). [Redrawn from Ref.* ***[143]****].*

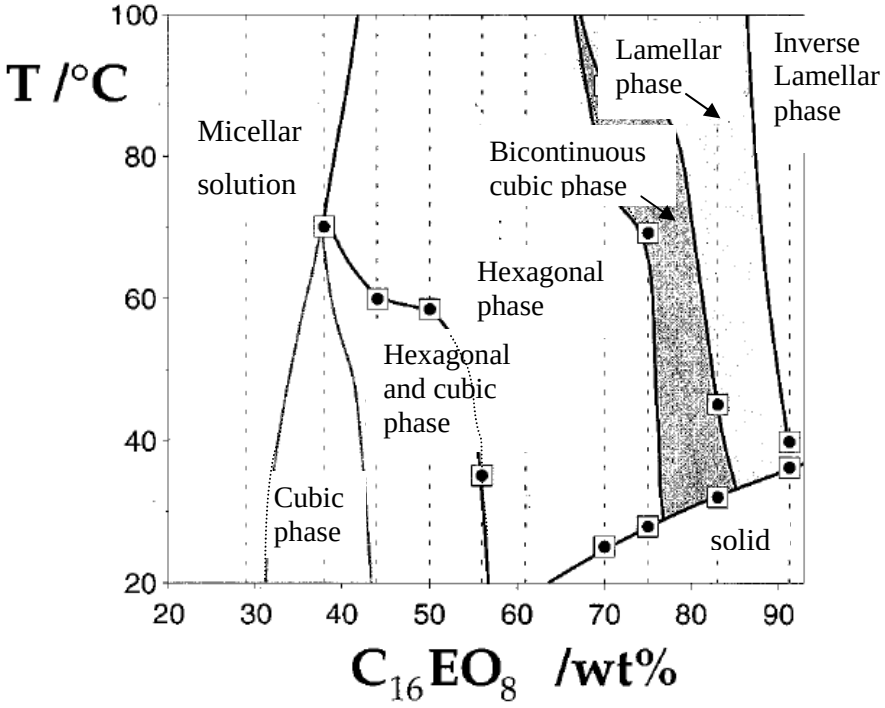

Figure 10. Pseudobinary phase diagram of $C_{16}EO_8$ and water with a fixed concentration of 1.92 M hexachloroplatinic acid. [Reproduced from Ref. ***[143]*** *].*

1.2.4. Formation of LLC template

In the process of electrodeposition from lyotropic liquid crystalline plating mixtures, the hydrophobic alkyl tails arrange in the interior of the surfactant rods, while the aqueous component occupies the interstitial spaces between individual rods [104, 118, 133]. Thus, electrodeposition of the metal occurs within the aqueous domain of the structure, resulting in materials with ordered architectures. The surfactant is later removed by dissolution in a large excess of water. Hence, the metal deposited onto the substrate has an architecture that is the inverse of the lyotropic liquid crystal template [104, 118, 133]. Figure 11 shows the schematic diagram on the preparation of mesoporous film from a hexagonal liquid crystalline phase and the expected nanostructure of a material produced.

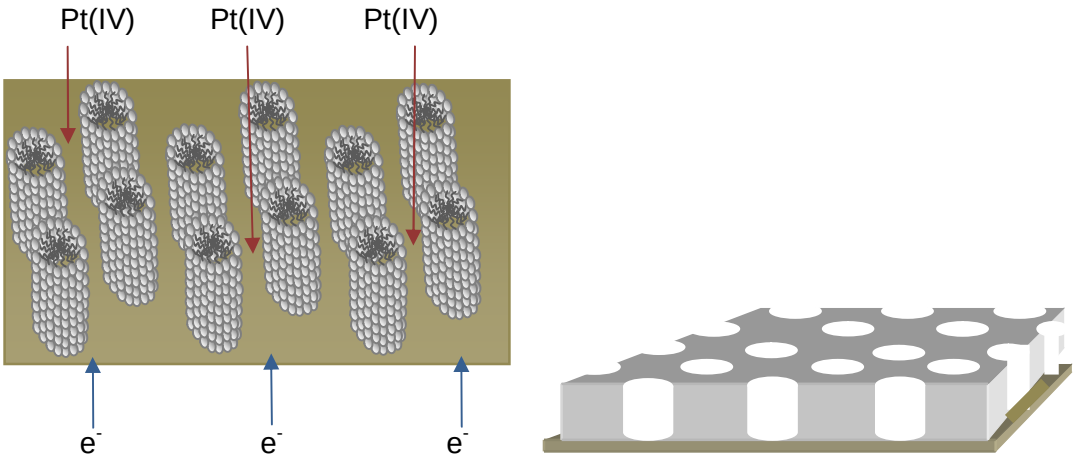

Figure 11. The arrangement of the hexagonal liquid crystalline phase for the electrodeposition of the metal, followed by the resultant mesoporous material obtained after washing out the surfactant ***[127]***.

Polyoxyethylene alkyl ethers, such as $C_{16}EO_8$, $C_{12}EO_8$ and Brij®56, are widely used in the preparation of mesoporous phases with water. Octaethyleneglycol monoheaxadecyl ether, $C_{16}(EO)_8$, is pure and it is stable at room temperature [144]. It was found that a mixture containing a hexagonal crystalline $C_{16}EO_8$ phase produced cylindrical pores with a pore diameter of approximately 2.5 nm [105]. ***Attard et. al.*** [133] also reported the pore to pore separation was found to be approximately 2.5 nm and it was estimated that each film contained 4.62 x 10^{12} pores cm^{-2}.

The pore diameters could be controlled either by using surfactants with shorter or longer chains than $C_{16}EO_8$ [145]. For instance, nanostructured platinum with pore diameters of approximately 1.8 nm could be produced when using $C_{12}EO_8$ as the surfactant [119]. Furthermore, the addition of swelling agents (such as heptane) to

the mixture helps to increase the diameter of the pores [104]. It was demonstrated that preparation from a quaternary mixture containing hexachloroplatinic acid, water, with equal molar ratio of $C_{16}EO_8$ and heptane, produced nanostructured platinum with pore diameters of approximately 4 nm.

An ideal nanostructured film with pores diameter of 2.5 nm and pore to pore separation of 5 nm, has been calculated to have a specific surface area of 21.9 $m^2 g^{-1}$, that is equivalent to a volumetric surface area of 360 $m^2 cm^{-3}$ [133]. The specific or volumetric surface area should be independent of film thickness [133]. However, the roughness factor values should increase proportionally with film thickness. Hence, the surface area of the electrodeposited metal was greatly influenced by any changes in the pore to pore separation, regularity of the nanostructure or surface roughness of a film [133].

1.2.5. Advantages and applications of mesoporous template

High surface area can be achieved with ordered nanostructured metals, consisting of regular pores electroplated from lyotropic phases. It has been reported that the specific surface area for the template deposited material increased by 65% when compared to Pt deposits from aqueous solutions [127]. In addition, ***Attard et. al.*** [118, 133] has shown that the specific surface area of mesoporous platinum powders (H_1-ePt) was approximately 60 $m^2 g^{-1}$ when compared to platinum black with 35 $m^2 g^{-1}$. The high surface area together with the ease of fabrication and mechanical stability of the mesoporous metals would be expected to be advantageous for a wide range of applications, for instance nanostructured platinum tips for the scanning electrochemical microscopy (SECM) [146], catalytic applications in fuel cells, batteries and sensors [104, 118, 147-152]. The nanostructured thin films of Pt [104] and Pd [123] have been applied in electroanalysis [105, 126], batteries and fuel cells

[103]. The mesoporous films have also been used for anodic stripping voltammetric analysis of Ag^{+}, Pb^{2+} and Cu^{2+} ions [153]. It has been demonstrated that mesoporous platinum electrodes not only provide high activity towards the oxidation of small organic molecules, but also tolerance to poisoning effects [103, 154-156].

In this project, a lyotropic liquid crystalline template has been employed in an attempt to produce an ordered array of spaced platinum centres by using a low charge density during electrodeposition. Initially, fabrication of mesoporous platinum film has been successfully produced via cyclic voltammogram, both in hexagonal phase and micellar solutions. Later, electrodeposition has been carried out using potential step method in hexagonal liquid crystalline phase with very low deposition charge density, with the aim of producing small centres instead of a mesoporous film. In this study, we have carried out the electrodeposition of platinum and gold in aqueous solution, but only platinum metal has been electrodeposited within the liquid crystalline template. In the following subsection, the electrodeposition of platinum and gold, as well as the chemistry of the metals, will be discussed briefly.

1.3. Electrochemistry of noble metals

1.3.1. Platinum

Platinum is widely known as a good catalyst for many chemical and electrochemical reactions including oxygen reduction, hydrogen oxidation, methanol oxidation and hydrogenations [157, 158]. Platinum has several oxidation states, ranging from 0 to +6. However, the common and stable oxidation states are platinum(0), platinum(II) and platinum(IV) [159]. Platinum(IV) has a d^6 electron configuration. The complexes of platinum(IV) can be either neutral or anionic and are generally octahedral [160].

1.3.1.1. Chemistry of Platinum (IV) in aqueous chloride ion solutions

The kinetics of the ligand substitution at platinum metal complexes is very slow [161]. Platinum reacts readily with aqua regia to form chloroplatinic acid, H_2PtCl_6 [159]. The hexachloroplatinate ion hydrolyses in aqueous solution [162-165] according to equation (1.1 - 1.2) and it was reported that the reaction is catalysed by a product of the hydrolysis [166], platinum(II) [167], light [168] and platinum black [166].

$$PtCl_6^{2-} + H_2O \rightleftharpoons PtCl_5H_2O^- + Cl^- \quad (1.1)$$

$$PtCl_5H_2O^- + H_2O \rightleftharpoons PtCl_4(H_2O)_2 + Cl^- \quad (1.2)$$

Thus at low concentrations of chloride ion in the electroplating bath, the hexachloroplatinate ion tends to slowly hydrolyses to form $PtCl_5H_2O^-$. The degree of hydrolysis is controlled by the stability constant, $\boldsymbol{K}$ (see equation (1.3)).

$$\boldsymbol{K} = \frac{\left[PtCl_6^{2-}\right]}{\left[PtCl_5H_2O^-\right]\left[Cl^-\right]} \quad (1.3)$$

According to equation (1.4) , the hydrolysis reaction can be followed by rapid deprotonation of the aquo-complex upon increasing pH to form $PtCl_5(OH)^{2-}$ [164, 169, 170], where $\boldsymbol{K_a}$ is the acid dissociation constant [164].

$$PtCl_5H_2O^- \rightleftharpoons PtCl_5(OH)^{2-} + H^+ \quad (1.4)$$

$$\boldsymbol{pK_a} = \frac{\left[PtCl_5(OH)^{2-}\right]\left[H^+\right]}{\left[PtCl_5H_2O^-\right]} \sim 3.5 \quad (1.5)$$

In neutral aqueous solutions of K_2PtCl_6, there is a significant amount of the hydrolysed species that also reduces to platinum [169]. In addition, the hexachloroplatinate ion also dissolves in sodium hydroxide to form $Pt(OH)_6^{2-}$ [166, 171]. The metal complexes of platinum(IV) has been characterized using ^{195}Pt NMR [164, 172, 173], infra-red and ultra-violet spectroscopy [167, 174, 175]. ***Kramer et. al.*** [172] reported that only two species are present at pH ~ 1 in aqueous 0.48 M $H_2PtCl_6.H_2O$. Using ^{195}Pt NMR spectroscopy, two peaks were observed at 8 ppm and 510 ppm corresponding to $PtCl_6^{2-}$ and $PtCl_5(H_2O)^-$ respectively (see Figure 12). The UV-Vis spectra of hexachloroplatinate(IV) in aqueous solution exhibit intense ligand-to-metal charge-transfer absorption bands at 262 and 260 nm that are assigned to $PtCl_6^{2-}$ and $PtCl_5(H_2O)^-$ respectively [174]. Two less intense ***d-d*** transition bands of platinum(IV) are observed in the visible-light region at 353 and 452 nm [174, 175].

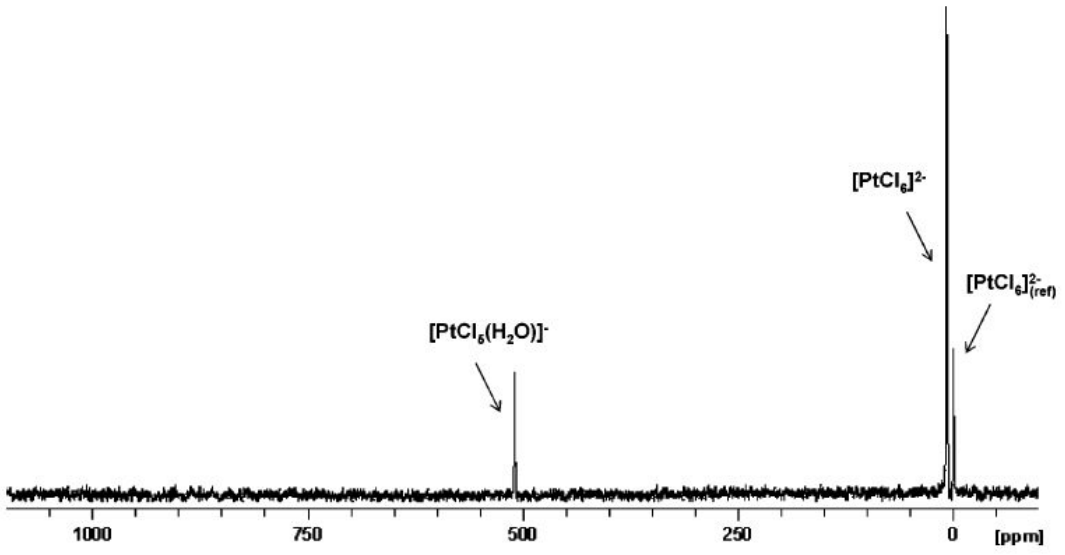

*Figure 12. ^{195}Pt NMR spectrum of an aqueous solution 0.48 M H_2PtCl_6 (Reproduced from Ref. **[172]**).*

1.3.1.2. Electrodeposition of Platinum

Studies on the electroplating baths for deposition of platinum were started in the 1800s [176] with solutions containing complexes with ligands such as Cl^- [177-180], NH_3 [181, 182], NO_2^- [183] and H_2O [184]. These complexes are more stable than the simple salts electrolytes, however they show a smaller degree of hydrolysis in the bath solutions [176]. ***Roseleur*** and ***Lannaux*** were the first to discover the platinum plating solution by dissolving hexachloroplatinate(IV) acid in a boiling solution containing ammonium and sodium phosphates [185]. In electrolytes containing sodium and potassium salts of hexahydroxyplatinate ion, $Na_2Pt(OH)_6$ and $K_2Pt(OH)_6$, dense and bright deposits are formed. However, this alkaline hexahydroxyplatinate bath solution has low stability due to carbonation reactions in atmospheres containing carbon dioxide [176] and also it easily hydrolyses according to equation (1.6).

$$Na_2Pt(OH)_6 \rightarrow PtO_2 + 2NaOH + 2H_2O \qquad (1.6)$$

Skinner [186] reported that the pH control (~ pH 10) and high temperature (91ºC to 95ºC) are necessary for maximum efficiency when plating in tetraammineplatinum(II) compounds. The almost neutral solution of ammonium hexachloroplatinate in water has also been used to electrodeposit platinum and it was reported that the morphology, microstructure and the electrochemical properties of the platinum thin films are dependent on the deposition potential [187]. ***Atkinson*** demonstrated that the hardness of deposited platinum in hexachloroplatinate(IV) acid plating bath solution depends on the rate of deposition [188]. The deposited platinum is soft and ductile at a deposition rate of 15 – 20 microns/hr. In this study, platinum has been electrodeposited using hexachloroplatinic acid (H_2PtCl_6) in acidic media. ***Feltham et. al***. [189] reported that for electrodeposition from chloroplatinic acid electrolytes three steps should be considered and the relevant standard potentials were estimated from thermodynamic data [190];

$$PtCl_6^{2-} + 2e^- \rightarrow PtCl_4^{2-} + 2Cl^- \qquad \boldsymbol{E^o} = 0.726\ \boldsymbol{V\ vs.}\ \text{SHE} \qquad (1.7)$$

$$PtCl_4^{2-} + 2e^- \rightarrow Pt + 4Cl^- \qquad \boldsymbol{E^o} = 0.758\ \boldsymbol{V\ vs.}\ \text{SHE} \qquad (1.8)$$

and/or $$PtCl_6^{2-} + 4e^- \rightarrow Pt + 6Cl^- \qquad \boldsymbol{E^o} = 0.744\ \boldsymbol{V\ vs.}\ \text{SHE} \qquad (1.9)$$

Several authors [191, 192] suggested the electrodeposition of platinum proceeds through the reduction of platinum(IV) to platinum(II) to platinum(0). ***Whalen et al.*** [187] and ***Baumgärtner*** [176] proposed that in the presence of Pt(0) and at high concentrations of hydrochloric acid in solutions containing $PtCl_6^{2-}$, $PtCl_4^{2-}$ is formed as an intermediate in the reduction process of $PtCl_6^{2-}$ as shown in equation (1.10).

$$PtCl_6^{2-} + Pt + 2Cl^- \rightleftharpoons 2PtCl_4^{2-} \qquad (1.10)$$

Sherstyuk et. al. [193] reported that platinum with crystallographic orientation of Pt(100) on a glassy carbon surface can be obtained in the presence of excess chloride in hexachloroplatinate(IV) plating bath solution. The deposition charge required to obtain the same specified specific surface area in the presence of chloride ions were 4-6 times higher than those deposited in the hexachloroplatinate(IV) solutions in the absence of additives. It was suggested that the reduction of platinum chloride complex has been inhibited by the presence of excess chloride ions [193, 194].

The mechanism of platinum(II) reduction has been reported previously [181-184], however only a few studies on the mechanism of platinum(IV) reduction have been carried out. Hence, in this study, we also aim to understand further the mechanism of the reduction of platinum(IV). This was carried out with the help of rotating disc electrode and microelectrodes. In this study, platinum has been electrodeposited onto microelectrode at variable potentials and charge densities.

1.3.2. Gold

For millennia, bulk gold has been recognised for its great beauty and value. Gold in a bulk form does not react with air and corrode. Gold has an electronic configuration of $5\boldsymbol{d}^{10}\ 6\boldsymbol{s}^{1}$ and gold crystals have face-centred cubic structures. The gold's electronic structure determines its nobility. The relativistic stabilisation of the 6***s*** level contribute to its chemical inertness when in massive form [195, 196]. The electrons in the 5***d*** level become easily mobilised and activated for the chemical reaction. This explains the predominace of Au(III) and Au(V) [195]. However, Au(V) is not a common oxidation state. It is more desirable to gain another electron to complete the $6\boldsymbol{s}^{2}$ level rather than to lose the $\boldsymbol{s}^{1}$ electron as the first ionisation energy for gold is high. Thus this accounts for the formation of Au(-I) [197, 198].

However, in recent years, researchers have discovered that gold in the form of nanocrystals exhibit a remarkable activity as a heterogeneous catalyst for a wide range of redox reactions. The presence of gold alone or alloyed with palladium helps to catalyse selective oxidation reactions such as alkene epoxidation and alcohol oxidation [14, 199]. In addition, gold nanocrystals can activate the formation of carbon dioxide from carbon monoxide and dioxygen at temperatures as low as 197 K [13, 14, 20, 39].

1.3.2.1. Chemistry of gold(I) and gold(III) in aqueous chloride solutions

In aqueous chloride solutions, the ionic gold may exist in the form of $AuCl_2^-$ and $AuCl_4^-$ complex ions [200, 201]. There are three possible redox couples in the system [201-203] and the reactions are shown in equations (1.11-1.13).

$$AuCl_2^- + e^- \rightleftharpoons Au + 2Cl^- \qquad E^o = 1.150\ V\ vs.\ \text{NHE} \qquad (1.11)$$

$$AuCl_4^- + 3e^- \rightleftharpoons Au + 4Cl^- \qquad E^o = 1.001\ V\ vs.\ \text{NHE} \qquad (1.12)$$

$$AuCl_4^- + 2e^- \rightleftharpoons AuCl_2^- + 2Cl^- \qquad E^o = 0.925\ V\ vs.\ \text{NHE} \qquad (1.13)$$

The most common oxidation state in aqueous chloride ions solutions of gold is gold(III) [203]. Gold(I) ions are very unstable and tend to disproportionate to Au(0) and strongly solvated Au(III) species [200, 204]. The disproportionation reaction of the gold(I) ions is shown in equation (1.14);

$$3AuCl_2^- \rightleftharpoons AuCl_4^- + 2Au + 2Cl^- \qquad (1.14)$$

However, the formation of gold(I) is possible when the concentration of gold is low and at very high chloride concentrations. ***Diaz et. al.*** [202] reported that the kinetics of the gold disproportionation reaction is slow.

1.3.2.2. Electrodeposition of gold

Several studies on the electrochemistry of gold in aqueous solutions particularly in the presence of CN^- and Cl^- ions have been reported [200, 201, 204-206]. In the presence of air or hydrogen peroxide, gold dissolves in cyanide solutions to form $[Au(CN)_2]^-$ [160]. Potassium gold cyanide solution is one of the most commonly used industrially for gold deposition [207]. The gold cyanide plating baths operate at high pH. The hardness and brightness of the gold deposits can be increased with codeposition of impurities such as antimony [208]. The codeposition of silver, nickel, copper and cobalt is used for decorative purposes. However, the alkaline, soft gold deposits are not suitable for applications in the microelectronics industry. The study of the reduction of gold cyanide complexes has been reported by ***Harrison et.***

al.. The mechanism of reduction of gold from gold plating bath solutions containing cyanide ions is shown in equation (1.14) [205, 207, 209].

$$\boldsymbol{Au(CN)_2^-} + \boldsymbol{e^-} \rightarrow \boldsymbol{Au} + 2\boldsymbol{CN^-} \qquad \boldsymbol{E^o} = -0.61 \text{ V } \boldsymbol{vs}. \text{ SHE} \qquad (1.15)$$

The reduction in gold cyanide complex occurs at a very negative potential, thus it coincides with the potential for the reduction of hydrogen ions. This leads to lower efficiency in the gold plating [210].

Under suitable conditions, the $AuCl_4^-$ solutions may be reduced by various reducing agents to give highly coloured solutions containing colloidal gold [160]. ***Komsiyska*** and ***Staikov*** [211] have studied the mechanism for the reduction of gold(III) chloride ions in perchloric acid and the overall reaction is shown in equation (1.16) [212]. ***Harrison et. al***. [201] also reported similar mechanism for the gold deposition from chloride solution in basic media.

$$\boldsymbol{AuCl_4^-} + 3\boldsymbol{e^-} \rightarrow \boldsymbol{Au} + 4\boldsymbol{Cl^-} \qquad \boldsymbol{E^o} = 1.0 \text{ V } \boldsymbol{vs}. \text{ SHE} \qquad (1.16)$$

The reaction mechanisms proposed for the gold deposition from solutions containing $[AuCl_4]^-$ ions has been reported [204, 213]. The reaction involves two steps of charge transfer together with the chemical reaction as shown below;

$$\boldsymbol{AuCl_4^-} \rightleftharpoons \boldsymbol{AuCl_2^+} + 2\boldsymbol{Cl^-} \qquad (1.17)$$

$$\boldsymbol{AuCl_2^+} + 2\boldsymbol{e^-} \rightarrow \boldsymbol{AuCl_2^-} \qquad (1.18)$$

$$\boldsymbol{AuCl_2^-} + \boldsymbol{e^-} \rightarrow \boldsymbol{Au} + 2\boldsymbol{Cl^-} \qquad (1.19)$$

Gallego et. al. [200] reported that the cathodic current peaks at +1.0 V and +0.675 V corresponded to the electroreduction of $AuCl_2^-$ and $AuCl_4^-$ respectively, in the

presence of concentrated hydrochloric acid solutions. The dissolution of gold occurred at potentials greater than +0.9 V ***versus*** SCE. As the concentration of the chloride ions at the electrode surface diminished with potential, the anodic stripping current becomes diffusion controlled [200]. The inhibition of anodic dissolution of gold may be attributed to the low concentration of chloride ions in the solution and/or due to the formation of a surface oxide that passivates the gold metal [206, 211, 214].

1.3.3. Electrochemistry of platinum and gold

For many years, platinum has been widely studied especially for its application as a catalyst in fuel cells, batteries and water electrolysis. The hydrogen evolution reaction is a fast reversible reaction on platinum or platinum-based alloys [215]. In addition, ***Huang et. al.*** developed nanostructured platinum films that catalyse the hydrogen evolution reaction [216]. The catalytic activity for the hydrogen evolution reaction dramatically increases on gold substrates modified with platinum, when compared with pure polycrystalline gold electrodes [217].

At the cathode of fuel cells, the oxygen reduction reaction is a very slow and irreversible reaction even on Pt electrodes [218, 219]. ***El-Deab et. al.*** [220] demonstrated that the reduction of oxygen reaction is structure-sensitive, and the final product depends on the orientation of the gold substrate. ***Yeager*** and ***Sarapuu et. al.*** reported that the mechanism of oxygen reduction reaction depends on the nature of the electrode and the pH of the electrolyte [28, 221]. In alkaline media, a four-electron reduction of oxygen to water was observed at low overpotentials on the Au(100) plane [220, 222]. On the other hand, the Au(111) crystal faces reduce the oxygen by two-electron process to produce hydrogen peroxide as the final product [220]. ***Kim*** [223] reported that the four-electron oxygen reduction reaction on Au(100) plane proceeds via an intermediate (HO_2^-). In acidic media, the oxygen reduction reaction on gold proceeds via a two-electron reduction to form hydrogen

peroxide [222]. On the other hand, platinum supports a complete four-electron reduction of oxygen to water at relatively low overpotentials [30, 34, 218]. However, it has been discovered that platinum also suffers from the 'poisoning effect' during the oxidation of carbon monoxide [224, 225]. The poison species (CO and HCOOH) produced during the process, adsorbs strongly onto the platinum surface hence blocks the active sites [226]. This results in a dramatic decrease in fuel cell efficiency.

Napporn et. al. [227] have shown that dispersed platinum catalysts provide higher catalytic activity as well as lessen the poisoning effect. Au metal is unique as it is an inert metal in the bulk form, but it provides high catalytic activity at nanoscale [39]. The electrodeposition of gold nanoparticles onto gold electrodes has shown an increase in the electrocatalytic activity for the oxygen reduction reaction in acidic media [22, 46]. ***Cameron et. al.*** [13] demonstrated that Au nanoparticle catalysts were found to be effective in oxidation of carbon monoxide.

In recent years, there has been a considerable interest in developing Pt-Au alloy [15, 17, 217, 228-232]. It was also reported that the combination of Pt-Au alloy has shown high catalytic activity towards hydrogen evolution, oxygen reduction [217, 229, 232] and oxidation of methanol [230]. ***Van Brussel et. al.*** [231] have observed that the electrocatalytic activity of polycrystalline gold electrodes modified by Pt was lower than that of the bulk electrode in the negative potential scan, but significantly higher in the positive scan in oxygen reduction. ***Dešić et. al.*** [217] have also found that Au-Pt electrodes showed higher oxygen activities than bulk platinum. In addition, the activity for the oxygen reduction in acid media increases as the Pt content in Pt-Au alloy increases. Moreover, ***Zhang et. al.*** [232] demonstrated the presence of Au stabilizes the Pt-Au catalysts and it minimises the dissolution of platinum during the oxygen reduction reaction [232, 233]. Thus, a promising approach is to develop a catalyst with the combination of Au and Pt nanoparticles. This development of catalyst not only helps to reduce the cost of platinum use in the catalysts but also aims to retain its catalytic activity [13]. The cyclic voltammograms

in sulphuric acid of platinum and gold surfaces have been widely studied and the typical responses are shown in Figure 13(a) and (b) respectively [234].

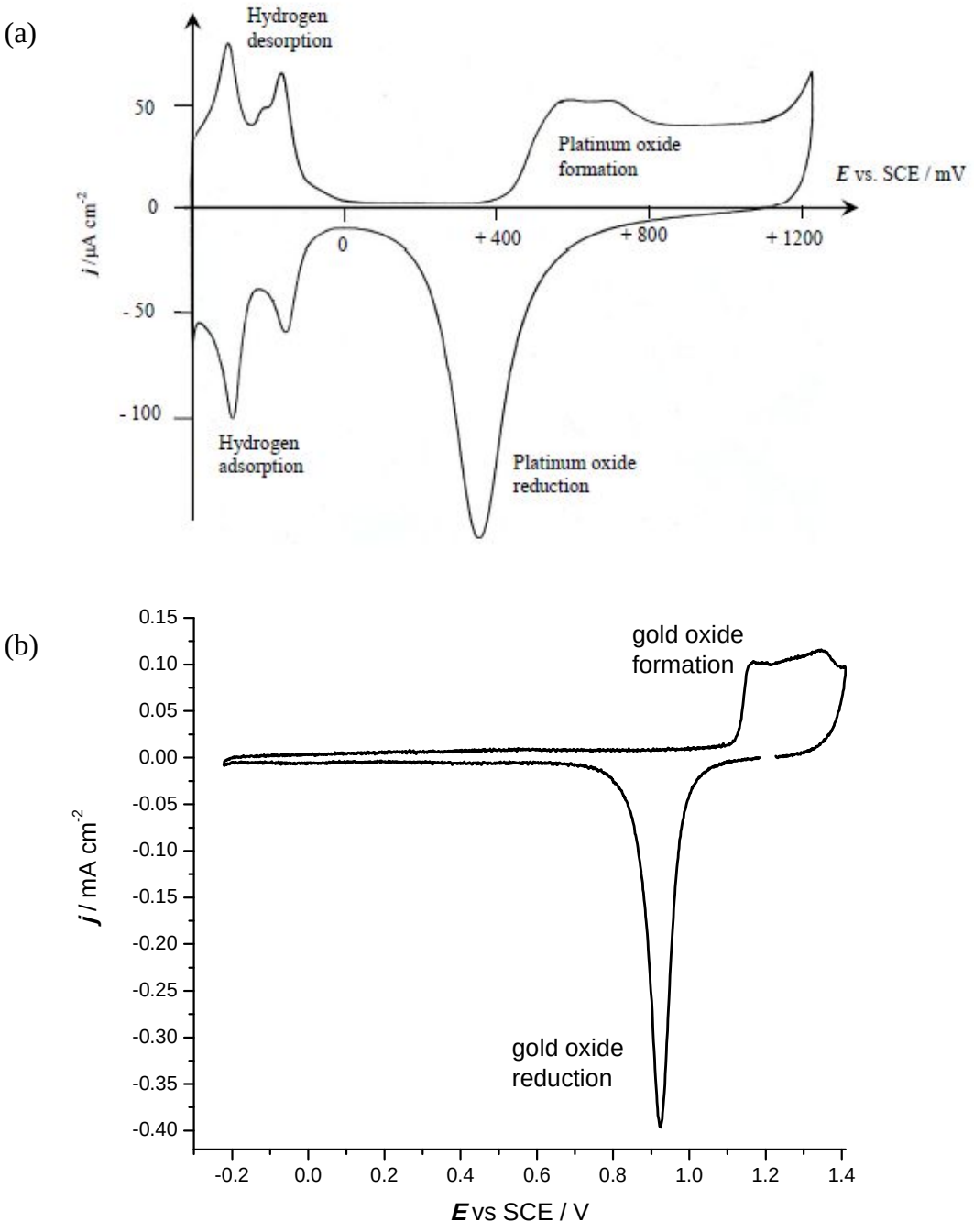

Figure 13. Cyclic voltammograms in 1 M sulphuric acid for a clean **(a)** *platinum electrode (scan rate 100 mV* s^{-1}*) and* **(b)** *gold electrode (scan rate 50 mV* s^{-1}*). [Figure(a) reproduced from reference* ***[19]****].*

In the next subsection, the kinetics of electron transfer are discussed, followed by the processes involved in the nucleation and growth of metal centres.

1.4. Electron-transfer reactions

For a simple electron transfer reaction;

$$O + ne^- \rightleftharpoons R \tag{1.20}$$

when the reaction is at equilibrium, there will be no current flowing through the system. Hence, the potential of the working electrode can be calculated from the ***Nernst*** equation involving the concentrations of O and R in bulk solution, c_O^∞ and c_R^∞ respectively [19, 235];

$$E_e = E_e^o + \frac{RT}{nF} \ell n \frac{c_O^\infty}{c_R^\infty} \tag{1.21}$$

where the equilibrium potential and formal potential are indicated as E_e and E_e^o respectively. In the presence of large excess of electrolyte, the activity coefficients of O and R are relatively similar. Thus, concentrations are used in the ***Nernst*** equation.

At any potential, the magnitude of the current flowing through the cell depends on the kinetics of electron transfer. Therefore, the measured current density, j is expressed by

$$j = j_a + (-j_c) \tag{1.22}$$

where j_a and j_c are the partial anodic and partial cathodic current densities respectively. (By convention, the cathodic current density is negative).

At the equilibrium potential, since no net current flows; the anodic and cathodic partial current densities are equal and known as the exchange current density, $\boldsymbol{j}_o$ [19].

$$\boldsymbol{j}_o = \boldsymbol{j}_a = -\boldsymbol{j}_c \tag{1.23}$$

At any other potential, a current will flow and its magnitude will depend on the kinetics of electron transfer. The kinetics are most easily discussed in terms of the overpotential, $\boldsymbol{\eta}$, that is, the deviation of the applied potential ($\boldsymbol{E}$) from the equilibrium potential, $\boldsymbol{E_e}$.[19, 235].

$$\eta = \boldsymbol{E} - \boldsymbol{E_e} \tag{1.24}$$

The current density at any potential is discussed by the ***Butler Volmer*** equation [19, 235];

$$\boldsymbol{j} = \boldsymbol{j}_o\left[\left(\exp\frac{\alpha_a \boldsymbol{nF}}{\boldsymbol{RT}}\eta\right) - \left(\exp\frac{-\alpha_c \boldsymbol{nF}}{\boldsymbol{RT}}\eta\right)\right] \tag{1.25}$$

This is the fundamental equation of electrode kinetics that shows the current density varies with exchange current density, overpotential and the transfer coefficient, $\boldsymbol{\alpha}$. At potentials away from equilibrium potential, it is either anodic or cathodic partial current is dominant. At high positive overpotentials, the second term can be ignored, hence the anodic current density [235] is given by:

$$\boldsymbol{j} = \boldsymbol{j}_o\left(\exp\frac{\alpha_a \boldsymbol{nF}}{\boldsymbol{RT}}\eta\right) \tag{1.26}$$

Taking logarithms on both sides of equation (1.26) leads to the ***Tafel*** equation (1.27);

$$\log \boldsymbol{j} = \log \boldsymbol{j}_o + \frac{\alpha_a \boldsymbol{nF}}{2.3\boldsymbol{RT}}\eta \tag{1.27}$$

In the following subsection, the basic concepts of nucleation and growth of the metal deposits will be discussed.

1.5. Nucleation and growth of metal centres

The formation of a metal phase involves the electrochemical nucleation and growth of the metal centres [19]. Nucleation is the difficult step in the formation of metal centres on a foreign substrate. The nucleus has to reach a certain size for it to become stable and grow further, as small nuclei have the tendency to dissolve. The surfaces are unstable while solids are stabilised by the atom-atom interaction in the volume. The formation of stable centres requires an overpotential to drive the electron transfer reaction [19, 236]. Once the thermodynamically stable nuclei of metal centres are formed, the growth of nuclei will be rapid. These metal centres will grow further with a characteristic shape such as hemispherical or cones, and at the same time, more new metal centres will appear [19]. The increase in size and number density of nuclei leads to an increase in the electroactive area [237]. The number density of nuclei will depend on the electrode surface and its pre-treatment, as well as the metal that is to be deposited [19].

In order to study the early stages of metal deposition, the best experimental technique is to carry out chronoamperometry experiments. The electrodeposition of metal occurs by applying an electrode potential that is more negative with respect to the equilibrium potential. Thus, the occurrence of nucleation process and the growth of nuclei can be observed as a rising transient of current with time. The rate determining step in the nuclei growth, either mass transfer or electron transfer control, can be deduced from the shape of the transients. The shape of the chronoamperometry will also depend on whether the nuclei growth is two or three dimensional and the kinetics of nucleation. [19]. In two dimensional nucleation, the deposit grows as a monolayer across the surface. Further growth requires nucleation of a second layer. In three dimensional nucleation, the nucleus grows as a hemisphere or cone, and a thick deposit can result without further nucleation. Two limiting forms of nucleation kinetics are instantaneous and progressive nucleation. Instantaneous nucleation is a process when nuclei are formed immediately at all available sites after applying an overpotential for it to occur [238]. Progressive

nucleation takes place when the metal centres gradually form, following first order kinetics. [19, 236]. Figure 14 illustrates the progressive nucleation and hemispherical growth of nuclei in the electrodeposition of metal layer on a macroelectrode surface [19, 236].

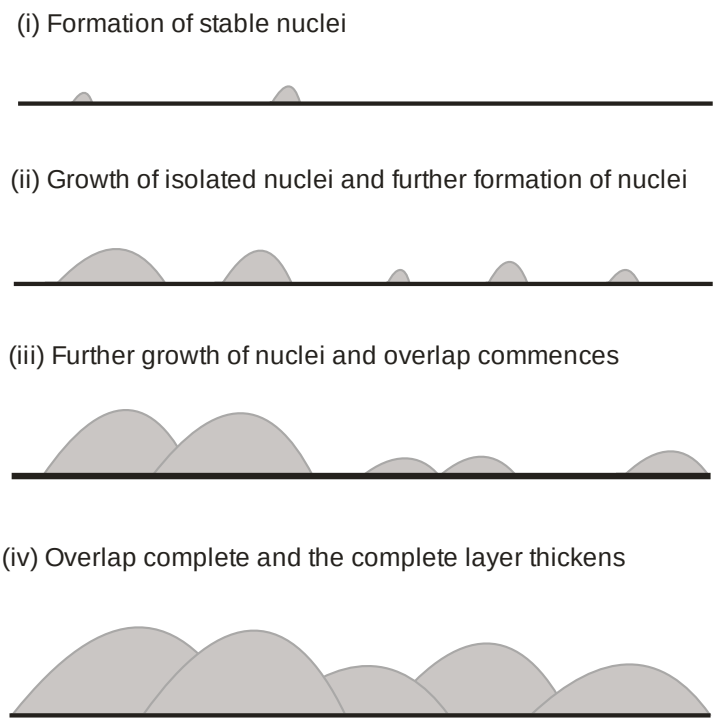

*Figure 14. Steps involved in the nucleation and growth of hemispherical nuclei on a macroelectrode surface. [Reproduced from Reference **[19, 236]**].*

Figure 15 shows the schematic diagram of typical response for current-time transient during the process of nucleation and growth of metal nuclei. Initially at any potential, no nuclei will exist and the current density is zero. As the nucleation overpotential is applied, the number of nuclei and the surface area of the metal centres increases with time, and this leads to a rising current – time transient [237]. Initially, the nuclei grow independently of each other and hemispherical diffusion zones form around each nucleus. As the hemispherical diffusion zones overlap, the mass transfer becomes linear [237]. Thus, the gradient for the transient will decrease

[19]. The overlapping nuclei centres will eventually form a complete layer and then, thickens. The thickening of the metal deposits on the electrode surface will either occur under diffusion control when a peak is observed followed by a Cottrell decay or form a plateau, when the thickening takes place under diffusion controlled or electron transferred when a plateau will be observed.

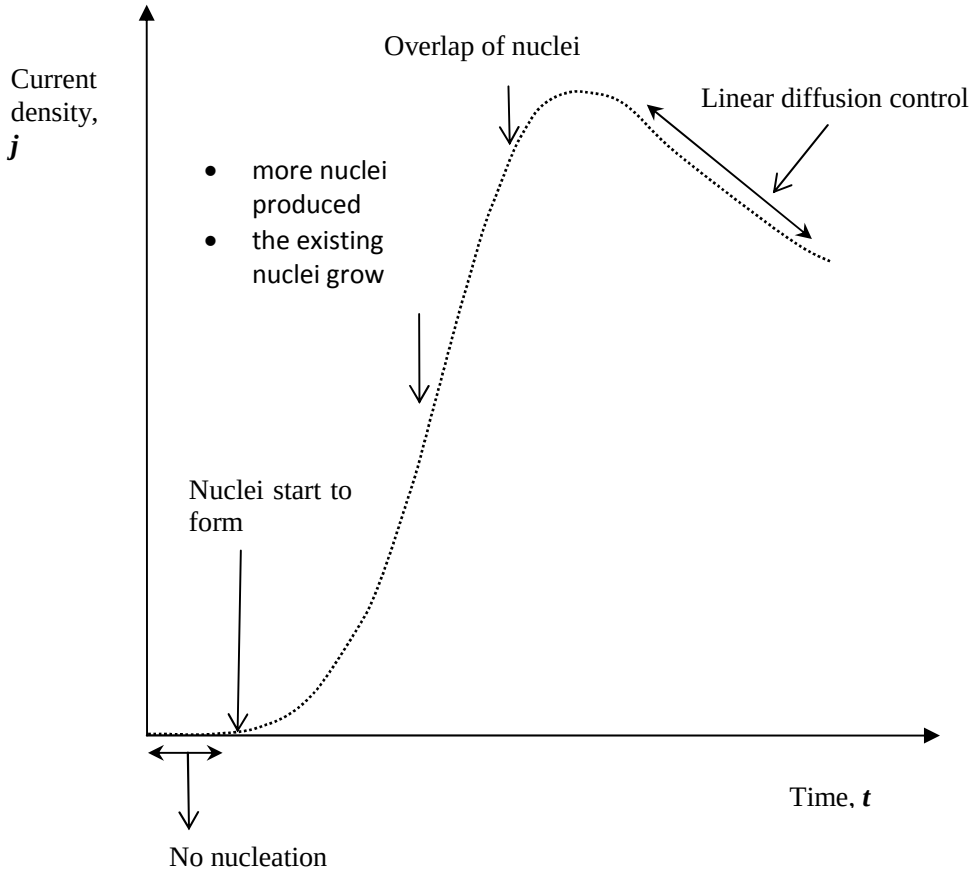

Figure 15. Typical current density-time transients for the nucleation and growth of metal deposits.

The rate of both nucleation and growth increases with applied overpotential [19]. At high overpotential, the timescale of the rise decreases (see Figure 16). As the potential is made more positive, there is still rising current-time transient observed. However, at the more negative overpotentials, the current-time transients overlap

beyond a peak, followed by smooth falling transients. The thickening of the metal layer under diffusion control leads to the falling of current density-time transients.

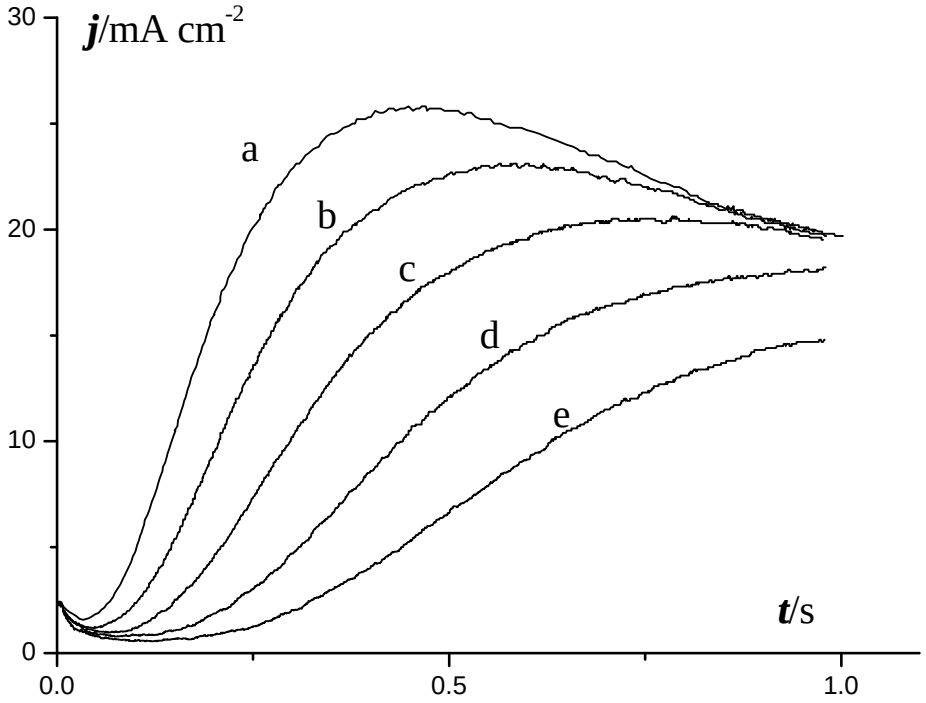

Figure 16. Current density-time transients for the nucleation and growth of a palladium deposit on a vitreous carbon electrode for various overpotentials. The potentials are stepped from 300 mV to **(a)** *-30 mV* **(b)** *-20 mV* **(c)** *-10 mV* **(d)** *0 mV and* **(e)** *+10 mV with respect to SCE. [Reproduced from Reference**[19]**].*

Figure 17 shows a typical cyclic voltammogram for Cu(II)/Cu(0) couple reaction recorded at vitreous carbon electrode in a solution containing low concentration of copper(II) sulphate in aqueous potassium chloride solution. On the forward scan, the current density is zero at the initial potential. As the potential is applied, the cyclic voltammogram will give a very steep reduction wave as the Cu(II) is reduced to Cu(I). The current density reaches a steady state until the overpotential (at -0.35 V ***versus*** SCE) is applied for the nucleation of Cu(0) on the polished vitreous carbon electrode surface to occur. At this potential, another steep reduction wave is observed. This reduction wave corresponds to the reduction of Cu(I) to Cu(0).

Again, the cyclic voltammogram reaches a plateau that corresponds to the mass transfer controlled reaction taking place.

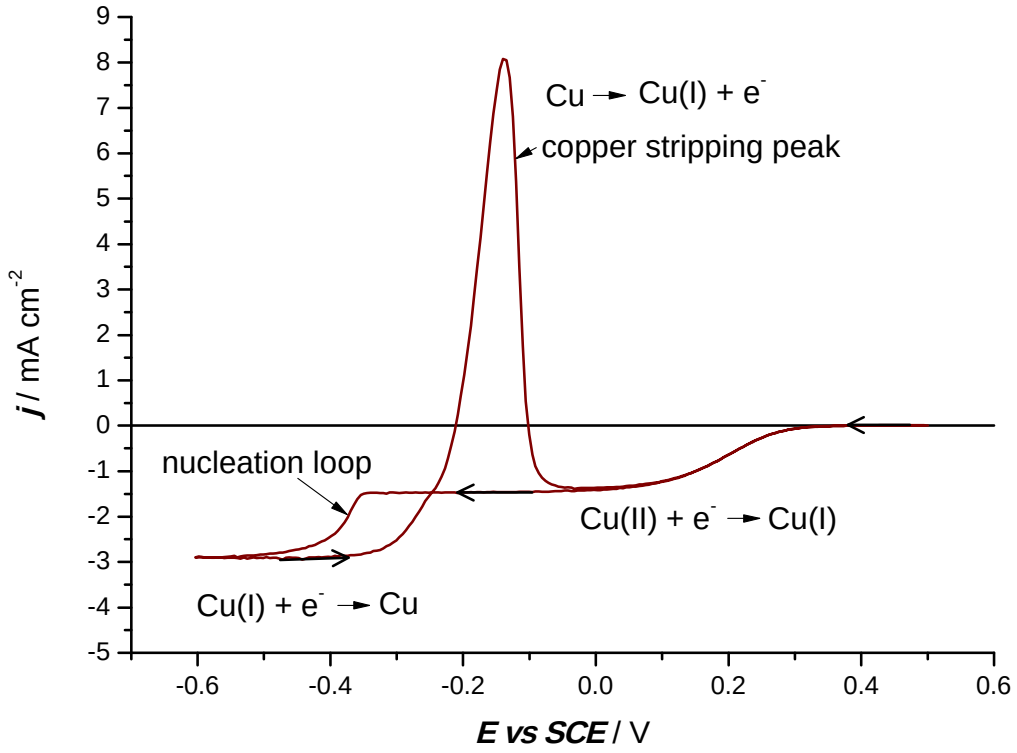

Figure 17. Cyclic voltammogram for the deposition of copper recorded at gold rotating disc electrode at 900 rpm in a solution containing copper(II) sulphate in the presence of chloride electrolyte.

On the reverse scan of the cyclic voltammogram, the copper metal deposition continues to occur on the newly deposited metal phase until the reduction of Cu(I) to Cu(0) is no longer possible and the equilibrium potential is reached. A nucleation loop is observed between -0.52 V and -0.25 V ***versus*** SCE. Therefore the current density obtained on the reverse scan is higher indicating the formation of copper is easier on the newly deposited metal phase when compared to polished vitreous carbon electrode. Thus, the thickening of the copper layer deposits can occur readily on the reverse scan. As the potential is made more positive after the equilibrium potential, the copper started to oxidise and a sharp stripping peak can be observed

between -0.25 V and 0 V ***versus*** SCE. In addition, the charge under the stripping peak and the cathodic charge for the Cu(I) to Cu(0) are similar.

In this research, the electrodeposition of gold and platinum deposits mainly on microelectrodes are carried out using chronoamperometry. The electrodeposition on microelectrodes will be discussed in the following subsection.

1.5.1. Electrodeposition on microelectrodes

The rate of mass transfer is very high at a small microdisc electrode and a steady state mass transport regime can be rapidly established. The diffusion controlled current density measured in the steady state condition [19] is given by

$$j_L = \frac{4nFDc^{\infty}}{\pi r} \tag{1.28}$$

$$\text{or} \qquad j_L = nFk_m c^{\infty} \tag{1.29}$$

where k_m is the steady state mass transfer coefficient;

$$k_m = \frac{4D}{\pi r} \tag{1.30}$$

and D is the diffusion coefficient, c^{∞} is the bulk concentration and r is the electrode radius.

The mass transfer coefficient can be increased by reducing the radius of the microelectrode. Thus, as the mass transport at the electrode surface is enhanced, the current to the electrode surface increases [236]. Moreover, the small area of the microelectrode allows relatively low currents to be passed, hence lowered potential ohmic drop, IR_u, where R_u is the uncompensated resistance. The interference from

double layer charging current is also decreased, thus this improves the techniques in potential step experiments and fast scan cyclic voltammetry [236]. In addition, when working with microelectrodes, it is possible to investigate the kinetics of the nucleation, the rate determining step and the mechanism involved in the growth of the metal centres [19, 236].

The metal deposition at a microdisc electrode occurs in a similar manner as on a macroelectrode surface. The nucleation, growth of metal centres and overlapping of the metal centres occur similarly until they cover all the available sites on the electrode surface and eventually thickens (as shown in Figure 18). The rate of metal deposition depends either on the rate of mass transfer of metal ions in solution or the kinetics of the electron transfer at the electrode surface. In short timescale experiment, the microdisc electrode will experience linear diffusion field to a plane electrode. Once the microelectrode experiences a hemispherical diffusion field, the metal nuclei start to grow faster on the perimeter of the metal layer deposits. This phenomenon is known as the "edge" effect [236]. Figure 19 shows the "edge" diffusion effect on a 50 µm diameter gold electrode after electrodeposition of platinum. The characteristic of the metal deposits is dependent on the electrochemical parameters used for the electrodeposition. The layer thickness of the metal phase can be controlled via the deposition charge being passed.

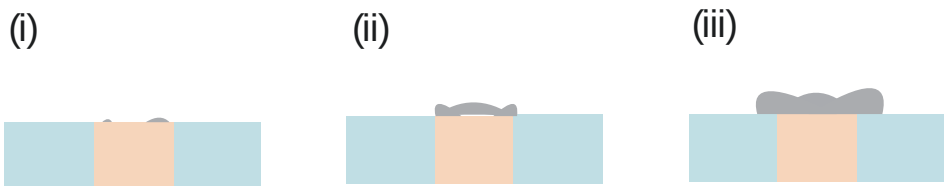

Figure 18. The process involved in the growth of a metal deposit on a microdisc electrode: (i) nucleation and growth of stable nuclei, (ii) complete coverage of metal deposits onto the electrode surface in a spherical diffusion field, (iii) the layer thickens and grows over the insulating sheath. [Redrawn from reference ***[236]****].*

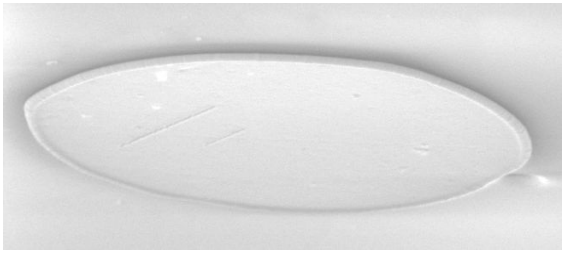

Figure 19. The surface of a microdisc electrode showing the "edge" diffusion effect after experiencing spherical diffusional field.

In this research, platinum and gold have been electrodeposited onto microelectrodes, both in aqueous and liquid crystalline phase. Despite the large surface area of mesoporous microelectrodes, it was shown that they still retain the mass transport efficiency [126, 153, 239]. Hence, together the high surface area of the nanostructure and the unique characteristics of microlectrodes will make them interesting for the application in various fields [103, 104, 119, 121, 126, 153, 239, 240]. In this study of electrodeposition, different types of electrodes have been employed, namely microdisc, macrodisc, microband and microwire electrodes. However, these electrodes have different diffusional fields. The microwire electrode has a cylindrical diffusion field when compared to linear diffusion profile to a plane macrodisc electrode. At a microdisc electrode the diffusion field is linear at short times and hemispherical at longer times as the steady state is reached. [236].

1.6. Characterisation of surfaces

The main technique used in this study was scanning electron microscope (SEM). In this technique, a beam of electrons directed at the specimen accelerated to an energy usually between 1 keV and 30 keV [241]. The scanning electron microscope consists of the electron gun, condenser lenses and vacuum system. The electron gun is usually the tungsten filament thermionic emission type. However, for higher

resolution, the field emission gun (FEG) is used, that is 100 times brighter than the filament [241]. A typical SEM with a tungsten filament and an objective lens $\boldsymbol{C_s}$ of 20 mm will have a resolution of around 5 nm. A high resolution of ~ 1 nm can be achieved when using FEGSEM. The data collections are acquired gradually, pixel by pixel, and line by line. Thus, the imaging data can be adjusted by varying the electrical signal with an amplifier. An environmental scanning electron microscope (ESEM) was available in the laboratory and was used for routine images. The ESEM typically operates at pressures in the region of 1 – 10 torr, where as a normal SEM (i.e. high vacuum mode) usually operates with a pressure below 10^{-6} torr [241, 242]. There is no pre-treatment required prior to the examination as the ESEM allows the imaging of uncoated non-conducting samples [241]. Thus, the finished electrode surface after the process of electrodeposition can be immediately observed using the ESEM. In addition, the sample can be examined in wet mode when using the ESEM. On the other hand, the sample examined using normal SEM has to be in vacuum condition. The electrical nonconductive sample also requires careful pre-treatment, that is, to coat the sample with a thin conducting layer of gold or carbon [241, 242]. An extra care is required to ensure that the coating does not cover any fine surface detail.

Alternative approaches to understanding the surface morphology would include transmission electron microscope (TEM) [157, 243, 244], atomic force microscopy (AFM) [109] and scanning tunnelling microscopy (STM) [102]. In transmission electron microscope, the features are similar to the scanning electron microscope. However, the images are produced and magnified in different ways. The TEM provides information about the internal structure of thin specimens, whereas the SEM can only show the morphology of the bulk specimens [241]. In addition, the specimen preparation for transmission electron microscopy is more complicated than for scanning electron microscopy. The examination of the specimen using AFM or STM can be carried out in air, liquid or vacuum [241]. In addition, both the AFM and STM can be operated under electrochemical control and this allows the observation of the birth and growth of the nuclei in-situ in real time [102, 241].

Thus, it is essential to have atomically flat substrates in order to observe the process of nucleation and growth of the nuclei. Nevertheless, the AFM images require computer processing and the interpretations of the AFM images are not straightforward as with an SEM [241].

1.7. Purpose of the project

The long term aim of this research project has been to prepare surfaces with controlled size and dispersion of small size particles by using electrochemical deposition. The small size particles are reported to enhance catalytic performance thus, reduce the amount of expensive metals such as platinum and gold loaded onto an inert substrate. However, it is a very challenging objective in order to produce well-distributed, very small centres of platinum and gold. The electrodeposition of platinum and gold has been studied using cyclic voltammogram as well as chronoamperometry experiments. The electrochemical deposition parameters such as deposition potential, deposition charge density are controlled, with the aim to produce small platinum centres. However, the deposition of metal is also influenced by the initial condition of the substrate. The difficulty encountered during this study is to have similar conditions of the starting materials, specifically reproducibility of the electrode surface after polishing. It is important to ensure that the electrode surface is free from any metal (platinum or gold) deposits prior to the elctrodeposition. Hence, various carbon subtrates that includes the ‘disposable’ carbon fibre and carbon paper microband electrodes have been used in aqueous plating bath solutions. However, the electrodepositiion of platinum in the liquid crystalline media cannot be carried out using the disposable electrode as it is brittle when placed in the high viscosity of the plating mixture. Thus, the nanostructured platinum has been investigated on gold electrode.

In all of this research, the presence of the platinum deposits as well as gold have been characterised by recording cyclic voltammograms in sulphuric acid solution. The morphology of the deposits has also been observed using the scanning electron microscope. These small centres have been investigated for their catalytic response for the hydrogen evolution and oxygen reduction reactions.

Further experimental details will be discussed in Chapter 2 that includes the chemicals, equipment and techniques used throughout this research. In Chapter 3, the electrodeposition of gold onto vitreous carbon is presented. This chapter is included in order to make comparison between the electrodeposition of platinum and gold from hexachloroplatinate(IV) acid and tetrachloroaurate(III) hydrate respectively.

Initial studies to understand the mechanism of the electrodeposition of platinum using hexachloroplatinic acid as the electroplating bath are discussed in Chapter 4. This is followed by investigations on the conditions for deposition of small platinum centres onto various carbon substrates from aqueous plating bath solutions. Chapter 5 includes the discussion on electrodeposition of platinum on gold electrodes, both in the aqueous solutions as well as in the presence of lyotropic liquid crystalline media, particularly in the hexagonal phase.

Chapter 2

2 Experimental

In this chapter, the chemicals, fabrication of electrodes, instrumentation and the characterisation used in this research will be explained in detail. This is followed by a presentation of the procedures for the electrodeposition of platinum and gold, fabrication of mesoporous platinum electrode and the characterisations of gold nanoparticles and platinum deposits, both from the aqueous solution as well as the lyotropic liquid crystals mixture.

2.1. Chemicals

Table 1 lists the reagents which have been used in this research work. All solutions were prepared with deionised water (resistivity of 18 MΩ.cm) from a Purite Select water purifying system. Where not otherwise stated, solutions were deoxygenated with a stream of argon through the cell before any measurements were taken.

Table 1. Chemicals and metals used in this research.

Name	***Formula***	***Supplier***	***Grade***
Hydrogen hexachloroplatinate (IV) hydrate	$H_2PtCl_6.\mathbf{x}H_2O$	Aldrich	99.9 %
Hydrogen tetrachloroaurate (III) hydrate	$HAuCl_4.3H_2O$	Aldrich	99.9 %
Lithium chloride	LiCl	BDH	99.0 %
Potassium chloride	KCl	BDH	99.5 %
Perchloric acid	$HClO_4$	Aldrich	70 %
Hydrochloric acid	HCl	BDH	sp. Gr. 1.18
Sulphuric acid	H_2SO_4	BDH	sp. Gr. 1.84
Octaethyleneglycol monohexadecyl ether	$C_{32}H_{66}O_9$	Aldrich	98.0 %
Potassium hydroxide	KOH	BDH	85.0 %
Oxygen	O_2	BOC Gases	
Argon	Ar	BOC Gases	
Nitrogen	N_2	BOC Gases	
Indium	In	Aldrich	99.9 %

Name	*Formula*	*Supplier*	*Grade*
Gold wire (Ø = 25 µm, 50 µm, 60 µm, 200 µm)	Au	Goodfellow	99.9+ %
Platinum wire (Ø = 50 µm)	Pt	Goodfellow	99.9+ %
Glassy carbon (Ø = 3 mm)	C	Tokai Carbon	
Carbon fibres (Ø = 7 µm)	C	Toray	
Carbon paper (0.26 mm thickness)	C	Toray	
Mercury	Hg	Alfa Aesar	99.998 %
Mercury(I) chloride	Hg_2Cl_2	Alfa Aesar	99.5 %
Mercury(I) sulphate	Hg_2SO_4	Fluka	97 %
Epofix resin and hardener		Struers	
Silver paint		RS Component	
Silver loaded epoxy resin		RS Component	
Silver loaded epoxy hardener		RS Component	

2.2. Fabrication of electrodes

Rotating disc electrodes, microdiscs, macrodiscs and microcylinder electrodes have been used in this research. Further details of these electrodes will be given below. The fabrication of reference electrodes is also explained in detail later.

2.2.1. Rotating disc electrode

The rotating working electrodes employed were gold and glassy carbon. A 5 mm diameter gold rotating disc electrode (as shown in Figure 20) was purchased from Pine Instruments (Pine electrode model AFE3T050AU; serial no. 10694). A glassy carbon rotating disc electrode was fabricated in the Mechanical Workshop, University of Southampton using a 3 mm diameter glassy carbon rod (Tokai Carbon Co. Ltd.) sealed in glass and covered with polytetrafluoroethylene (PTFE).

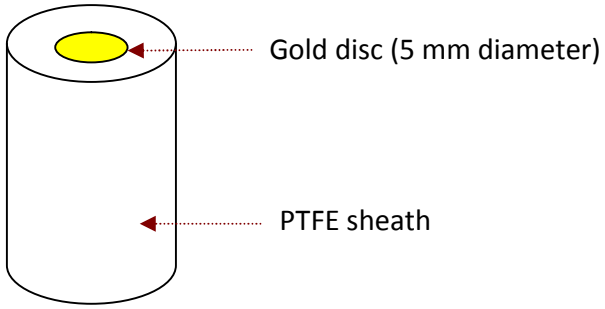

Figure 20. The schematic diagram of the gold rotating disc electrode.

Prior to the experiment, the rotating disc electrode was cleaned initially with silicon carbide paper C-1200 (to remove platinum deposits), followed by alumina suspension 5 µm, then a 2-step polishing with alumina slurries of 1 µm and 0.3 µm on velvet polishing pads (Buehler) and finally rinsed with purified water.

2.2.2. Microdisc, macrodisc and microwire electrodes

2.2.2.1. Gold microdisc electrode

The gold microdiscs of 25 µm, 50 µm and 60 µm diameter were fabricated in soda glass (as shown in Figure 21) using microwires supplied by Goodfellow Metals. The

gold microelectrode was sealed in glass, with an approximately 1 cm length exposed for connection. These were prepared by the glassblower in School of Chemistry, University of Southampton.

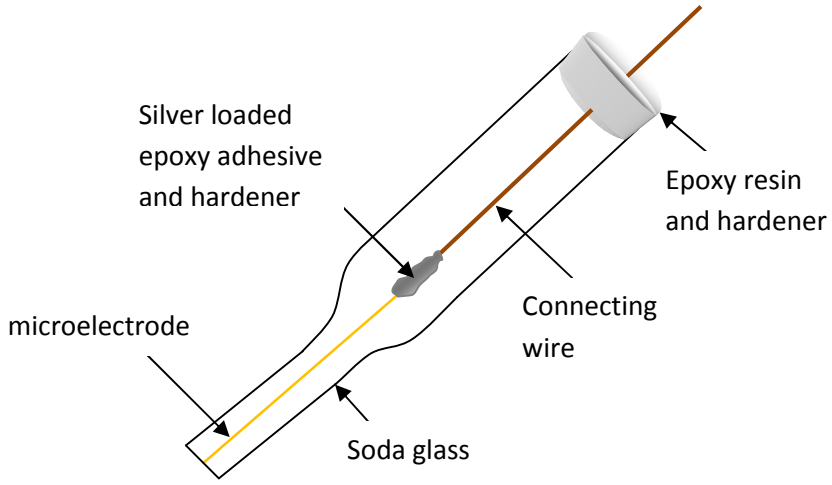

Figure 21. The schematic diagram of the gold microdisc electrode.

To make the contact, one end of the connecting wire was dipped into an equal mixture of silver loaded epoxy adhesive and hardener. It was immediately inserted into the glass tube to make contact with the exposed gold microwire. Once the contact has been made, the connecting wire was held in place by putting a mixture of quick set epoxy resin and hardener around the wire onto the glass. The epoxy mixture was left to dry and hardened.

The assembled microelectrode was initially polished with silicon carbide CC-240, CC-600, CC-1200 consecutively, followed by alumina lapping film of 12 µm (yellow), 5 µm (brown) and 1 µm (green). A cyclic voltammogram in 1 M sulphuric acid scanned at 100 mV s^{-1} was carried out to ensure there is a connection in the microelectrode. The microelectrode was finished by polishing with alumina powder 0.3 µm on a polishing cloth and rinsed with purified water. A clean cyclic voltammogram in acid solution showing the features of gold reduction/oxidation peaks was to be achieved before it was ready to be used. A scanning electron

microscopy image of the electrode surface was also taken before conducting further experiment; satisfactory electrodes showed no features on a 1µm scale.

Before every experiment, the microelectrode was polished on a polishing wheel for with silicon carbide CC-1200, then on nylon polishing cloth with 5 µm alumina suspension followed by a 2-step polishing with alumina powder 1 µm and 0.3 µm. Finally the microelectrode was rinsed with purified water.

2.2.2.2. Carbon microdisc electrode

The carbon fibre disc electrode of 7 µm diameter sealed in soda glass was prepared by the glassblower, School of Chemistry, University of Southampton. The connecting wire and the carbon fibre were made in contact by using indium. The microelectrode was polished with 1 µm alumina powder, followed by 0.3 µm and finally rinsed with purified water.

2.2.2.3. Carbon microband paper electrode

The carbon paper (Toray carbon paper, TGPH-090) of thickness 0.26 mm with a length of 10 mm and a height of about 40 mm was cut. The sides of the carbon paper were later insulated with clear nail polish leaving an allowance for connection (see Figure 22). A new surface of carbon paper was revealed by cutting the edge of the paper, hence only a band of carbon paper exposed for electrodeposition. There is no pre-treatment to the surface of the microband carbon paper. Once the surface is revealed, it is readily use for experimental measurement. The connection was made using a crocodile clip attached to the carbon paper.

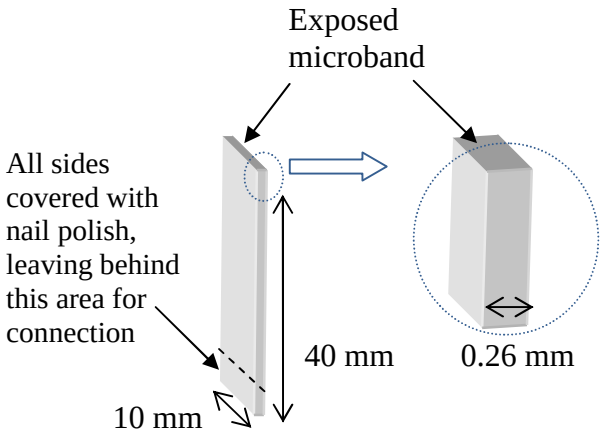

Figure 22. Schematic diagram of carbon paper microband used as working electrode.

2.2.2.4. Carbon fibre microcylinder electrode

A carbon fibre wire electrode of 7 µm diameter with a length of 5 mm was used as the working electrode in a three electrode system in one compartment glass cell. Figure 23 shows the schematic diagram of the fabrication of carbon fibre wire electrodes.

A glass capillary tube with 1 mm and 2 mm for inner and outer diameter respectively, was purchased from World Precision Instruments, Inc. The glass capillary tube was cut into an approximately 10 mm long, followed by rinsing with purified water and kept in the oven for about 30 minutes.

Later, a piece of carbon fibre of 7 µm diameter was inserted into the capillary tube using a cross-locking tweezer. A connecting wire initially dipped with an equal mixture of silver loaded epoxy adhesive and hardener, was inserted into the capillary tube to make the contact with the carbon fibre. The silver loaded epoxy adhesive and

hardener were left to dry. Once the connection had been made, the capillary tube was filled with epoxy resin and hardener and it was left overnight to settle and cure.

One end of the tube has an extended carbon fibre that is intended to be used as a microcylinder or microwire carbon electrode. The length of the exposed carbon fibre wire was measured using a ruler of high precision, with smallest division of 0.5 mm. The carbon fibre was also measured using the scanning electron microscope. The error arising from the length measurement of the carbon fibre was (± 0.5) mm.

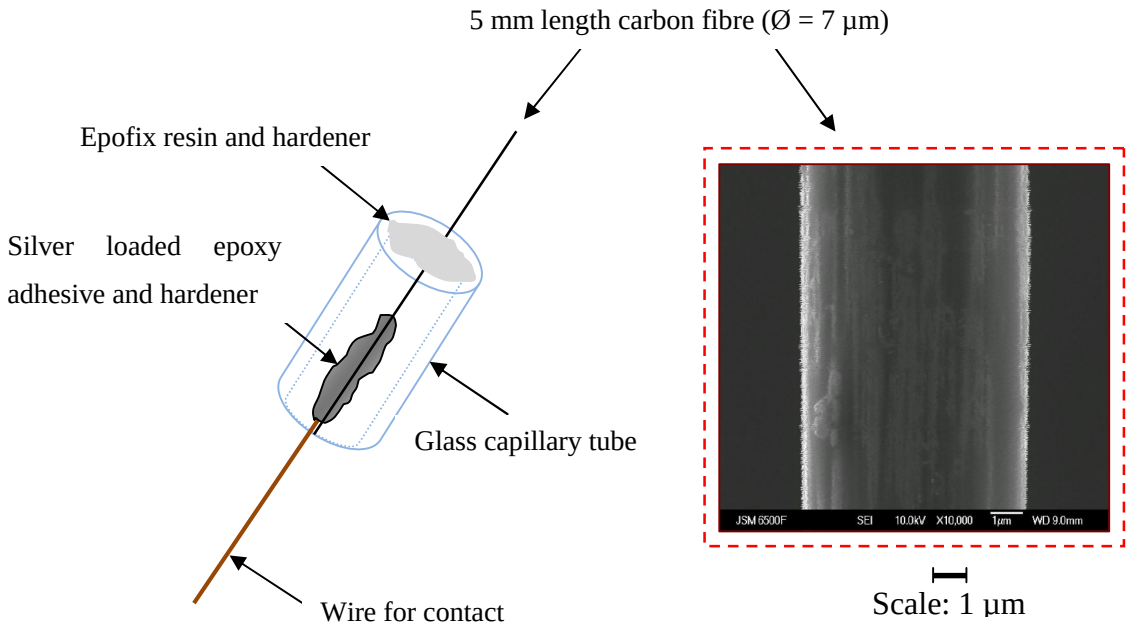

Figure 23. The schematic diagram of a 7 µm diameter carbon fibre wire electrode.

This working electrode can be used immediately without any pretreatment before carrying out any voltammetric experiment. It is important for the electrode surface to be free from platinum before commencing any experiments. It was therefore intended to be used only for one electrodeposition experiment and to be characterised later. Hence, this successful fabrication of disposable cheap electrode helps to save time from polishing the electrode surface.

2.2.2.5. Glassy carbon disc macroelectrode

A 3 mm diameter glassy carbon disc (Tokai Carbon Co. Ltd.) was fabricated in a soda glass by the glassblower, School of Chemistry, University of Southampton. A small amount of silver paint was painted onto the glassy carbon. Indium was cut into tiny pieces and placed inside the tube. The indium was melted using a hot air gun and the connecting wire was inserted immediately. The connecting wire was kept in place by applying a mixture of quick set epoxy resin and hardener onto the connecting wire and glass tube. Prior to recording experiments, the glassy carbon electrode was polished with silicon carbide CC1200, followed by a suspension of aluminium oxide 5 µm, then alumina powder of 1 µm and 0.3 µm on a polishing cloth.

2.2.2.6. Reference electrodes

The reference electrode employed in the experiments was either a laboratory constructed saturated calomel electrode (SCE) or saturated mercury sulphate electrode (SMSE) as shown in Figure 24. The reference electrode was prepared according to the procedure described by ***P. N. Bartlett*** [245]. The two components of glass used in the making of reference electrode, consist of an inner tube with a platinum wire and outer glass tube, were prepared by the glassblower in School of Chemistry, University of Southampton.

The inner tube was filled with a drop of mercury until the platinum wire was covered. This was followed by the calomel paste (a mixture of Hg_2Cl_2 / KCl) and later packed with glass wool to hold the paste in place. The outer glass tube was designed with a porous sinter at one end. It was filled with saturated potassium chloride solution with few grains of potassium chloride crystals. The inner and outer tubes were screwed together, making sure that no bubbles were trapped inside the

electrode. The assembled electrode was stored in saturated potassium chloride solution when not in use.

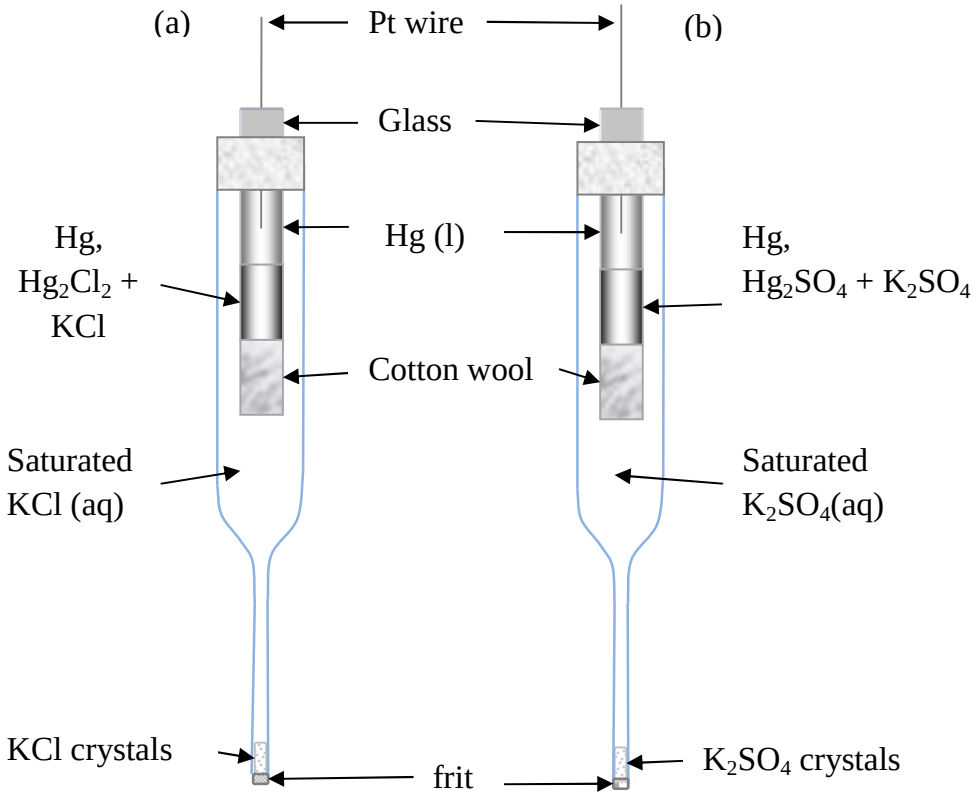

Figure 24. The schematic diagram of the laboratory constructed **(a)** *saturated calomel electrode (SCE)* **(b)** *saturated mercury sulphate electrode (SMSE).*

Before taking measurements, the reference electrode was rinsed with purified water to remove the potassium chloride solution from the outer glass. For fabricating the saturated mercury sulphate reference electrode, the calomel paste was replaced with a mixture of Hg_2SO_4/K_2SO_4 and the outer tube was filled with saturated mercury sulphate solution instead. The saturated mercury sulphate electrode was stored in saturated mercury sulphate solution during storage. The saturated calomel electrode was tested against saturated mercury sulphate electrode, and the potential difference

between the two electrodes was 0.42 ± 0.01 V. The choice of reference electrode depended on the solution being studied but all potentials in this thesis have been converted with reference to the saturated calomel electrode (SCE).

2.3. Electrochemical cells and instrumentation

In this research, rotating disc, macro and micro disc electrodes as well as microcylinder electrodes were employed. The detail of instrumental configuration for each of the electrode is explained below. All experiments were carried out at room temperature.

2.3.1. Rotating disc electrode experiments

The voltammetric experiments were carried out in a three electrode, two compartment glass cell with a 5 mm diameter gold (Pine instruments) or 3 mm diameter homemade glassy carbon rotating disc electrode. Figure 25 shows the schematic diagram of the instruments and the 2-compartment cell used in the rotating disc electrode experiments. A platinum mesh was used as secondary electrode. The reference electrode used was either saturated calomel or saturated mercury sulphate electrode.

The rotation of the disc electrode was controlled with an EG and G Parc unit, model ***616***. The rotating disc electrode experiments were carried out at controlled potential using a home-built potentiostat with potential waveforms generated from a data acquisition board (National Instruments LabVIEW™ 5.1). The data obtained was then exported into Origin 8 to be analysed further.

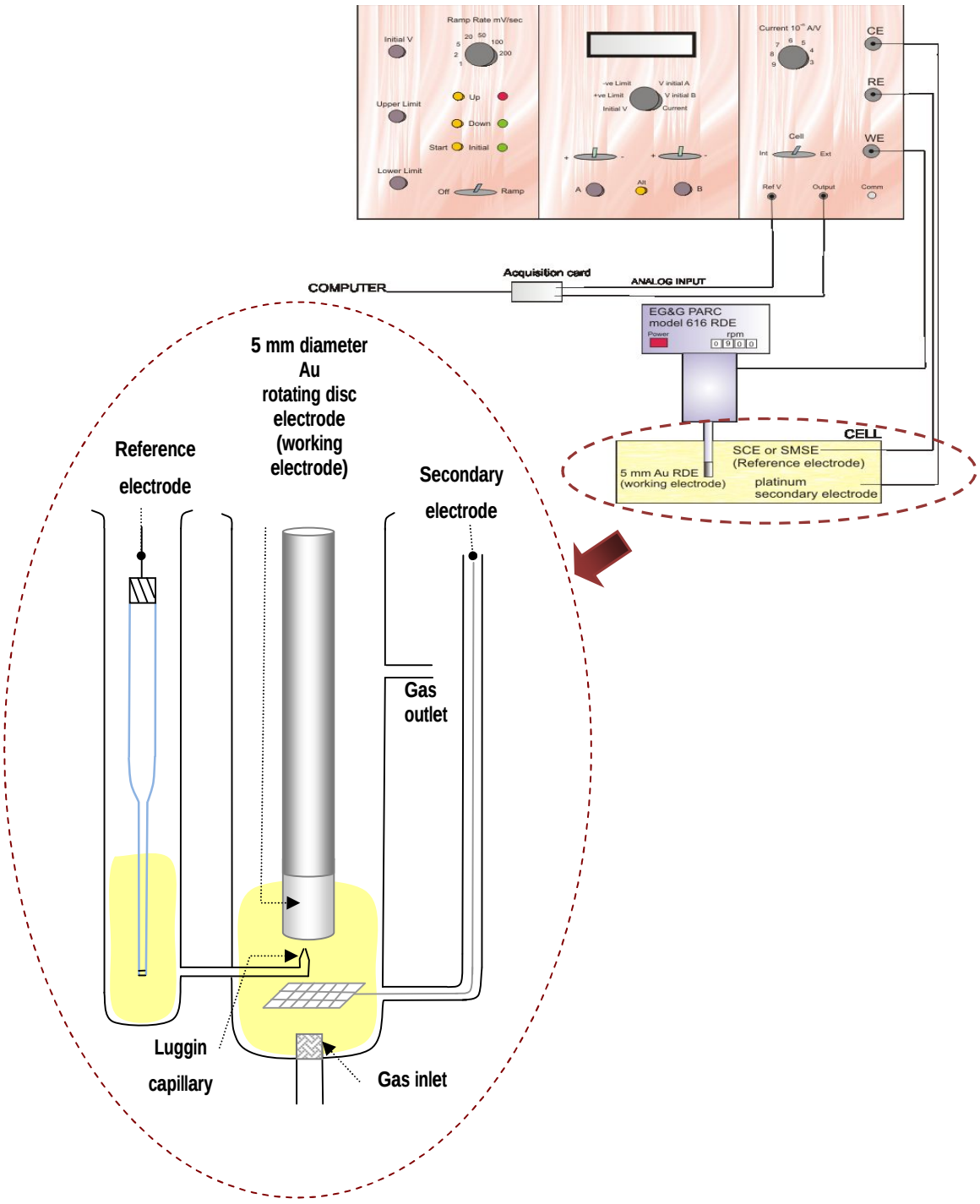

Figure 25. Schematic diagram of the setup of the instrument connected to a three-cell electrode with a fixed platinum secondary electrode, rotating disc electrode and a reference electrode placed in the second compartment at room temperature.

2.3.2. Microelectrode experiment

The voltammetric experiments were carried out using a two electrode system in a three neck pear-shaped cell placed inside an earthed aluminium Faraday cage. Gold microdisc and carbon fibre electrodes were used as the working electrodes. The reference electrode used in the experiments also served as a counter electrode. All connections were made using shielded cables to reduce noise.

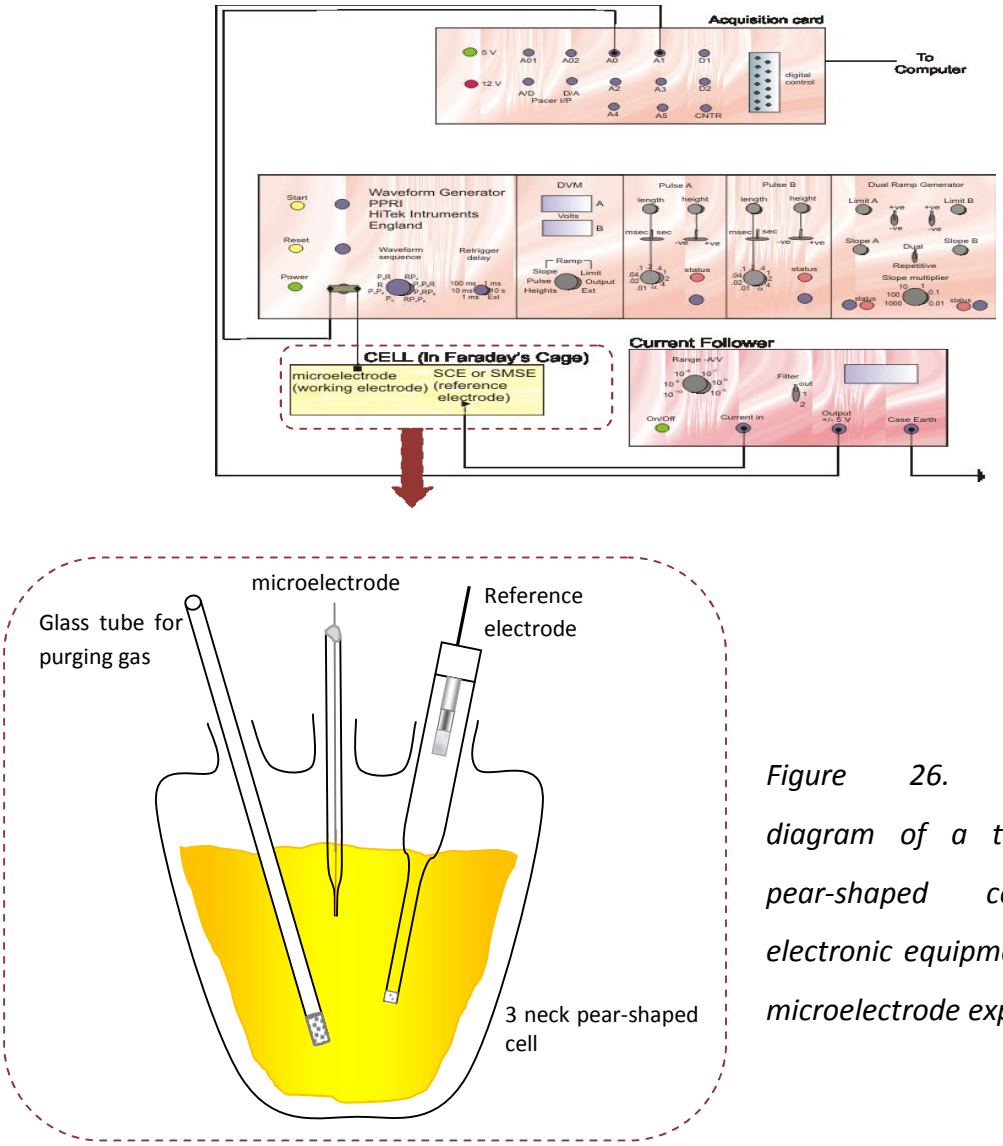

Figure 26. Schematic diagram of a three neck pear-shaped cell with electronic equipment for the microelectrode experiment.

A home-made current follower and a HiTek waveform generator, model PPR1 was used to measure the current and obtain a controlled potential for the required electrode potential range together with data acquisition software (National Instruments LabVIEW™ 5.1). The data were later transferred and analysed in Microcal Origin. The schematic diagram of a 3-neck cell together with the setup of the instruments for the microelectrode experiments were shown in Figure 26.

2.3.3. Microcylinder electrode experiment

The experiments were carried out using a three electrode system in a one-compartment glass cell placed in a Faraday cage. The working electrode was a 7 μm diameter carbon fibre with a length of 5 mm exposed to the solution. The carbon fibre wire electrode was introduced into the solution by using a micropositioner and controlled stage as shown in Figure 27. Saturated calomel and saturated mercury sulphate electrode have been used as the reference electrode depending on the nature of the experiment. A loop of platinum mesh was used as the counter electrode.

A micro Autolab Type III with the General Purpose Electrochemical System (GPES) version 4.9 © Copyright 2007 EcoChemie was used to obtain the voltammetry and the chronoamperometry. The data were later analysed using the standard software.

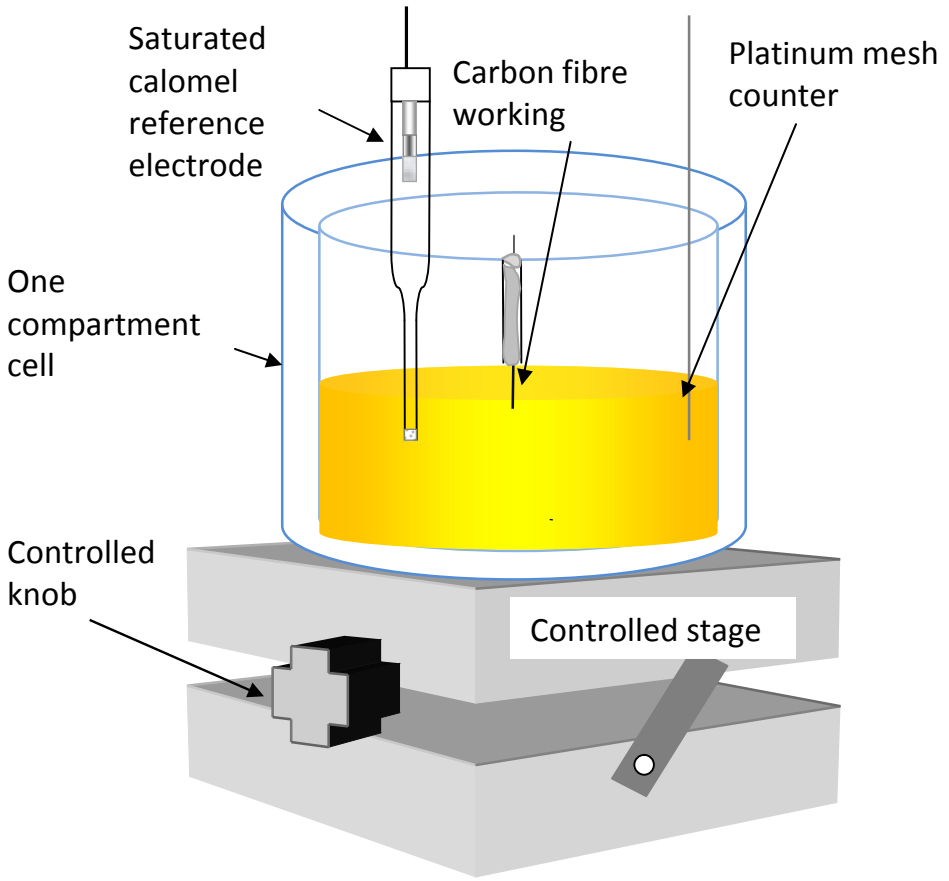

Figure 27. The schematic diagram for the set-up of microcylinder carbon fibre electrode experiment.

2.4. Electrodeposition of platinum

In this research, the source of platinum in plating bath solution was from hydrogen hexachloroplatinate (IV) hydrate. In most experiments, a volume of 25 – 30 mL containing 5 mM hexachloroplatinate(IV) in 0.1 M hydrochloric acid was used in the electrochemical deposition experiment. This clear yellow aqueous solution was found to be stable as reproducible voltammograms were produced over a range of time of up to one month. The working electrodes used in the electrodeposition of platinum were gold microdisc electrodes, gold and glassy carbon rotating disc

electrodes and carbon fibre electrodes. All of the electrochemical deposition experiments were carried out at room temperature.

2.5. Electrodeposition of gold

A solution containing 1 mM hydrogen tetrachloroaurate hydrate and 0.1 M hydrochloric acid was used as the electroplating bath for electrodeposition of gold. A volume of 25 – 30 mL of this clear yellow aqueous solution was placed in a three neck pear-shaped cell. The electrodeposition experiment was conducted at room temperature. Chronoamperometry method was applied until the desired charge had been passed.

The working electrodes employed in this research were glassy carbon, either in the form of rotating disc or stationary electrodes. Prior to the electrodeposition experiment, the glassy carbon was electrochemically cleaned in 1.0 M hydrochloric acid in the range between 0 V to +1.4 V ***versus*** SCE. This was carried out in order to remove electrochemically the electrodeposited gold particles on the carbon electrode. This was followed by polishing with 1 micron and 0.3 micron alumina slurries consecutively.

2.6. Mesoporous platinum electrode

The mesoporous platinum electrode was prepared according to the procedure described by ***Attard et. al.*** [105]. The preparation of the platinum plating mixture and the fabrication of the mesoporous platinum electrode will be described below in details.

2.6.1. Platinum plating mixture

The platinum plating mixture consists of octaethyleneglycol monohexadecyl ether, hexachloroplatinate (IV) acid and water. The required weight percentage of each substituents were mixed together in a sealed vial and subsequently heated up to 40ºC for 30 minutes. The weight percentage of the substituents was determined from the ternary phase diagram (shown in Figure 28) reported by ***Attard et. al***. [143].

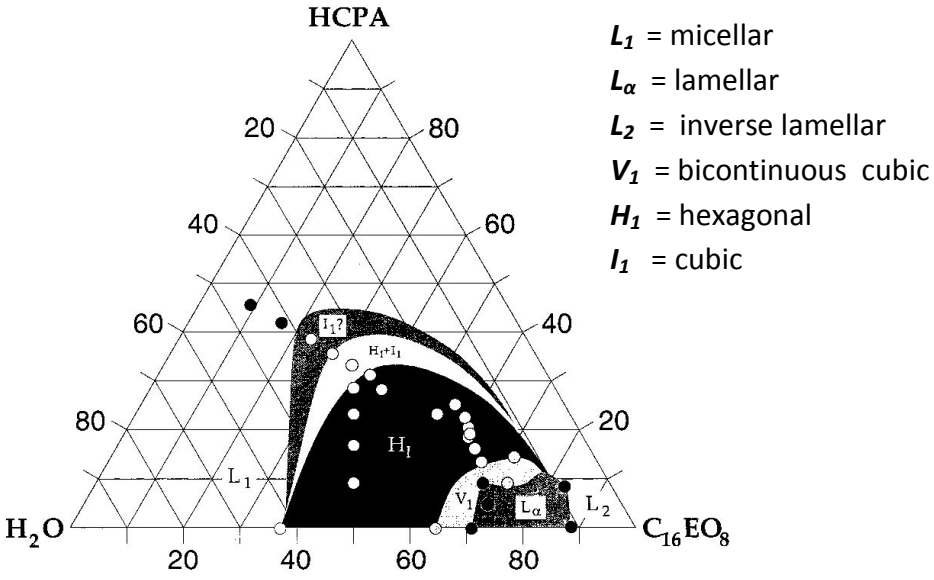

Figure 28. Ternary phase diagram of octaethyleneglycol monohexadecyl ether ($C_{16}EO_8$), hexachloroplatinate (IV) acid (HCPA) and water (H_2O) at 40ºC. Note that the phase boundaries are hypothetical and are drawn as a guide to the eye. [Reproduced from Ref. ***[143]*** *].*

The platinum plating mixture used in this study contained 0.42 g octaehyleneglycol monohexadecyl ether, 0.29 g water and 0.29 g hexachloroplatinate (IV) acid. The mixture was stirred until it formed a homogeneous mixture. The resultant viscous

mixture was again reheated for another 30 minutes. Later, the mixture was left to cool to room temperature.

Another approach was made by using 0.08 g of hexachloroplatinate (IV) acid with 0.46 g surfactant and 0.46 g water. Figure 29 shows the phase diagrams of octaehyleneglycol monohexadecyl ether, water and hexachloroplatinate (IV) acid for compositions that are 50 wt. % surfactant: 50 wt. % water.

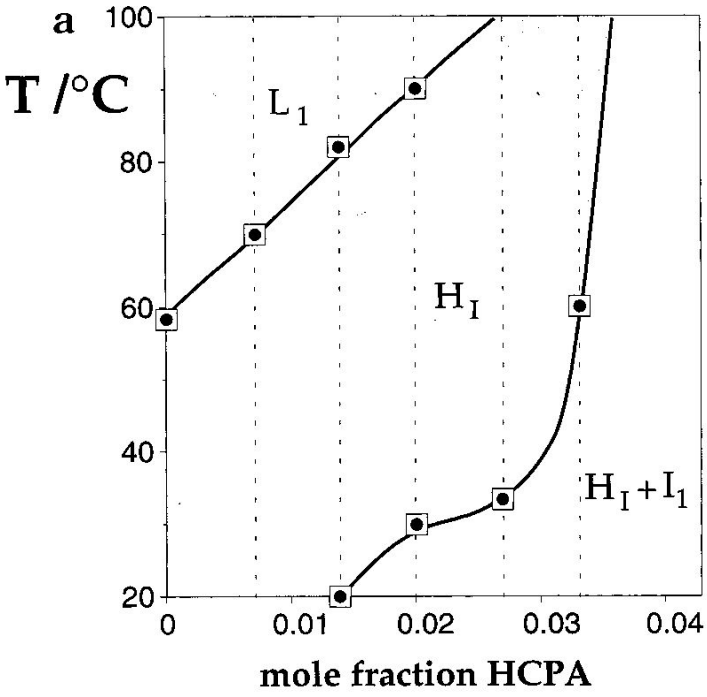

L₁ = micellar phase
H₁ = hexagonal phase
(***H₁*** + ***I₁***) = hexagonal and cubic phase

Figure 29. Phase diagram of octaethyleneglycol monohexadecyl ether ($C_{16}EO_8$) and hexachloroplatinate (IV) acid (HCPA) with a fixed weight percentage (50 wt. %) of surfactant and water. (taken from Ref. ***[143]****).*

Both platinum plating mixtures aim to produce the hexagonal phase of lyotropic liquid crystal. The hexagonal lyotropic liquid crystal phase was confirmed by observing the mixture under the polarising light microscope.

2.6.2. Polarising light microscope

The phase structure of the lyotropic liquid crystals are determined by observing the texture of the plating mixture under a polarising optical microscope. The platinum plating mixture was observed under polarising light microscope (Olympus BH2) equipped with a Linkam TMS 90 heating / cooling stage. A minute amount of the plating mixture was sandwiched between a glass slide with a cover slip and the sample is placed between two crossed polarisers, that is, 90º to each other. As light passes through the sample, the polarisation changes due to the birefringence of the plating mixture, therefore exposing the optical texture of the lyotropic liquid crystalline phase.

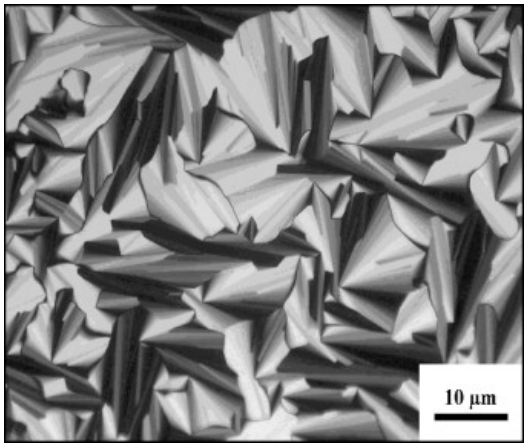

Figure 30. Image of the hexagonal liquid crystalline phase observed under polarising optical microscope. [Reproduced from reference ***[246]****].*

In this research, the ternary plating mixture was prepared for the hexagonal phase and the micellar solution. The hexagonal phase of lyotropic liquid crystal exhibits birefringence, therefore it is anisotropic medium [138]. The observation of fan-like optical texture showed the characteristics of hexagonal phase ($\boldsymbol{H_I}$) of lyotropic liquid crystals. These features are consistent with those reported by ***Zhong et.al.*** (see Figure 30) [246]. Moreover, the hexagonal phase was stable even up to 80ºC. The micellar solution is optically isotropic, hence does not produce optical texture. It shows no birefringence, therefore it appears black between crossed polarizers [247]. However,

cubic phase is also isotropic. The micellar solution and the cubic phase can be distinguished by the massive difference in viscosities between them [145].

2.6.3. Fabrication of small platinum centres

The resultant platinum plating mixture was placed on a mesh of platinum wire that acts as a secondary electrode. The reference electrode (SCE) and the working electrode were introduced into the plating mixture as shown in Figure 31. The working electrodes used were gold electrodes fabricated in glass with a diameter in the range between 25 and 60 µm.

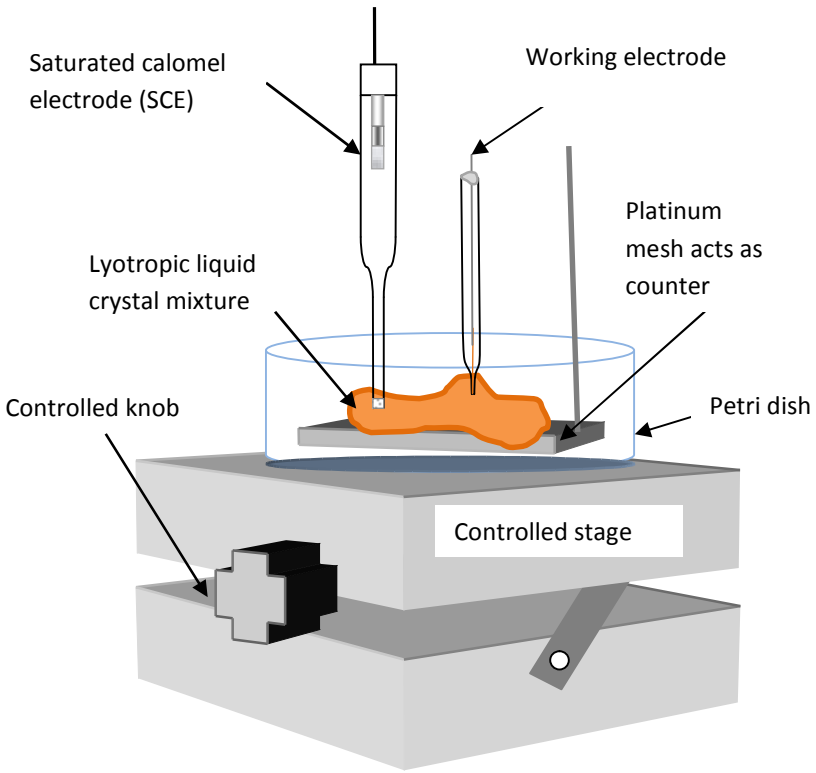

Figure 31. Schematic diagram showing the arrangement of the three electrodes (working, counter and reference electrodes) for the electrodeposition of mesoporous platinum.

A fixed potential (between - 0.2 V and +0.2 V ***versus*** SCE) was applied to electrodeposit the platinum nanoparticles. The duration of electrodeposition time was varied in order to pass through sufficient amount of charge density to electrodeposit platinum nanoparticles of sizes less than 100 nm. The deposition charge density was controlled so that very low charge density passed with the aim of depositing small centres instead of a mesoporous film. The platinum nanoparticles were electrodeposited around the template made by the surfactant.

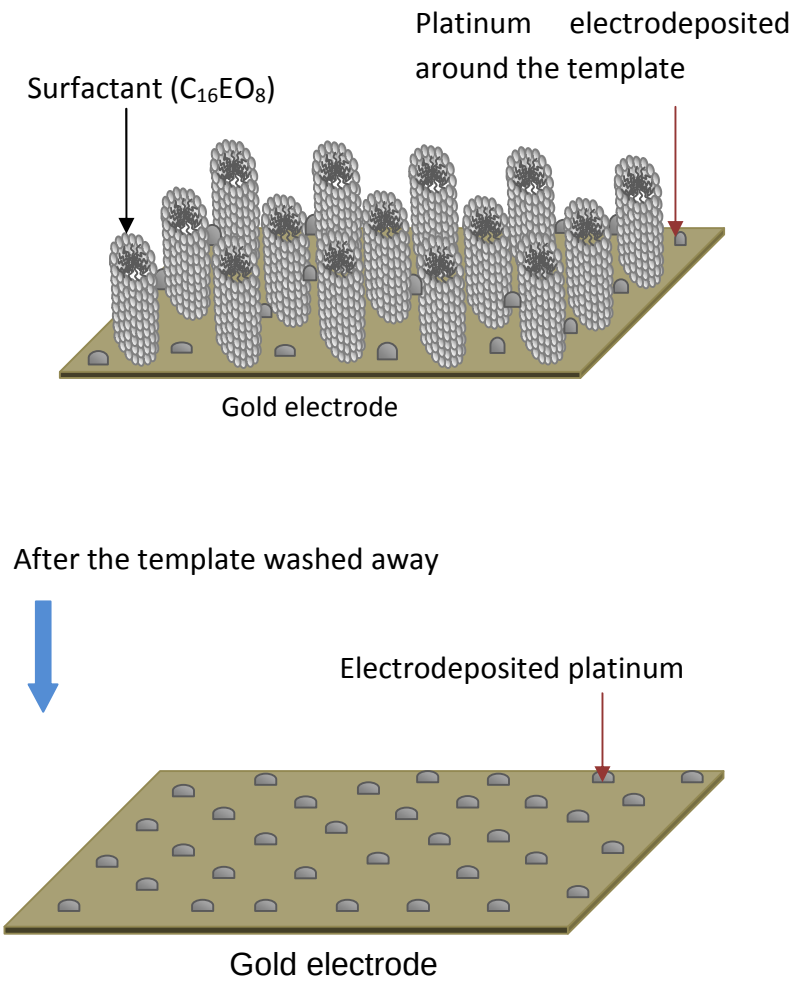

Figure 32. Schematic diagram of the process of electrodeposition of platinum nanoparticles using lyotropic liquid crystal template.

After electrodeposition, the microelectrode was soaked in stirred water for two days (by changing the water every 30 minutes except overnight) to remove most of the surfactant. The schematic diagrams showing the process of electrodepositing platinum around the template and the expected outcome of the electrodeposited platinum nuclei after removing the surfactant are shown in Figure 32. The diagram of the evenly distributed metal centres on the gold substrate is hypothetical. The mesoporous platinum electrode was confirmed by recording cyclic voltammograms in acid solution. Later, further characterisations were carried out to determine the catalytic activity. This will be mentioned in detail later in the results section.

2.7. Characterisations

The presence of electrodeposited platinum on the electrode was confirmed in acid solution and later the morphology of the electrode surface observed under scanning electron microscopy. Details of the experiment will be discussed below. In this thesis, all the measured current is presented in current density. It is calculated from the measured current divided by the geometric area of working electrode.

2.7.1. Cyclic voltammetry in acid solution

Before and after the electrodeposition in plating bath solution, the working electrode was characterised by recording cyclic voltammograms in 1 M sulphuric acid. The initial voltammogram was to ensure that no platinum was present on the working electrode before experiments commenced. The typical voltammograms for platinum coated on gold and carbon electrode are shown in Figure 33 and Figure 34 respectively. The details of the cyclic voltammograms will be discussed in chapters 4 and 5.

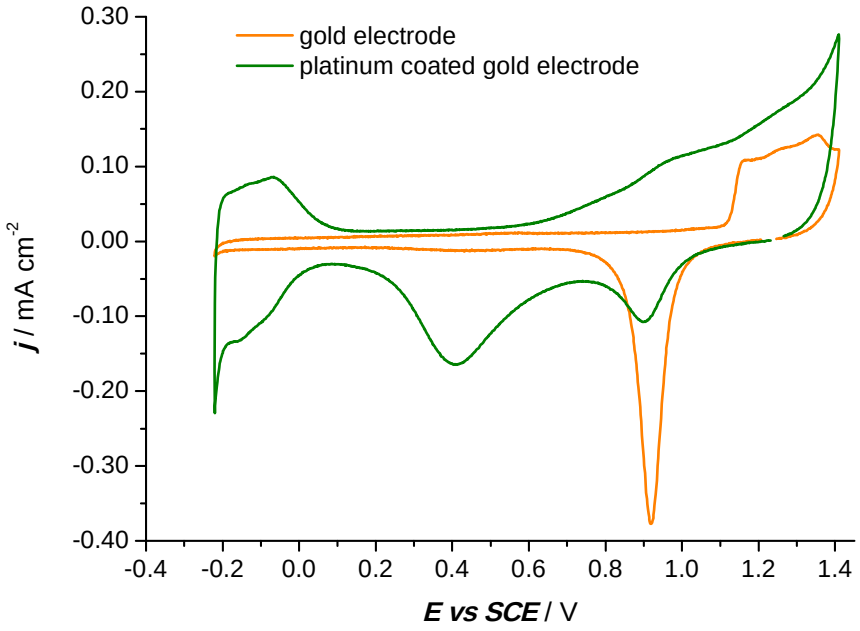

Figure 33. Cyclic voltammograms scanned at 50 mV s^{-1} in 1 M sulphuric acid for a 5 mm diameter gold and partially platinum coated gold electrode rotated at 900 rpm.

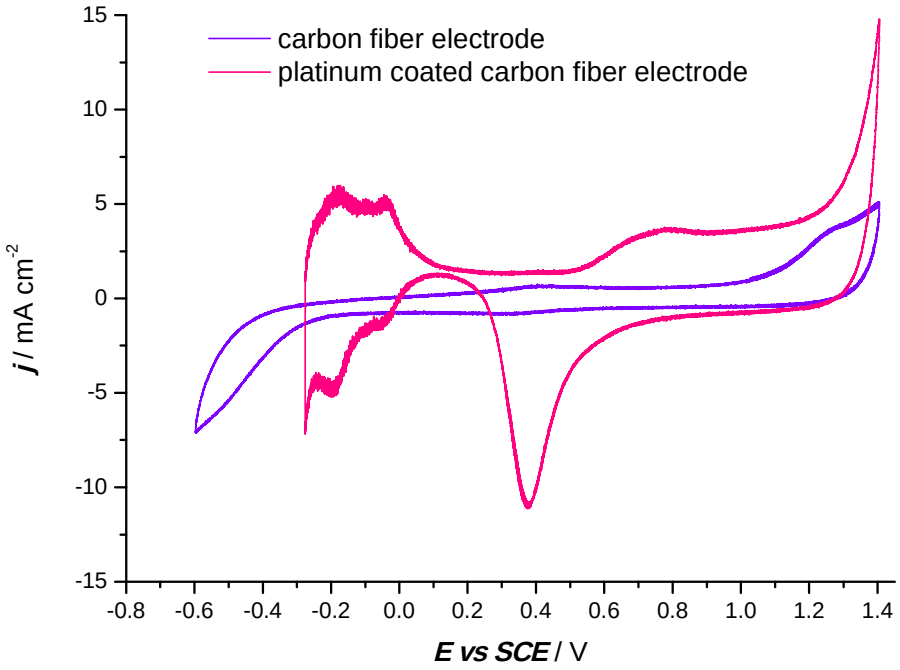

Figure 34. Cyclic voltammograms in 1 M sulphuric acid recorded on 7 µm diameter carbon fibre electrode and platinum coated carbon electrode Scan rate 50 mV s^{-1}.

2.7.2. Faraday's Law

Faraday's law states that the quantities of substances consumed/formed in an electron transfer are proportional to the amount of charge, ***Q*** (in C) passed and consumed at the electrode [32, 238].

$$\boldsymbol{Q} = \boldsymbol{mnF} \tag{2.1}$$

where ***m*** is the number of moles of product formed, ***n*** is the number of electrons involved and ***F*** is Faraday's constant (96485 C mol^{-1}).

Assuming that the quantity of charge is mainly due to the Faradaic equation (2.2), the thickness of platinum layer deposited onto the electrode can be estimated from the amount of charge passed, ***Q***, the area of the electrode, $\boldsymbol{A_{geo}}$, the molecular weight, ***M*** and density of platinum, $\boldsymbol{\rho}$ respectively (See equation (2.3)).

$$\boldsymbol{PtCl_6^{2-}} + 4\boldsymbol{e^-} \rightarrow \boldsymbol{Pt} + 6\boldsymbol{Cl^-} \tag{2.2}$$

$$\text{layer of thickness} = \frac{\boldsymbol{QM}}{4\boldsymbol{F}\rho\boldsymbol{A_{geo}}} \tag{2.3}$$

The real surface area of platinum was determined by integrating the area under the hydrogen adsorption peak (with correction for double layer charging), that is, the adsorption charge, $\boldsymbol{Q_{ads}}$. Thus the electroactive area can be calculated by dividing the adsorption charge with the charge density for a monolayer, $\boldsymbol{Q_{mono}}$ that was reported to be 210 µC cm^{-2} [234, 248].

$$\boldsymbol{A_{electroactive}}\ (\text{in } \boldsymbol{cm^2}) = \frac{\boldsymbol{Q_{ads}}\ (\text{in } \mu\boldsymbol{C})}{\boldsymbol{Q_{mono}}\ (= 210\ \mu\boldsymbol{C}\ \boldsymbol{cm^{-2}})} \tag{2.4}$$

Hence, the value of the roughness factor can be obtained by dividing the electroactive area with the geometric surface area of the electrode.

$$R_f = \frac{A_{electroactive}}{A_{geometric}} \tag{2.5}$$

However, for lower deposition charge density, it is impossible to calculate the adsorption charge as the hydrogen adsorption/desorption peaks were not resolved.

The specific catalyst area, S can be calculated using the platinum electroactive area, $A_{electroactive}$ and the platinum loading, W [102]. The platinum loading, W (μg cm^{-2}) is derived from equation (2.7);

$$S = \left(\frac{A_{electroactive}}{A_{geometric} \times W} \right) \times 100 \tag{2.6}$$

$$W = \frac{QM}{4F} \tag{2.7}$$

where Q and M are the amount of charge passed and the molecular weight of platinum respectively.

2.7.3. Electrocatalytic activity reactions

The catalytic responses of platinum nanoparticles towards the hydrogen evolution and oxygen reduction reactions in acid media are investigated. The catalytic activities of gold nanoparticles on carbon were determined in oxygen reduction reaction in basic solution. Further explanations on these reactions are mentioned below.

2.7.3.1. Hydrogen evolution

The catalytic activity for the hydrogen evolution was measured out in 1 M sulphuric acid saturated with argon. The voltammogram was scanned from -0.2 V to -0.8 V ***versus*** SCE at a scan rate of 100 mV s^{-1}.

2.7.3.2. Oxygen reduction in acidic media

Oxygen reduction was studied in 0.1 M perchloric acid saturated with oxygen. A saturated calomel electrode was used as the reference electrode. The voltammogram was recorded between +0.8 V to -0.2 V ***versus*** SCE at a potential scan rate of 10 mV s^{-1}.

2.7.3.3. Oxygen reduction in basic media

The electrodeposited gold particles on the glassy carbon electrode were characterised in 0.5 M potassium hydroxide saturated with oxygen. Cyclic voltammogram was scanned between 0 V to -0.4 V versus SCE at a scan rate of 1 mV s^{-1}.

2.7.4. Scanning Electron Microscopy (SEM)

The morphology of the electrode surface was monitored using scanning electron microscopy. An environmental scanning electron microscope model Philips ***XL30SEM*** with Energy Dispersive X-ray Analysis (EDX) available in the laboratory was used for routine imaging. A ***Jeol JSM-6500F*** thermal field emission scanning electron microscope fitted with a secondary electron (SE) detector and EDX was

used when higher resolution was desirable. The images taken for rotating disc electrodes were under Hi-Vac mode using secondary electron detector at a beam of 20 kV. For the microelectrodes, the images were recorded under wet mode using gaseous secondary electron (GSE) detector at an accelerating voltage of 12 - 15 kV.

The next chapter will include the mechanism of tetrachloroaurate(III) in hydrochloric acid electrolyte, thus deposition of gold nanoparticles on carbon substrates with controlled deposition parameters.

Chapter 3

3 *Electrodeposition of gold nanoparticles*

Early experiments with gold and platinum deposition showed that gold deposition is a much simpler reaction. Hence gold deposition was used to define the approaches to the investigation of small electrodeposited metal centres.

3.1. Cyclic voltammetry in hydrogen tetrachloroaurate (III) hydrate on carbon substrate

Before each experiment, the polished vitreous carbon disc electrode was used to record a cyclic voltammogram in 1 M sulphuric acid. This was to ensure that the surface is free from contamination by gold. Figure 35 shows the cyclic voltammogram obtained at a polished carbon electrode surface at a scan rate of 100 mV s^{-1}. A double layer region can be seen negative to +1.2 V ***versus*** saturated calomel reference electrode. Oxygen evolution starts from +1.2 V ***versus*** SCE and no hydrogen evolution can be observed at potentials positive to -0.6 V. There are small anodic oxidation and cathodic reduction peaks at +0.5 V and +0.4 V

respectively. These peaks correspond to the oxidation and reduction of the surface functional groups such as quinone-hydroquinone redox couple [249].

$$\boldsymbol{C=O}\ \text{(quinone)} + \boldsymbol{H^+} + \boldsymbol{e^-} \rightleftarrows \boldsymbol{C\text{-}OH}\ \text{(hydroquinone)} \qquad (3.1)$$

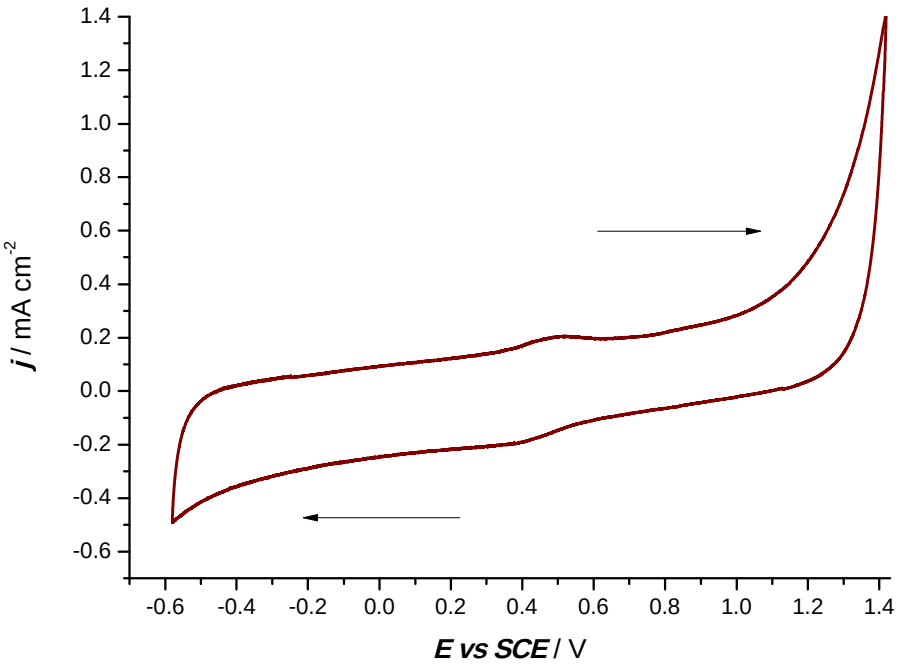

Figure 35. Cyclic voltammogram (3rd scan) in 1 M sulphuric acid recorded at a 3 mm diameter carbon electrode at room temperature. Scan rate 100 mV s-1.

3.1.1. Reduction of gold(III) on glassy carbon rotating disc electrode

A cyclic voltammogram in 1 mM hydrogen tetrachloroaurate(III) and 0.1 M hydrochloric acid degassed with argon was recorded on a 3 mm diameter glassy carbon rotating disc electrode as shown in Figure 36. The rotating disc electrode was rotated at 900 rpm and the scan rate was 1 mV s^{-1}.

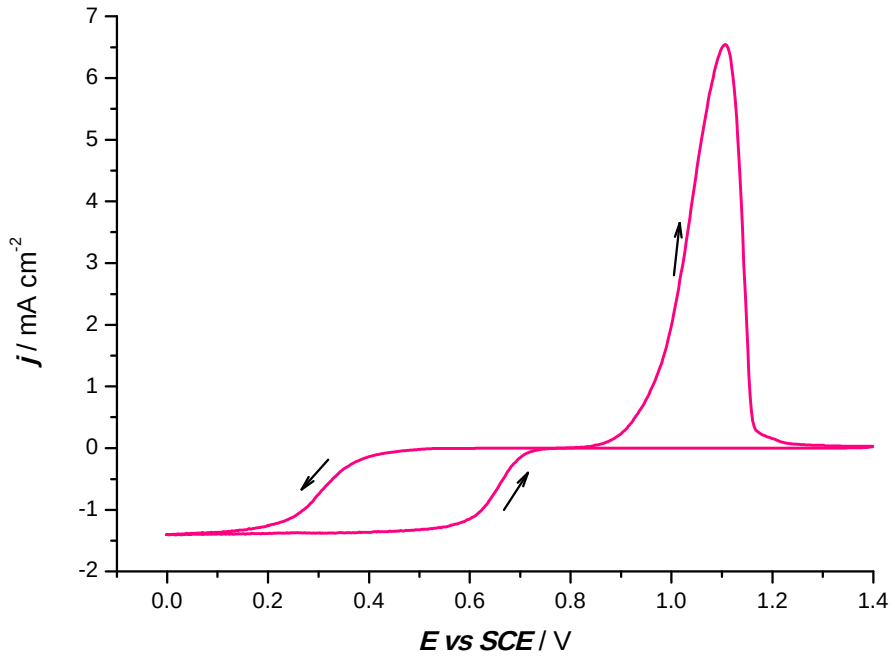

Figure 36. Cyclic voltammogram in 1 mM $HAuCl_4$ and 0.1 M HCl degassed with argon recorded at a 3 mm diameter glassy carbon rotated at 900 rpm. Scan rate 1 mV s^{-1} recorded at room temperature

The scan was started at +1.4 V. The cyclic voltammogram shown in Figure 36 presents the typical characteristics of an electrodeposition process on a foreign substrate with subsequent removal of the deposited layer. A clear steady state reduction wave was observed with a significant hysteresis. A well-defined oxidation peak was observed on the reverse sweep. On the forward scan, the half wave potential of the reduction wave occurs at +0.33 V ***versus*** SCE, but it is shifted by approximately +200 mV on the reverse sweep. This is consistent with a nucleation loop [203]. The electrodeposition of gold onto gold coated carbon electrode surface is much easier than on a clean carbon electrode surface [115, 203]. Thus less overpotential is required, hence the $E_{½}$ for the backward scan is shifted to a more positive potential, +0.70 V. The deposition of gold has a cathodic charge of 1.4 C cm^{-2}, thus a thick layer of gold has been deposited onto the electrode. The anodic charge is about 70 % of the total cathodic charge, hence not all of the gold deposited

has been dissolved into the solution. On the reverse scan, the reduction wave (deposition) and the oxidation peak (dissolution) of gold are separated by a region of zero current indicating that the kinetics of the Au/Au(III) couple is slow even on a gold surface [19, 203]. Similar overall response has been reported by ***Schmidt et. al.*** for the voltammogram recorded on glassy carbon in solution containing $AuCl_4^-$ in concentrated LiCl [203]. The potential at which the crossover of forward and reverse currents occurs at +0.77 V ***versus*** SCE (~ +1.01 V ***versus*** SHE). This value agrees well with the standard equilibrium potential for the reduction of Au(III) to Au(0), +1.00 V ***versus*** SHE as reported in literature [212].

Further investigation on the reduction of gold(III) on a 3 mm diameter gold coated glassy carbon rotating disc electrode was carried out by varying the rotation rates. Figure 37 shows a set of linear sweep voltammograms of the gold(III) reduction recorded in the same gold plating bath solution. The voltammograms were recorded at 1 mV s^{-1}.

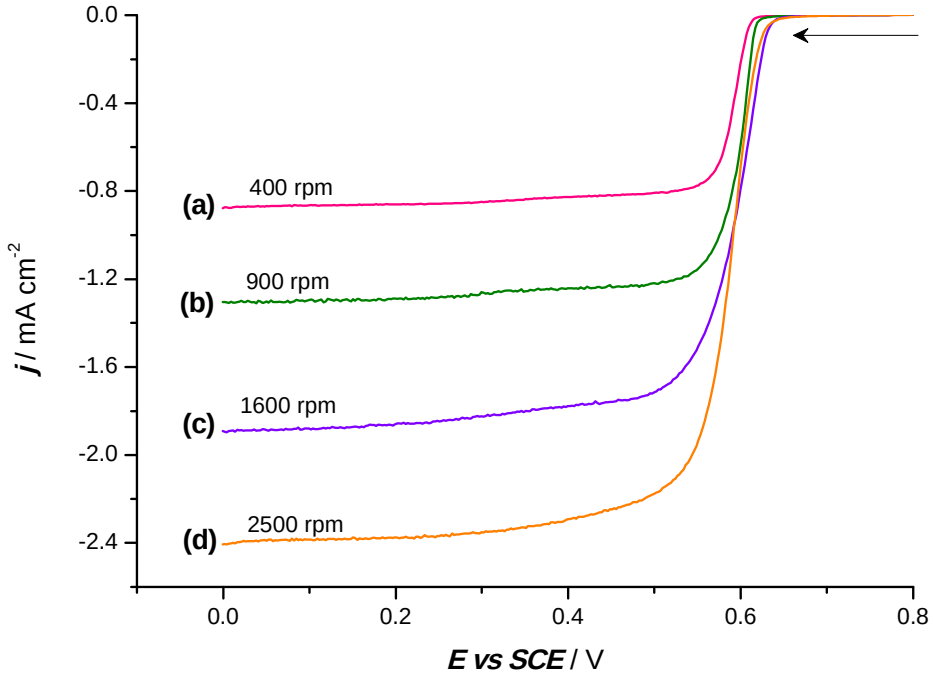

Figure 37. Linear sweep voltammograms recorded at different rotations on a gold coated vitreous carbon RDE (Ø = 3 mm) in 1 mM $HAuCl_4$ and 0.1 M HCl degassed with argon at room temperature. Scan rate 1 mV s^{-1}.

At all rotation rates, a limiting current is achieved at potentials negative to +0.5 V. The ($E_{¾} - E_{¼}$) of the gold(III) reduction wave is 0.03 V. Steep voltammograms are observed due to (a) an increase in number of nuclei and (b) an increase in the surface area of each nucleus adding to the consequences of the increase in overpotentials in the foot of the wave. As expected, the reduction of gold(III) is easier to occur at a gold coated glassy carbon surface, hence the onset of the reduction of gold(III) starts at a more positive potential with an average $E_{½}$ of +0.59 V, in line with the half wave potential of the reduction wave seen on the reverse sweep in Figure 36.

The current density at +0.4 V ***versus*** SCE was plotted against the square root of the rotation rates of the electrode, ranging from 400 rpm to 3600 rpm. A linear graph that passes through the origin was obtained as shown in Figure 38. Hence, the reaction is fully mass transport controlled in the plateau region. The linear plot obeys the ***Levich*** equation, thus the diffusion coefficient can be calculated by applying the ***Levich*** equation (3.2) [19], to a set of limiting currents at +0.4 V ***versus*** SCE at different rotation rates:

$$j_L = 0.201\, nFD^{\frac{2}{3}} \upsilon^{-\frac{1}{6}} c^{\infty} \omega^{\frac{1}{2}} \qquad (3.2)$$

Taking into account the Faraday constant, F = 96485 C mol^{-1}, an electrode area, A = 7.1 × 10^{-2} cm^2, a kinematic viscosity, υ = 1 × 10^{-2} cm^2 s^{-1}, three electron exchanged, n = 3 e$^-$, the concentration of hydrogen tetrachloroaurate (III), c^{∞} = 1.0 × 10^{-6} mol cm^{-3} and the angular rotation rate of the disc, ω in rpm. The diffusion coefficient of gold (III), D can be calculated from the slope and it was estimated to be 4.1 × 10^{-6} cm^2 s^{-1}. This value is low compared to that reported in the literature, 9 × 10^{-6} cm^2 s^{-1} [250], for $AuCl_4^-$ but close to that for most metals in aqueous solutions.

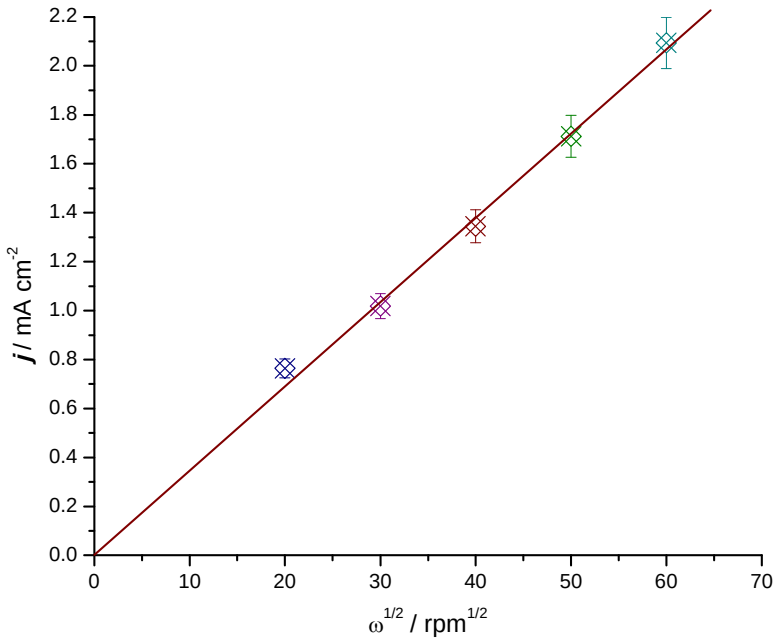

Figure 38. Current density (j / mA cm^{-2}) versus the square root of rotation rate ($\omega^{1/2}$ / rpm$^{1/2}$) recorded at +0.4 V versus SCE. Error bars are derived from 5 % of each data set value.

3.1.2. Reduction of gold(III) on stationary glassy carbon electrode

The reduction of gold(III) has also been carried out in other carbon working electrodes; stationary glassy carbon and carbon paper. This is to observe the electrodeposition of gold on different carbon substrates. Figure 39 shows three consecutive cyclic voltammograms in the same gold plating bath solution recorded on a 3 mm diameter stationary glassy carbon electrode. The scan rate was 1 mV s^{-1}. The cyclic voltammograms were scanned in a potential range between +0.8 V and 0 V ***versus*** SCE in order to observe only the reduction wave of tetrachloroaurate(III) on a glassy carbon electrode in a non-steady state diffusion control.

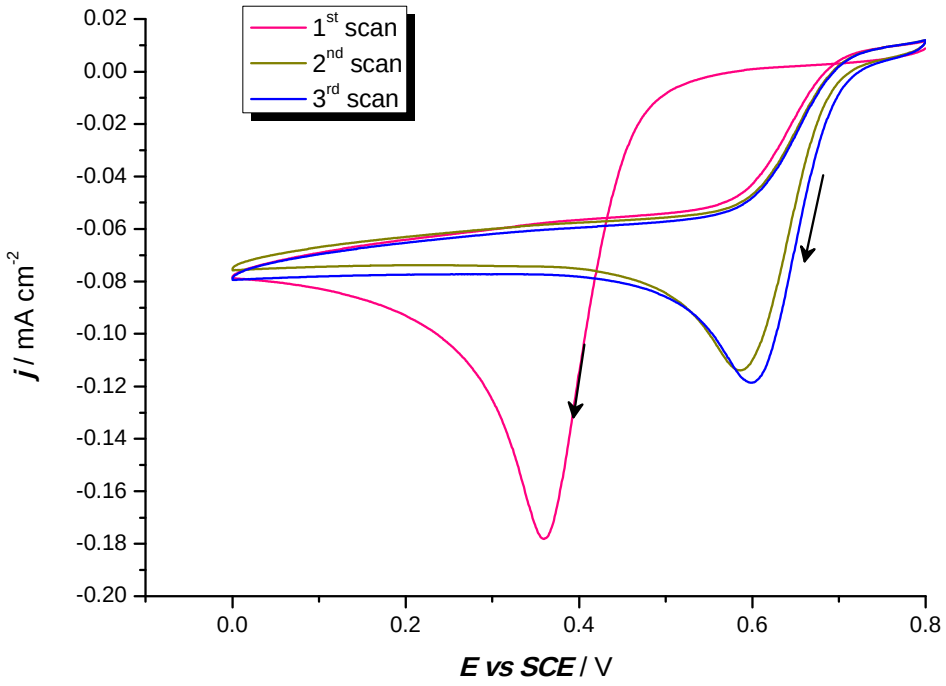

Figure 39. Three consecutive cyclic voltammograms in 1 mM $HAuCl_4$ and 0.1 M HCl degassed with argon recorded on a 3 mm diameter stationary glassy carbon electrode in a non-steady state diffusion controlled. Scan rate 1 mV s^{-1}.

A steep reduction peak can be observed in all the three cycles. The half height potential of the reduction peak for the first scan is +0.42 V ***versus*** SCE. The first scan shows a characteristic nucleation loop [203] and higher current density is observed on the reverse scan at potential positive to +0.43 V. This indicates that a greater overpotential is required for nucleation to occur on a polished glassy carbon electrode when compared to deposition of gold onto gold nuclei. Thus, the half peak potential of the second scans onwards were shifted to a more slightly positive, that is +0.65 V. The peaks on the second and third scans were smaller than that on the first scan probably because the positive potential limit does not allow complete recovery of the gold(III) concentration in the diffusion layer.

3.1.3. Reduction of gold(III) on carbon paper microband electrode

In another experiment, the cyclic voltammograms were recorded on a microband of carbon paper (Toray carbon paper, TGPH-090) of thickness 0.26 mm with a length of (9.0 ± 0.5) mm and a height of 40 mm. All the sides of the carbon paper are insulated with nail polish, leaving behind some exposed area for connection. Prior to the experiment, new carbon paper band was revealed by cutting one end of the carbon paper and it was used immediately without any pretreatment by polishing. The exposed area of the working electrode is 2.3 mm^2. The other end of the carbon paper is used for connection using a crocodile clip. The edge of the carbon paper was immersed in a solution containing 1 mM hydrogen tetrachloroaurate (III) and 0.1 M hydrochloric acid. Two consecutive cyclic voltammograms were scanned at 1 mV s^{-1} as shown in Figure 40.

The reduction of gold(III) on a carbon paper starts at +0.62 V ***versus*** SCE with the half wave potential at +0.56 V. This indicates that the nucleation of gold on carbon paper is more facile than on polished glassy carbon. This can be arising from the presence of more active nucleation sites on the carbon paper than on the glassy carbon. A nucleation loop can also be observed in the first scan indicating a greater overpotential is still needed for the nucleation to take place on the carbon paper. Thus, the backward scan of the first voltammogram overlaps with the forward and backward scans of the second cyclic voltammogram. A limiting current has also been achieved at potential negative to +0.50 V ***versus*** SCE showing that deposition process becomes diffusion limited.

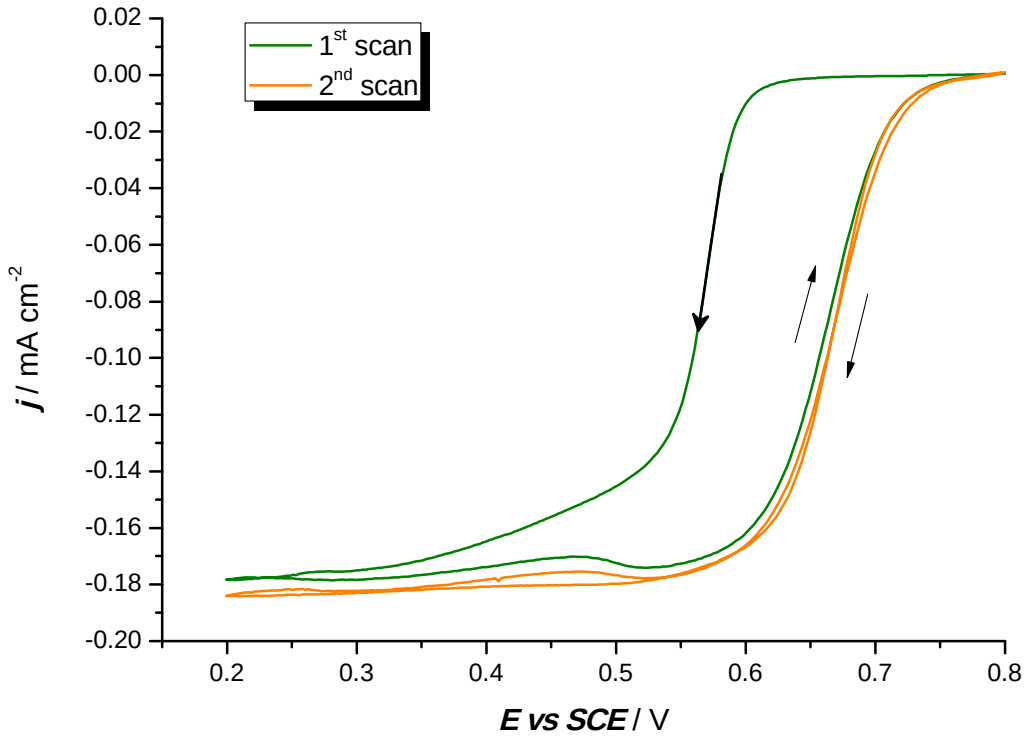

Figure 40. Cyclic voltammograms recorded on a strip of carbon paper (2.3 mm^2) in 1 mM $HAuCl_4$ and 0.1 M HCl degassed with argon. Scan rate 1 mV s^{-1}.

3.2. Electrodeposition of gold at various potentials

The reduction of gold(III) in 1 M hydrogen tetrachloroaurate (III) hydrate in 0.1 M hydrochloric acid was further investigated using single and double step chronoamperometry. The gold electrodeposition on a glassy carbon electrode was carried out at different potentials ranging from +0.8 V to 0 V ***versus*** SCE. The distribution of gold nuclei on another carbon substrate was also investigated using a microband carbon paper within similar deposition potential range.

3.2.1. Single potential step (deposition only)

In the single potential step experiments, the deposition parameters such as deposition time and deposition charge density are controlled as a function of deposition potential. The deposition time was fixed, therefore the charge density passed varies with the deposition potential. Hence, the amount of gold nuclei deposited on the surface will also depend on the potential. With a fixed deposition charge density, the loadings of nuclei on the electrode surface depend on deposition potential. Hence, the size and distribution of the gold nuclei will be different with overpotential.

3.2.1.1. Chronoamperometry at fixed deposition time

The reduction of gold(III) on glassy carbon was further investigated at various potentials ranging from +0.6 V to 0 V. The working electrode was a 3 mm diameter glassy carbon stationary electrode in the same gold plating bath solution. The electrode was polished before each experiment to ensure no gold remained on its surface. The potential was stepped from +0.8 V ***versus*** SCE to various deposition potentials for a fixed deposition time. The deposition time was fixed in order to observe the shape of the current density-time transients with deposition potentials and also the distribution (the number density and size) of nuclei onto the electrode surface within the limited deposition time. The chronoamperometry for the electrodeposition at various potentials is shown in Figure 41.

The chronoamperometry recorded at potentials negative to +0.35 V (indicated as (a) to (c)) showed the characteristic current increase due to rapid processes of nucleation and growth of the gold nuclei [19, 237], followed by falling transients. The currents and the charge passed are very similar for the three potentials. At this plateau region, the current density tends to be mass transport controlled. The deposition charge densities integrated from the current transients are in the range of 4.4 to 5.2 mC cm^{-2} (see Table 2). The number density of nuclei on the electrode (at high overpotential)

would be expected to be higher than the deposition carried out at very positive potentials. On the other hand, at very positive potentials as shown in Figure 41(d – f), slight rising transients are observed over a period of time indicating that a slow nucleation process takes place on the glassy carbon surface. The morphology of the electrode surface after the electrodeposition can be seen in section 3.3 (Figure 46). The distribution of the nuclei onto the surface will be described further in the latter subsection.

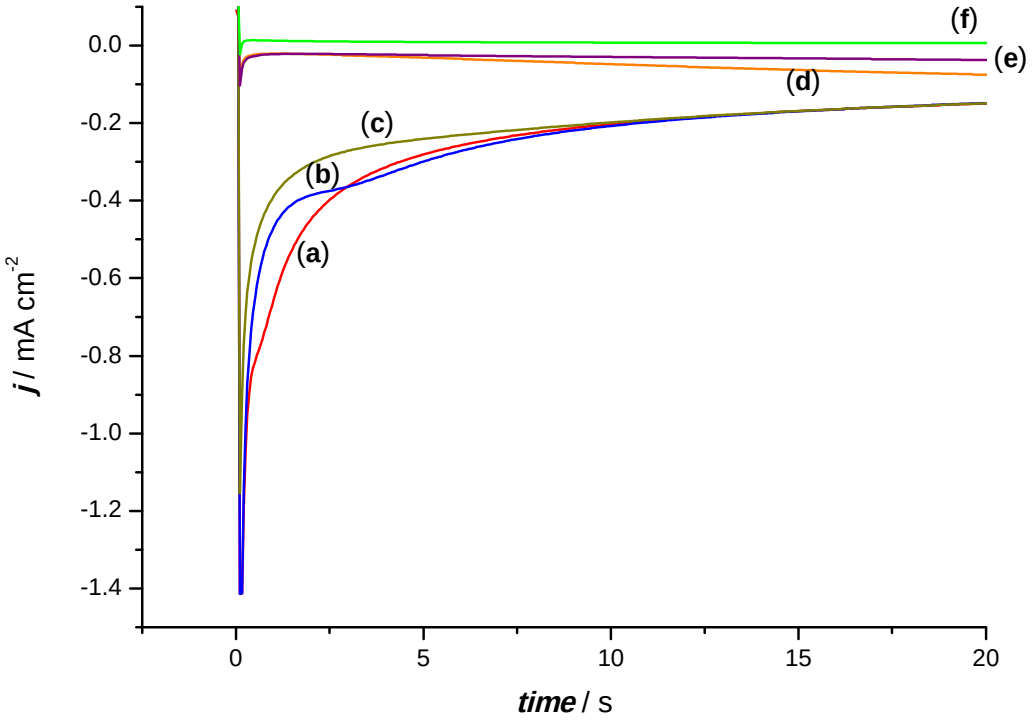

Figure 41. Chronoamperometric transients recorded in 1 mM $HAuCl_4$ + 0.1 M HCl degassed with argon, after stepping from +0.8 V versus SCE to various potentials for a fixed deposition time; **(a)** *0 V* **(b)** *+0.2 V* **(c)** *+0.35 V* **(d)** *+0.45 V* **(e)** *+0.5 V* **(f)** *+0.6 V . WE: stationary 3 mm diameter GC electrode.*

Table 2. Charge density passed as a function of potential at fixed deposition time (20 s).

Potential step to	Charge density, q / mC cm^{-2}
(a) 0 V	5.2
(b) +0.2 V	5.1
(c) +0.35 V	4.4
(d) +0.45 V	0.9
(e) +0.5 V	0.6
(f) +0.6 V	0.2

3.2.1.2. Chronoamperometry at fixed deposition charge density

The electrodeposition of gold was further investigated using a glassy carbon rotating disc electrode. The working electrode was rotated at 900 rpm in a solution containing 1 mM $HAuCl_4$ and 0.1 M HCl. The potential was stepped from +0.8 V ***versus*** SCE to various positive potentials where the reduction waves started to occur (in the range between +0.625 V and +0.5 V). The rotation of the electrode created a hydrodynamic condition, hence higher current densities were obtained (when compared to Figure 41). Figure 42 shows the chronoamperometry recorded at a glassy carbon electrode rotated at 900 rpm with a fixed charge density of 5 mC cm^{-2}.

For the potential stepped to +0.575 V and +0.50 V, rising transients are observed. In these cases, the process of nucleation of gold nuclei occurs rapidly on the surface of the glassy carbon electrode as a sufficient overpotential had been applied. However, at very positive potentials (+0.60 V and +0.625 V), slight rising transients are observed over a period of time. In this case, a longer deposition time is required to achieve the deposition charge density of 5 mC cm^{-2}. Thus slow process of nucleation and growth takes place at these potentials.

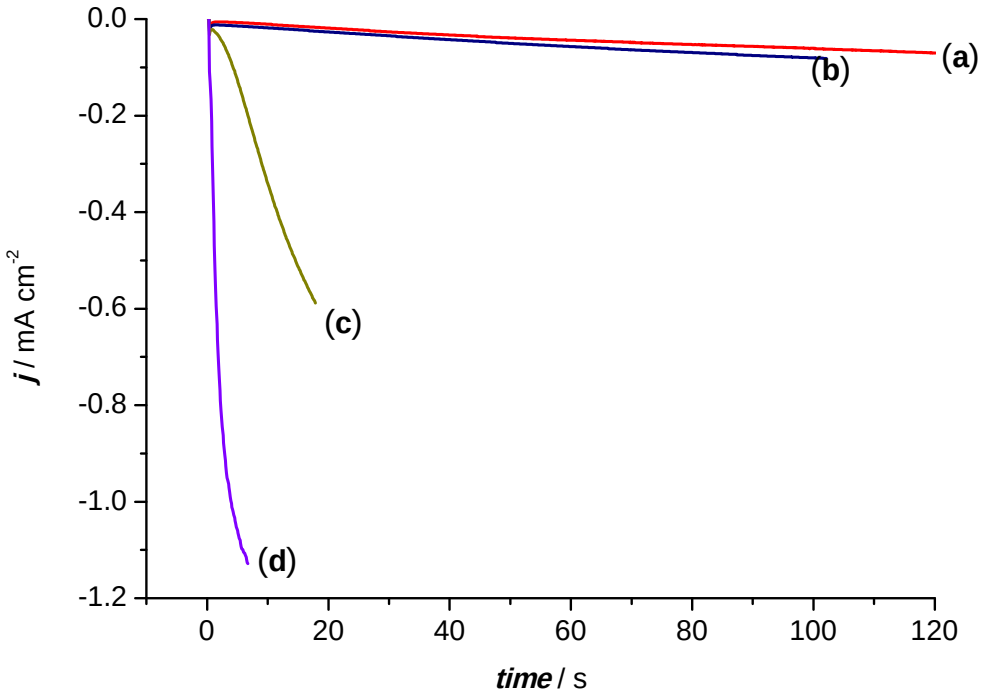

Figure 42. Chronoamperometry in 1 mM $HAuCl_4$ + 0.1 M HCl degassed with argon recorded at a glassy carbon rotating disc electrode (Ø = 3 mm). Rotation rate 900 rpm. Potential was stepped from +0.8 V versus SCE to various deposition potentials; **(a)** *+0.625 V* **(b)** *+0.60 V* **(c)** *+0.575 V* **(d)** *+0.50 V. Deposition charge density of 5 mC* cm^{-2}.

In other sets of chronoamperometry experiments, a stationary 3 mm diameter glassy carbon electrode was used as the working electrode. The potentials were stepped from +0.8 V ***versus*** SCE to a range of potentials between +0.45 V and +0.10 V. The deposition charge density was 10 mC cm^{-2}. Figure 43 shows the corresponding current density-time transients recorded at the glassy carbon electrode in 1 mM hydrogen tetrachloroaurate (III) hydrate.

The current density-time transients recorded at +0.25 V and +0.1 V ***versus*** SCE almost overlapped with each other, showing a rapid nucleation regime onto the electrode surface. The current density tends to reach mass transport control over a

period of time. However, at +0.35 V, a shoulder is initially seen but soon reaches the diffusion controlled deposition. Rising transients are observed at +0.45 V, followed by a steady state current density before reaching the maximum deposition charge density.

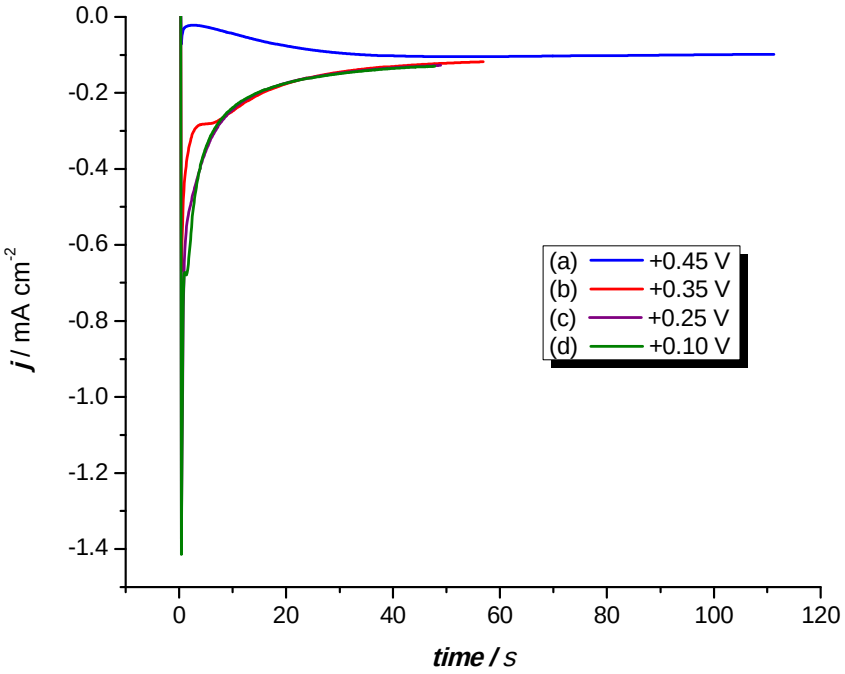

Figure 43. Chronoamperograms recorded in 1 mM $HAuCl_4$ and 0.1 M HCl degassed with argon, after stepping from +0.8 V versus SCE to various deposition potentials for a fixed deposition density (10 mC cm^{-2}). WE: 3 mm diameter stationary glassy carbon.

Figure 44 shows another set of chronoamperograms investigated using a microband of carbon paper of 0.26 mm thickness and (10.0 ± 0.5) mm length. A new surface of a band of carbon paper (A = 2.6 mm^2) was revealed by cutting the edge of carbon paper (all sides of the carbon paper insulated with clear nail polish). Once dried, it was used immediately without any polishing with alumina. A new piece of carbon paper was used in each of the experiment and a deposition charge density of 5 mC cm^{-2} was passed in all the transients. This experiment was carried out to observe the

transients produced on a microband, followed by the observation of the gold nuclei distributed on this substrate using scanning electron microscope (see section 3.3 (Figure 48).

The electrodeposition of gold at +0.63 V showed a slight rising transient over a period of time. A similar trend of current density-time transient was recorded on a glassy carbon electrode. As expected, a very slow nucleation process of gold nuclei takes place at the very positive potential. However, at +0.55 V and +0.59 V, rising transients are observed, to almost reach the diffusion controlled deposition. At very negative potentials (+0.45 V and 0 V), a rapid nucleation and growth process takes place, and is followed by falling transients forming almost a plateau. The current density tends to become mass transport controlled.

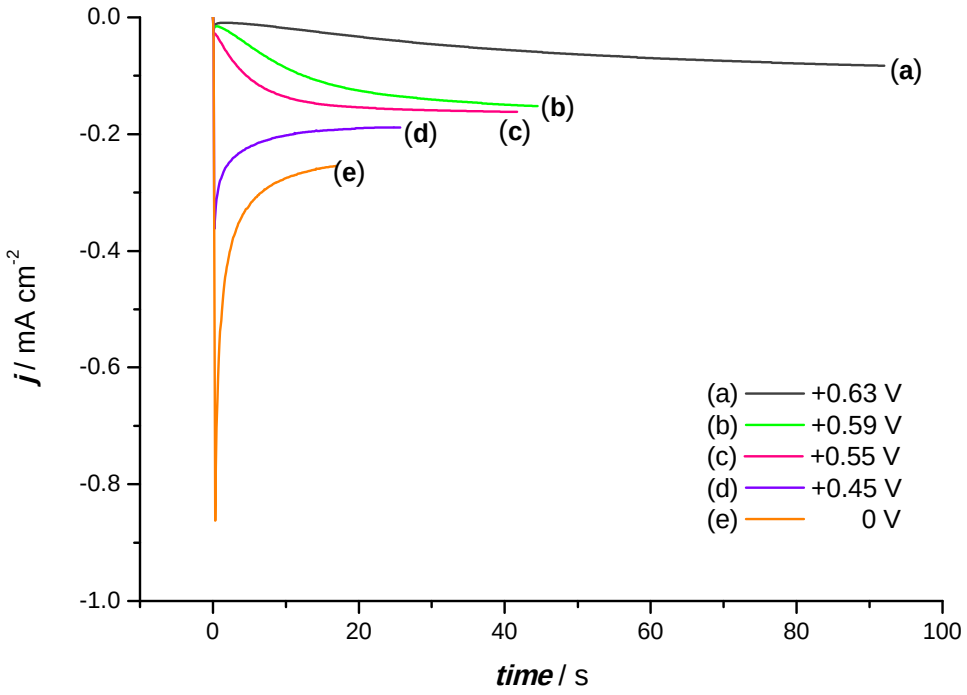

Figure 44. Chronoamperometry recorded at a strip of carbon paper (A = 2.6 mm^2) stepping from +0.8 V versus SCE to various potentials **(a)** *+0.63 V* **(b)** *+0.59 V* **(c)** *+0.55 V* **(d)** *+0.45 V* **(e)** *0 V in deoxygenated 1 mM $HAuCl_4$ + 0.1 M HCl. Deposition charge density of 5 mC cm^{-2}.*

As expected, rapid nucleation and growth process of gold nuclei on glassy carbon surface occurs at potential negative to +0.35 V versus SCE. The current density tends to be mass transport controlled at high overpotential. The nucleation process on the electrode surface is slow at low overpotential. Similar trend of current density-time transients are observed on a microband carbon paper.

3.2.2. Double potential steps at stationary glassy carbon electrode (deposition followed by stripping)

The oxidation of gold metal was studied using double potential steps. In this experiment, the first potential step was carried out to electrodeposit substantial gold onto the carbon surface. The second potential step was used to probe the extent of stripping as a function of potential.

The stationary glassy carbon electrode was initially stepped from +0.8 V to a high overpotential (+0.2 V ***versus*** SCE) in 1 mM hydrogen tetrachloroaurate (III) hydrate and 0.1 M hydrochloric acid. The first potential step was carried out at a fixed deposition time of 360 s with an average resultant charge density of 41 mC cm^{-2}. A substantial number of large gold nuclei were expected to be deposited within this period. This was followed by a second potential step to very positive potentials, at which the stripping of gold took place. The stripping potentials were in the range between +0.8 V and +1.2 V ***versus*** SCE (see Figure 36). The electrode was held at the second potential for 270 s. Figure 45 shows the chronoamperograms recorded after the double potential steps on a 3 mm diameter glassy carbon electrode. The insets display the magnification of the transients produced in the first and second potential steps. Table 3 shows the integrated deposition and stripping charge densities for the first and second potential steps respectively.

The current density-time transients in the first potential steps almost overlap with each other. The nucleation and growth of the gold nuclei at +0.2 V is rapid and followed by a decrease in current density due to mass transport controlled deposition. The stripping charge density recorded at +0.8 V and +0.9 V are small. These are in agreement with the stripping peak charge densities obtained when recording the full cyclic voltammograms in the same gold plating bath solution. At +1.0 V and +1.1 V, the decreasing current density takes a longer time to reach zero current. Thus, the stripping charge density at these two potentials is greater than those at +0.8 V and +0.9 V. This reflects almost complete stripping of gold taking place at these potentials. At +1.2 V, the current density drops to almost zero current very quickly. Less stripping of the gold occurs.

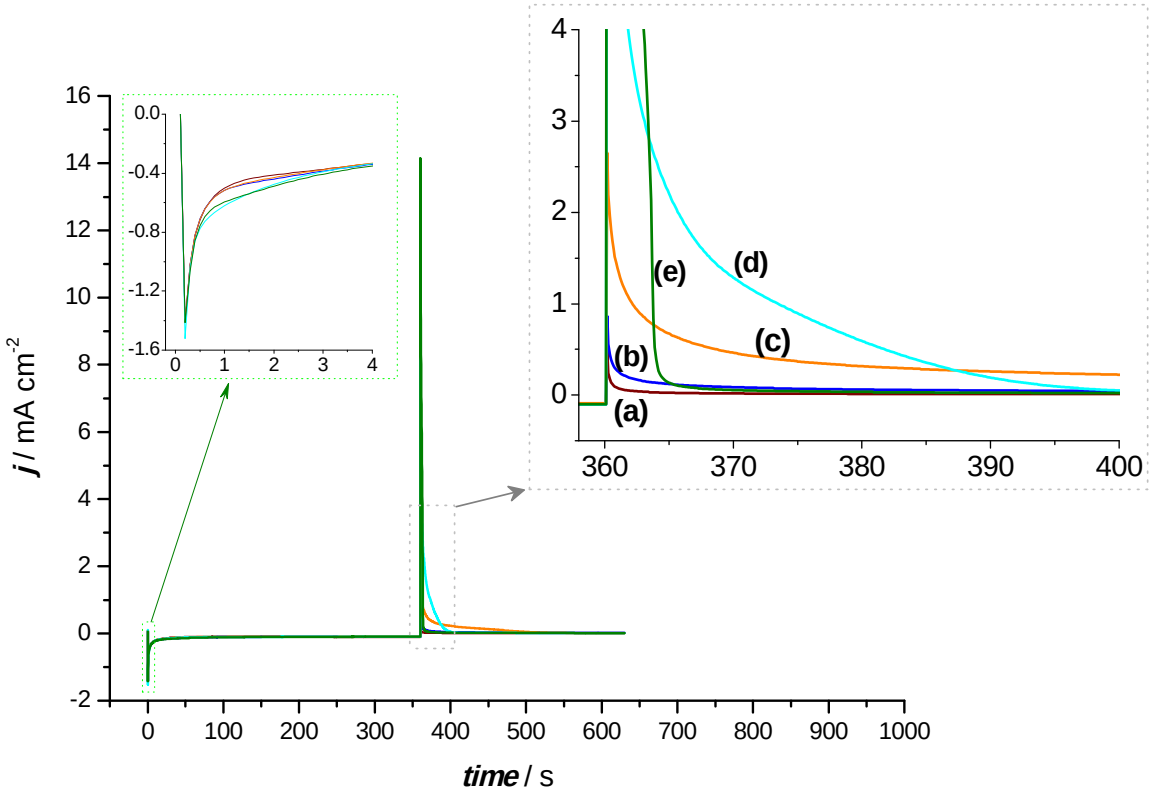

Figure 45. Chronoamperograms recorded at a glassy carbon (Ø = 3 mm) in 1 mM $HauCl_4$ + 0.1 M HCl degassed with argon, initially stepped from +0.8 V to +0.2 V vs. SCE for 360 s, then stepped again to various stripping potentials for 270 s; The second potential steps are **(a)** *+0.8 V* **(b)** *+0.9 V* **(c)** *+1.0 V* **(d)** *+1.1 V* **(e)** *+1.2 V.*

Table 3. Charge density integrated from the current density-time transients passed during the double potential steps shown in Figure 45.

	Initial deposition charge density, q_1 / *mC cm*$^{-2}$	***Stripping potentials versus SCE*** / V	***Stripping charge density,*** q_2 / *mC cm*$^{-2}$	$(q_1 - q_2)$ / *mC cm*$^{-2}$
(a)	*40*	*+0. 8*	*2*	*38*
(b)	*40*	*+0.9*	*8*	*32*
(c)	*39*	*+1.0*	*32*	*7*
(d)	*42*	*+1.1*	*44*	*-2*
(e)	*44*	*+1.2*	*29*	*15*

During the first potential step at +0.20 V, the deposition process is similar as shown in Figure 41, consecutively followed by oxidation process of gold nuclei at very positive potential. Similar observation of rapid nucleation and growth of gold nuclei occurs at high overpotential (+0.2 V). Most of the gold nuclei dissolve into the solution as the potential stepped to +1.0 V and +1.1 V with respect to SCE. In this process, the amount of gold remained on the electrode surface is reduced. The morphology of the electrode surface after the double potential steps is shown in Figure 49 in the following subsection. The gold oxidation process is not straightforward and passivation presumably due to oxide formation occurs at more positive potentials [200, 211].

3.3. Morphology of the electrode surface after electrodeposition

All of the electrode surfaces were examined before and after electrodeposition using the scanning electron microscopy. In most of the experiments, the images were taken under wet mode with an accelerating voltage of 15-20 kV. The electrodeposition of gold was carried out either with the limitation of deposition time or charge density. In all of the experiments, the substrate used was carbon; glassy carbon (either rotated or stationary) and also a microband of carbon paper.

3.3.1. Electrodeposition at fixed deposition time

Figure 46 shows the SEM images of selected surface of the glassy carbon electrode after undergoing potential steps at a fixed deposition time (20 s). The potential was stepped from +0.8 V to different deposition potentials (ranging from +0.6 V to 0 V ***versus*** SCE). Thus with limited deposition time, the charge density passed in each transient varied with respect to deposition potential.

After the potential step to +0.6 V with deposition charge density of 0.2 C cm^{-2} passed, there were hardly seen any visible gold nuclei on the carbon surface. Therefore the SEM image of this electrode is not shown in Figure 46. As the overpotential increases, the gold nuclei deposited on the electrode surface can be clearly observed. The gold nuclei produced at +0.5 V were very small and sparsely distributed (as shown in Figure 46(a)). This indicates a slow nucleation process at this very positive potential and the limited growth due to the deposition time being limited. It can be noted that the charge passed is very low equivalent to only a few monolayers. At +0.45 V, gold nuclei of various sizes ranging from 0.1 µm to 0.4 µm were observed. This indicates that nucleation had taken place. An increase in nuclei density with smaller gold nuclei (sizes range between 90 nm and 300 nm) was

observed after stepping to +0.2 V. As the deposition potential became more negative (0 V), instantaneous nucleation occurred. Also the charge density passed has increased substantially. Thus nuclei of mainly similar sizes (average size ~ 70 nm) can be clearly observed in Figure 46(d). This confirms that nucleation of gold on glassy carbon takes place at potentials negative to +0.5 V ***versus*** SCE. These images suggest that progressive nucleation shifts to instantaneous nucleation and growth with increasing overpotential [203, 237]. Throughout the SEM studies, uncertainties arise as nuclei below a critical size (< 50 nm) are not observed. This must always be recognised in the qualitative and quantitative interpretation of the data.

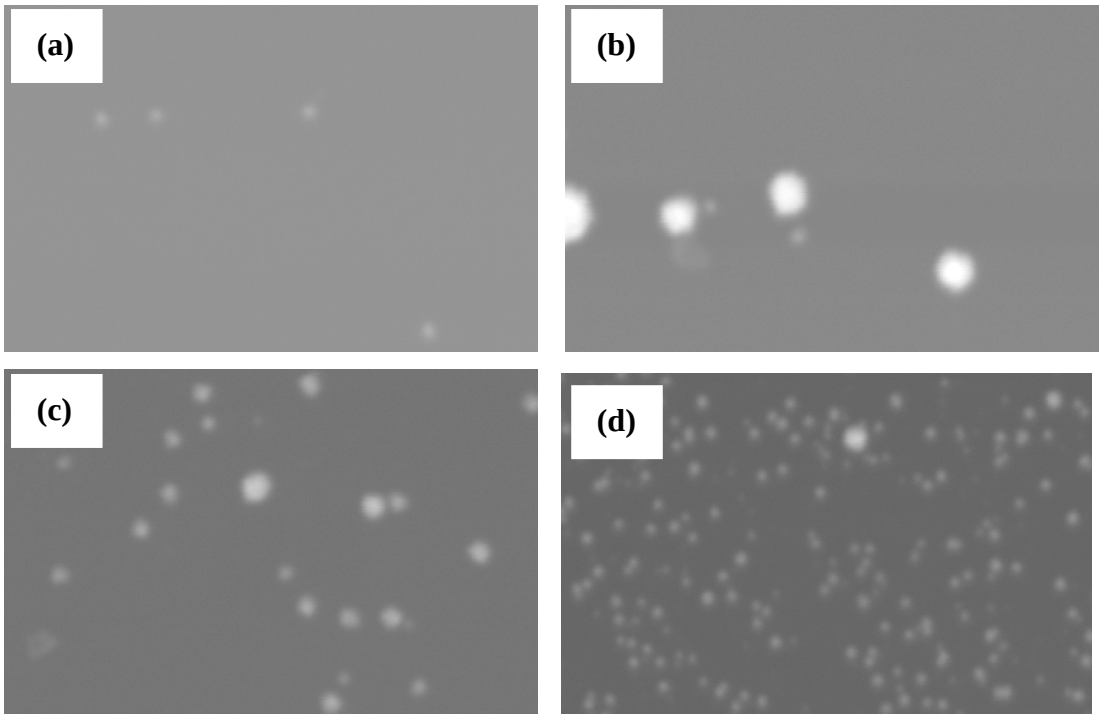

Figure 46. SEM images of gold nanoparticles electrodeposited on vitreous carbon electrode after undergoing chronoamperometry in 1 mM $HAuCl_4$ and 0.1 M HCl, stepping from +0.8 V versus SCE to various deposition potentials for a fixed deposition time (20 s). The potential was stepped to **(a)** *+0.5 V [q = 0.6 mC cm^{-2}]* **(b)** *+0.45 V [q = 0.9 mC cm^{-2}]* **(c)** *+0.2 V [q = 5.1 mC cm^{-2}]* **(d)** *0 V [q = 5.2 mC cm^{-2}]. WE: 3 mm diameter stationary GC electrode.*

3.3.2. Electrodeposition at fixed deposition charge density

3.3.2.1. Single potential step on stationary glassy carbon electrode

The reduction of gold(III) on a stationary glassy carbon electrode was further investigated at various deposition potentials ranging from +0.45 V to +0.1 V ***versus*** SCE. The deposition charge density was fixed at 10 mC cm^{-2}. Figure 47 shows the SEM images of the electrode surface taken after the maximum deposition charge density had been passed.

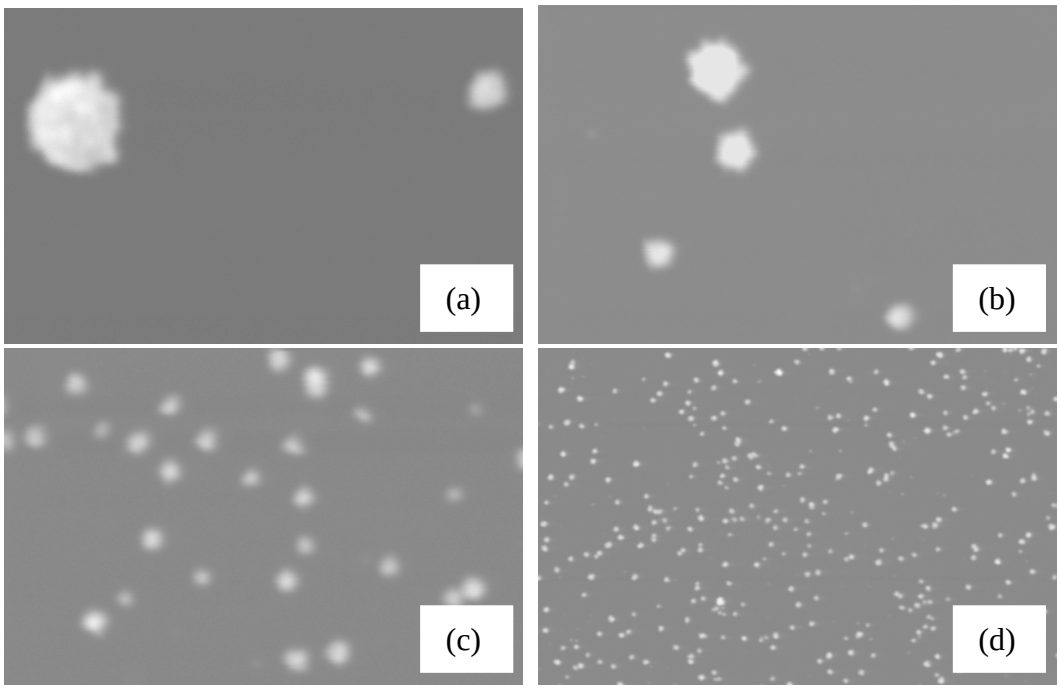

*Figure 47. SEM images of the glassy carbon electrode surface at a fixed deposition charge density of 10 mC cm^{-2}. The potential was stepped from +0.8 V to **(a)** +0.45 V **(b)** +0.35 V **(c)**&**(d)** +0.10 V. Images **(a-c)** has magnification 20,000x with a scale:* **1 µm** *and image **(d)** has magnification 5,000x.* Scale: **5 µm**.

Figure 47(a-b) clearly show that progressive nucleation has taken place over a period of time. At +0.45 V and +0.35 V, various sizes of gold nuclei are produced in the range of 500 nm to 1 μm and 300 nm to 700 nm respectively. Moreover, the number density of gold nuclei produced at very positive potentials is very low. At high overpotentials (+0.1 V), the nucleation process is rapid and produces gold nuclei of size ranging from 95 to 250 nm. Thus, the gold nuclei produced are of smaller sizes than those produced at +0.45 V with the same amount of charge density being passed. At more positive potentials, the growth of existing nuclei takes place more readily than the formation of further nuclei. The nuclei at more positive potentials are larger. However, the electrode surface has not been fully covered by the deposited gold nuclei as evidenced by the lower magnification image in Figure 47(d). This may be attributed to the active nucleation sites on the electrode surface. In addition, nuclei of diameter smaller than 50 nm could not be observed under scanning electron microscope even at high magnification.

3.3.2.2. Single potential step on a microband of carbon paper

The electrodeposition of gold was carried out on a strip of carbon paper with an exposed microband of area 2.6 mm^2. The microband electrode is 0.26 mm thickness and (10.0 ± 0.5) mm length. All the sides of the carbon paper are insulated with nail polish. A new surface of microband electrode is revealed by cutting the edge of the strip of carbon paper. The tip of the carbon paper is immersed into the solution containing 1 mM hydrogen tetrachloroaurate(III) and 0.1 M hydrochloric acid. The potential was stepped from +0.8 V ***versus*** SCE to various deposition potentials (range from +0.63 V and +0.45 V) with a deposition charge density of 5 mC cm^{-2} was passed (see Figure 44). The carbon microband paper was removed from the solution and rinsed with water. The surface of the microband electrode was observed under scanning electron microscope. Figure 48 shows the SEM images of the surface of the microband carbon paper and of a glassy carbon electrode after undergoing potential steps to various deposition potentials.

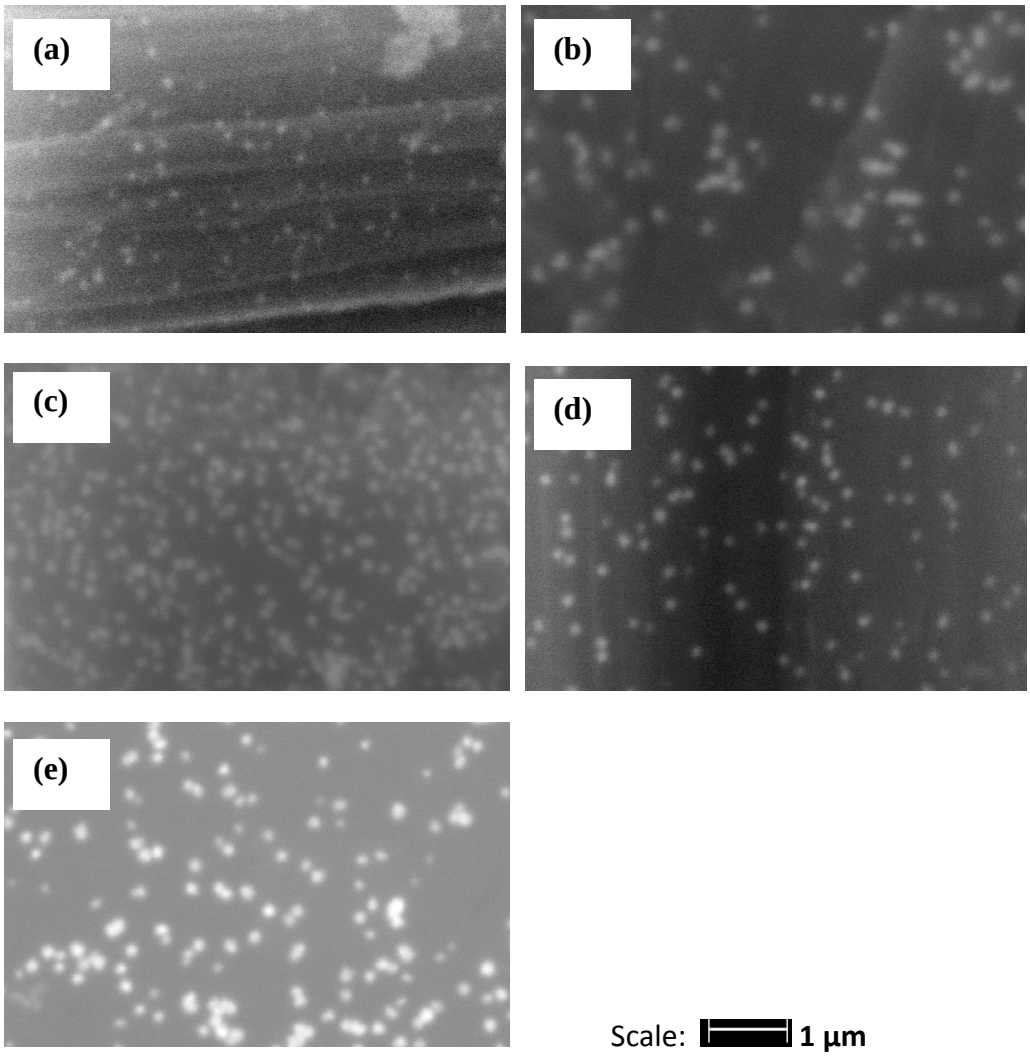

Figure 48. SEM images of electrochemically deposited gold nanoparticles on a band of carbon paper after undergoing electrodeposition of gold at different potentials for a fixed deposition charge density of 5 mC cm^{-2}; Potential stepped from +0.8 V versus SCE to **(a)** *+0.63 V* **(b)** *+0.59 V* **(c)** *+0.55 V* **(d)** *+0.45 V. For comparison, a SEM image of the gold coated glassy carbon electrode after stepping to +0.575 V (*5 mC cm^{-2}*) is shown in Figure* **(e)**.

The number density of gold nuclei on the carbon paper is greatest at +0.55 V. At all potentials, the number density of nuclei is higher than on glassy carbon. At +0.63 V, the nucleation and growth of gold nuclei are very slow. Less distributed and smaller

gold nuclei are observed at this positive potential even after reaching the maximum deposition charge density (5 mC cm^{-2}). However, it is possible that smaller gold nuclei have been produced but cannot be observed using the scanning electron microscope even with higher magnification. The gold nuclei deposited after the potential stepped to +0.59 V were almost the same size as those produced at +0.55 V. Nonetheless, the visible number density of nucleation centres observed at +0.59 V was not as much as observed at +0.55 V. Rapid nucleation and growth occurred after stepping the potential to +0.45 V, yet fewer nucleation centres were observed compared to a step to +0.55 V. The charge passed may also be contributed from the presence of smaller nuclei not observed, even at high magnification. When comparing Figure 48(c) and (e), the deposited gold nuclei have similar hemispherical shape and sizes, both on carbon paper and glassy carbon electrodes. In both cases, the active sites for gold nucleation are found to be not uniformly distributed on the electrode surfaces.

3.3.2.3. Double potential steps (deposition followed by stripping)

Figure 49 shows the morphology of the gold coated glassy carbon electrode after undergoing double potential steps in 1 mM hydrogen tetrachloroaurate (III) and 0.1 M hydrochloric acid. The glassy carbon electrode was initially stepped from +0.8 V to +0.2 V ***versus*** SCE for 360 s with an average charge density of 41 mC cm^{-2}. This was followed by another potential step to stripping potentials ranging from +0.8 V to +1.2 V for 270 s. It is assumed that after the first potential step, the deposition of gold has occurred and is widely distributed on the electrode surface. This is followed by the second potential step. Some of the gold nuclei had been stripped off from the electrode surface after the potential was stepped to a more positive potential. This is clearly observed in Figure 49(c) and (d), where most of the gold nuclei have been removed.

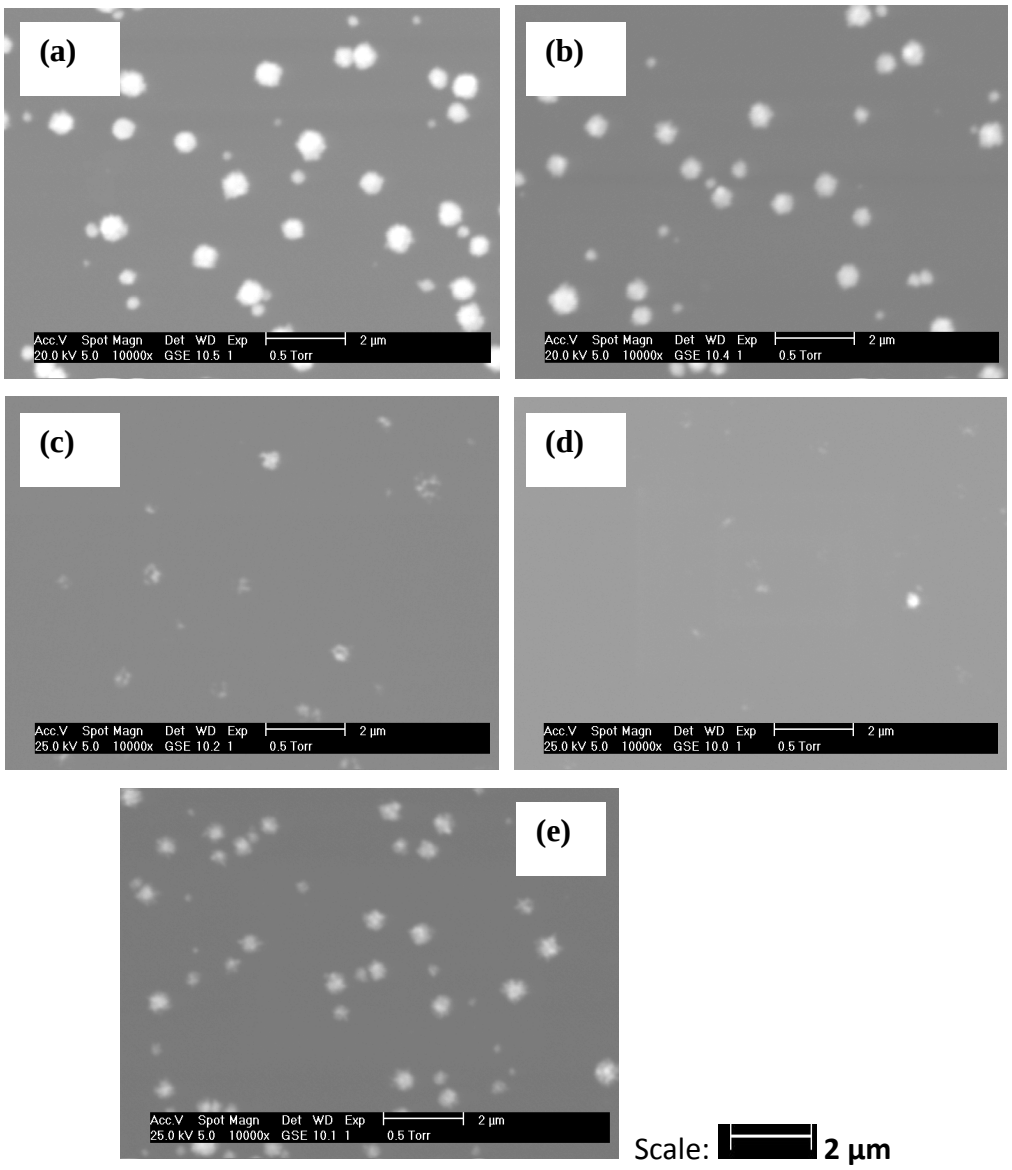

Figure 49. SEM images of vitreous carbon electrode surface (Ø = 3 mm) with presence of gold nanoparticles after undergoing double potential steps. For all electrodes, the potential was stepped initially from +0.8 V to +0.2 V versus SCE for 360 s, followed by another step to various stripping potentials for 270 s. The second potential steps are **(a)** *+0.8 V [$(q_1 - q_2) = 38$ mC cm^{-2}]* **(b)** *+0.9 V [$(q_1 - q_2) = 32$ mC cm^{-2}]* **(c)** *+1.0 V [$(q_1 - q_2) = 7$ mC cm^{-2}]* **(d)** *+1.1 V [$(q_1 - q_2) = -2$ mC cm^{-2}]* **(e)** *+1.2 V [$(q_1 - q_2) = 15$ mC cm^{-2}]. [where q_1 = initial deposition charge density, q_2 = stripping charge density].*

However at +0.8 V and +0.9 V, few nuclei are being stripped off at these potentials. Hence, the gold nuclei retain almost the same size as after the deposition step. At +1.2 V, a considerable amount of gold can be seen to remain on the electrode surface. The inhibition of the gold dissolution may be due to the formation of the gold oxide which can passivate the nuclei [211]. The microscopic observations of the electrode surface were found to be in agreement with the current-time transients. These gold coated glassy carbon electrodes were later characterised by cyclic voltammetry in acid. The catalytic responses for hydrogen evolution and oxygen reduction in alkaline media are also investigated. The results will be discussed in the following subsection.

3.4. Characterisation in acidic solution

3.4.1. Cyclic voltammograms after a single potential step

The gold coated glassy carbon electrodes were later characterised in 1 M sulphuric acid to confirm the presence of gold deposited onto the glassy carbon surface. The electrodeposited gold on glassy carbon electrodes were prepared by single potential step experiment. The potential was stepped from +0.8 V to a range of deposition potentials between +0.45 V and +0.10 V ***versus*** SCE. The electrodes were later removed from the plating bath solution after a deposition charge density of 10 mC cm^{-2} has been passed. The electrodes were rinsed with water and placed in a solution containing deoxygenated 1 M sulphuric acid. Figure 50 shows the cyclic voltammograms recorded on the gold coated glassy carbon electrode. The voltammograms were scanned at 100 mV s^{-1}.

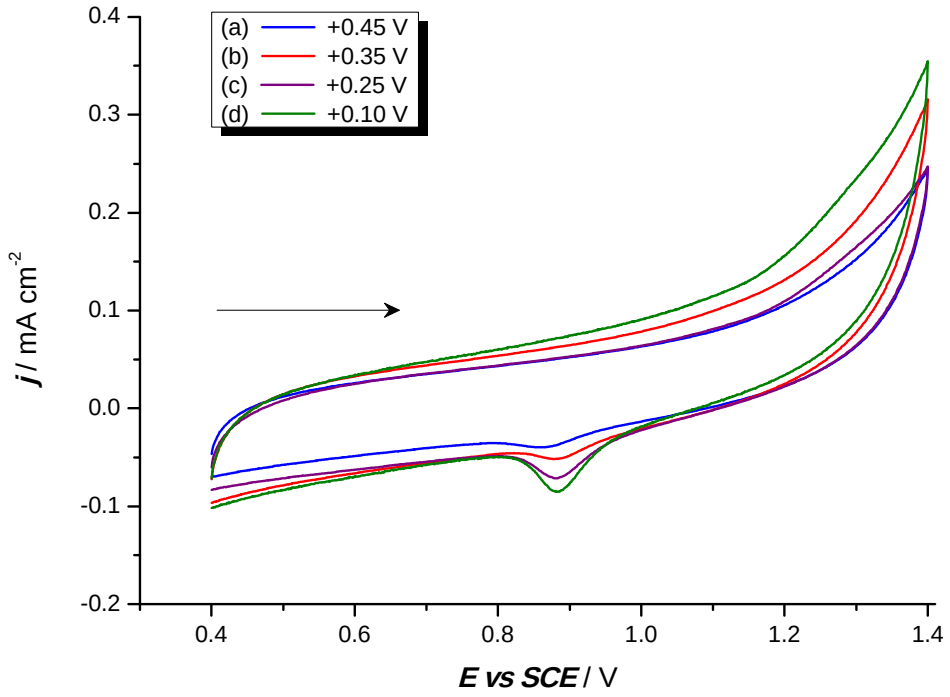

Figure 50. Cyclic voltammograms in 1 M sulphuric acid recorded on a gold coated glassy carbon electrode after undergoing potential step in gold plating bath solution from +0.8 V to various deposition potentials at a charge deposition density of 10 mC cm^{-2}. Scan rate 100 mV s^{-1}.

The cathodic peak at +0.89 V in all voltammograms in Figure 50 corresponds to the gold oxide reduction peak. The charge in the peak reflects the surface area of gold on the carbon electrode. This confirms the presence of gold nuclei on the electrode surface. However, the feature associated with the gold oxide formation is less clear. The oxidation current positive to +1.2 V corresponds to the oxygen evolution. As the deposition potential was made more negative, the gold oxide reduction peak increases. This may be due to the increase in the number density of the electrodeposited gold nuclei on the surface (see Figure 47).

3.4.2. Cyclic voltammograms after double potential step (deposition followed by stripping)

The electrodes were initially prepared by double potential steps experiment in 1 mM hydrogen tetrachloroaurate(III) in 0.1 M hydrochloric acid degassed with argon. The first potential step was carried out in order to produce substantial amount of gold on the glassy carbon electrode. This is followed by second potential step; the potential was stepped to oxidation potentials (ranging between +0.8 V and +1.2 V). In the latter process, some of the gold nuclei on the carbon surface were dissolute into the solution. The electrodes were removed from the gold plating solution and rinsed with water. The amount of gold nuclei remained on the carbon surface after the second potential step experiment is later characterised by the cyclic voltammogram in sulphuric acid. Figure 51 shows the cyclic voltammogram recorded in 1 M sulphuric acid at the gold coated glassy carbon electrode.

The cyclic voltammograms in Figure 51(a), (b) and (e) showed a reduction peak observed at +0.89 V ***versus*** SCE. The presence of gold oxide reduction peaks are in agreement with the SEM images recorded after the double potential steps in 1 mM hydrogen tetrachloroaurate (III) and 0.1 M hydrochloric acid (shown in Figure 49). After the second potential step to +0.8 V, +0.9 V and +1.2 V, most of the gold nuclei remain on the surface. However, after the potential stepped to +1.0 V and +1.1 V, most of the gold nuclei deposited have been removed from the surface (see Figure 49). The morphological observation is consistent with the cyclic voltammograms in Figure 51(c) and (d) showing no reduction peak in the same potential window. Hence, this indicates that the gold nuclei remaining on the electrode surface are not sufficient to produce the gold reduction peak. The characterisation of the gold coated glassy carbon in sulphuric acid, was followed by the investigation for its electrocatalytic properties.

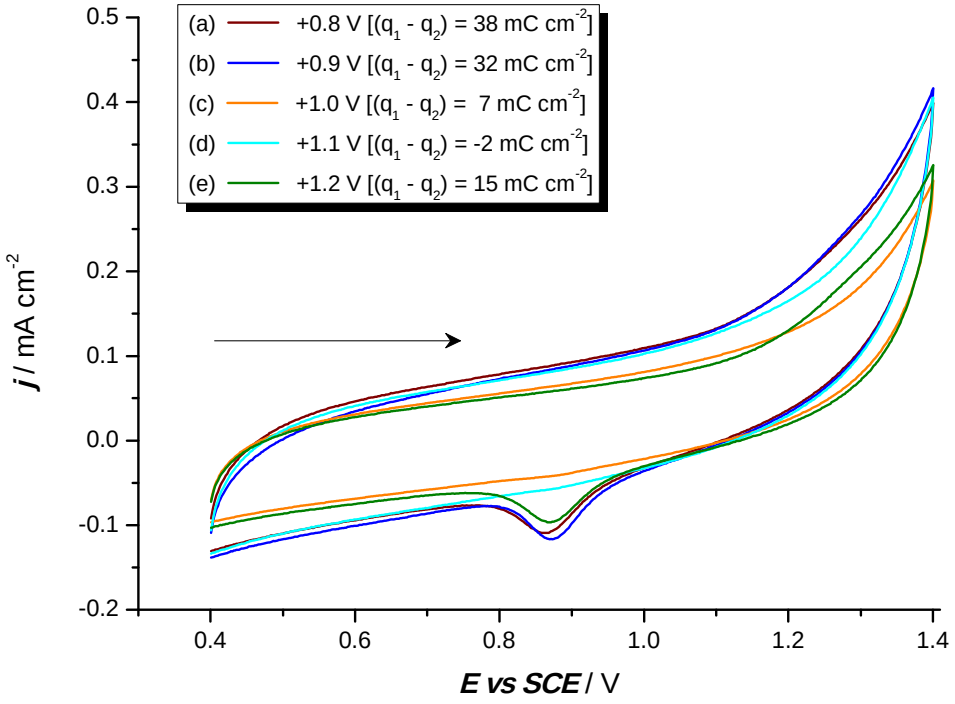

Figure 51. Cyclic voltammograms in 1 M sulphuric acid degassed with argon recorded on gold coated glassy carbon electrode (Ø = 3 mm) at a scan rate of 100 mV s^{-1}. The glassy carbon electrodes had undergone electrodeposition to +0.2 V vs. SCE for 360 s, followed by gold stripping at very positive potentials for 270 s; **(a)** *+0.8 V* **(b)** *+0.9 V* **(c)** *+1.0 V* **(d)** *+1.1 V* **(e)** *+1.2 V. [where q_1 = initial deposition charge density, q_2 = stripping charge density].*

3.5. Catalytic activity of isolated gold centres

The gold nanoparticles deposited on the glassy carbon electrode were also characterised by their catalytic acitivities for hydrogen evolution in acid and oxygen reduction in alkaline media. Further details on each set of experiments are discussed in the following subsection.

3.5.1. Hydrogen evolution

The catalytic activity of a gold coated glassy carbon electrode for hydrogen evolution was carried in 0.1 M hydrochloric acid. Linear sweep voltammograms were recorded in the range between -0.2 V and -0.8 V ***versus*** SCE at a scan rate of 100 mV s^{-1}. The gold nanoparticles were deposited onto the electrode surface with a fixed deposition charge density of 5 mC cm^{-2} at various deposition potentials. Figure 52 shows the hydrogen evolution for the gold coated glassy carbon electrodes and a bare glassy carbon electrode for comparison.

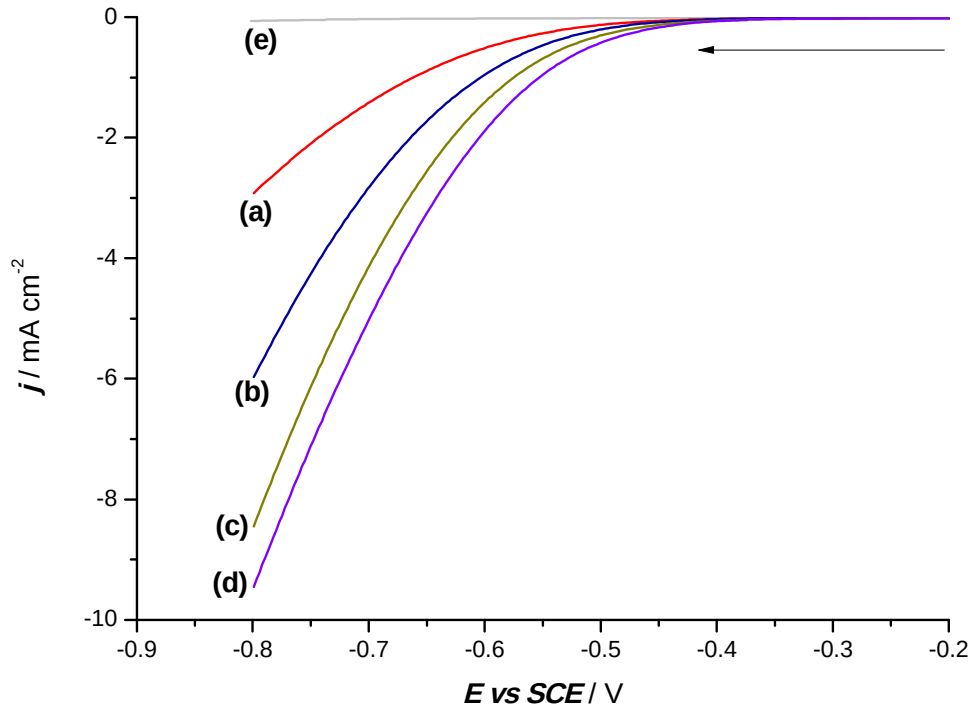

Figure 52. Hydrogen evolution recorded in 0.1 M hydrochloric acid at a scan rate of 100 mV s^{-1}. The gold coated glassy carbon electrodes had undergone chronoamperometry in gold plating bath solution, stepped from +0.8 V to **(a)** *+0.625 V* **(b)** *+0.60 V* **(c)** *+0.575 V* **(d)** *+0.50 V with a fixed deposition charge density of 5 mC cm^{-2}. Voltammogram* **(e)** *indicates the polished glassy carbon electrode. Rotation rate 900 rpm. (Ø = 3 mm).*

A polished glassy carbon electrode showed no catalytic activity for hydrogen evolution negative to -0.5 V ***versus*** SCE. However, there is a significant increase in the current density with gold coated glassy carbon electrodes. Despite the passing of the same charge, higher current densities were observed as the deposition potentials were made more negative. This may be attributed to the increase in total surface area of the gold centres on the electrode at this negative potential. Thus, gold coated glassy carbon electrodes have shown some catalytic activity for the hydrogen evolution. This data again supports the conclusions from the SEM; the morphology of the gold deposit depends strongly on the deposition potential.

3.5.2. Oxygen reduction

The oxygen reduction in alkaline media was carried out in 0.5 M potassium hydroxide saturated with oxygen. The linear sweep voltammograms were run from 0 V to -0.4 V ***versus*** SCE. The scan rate was 1 mV s^{-1}. The gold coated glassy carbon electrode were initially electrodeposited in 1 mM hydrogen tetrachloroaurate(III) and 0.1 M hydrochloric acid, stepping from +0.8 V to various deposition potentials at a fixed deposition time. Thus the deposition charge density passed on each electrode varied between 0.2 mC cm^{-2} and 5.2 mC cm^{-2}.

Figure 53 shows the linear sweep voltammograms in alkaline solutions saturated with oxygen, recorded at gold coated glassy carbon electrodes as well as on a bare glassy carbon electrode. It is clear that similar catalytic activities can be seen when there is an increase in charge density passed during deposition. The oxygen reduction starts at a more positive potential with the gold coated glassy carbon electrodes after deposition charge density of greater than 5 mC cm^{-2} has been passed. Although the deposition charge density passed were 5.2 mC cm^{-2} and 5.1 mC cm^{-2} at 0 V and +0.2 V respectively, the onset of the reduction wave differed by ~0.05 V. Therefore, even with a small increase in deposition charge density passed, the onset of the oxygen reduction reactions can be greatly influenced by the increase in amount of gold present on the electrode surface.

As the charge density passed was 0.2 mC cm^{-2}, the gold nuclei are hardly observed under scanning electron microscope, even at higher magnification. The catalytic activity towards oxygen reduction at this electrode was found to be less when compared to a polished glassy carbon electrode. However, with a reasonable distribution of gold nuclei on the glassy carbon, the catalytic activity increases when compared to a polished glassy carbon. Thus, the current density for oxygen reduction at a given potential increases with more nucleation centres on the glassy carbon surface. It appears that a critical size of nucleus is necessary for significant catalysis.

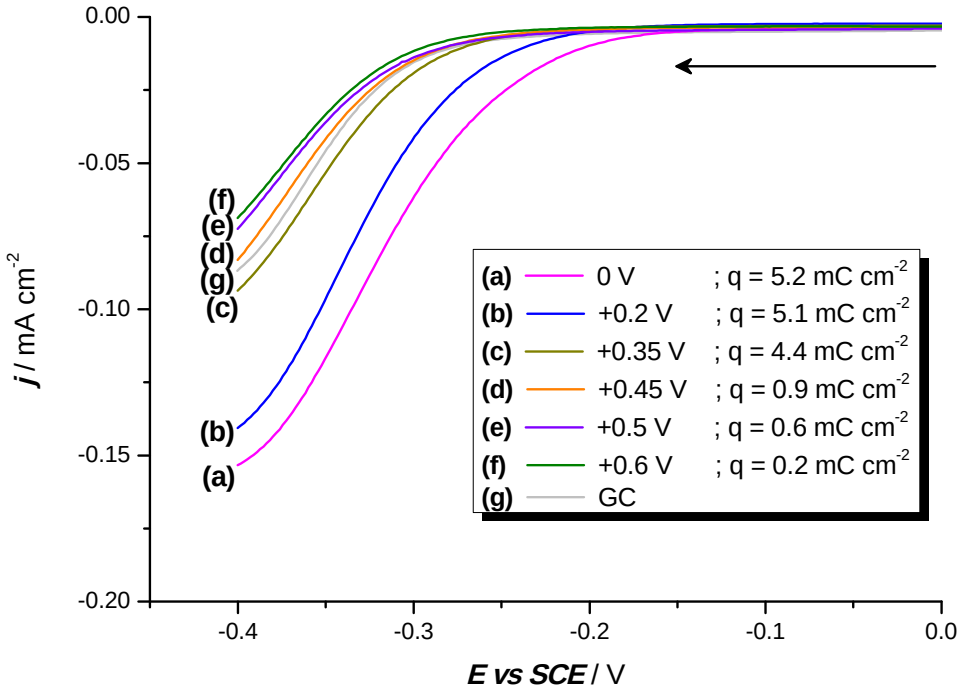

Figure 53. Linear sweep voltammograms in 0.5 M potassium hydroxide saturated with oxygen recorded on gold coated vitreous carbon electrode (Ø = 3 mm) at a scan rate of 1 mV s^{-1}. The gold coated vitreous carbon electrodes were initially stepped from +0.8 V versus SCE for 20 s to various deposition potentials; **(a)** *0 V* **(b)** *+0.2 V* **(c)** *+0.35 V* **(d)** *+0.45 V* **(e)** *+0. 5 V* **(f)** *+0.6 V. Linear sweep voltammogram* **(g)** *indicates the polished glassy carbon electrode.*

3.6. Conclusions

1. The reduction of gold(III) from hydrogen tetrachloroaurate(III) in acidic media presents a simple mechanism with one reduction wave, followed by a nucleation loop. Well-defined limiting current was obtained negative to +0.5 V ***versus*** SCE indicating a mass transport (diffusion) controlled reaction. The voltammetry of gold(III) reduction showed a slow electron transfer reaction for the Au(III)/Au couple.

2. The deposition chronoamperometry shows classical rising transients. The processes of nucleation and growth of the nuclei centres are rapid when sufficient overpotential has been applied.

3. The SEM images have shown that a complete layer of gold on all carbon surfaces is difficult to achieve. Despite large deposition charges being passed, the gold deposit formed isolated centres. These centres appear to have hemispherical shapes.

4. Complete stripping of gold is possible at some potential positive to +1.0 V ***versus*** SCE. However, passivation occurs at more positive potentials.

5. Small centres < 50 nm diameter cannot be observed using the scanning electron microscope. Thus, different techniques such as the study of catalytic activity must be carried out. However, it is difficult to find simple catalytic reactions for gold. Other alternative techniques would be using scanning tunneling microscope (STM) or atomic force microscopy (AFM).

6. The number density and size of gold centres can be controlled by selection of the potential and charge density. The morphology also depends on the form of carbon.

7. SEM images, the study of hydrogen evolution and of oxygen reduction in alkaline media show that the morphology and activity of the surfaces is very sensitive to the deposition potential. It is possible to create surfaces with highly dispersed large (> 1 μm) gold centres or surfaces with a large number of small centres (< 100 nm).

8. While not observable by SEM, it is reasonable to conclude that dispersed uniform gold nanocentres could be produced by low charge density deposition at large overpotential, approximately at potential of 0.0 V ***versus*** SCE.

Chapter 4

4 Electrodeposition of platinum on carbon substrate

In this research, the electrodeposition of platinum has been investigated from the solution containing hexachloroplatinate(IV) acid. In order to produce small platinum centres, it is necessary to know the conditions for the electrodeposition of platinum from this platinum salt. Therefore, it is important to understand the mechanism for the reduction of $PtCl_6^{2-}$. In recent years, there have been many reports on the electrodeposition of highly structured platinum deposits from the solutions containing hexachloroplatinate(IV) acid [23, 76, 104, 105, 109, 110, 127, 177-180]. However, there is very little literature on studies of the mechanism for the reduction of platinum(IV) complex. Several groups have reported voltammograms with multiple reduction waves that have been ascribed to the sequential reduction of platinum(IV) to platinum(II) to platinum metal [187, 189, 191, 192]. In this chapter, the mechanisms for the reduction of $PtCl_6^{2-}$ in the presence of hydrochloric acid will be discussed based on voltammetry. Moreover, evidence for the presence of

platinum centres obtained from the surfaces using scanning electron microscope will be reported.

The carbon substrates employed in this research are in the form of vitreous carbon rotating and stationary disc electrodes, carbon fibre microwire and microdisc electrodes. It is known that carbon supported platinum particles are widely used as electrocatalysts for both hydrogen oxidation and oxygen reduction in low temperature fuel cells [66, 102, 251]. This leads to an extensive investigation on the preparation of dispersed platinum nanoparticles on the inert carbon substrate to maximise the catalytic activity with less loadings of the expensive material [33]. In addition, carbon material provides good conductivity and thermal stability, low cost and good corrosion resistance under oxidizing conditions. The electrodeposition of platinum nanoparticles onto different forms of carbon substrates has been investigated using several approaches, such as cyclic voltammetry, potential step deposition and double-pulse chronoamperometry. The electrochemical conditions for the platinum deposition are varied, thus different platinum loadings onto the substrate are produced. The electrocatalytic activity of the prepared platinum coated carbon electrodes towards the oxygen reduction and hydrogen evolution reactions are also investigated.

4.1. Voltammetry of hexachloroplatinate(IV) solution

Unless otherwise stated, prior to the experiment, the vitreous carbon rotating disc electrode was polished with alumina. The polished vitreous carbon disc electrode was then employed in recording cyclic voltammograms in sulphuric acid solution to ensure that the electrode surface was free from contamination with platinum. The cyclic voltammograms with the polished electrode were reproducible as displayed in Figure 35 showing the slight oxidation/reduction of quinone-hydoquinone redox couple and the oxygen evolution at potentials positive to +1.2 V ***versus*** SCE.

4.1.1. Reduction waves of platinum(IV) in HCl on vitreous carbon RDE

Figure 54 reports a cyclic voltammogram recorded at a polished rotating glassy carbon electrode for an aqueous solution of 5 mM H_2PtCl_6 and 0.1 M HCl. The working electrode is rotated at 400 rpm. The negative potential limit was chosen to be -0.4 V ***versus*** SCE, as the hydrogen evolution on a platinum surface occurred just negative to -0.4 V.

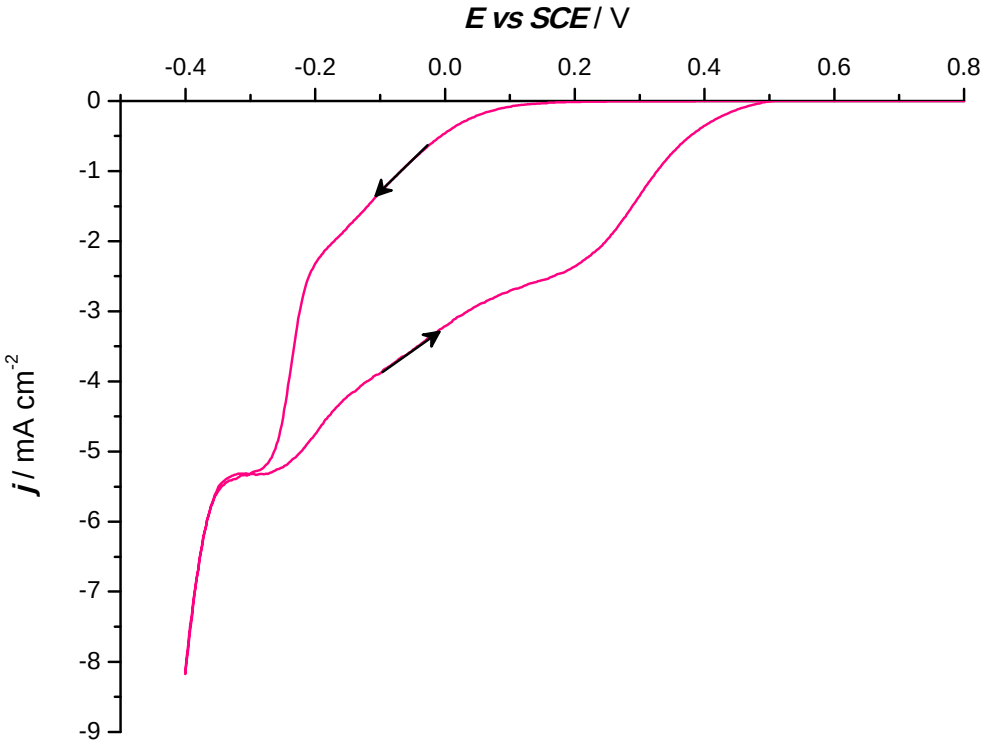

Figure 54. Cyclic voltammetry recorded at a 3 mm diameter glassy carbon disc electrode rotated at 400 rpm in 5 mM H_2PtCl_6 and 0.1 M HCl saturated with argon. Potential scan rate 20 mV s^{-1}.

On the forward scan, there is no cathodic current positive to +0.15 V. Two reduction waves are observed with half wave potentials at -0.08 V and -0.24 V ***versus*** SCE.

The reverse scan appears to be different from the forward scan as three reduction waves are observed. More importantly, cathodic current is observed at all potentials negative to +0.5 V ***versus*** SCE. In addition, the electrode surface showed a thin shade of greyish appearance after recording the cyclic voltammogram. Clearly, the shape of the voltammogram is determined by the nucleation of the platinum phase.

Three consecutive cycles of the cyclic voltammogram in 5 mM H_2PtCl_6 in 0.1 M HCl recorded on a polished vitreous carbon rotating disc electrode are shown in Figure 55. The vitreous carbon electrode is rotated at 900 rpm and the potential scanned at 50 mV s^{-1}. The three consecutive cycles are recorded continuously without repolishing the electrode after each complete cycle. The voltammograms of the second and third scans appear to be very similar to the backward scan of the first cycle. The half wave potential for the first reduction wave on the second scan onwards has shifted more positively to +0.35 V compared to the first scan voltammogram ($E_{½}$ = -0.05 V ***versus*** SCE). On the first scan, the second reduction wave appeare to be steeper ($E_{¾} - E_{¼}$ = 0.03 V) than the first reduction wave ($E_{¾} - E_{¼}$ = 0.14 V). However, after the second scan, the second reduction waves become more drawn out.

A significant increase in the hydrogen adsorption and desorption charges is observed in the potential range 0 V to -0.4 V as more platinum deposits onto the glassy carbon rotating disc electrode. The background current for 0.1 M HCl in absence of platinum(IV) was also recorded. The hydrogen evolution on glassy carbon surface only starts to occur at potentials negative to -0.8 V. For the platinum(IV) solution, substantial cathodic current is observed at all potentials less positive than +0.5 V ***versus*** SCE and three reduction waves are clearly seen. The reduction waves on the reverse and second scans onwards must be for the reduction of platinum(IV) at a newly platinum deposited electrode surface. The greyish appearance on the glassy carbon surface further confirms the deposition of platinum onto the electrode surface.

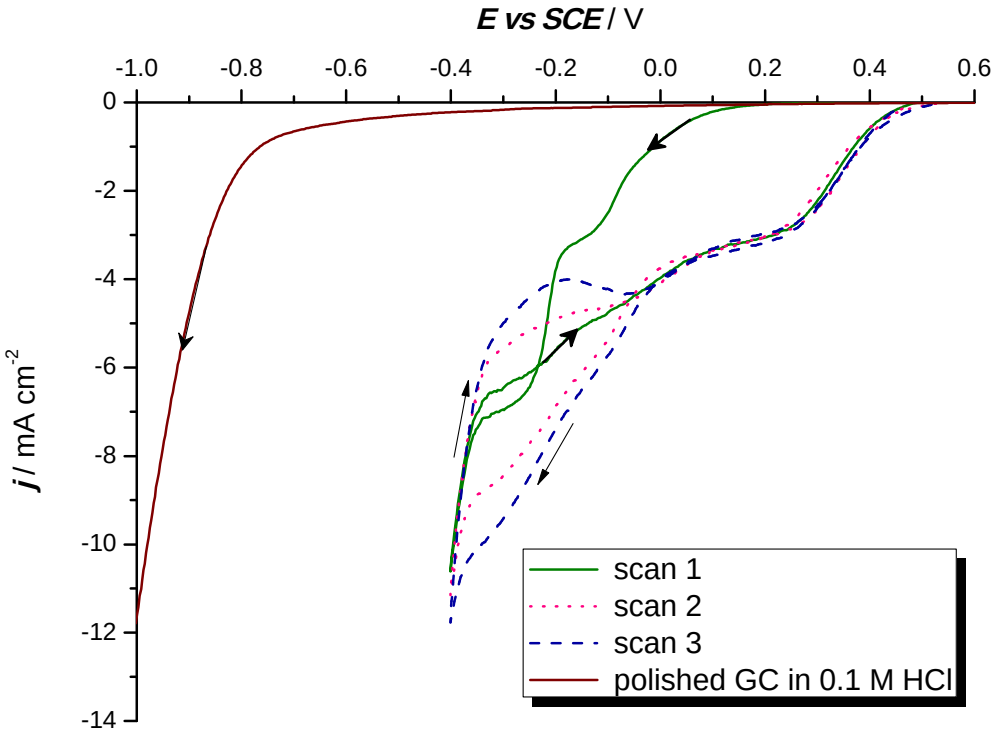

Figure 55. Three consecutive cyclic voltammograms in 5 mM H_2PtCl_6 + 0.1 M HCl recorded at glassy carbon RDE (Ø = 3 mm) and also in only 0.1 M hydrochloric acid (background current). Rotated at 900 rpm. Potential scan rate 50 mV s^{-1}.

Figure 56 shows linear sweep voltammograms recorded as a function of the rotation rate for a platinum coated glassy carbon disc electrode. The previously Pt coated glassy carbon electrode surface was intentionally used in order to avoid the features involving nucleation. At all rotation rates, three reduction waves are observed. The onset of the initial reduction wave starts to occur at +0.6 V ***versus*** SCE. The first wave is very drawn out along the potential axis. Nevertheless the limiting current density is approximately half the current density observed at -0.35 V. The limiting current measured at +0.1 V is proportional to the square root of the rotation rate. Hence, the first reduction reaction is mass transport controlled with respect to a species in solution. At the lowest rotation rate, the reduction waves are well resolved.

The subsequent second and third waves at 400 rpm are steeper. However, as the rotation rate is increased, the two waves become more drawn out. The current density at -0.35 V is strongly dependent on rotation rate. Thus, the reduction reaction at this potential is also mass transport controlled. However at higher rotation rates, the plateaux are poorly defined.

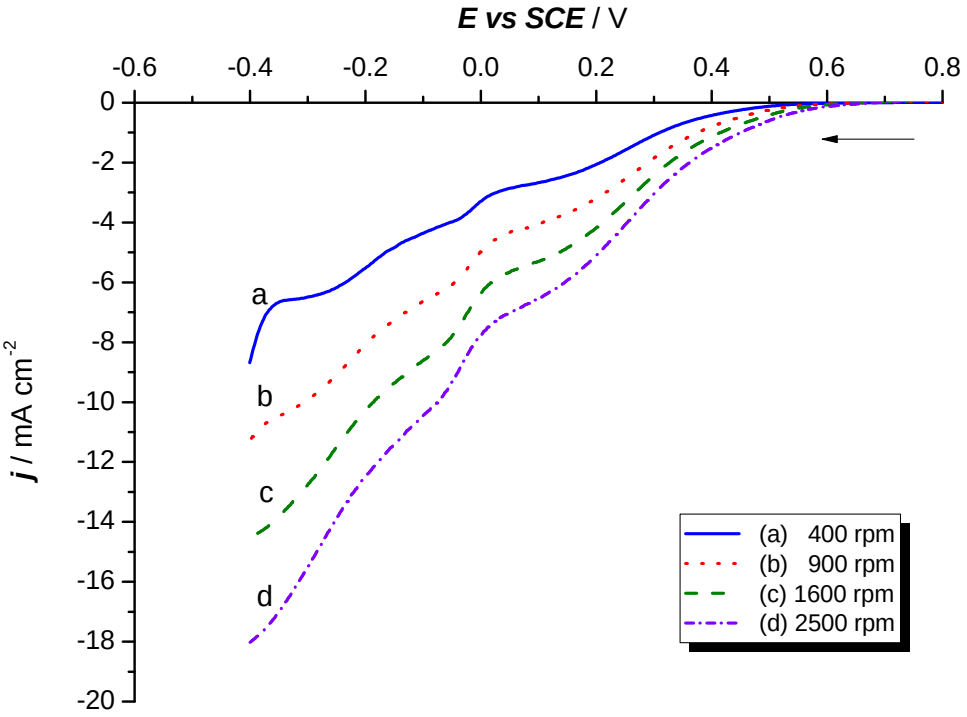

Figure 56. Linear sweep voltammograms recorded at a platinum coated glassy carbon RDE (3 mm diameter) in 5 mM H_2PtCl_6 and 0.1 M HCl, 20 mV s^{-1} and variable rotation rates.

In comparison to the background current recorded for hydrochloric acid in the absence of platinum(IV) (see Figure 55), these multiple reduction waves all lead to the deposition of platinum. The three waves suggest the presence of three independent platinum(IV) species in solution which are not interconverting on the time scale of the electrochemical experiments. This supported by the fact that the

limiting current ratios do not depend on the type of working electrode used. These species are thought to arise from the following chemistry:

$$PtCl_6^{2-} + H_2O \rightleftharpoons PtCl_5(H_2O)^- + Cl^-$$

$$PtCl_5(H_2O)^- + H_2O \rightleftharpoons PtCl_4(H_2O)_2 + Cl^-$$

There is both UV [174, 175] and NMR [164, 172] evidence to support the existence of these three species in solution. The ratio of limiting currents suggests that the species $PtCl_4(H_2O)_2$: $PtCl_5(H_2O)^-$: $PtCl_6^{2-}$ in 0.1 M hydrochloric acid are present in the ratio 10:3:7. Indeed assuming that the diffusion coefficient for $PtCl_6^{2-}$ is similar to that for $AuCl_4^-$, the limiting currents are close to those calculated for a mass transport controlled reaction. In no experiment was anodic current for the dissolution of platinum metal observed.

4.1.2. First reduction waves of platinum(IV)

In the previous cyclic voltammograms, multiple reduction waves were reported at potentials positive to -0.35 V ***versus*** SCE. In the following experiment, the negative limit of the voltammogram has been restricted to -0.15 V, just to focus on the first reduction wave. Figure 57 shows the voltammetric response for the first reduction wave recorded at a polished vitreous carbon disc electrode.

On the forward scan, the nucleation of platinum starts at about +0.2 V ***versus*** SCE. There is a strong hysteresis between the forward and reverse scans, consistent with a nucleation loop. There is an increase in the current density on the reverse scan at potential negative to +0.3 V. This arises because the increase in surface area of the platinum nuclei overshadows the decreasing overpotential for platinum(IV) reduction. Thus the characteristics of the voltammogram can be associated with the

process of nucleation and growth of platinum nuclei on the electrode surface. However, there is no anodic current present on the reverse scan showing no dissolution of platinum takes place. This is expected for a solution containing relatively low chloride ion concentration. The reflective black glassy carbon surface appears slightly dull at the end of the experiment.

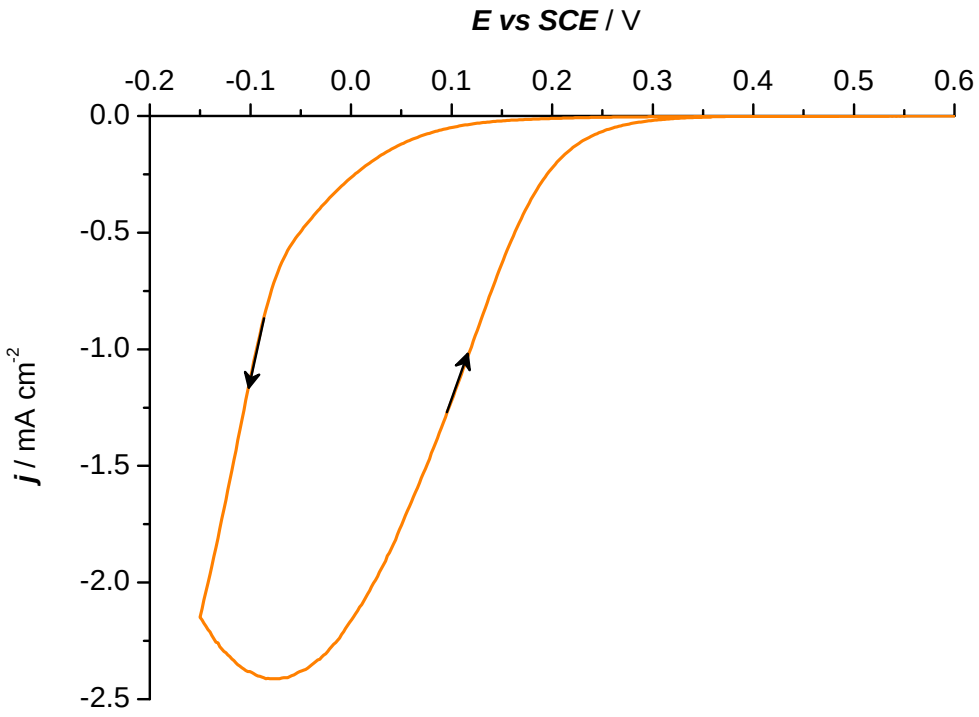

Figure 57. Cyclic voltammogram for the first reduction wave in 5 mM hexachloroplatinate(IV) in 0.1 M HCl, at a 3 mm diameter glassy carbon RDE rotated at 900 rpm. Scan rate 20 mV s^{-1}.

4.1.3. Reduction of platinum(IV) acid in hydrochloric acid on carbon fibre electrodes

Using similar conditions as for vitreous carbon rotating disc electrodes, the voltammograms for the reduction of hexachloroplatinate(IV) in hydrochloric

solution were recorded at a 7 μm diameter (5 mm length) carbon fibre wire electrode. The carbon fibre wire electrode was assembled and measured, so that the length of exposed carbon fibre was (5.0 ± 0.1) mm. This carbon fibre electrode does not require any pretreatment with alumina and it is intended to be used only for one set of experiments. The potential scan rate was 1 mV s^{-1}. Two consecutive cyclic voltammograms recorded at a carbon fibre wire electrode in the platinum plating bath solution are shown in Figure 58.

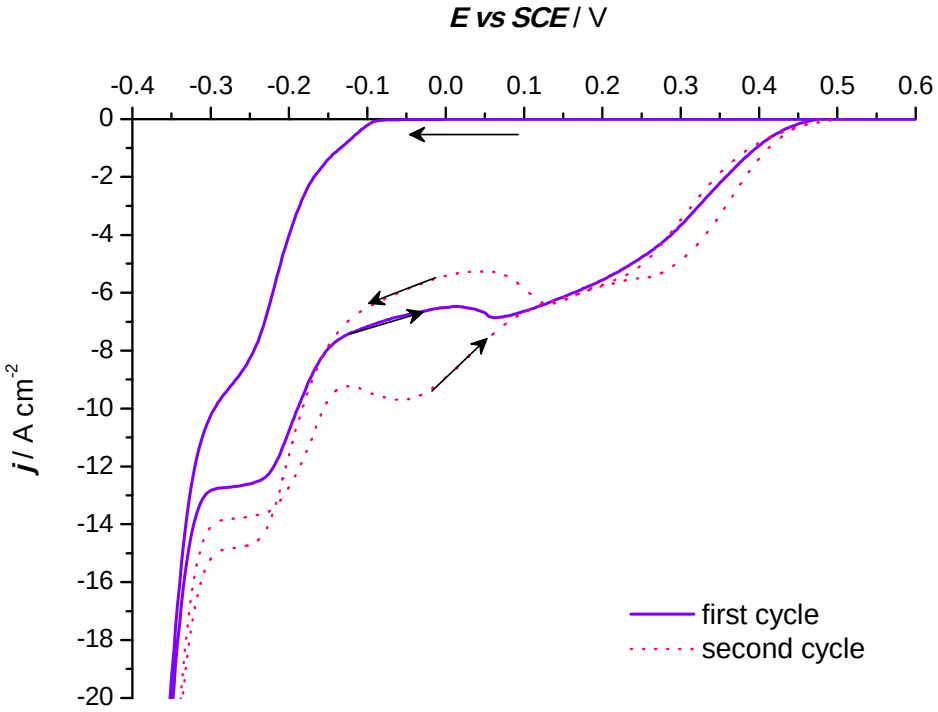

Figure 58. Cyclic voltammograms recorded at a 7 μm diameter carbon fibre wire (l = 0.5 cm) in 5 mM H_2PtCl_6 + 0.1 M HCl degassed with argon, 1 mV s^{-1}.

Two reduction waves were observed on the forward scan of the first cycle. The onset of the first reduction wave with a $E_{½}$ = -0.125 V ***versus*** SCE started at -0.1 V. The second reduction wave is steep ($E_{½}$ = -0.22 V ***versus*** SCE) with limiting current density at -0.25 V. This is followed by an increase in current density that is ascribed to hydrogen evolution. Multiple reduction waves are observed on the backward scan of the first cycle and these reduction waves also overlaps with the second cycle.

These reduction waves are thought to correspond to the presence of several platinum(IV) species in the bath solution. Thus, the voltammogram produced at carbon fibre wire electrodes has similar features as the voltammogram recorded on vitreous carbon rotating disc electrodes. However, a higher overpotential is required for the nucleation to take place on the carbon fibre wire electrode. This indicates the nucleation on the carbon fibre wire electrode is more difficult. The surfaces of the two forms of carbon must be different. With the presence of the deposited platinum onto both carbon substrates (vitreous carbon and carbon fibre wire electrodes), the platinum(IV) starts to reduce at similar positive potential.

Figure 59 shows a cyclic voltammogram for the first reduction wave recorded in the same plating bath solution on the carbon fibre wire electrode. Again, a nucleation loop can be observed when the negative limit is only at -0.15 V ***versus*** SCE.

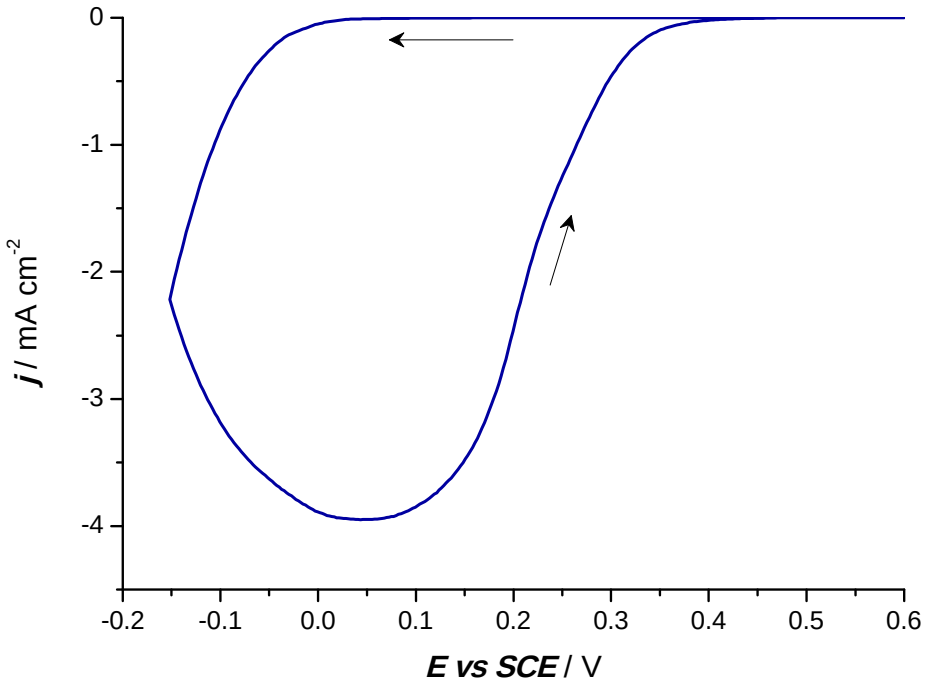

Figure 59. Cyclic voltammetry for the first reduction wave of hexachloroplatinate(IV) (5 mM) in hydrochloric acid (0.1 M) recorded at 7 µm diameter carbon fibre. Scan rate 1 mV s^{-1}.

On the forward scan, the platinum starts to nucleate on the electrode surface at about +0.05 V versus SCE. There is an increase in the current density on the reverse scan at potentials negative to +0.5 V. This increase in current density is associated with the process of nucleation and growth of platinum nuclei on the electrode surface. There is no dissolution of platinum taking place over the potential window investigated as no anodic current is observed on the reverse scan.

4.1.4. Reduction waves in aqueous solution of hexachloroplatinate(IV) acid

In Southampton, mesoporous Pt films have generally been deposited from a liquid crystal medium containing only aqueous hexachloroplatinic acid without any addition of other electrolyte [104, 105, 127]. It was therefore of interest to investigate the reduction waves of H_2PtCl_6 produced without the presence of hydrochloric acid. The voltammetric response recorded in absence of electrolyte in the medium is made possible by using microelectrodes. Figure 60 reports two subsequent cyclic voltammograms for the aqueous solution of hexachloroplatinic acid.

Once again the voltammograms produced are very similar to those reported in the presence of hydrochloric acid. On the forward scan of the first cycle, there is a steep reduction wave with a half wave potential at -0.25 V ***versus*** SCE, followed by an increase in current density. It is clear that a large overpotential is required for the nucleation of the platinum centres to occur, thus a significant cathodic current can only be observed at -0.2 V ***versus*** SCE. The reverse scan produced three drawn out cathodic waves. The reduction waves of the second cycle overlap with the reverse scan of the first cycle with cathodic current occurring at all potentials negative to +0.6 V. There is an increase in the hydrogen adsorption and desorption as more platinum is deposited onto the carbon fibre. Thus, voltammograms with similar

multiple waves on the backward scans are observed, with and without the presence of hydrochloric acid, in the plating bath solution.

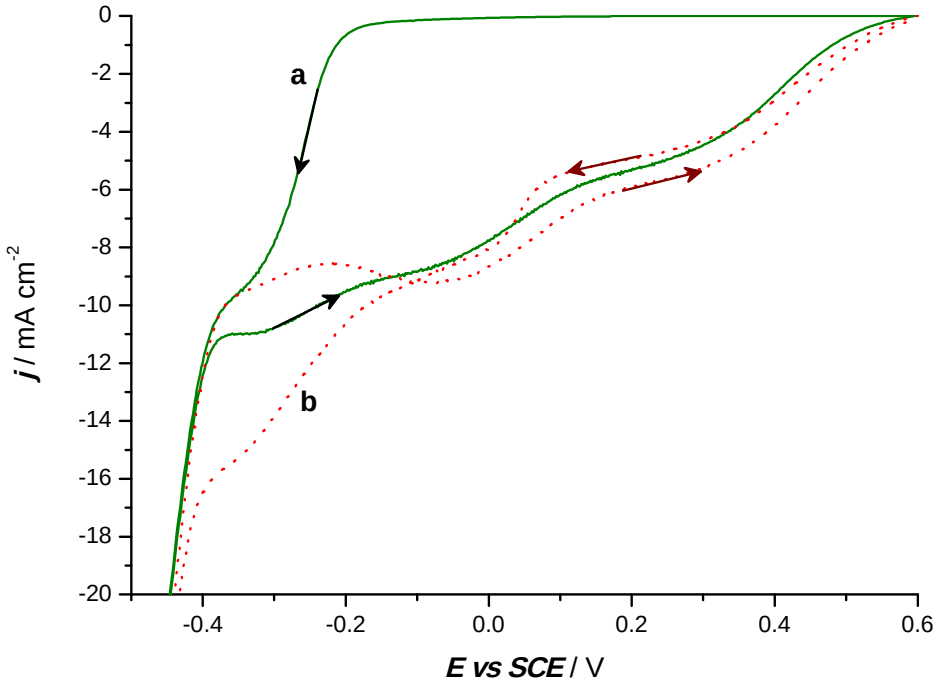

Figure 60. Two consecutive cyclic voltammograms recorded on a 7 µm diameter (l = 5 mm) carbon fibre in aqueous solution containing only 5 mM H_2PtCl_6 deoxygenated with argon; **(a)** *first scan and* **(b)** *second scan. Potential scan rate 20 mV s^{-1}.*

The voltammetry is consistent with all the cathodic waves being associated with the reduction of platinum(IV) to platinum(0). If platinum(II) is formed during the reduction process, it is unstable under the conditions of the experiments. All of the voltammograms recorded at the glassy carbon rotating disc and carbon fibre electrodes have shown that a large overpotential is required for the nucleation of a platinum metal. Hence, the nucleation is a difficult process. Further investigation on the electrodeposition of platinum used a potential step technique with carbon fibre wire electrodes as the substrate.

4.2. Electrodeposition of platinum at various potentials

The electrodeposition of platinum on vitreous carbon electrodes has shown that the voltammetric response during the initial cycles was dependent on the nature of the electrode surface. The complete removal of platinum from the vitreous carbon electrode surface after each experiment was difficult to achieve, and it required extensive polishing of the electrode surface. This is because the platinum nuclei adhere well to the glassy carbon surface. Also they do not dissolve anodically. Therefore, it was desirable to use a 'disposable' substrate. Thus, a 7 µm diameter carbon fibre wire electrode with 5 mm length was used for further experiments. This carbon fibre electrode can be used only for one experiment and no polishing is involved prior to the experiment.

4.2.1. Current density transients

Current density transients for potential steps from +0.6 V to a series of negative potentials ranging from -0.25 V to 0 V are shown in Figure 61. Well formed rising transients are observed and they are consistent with the nucleation and growth of a new phase. However, the timescale of the transients is unusually long. Even the increase in current density at the limiting current plateau region of the most negative waves in the voltammograms (that is, -0.25 V) takes over 300 s. This potential is 0.75 V negative to the onset of the reduction waves on the reverse scan of the voltammogram (see Figure 54). Moreover, the timescales of the rising transients is insensitive to the applied potential. In contrast, at short times, the current density depends strongly on potential.

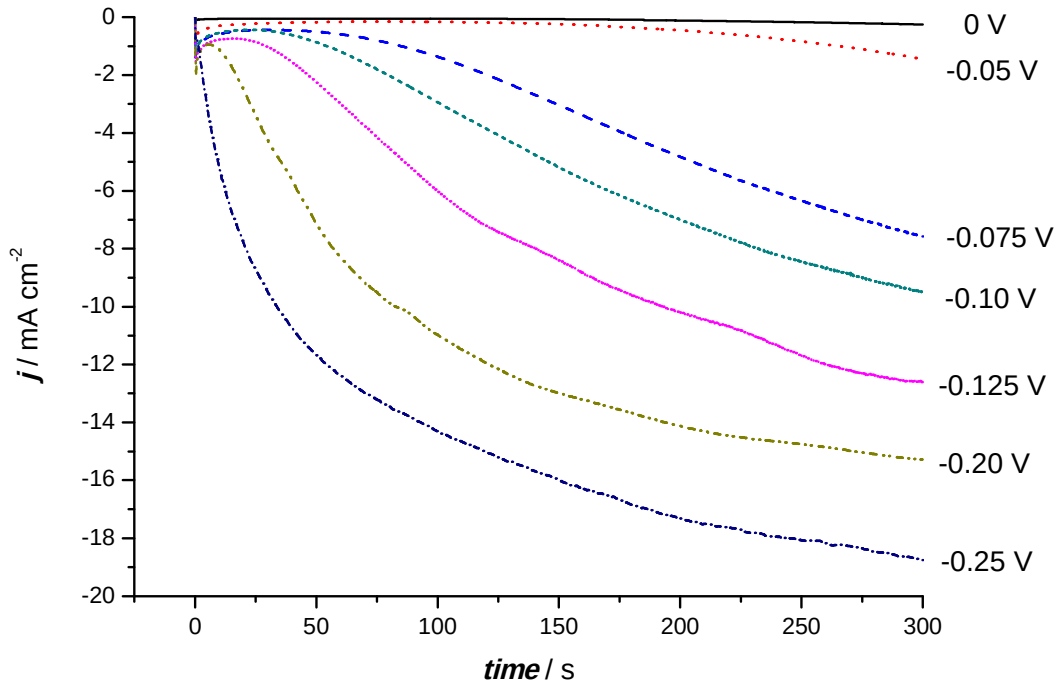

Figure 61. Chronoamperometry in 5 mM H_2PtCl_6 and 0.1 M HCl degassed with argon. The working electrode is a 7 µm diameter (l = 5 mm) carbon fibre wire. The potential was stepped from +0.6 V versus SCE to various potentials for a fixed duration time (i.e. 300 s). Each transient was recorded with a new fibre.

The investigation on the nucleation of platinum was further extended to the more positive potentials. There is a slight increase in the current density on a 1800 s timescale when the potential was stepped to +0.1 V ***versus*** SCE. At +0.2 V, there was no observable rise in current density even when the transient response was recorded for 3 h. Thus, nucleation does not occur at potentials positive to +0.1 V.

4.2.2. Morphological observations

In a separate chronoamperometry experiment, the potential was stepped for 40 s to -0.25 V, -0.125 V and 0 V. For the potential step to +0.1 V, the deposition time was 3600 s to ensure that sufficient deposition charge density passed in order to view small platinum centres on the carbon fibre. The morphology of a new carbon fire wire electrode and the platinum centres deposited onto carbon fibres after undergoing the potential steps are shown in Figure 62.

Typical SEM images display the hemispherical shape of platinum centres deposited onto the carbon fibre wire electrode surface. The number of platinum centres increases with deposition at more negative potentials. In addition, the size of the platinum centres produced at -0.25 V ranges between 0.2 µm and 1.8 µm. Within the limited deposition time, the amount of deposition charge density passed decreases as the deposition potentials are made more positive. Thus, the diameter of the platinum nuclei deposited are smaller. At -0.125 V, the deposited platinum centres are sparsely distributed with smaller diameter nuclei (ranging from 80 nm to 500 nm). Very few platinum centres can be observed at 0 V. However, the scanning electron microscope can only detect nuclei of size greater than 50 nm. Hence, there is a possibility of much smaller platinum centres that are not visible even when viewing at higher magnification.

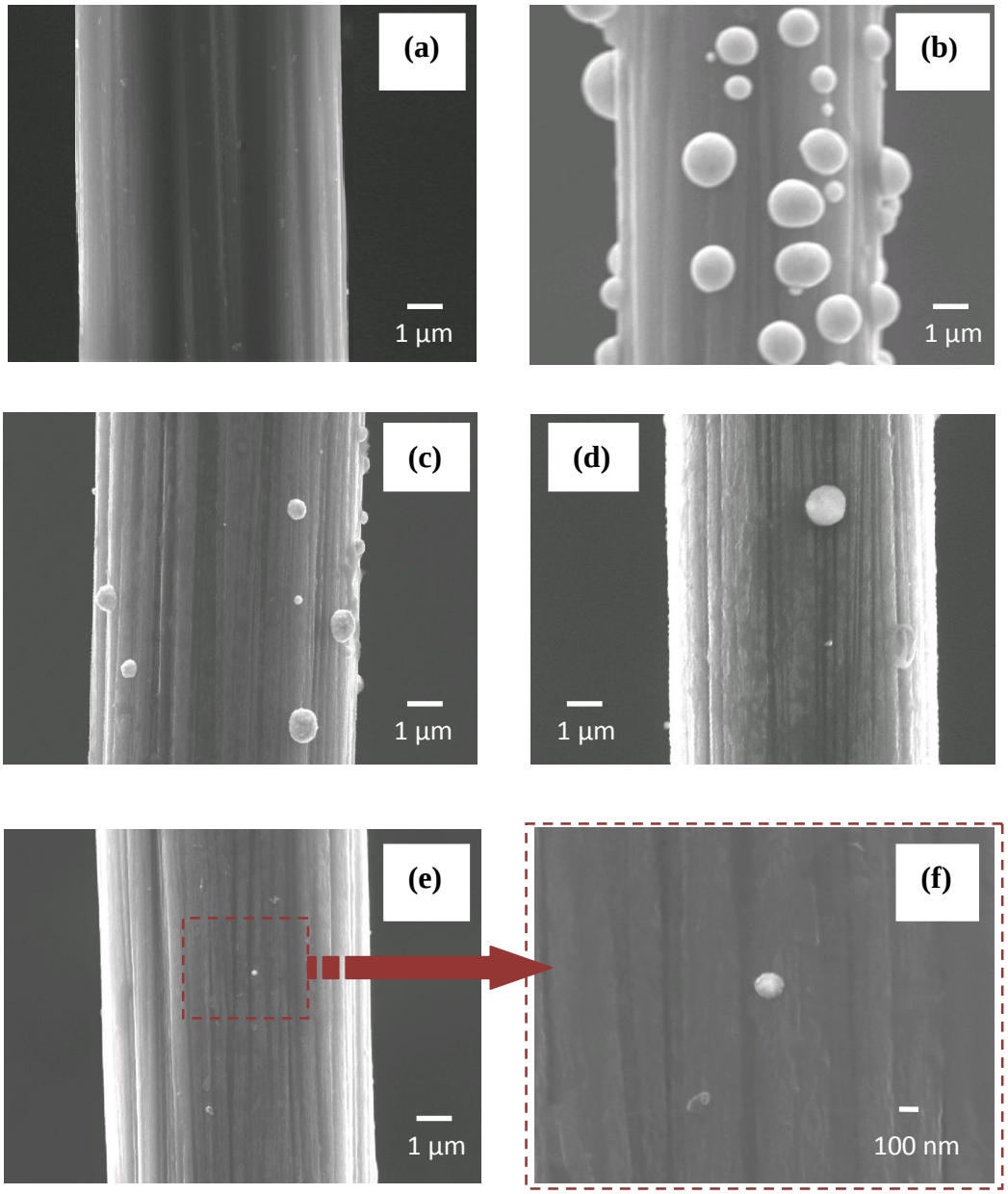

Figure 62. SEM images of sections of platinum coated carbon fibre wires 7 µm diameter (l = 5 mm) after electrodeposition in a deoxygenated 5 mM H_2PtCl_6 and 0.1 M HCl after stepping to various deposition potentials for 40 s to; ***(b)*** *-0.25 V* ***(c)*** *-0.125 V* ***(d)*** *0 V and* ***(e)*** *+0.1 V versus SCE for 3600 s (at 20k magnification)* ***(f)*** *+0.1 (at 50k magnification). A new carbon fibre wire electrode is shown in figure* ***(a)****.*

Figure 62(e & f) show the image of the electrode surface after undergoing potential step to +0.1 V ***versus*** SCE for 3600 s. The platinum centre has a diameter of approximately 130 nm. The presence of platinum centres on the carbon fibre was confirmed with the increase in the catalytic activity for hydrogen evolution in 1 M sulphuric acid solution (See Figure 63).

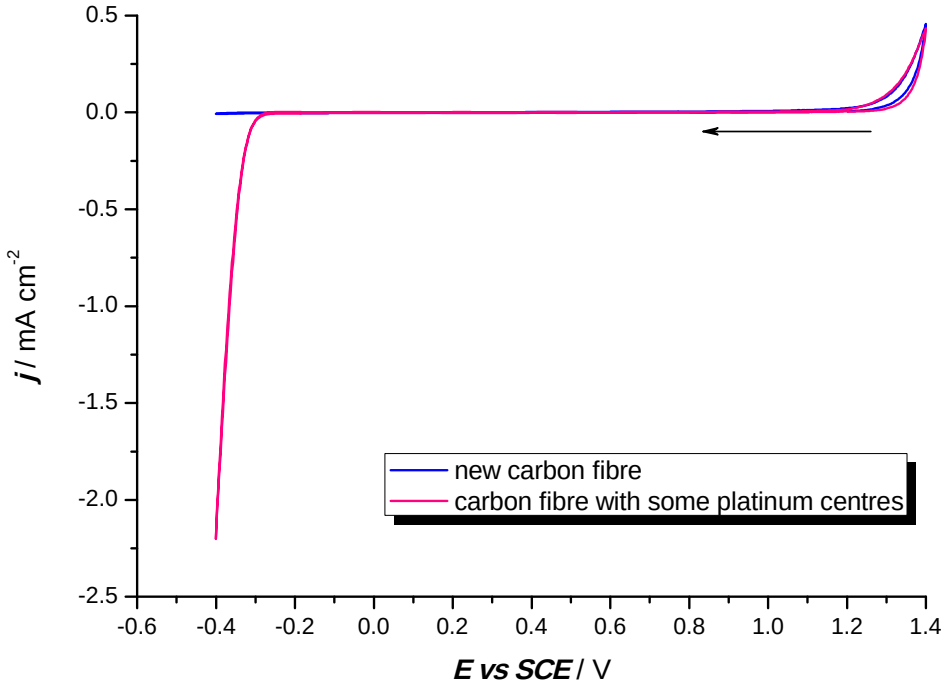

Figure 63. Cyclic voltammetry in 1 M sulphuric acid degassed with argon with a scan rate of 100 mV s^{-1} recorded on a platinum coated carbon fibre wire (after the electrodeposition for 3600 s in the same plating bath solution) and freshly cut carbon fibre wire electrode.

Therefore, electrodeposition of platinum can also be achieved at +0.1 V ***versus*** SCE but requires a longer deposition time to nucleate platinum centres. It is also believed that all potentials negative to +0.5 V will also lead to the deposition of platinum provided nucleation is initiated. To test this hypothesis, further investigation are carried out by combining different potential steps to initiate the nucleation and control the growth of the platinum centres.

4.3. Single and double step chronoamperometry

4.3.1. Single potential step experiments

A set of single potential step experiments was carried out in a solution containing hexachloroplatinate(IV) and hydrochloric acid for different deposition times ranging from 20 s to 100 s. The potential was stepped from +0.6 V to a very negative potential (that is -0.25 V ***versus*** SCE) for different deposition times and the total charge passed was recorded. For every single experiment, a new carbon fibre wire electrode was used. Figure 64 shows the current density-time transients for the set of single potential step experiments.

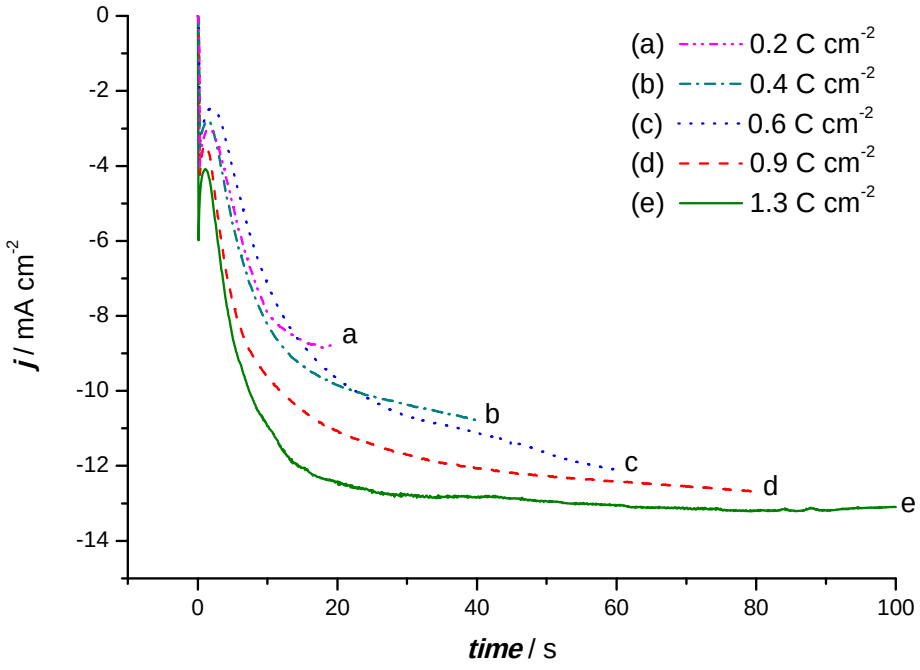

Figure 64. Single potential step chronoamperograms recorded in 5 mM H_2PtCl_6 and 0.1 M HCl degassed with argon on a carbon fibre wire of 7 µm diameter (l = 5 mm). The potential was stepped from +0.6 V to -0.25 V versus SCE for various deposition time. Each transient was recorded with a fresh fibre.

In all of the experiments, rising transients are observed initially resulting from the nucleation and growth of the platinum nuclei onto the carbon fibre. The response also shows good reproducibility between electrodes. The current density tends to reach its mass transport controlled value after about 20 s of deposition time. The transients can be seen to vary slightly probably due to differences in the surface of different carbon fibres. These platinum coated carbon fibres were later monitored using a scanning electron microscope.

4.3.1.1. Scanning electron microscope images

The corresponding SEM images of the electrodes are shown in Figure 65. The platinum centres have hemispherical shapes and they are sparsely distributed at the shortest deposition time.

Assuming that all the charge passed leads to platinum deposition, these electrodes have platinum loadings ranging from 92 µg cm^{-2} to 460 µg cm^{-2}, after deposition charge passed between 0.2 C cm^{-2} and 0.9 C cm^{-2} respectively. The size of the platinum nuclei varies between 0.2 µm and 2 µm. As the deposition charge density passed increases, more platinum centres are deposited onto the active sites of the carbon fibres. At longer deposition times, the platinum centres tend to grow to a maximum diameter and more nuclei start to form close to existing centres. However, there is still an incomplete coverage of the electrode surface even after passing a deposition charge density of 0.9 C cm^{-2}.

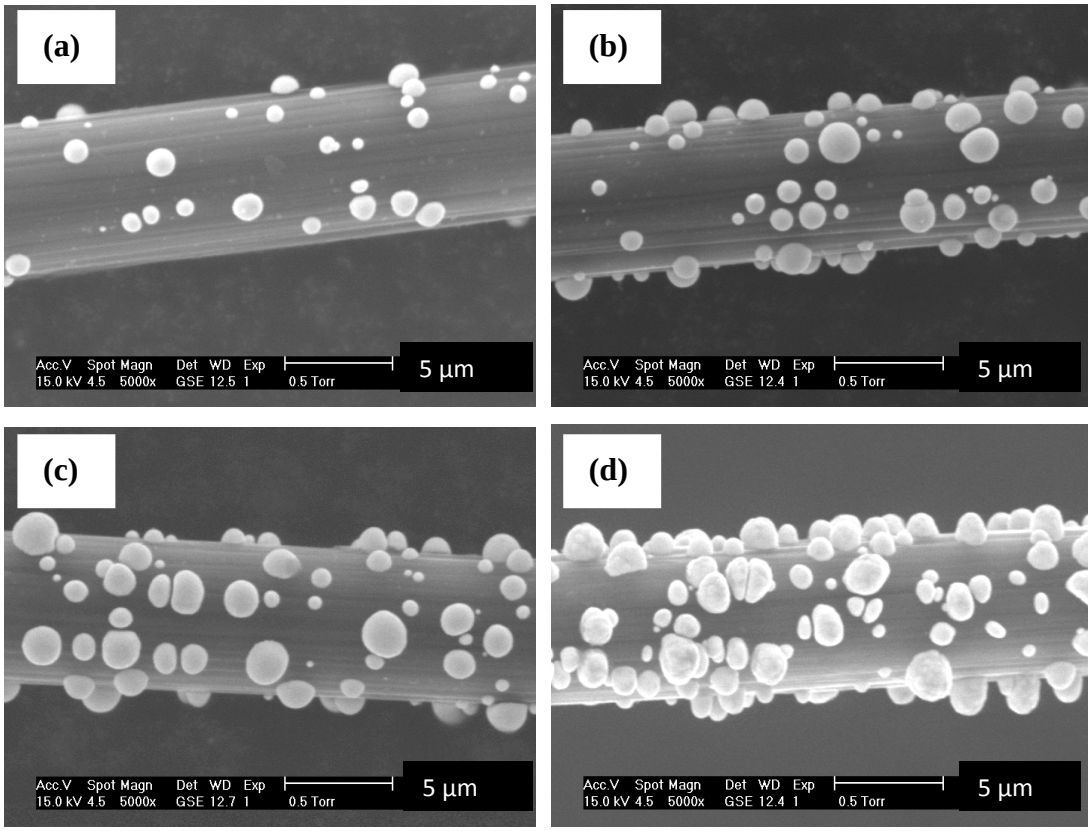

Figure 65. SEM images of a section of carbon fibre wire electrode after undergoing potential step in 5 mM H_2PtCl_6 and 0.1 M HCl degassed with argon, stepped from +0.6 V to +0.2 V versus SCE; **(a)** *0.2 C cm^{-2}* **(b)** *0.4 C cm^{-2}* **(c)** *0.6 C cm^{-2}* **(d)** *0.9 C cm^{-2}.*

4.3.1.2. Cyclic voltammogram in acid solution

The increase in surface area of platinum can be characterised by recording the cyclic voltammogram in 1 M sulphuric acid and comparing the charges for the hydrogen adsorption or the reduction peak of platinum oxide. Figure 66 shows cyclic voltammograms in 1 M sulphuric acid saturated with argon recorded at modified carbon fibre electrodes. The cyclic voltammogram at a new carbon fibre wire electrode is also included. In the same current density-potential window, the voltammogram at a bare carbon fibre electrode shows the absence of oxidation or

reduction peaks that correspond to the presence of platinum oxide. As the amount of platinum deposited onto the carbon fibre increases, the platinum oxide reduction/oxidation and hydrogen adsorption/desorption peaks also increase. The integrated area under the hydrogen adsorption peaks corresponds to the adsorption charge. Thus, the electroactive area of deposited platinum can be calculated using the adsorption charge. Hence, the 'roughness factor' for these electrodes can be calculated and they are found to be in the range between 5 and 32. It should be emphasised that this roughness factor will be low because of the form of the deposit.

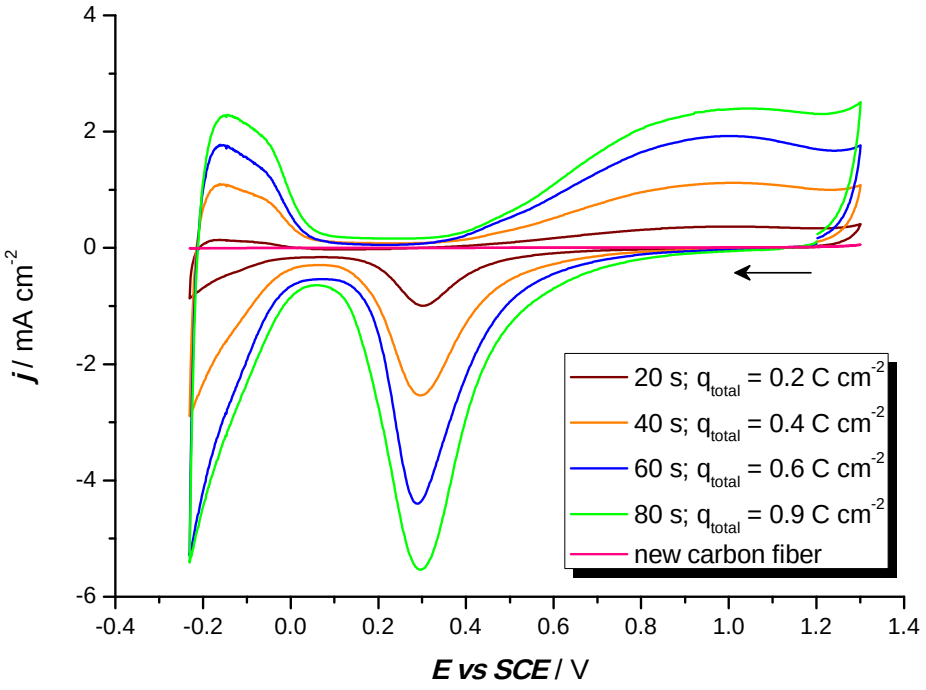

Figure 66. Cyclic voltammetry in 1 M sulphuric acid degassed with argon recorded on freshly cut carbon fibre wire and the platinum coated carbon fibre wire electrodes after undergoing single potential step in the platinum plating bath solution from +0.6 V to -0.25 V versus SCE for various deposition time. (conditions as for Figure 64). Scan rate 100 mV s^{-1}.

Moreover, the specific catalyst area calculated for these electrodes ranges from 5.6 $m^2\ g^{-1}$ to 9.9 $m^2\ g^{-1}$. Among these modified carbon fibre electrodes, the maximum specific catalytic area with 9.9 $m^2\ g^{-1}$ was achieved when the deposition charge density of 0.6 C cm^{-2} was passed. This was followed by the deposition charge density of 0.4 C cm^{-2} with specific catalytic area of 8.5 $m^2\ g^{-1}$. As expected, the lowest specific catalytic area was obtained at the lowest platinum loading when the deposition charge density passed was 0.2 C cm^{-2}. However, with the highest platinum loadings of 460 µg cm^{-2} after passing 0.9 C cm^{-2} (see Figure 65(d)), the specific catalyst area was found to be 6.8 $m^2\ g^{-1}$. Table 4 shows a summary for the value of roughness factor, specific catalytic areas and corresponding platinum loadings. Those findings agree well with the morphological observation of the carbon fibre electrodes. Figure 65(c) and (b) display more isolated platinum centres when compared to Figure 65(a). Even though Figure 65(d) has shown presence of more platinum loadings, the centres are arranged closely to each other. Thus, this leads to a decrease in the specific catalytic activity.

Table 4. The roughness factor (R_f), specific catalytic area (S) with corresponding amount of platinum loadings (W) and charge density passed (q_{passed}). WE: platinum coated carbon fibre wire prepared via single potential step. Conditions as for Figure 60 and 61.

q_{passed} / C cm^{-2}	W / µg cm^{-2}	R_f	S / $m^2\ g^{-1}$
0.2	92	5	5.6
0.4	184	16	8.5
0.6	276	27	9.9
0.9	460	32	6.8

4.3.2. Double potential steps experiments

In this section we present the results of experiments designed to initiate and control the growth of the platinum centres. This involved recording a number of double potential step experiments. The potential was initially stepped to -0.25 V ***versus*** SCE for various deposition times ranging from 20 s to 100 s. This was followed by a potential step to +0.2 V until the total cathodic charge passed was ten times the initial deposition charge. The potential was stepped to a very negative potential in order to initiate the deposition of platinum centres. The second potential was chosen to be +0.2 V as it has already been demonstrated that no nucleation of platinum takes place although the deposition of platinum is mass transport controlled at this potential. The objective of this experiment is to demonstrate that deposition of platinum can occur at more positive potentials following the formation of platinum centres. The current density-time transients for the double potential steps are displayed in Figure 67.

As expected, rising transients were observed during the first potential step. These transients are highly reproducible. As the potential was stepped to +0.2 V, the current density initially increased then later became almost constant. At shorter deposition times at -0.25 V, the current density in the second potential step increases with the length of the first pulse. This indicates that higher number of platinum nuclei deposited during the first potential step. As the deposition time at -0.25 V reaches 80 s, the number of nuclei becomes independent of the duration of the first potential step. This may be attributed to the formation of platinum nuclei at all active sites available on the substrate. Nevertheless, the duration is surprisingly long for the available surface active sites to be saturated for nucleation. When the deposition time of the first pulse is longer, the current density during the second potential step is ~ -5 mA cm^{-2} as compared with the steady state current of ~ -15 mA cm^{-2} when the potential is held at -0.25 V. This is similar to the ratio of current densities on the

voltammogram observed at a platinum coated vitreous carbon disc electrode (see Figure 56).

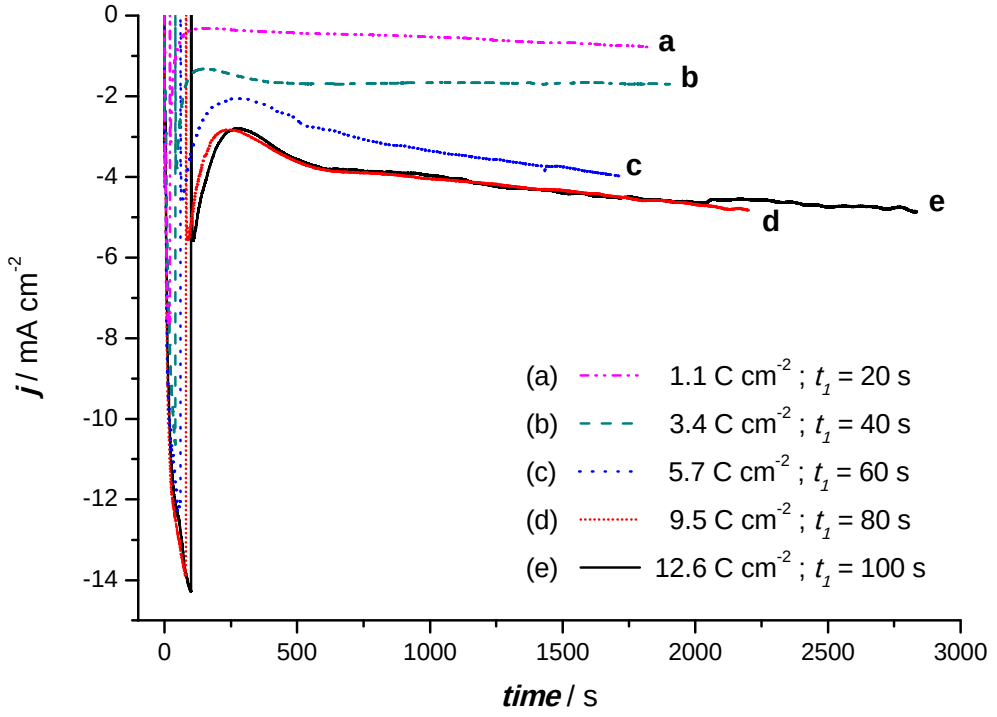

Figure 67. Double potential steps chronoamperograms recorded in 5 mM H_2PtCl_6 and 0.1 M HCl degassed with argon on a carbon fibre wire 7 µm diameter (l = 5 mm). The initial potential was stepped from +0.6 V to -0.25 V versus SCE for different duration (t_1), then stepped to +0.2 V until the total charge is 10 times the initial charge.

4.3.2.1. Characterisation

The morphology of the section of the platinum coated carbon fibre wire electrodes after the single and double potential step experiments was observed using a scanning electron microscope. The typical SEM images of the carbon fibre electrodes are shown in Figure 68. From the visual observation of the SEM images, it can be

concluded that further deposition of platinum occurs during the second potential step at +0.2 V. As expected, the number of the hemispherical platinum centres increases with time at -0.25 V. The deposition of platinum nuclei onto the electrode surface, however, does not form a complete layer. The nucleation of platinum is limited to available active sites and the deposited centres seem unable to grow beyond a critical size. Moreover, it can be seen that the number of platinum centres increases significantly during the second potential step to +0.2 V. As discussed earlier, there is no nucleation taking place at this potential, thus it must be concluded that small platinum centres have been formed at the end of the first potential step, yet too small to be observed by the scanning electron microscope.

Sherstyuk et. al. [193] reported that the platinum nuclei are composed of a large number of small crystallites observed under a high resolution scanning electron microscope. Using atomic force microscopy ***Penner et. al.*** [108, 114] also reported the presence of platinum nanocrystals on both defect sites and defect-free regions of the graphite basal plane. The modified carbon fibre electrodes deposited by double potential steps in the platinum plating bath solution produced platinum loadings between 560 µg cm^{-2} and 4780 µg cm^{-2}. The total amount of deposition charge passed was ten times the initial deposition charge. The increase in the platinum loadings is in agreement with the morphological observations of these electrodes (see Figure 68).

In addition, the charges under the hydrogen adsorption and platinum oxide reduction peaks also increase (as shown in Table 5). Therefore, the rise in the amount of platinum deposited confirms that further deposition of platinum occurs at very positive potential (+0.2 V ***versus*** SCE). As expected, the roughness factor (***R_f***) of these modified electrodes increases with the amount of platinum deposited. However, the specific catalytic area, ***S*** of the deposited platinum remains almost constant with an increase in platinum loadings. The maximum specific catalytic area of 1.4 m^2 g^{-1} was achieved when the deposition charge density of 3.4 C cm^{-2} was passed. The active sites for nucleation became saturated. Therefore with an increase

in deposition charge density passed, the platinum grows further and tends to agglomerate with the neighbouring centres. This leads to a decrease in specific catalytic area of the deposited platinum centres. Thus, the distribution of the platinum centres influences the specific catalytic activity. Hence, a reasonable specific catalytic activity can be achieved when isolated platinum centres are produced.

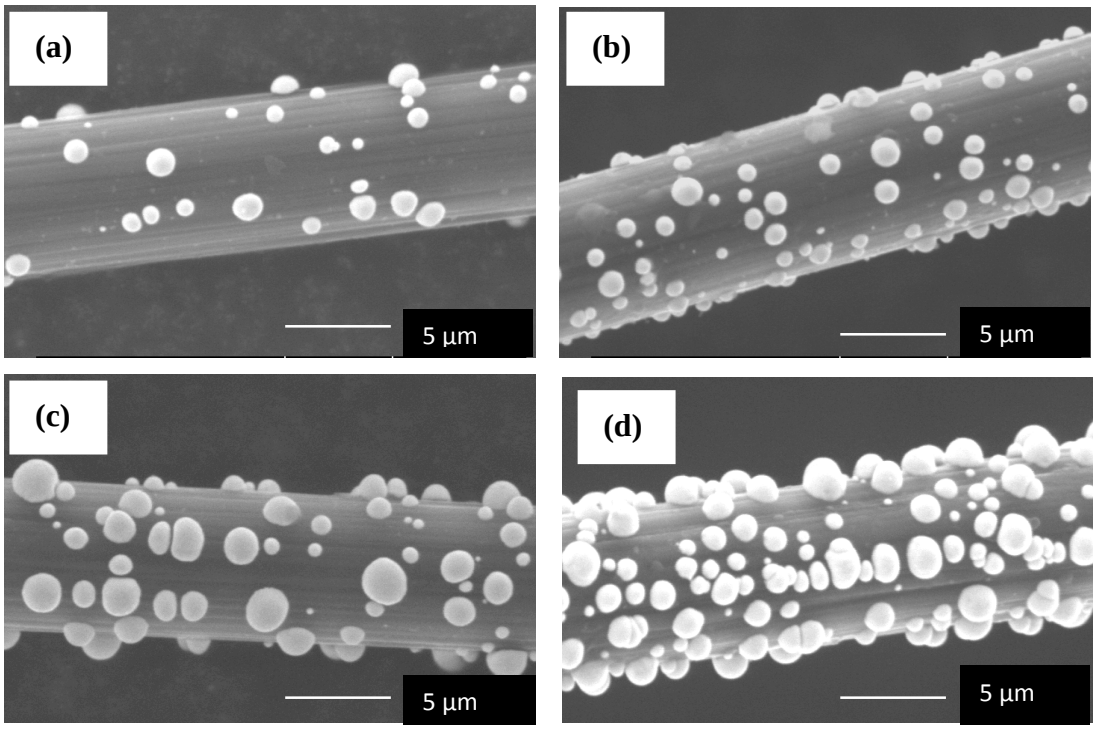

Figure 68. SEM images of sections of carbon fibre wire electrodes after (a) single potential step from +0.6 V to -0.25 V for 20 s (0.2 C cm^{-2}) (b) double potential steps from +0.6 V to -0.25 V versus SCE for 20 s (0.2 C cm^{-2}), then stepped to +0.2 V (1.1 C cm^{-2}) (c) single potential step from +0.6 V to -0.25 V for 60 s (0.6 C cm^{-2}) (d) double potential steps from +0.6 V to -0.25 V versus SCE for 60 s (0.6 C cm^{-2}), then stepped to +0.2 V (5.7 C cm^{-2}). Solution: 5 mM H_2PtCl_6 and 0.1 M HCl saturated with argon.

Table 5. The roughness factor (R_f), specific catalytic area (S) with amount of platinum loadings (W) and the corresponding amount of charge passed. WE: platinum coated carbon fibre wire prepared via double potential steps. Conditions as for Figure 67 and 68.

Q_{passed} / C cm^{-2}	W / µg cm^{-2}	R_f	S / m^2 g^{-1}
1.1	556	7	1.2
3.4	1700	23	1.4
5.7	2895	35	1.2
9.5	4780	59	1.2

In addition, the catalytic activity of the electrodes was investigated by comparing the current density observed on the onset of the oxygen reduction reaction in 0.5 M perchloric acid solution.

4.3.2.2. Catalytic response towards oxygen reduction reactions

The oxygen reduction reaction was investigated in 0.5 M perchloric acid saturated with oxygen at a set of platinum coated carbon fibre wire electrodes with platinum loadings ranging from 556 µC cm^{-2} to 4780 µC cm^{-2}. These electrodes were prepared as described in the previous section. Figure 69 shows the onset of the oxygen reduction waves recorded at such platinum coated carbon fibre electrodes.

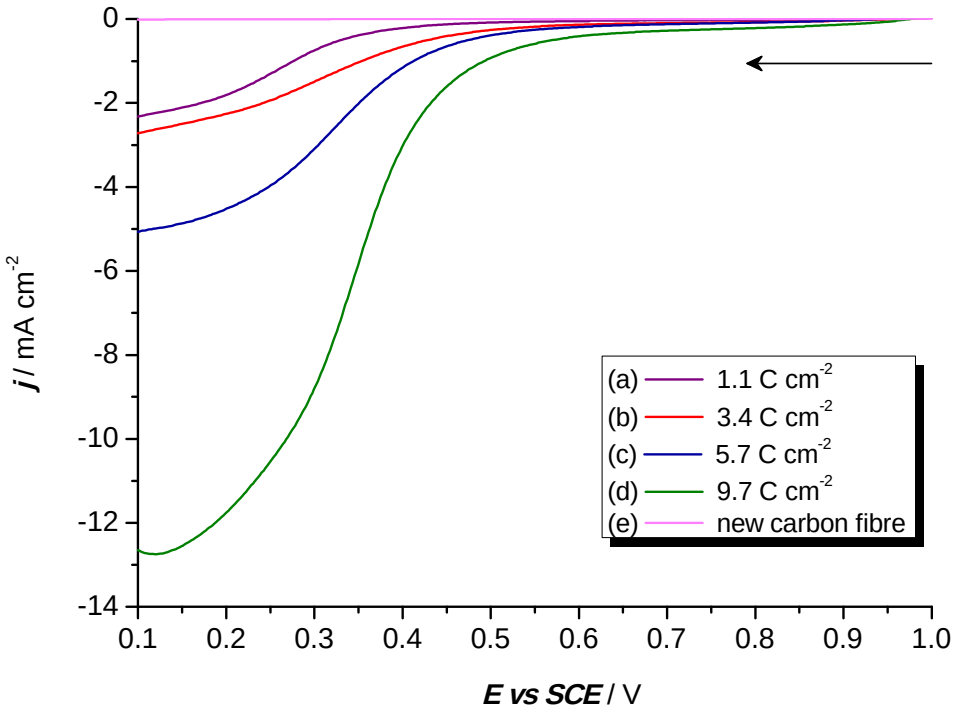

Figure 69. Voltammograms recorded with platinum coated carbon fibres of 7 µm diameter (l = 5 mm) in 0.5 M $HClO_4$ saturated with oxygen at a scan rate of 100 mV s^{-1}.

The onset of oxygen reduction shifts to more positive potentials as the amount of platinum deposited onto the substrate increases. An increase in platinum loadings, that is an increase in the electroactive area of platinum, leads to an increase in current density. As expected, a clean carbon fibre electrode does not catalyse the reduction of oxygen in this potential range as there is almost zero current being observed in the same potential range. Hence, these platinum coated carbon electrodes show catalytic activity for the oxygen reduction reaction when compared to a bare carbon fibre substrate. The responses are also similar to fuel cell cathode materials with similar loadings.

4.4. Potential steps at fixed deposition potentials

A set of chronoamperometry experiments in the same platinum electroplating bath solution were carried out at a shorter deposition time. The potential was stepped from +0.6 V to a very negative potentials, that is, -0.25 V ***versus*** SCE. Deposition times ranging from 1 s to 40 s were applied, hence less deposition charge density passed in each potential step experiment. A new piece of carbon fibre wire electrode of 7 µm diameter, with a length of 5 mm was used in each of the experiments. The current density-time transients for shorter deposition times are shown in Figure 70. Reproducible and rising transients are observed over a period of time. However, it takes a longer deposition times to reach the steady state current density. These platinum coated carbon fibre electrodes were then investigated in 1 M sulphuric acid.

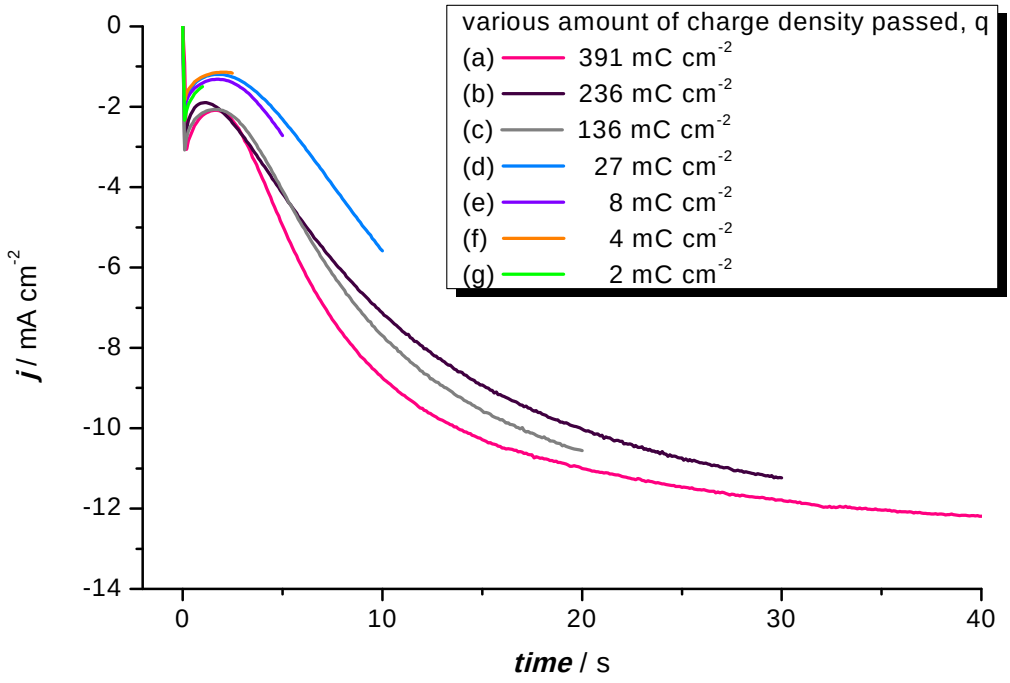

Figure 70. Chronoamperometry in 5 mM H_2PtCl_6 in 0.1 M HCl recorded at 7 µm diameter carbon fibre (l = 5 mm) at various deposition time; **(a)** *40 s* **(b)** *30 s* **(c)** *20 s* **(d)** *10 s* **(e)** *5 s* **(f)** *2.5 s and* **(g)** *1 s. Each transient was recorded for a step from +0.6 V to -0.25 V versus SCE.*

4.4.1. Characterisations in acid solution

Figure 71 shows the platinum oxide reduction peaks in 1 M sulphuric acid recorded at a scan rate of 100 mV s^{-1}. For deposition times longer than 20 s with deposition charge passed ranging from 136 mC cm^{-2} to 391 mC cm^{-2}, the reduction of platinum oxide and the hydrogen adsorption/desorption peaks (not shown) increase with the amount of platinum deposited onto the carbon fibre electrodes. The amount of platinum loadings ranges from 69 µg cm^{-2} to 198 µg cm^{-2}. However, the platinum oxide reduction peaks are not observed with platinum coated carbon fibres with deposition charges passed smaller than 136 mC cm^{-2} (equivalent to platinum loading of 69 µg cm^{-2}). This may be attributed to an amount of platinum on the carbon fibres insufficient to produce platinum oxide reduction currents significantly larger than the background currents on the carbon surface.

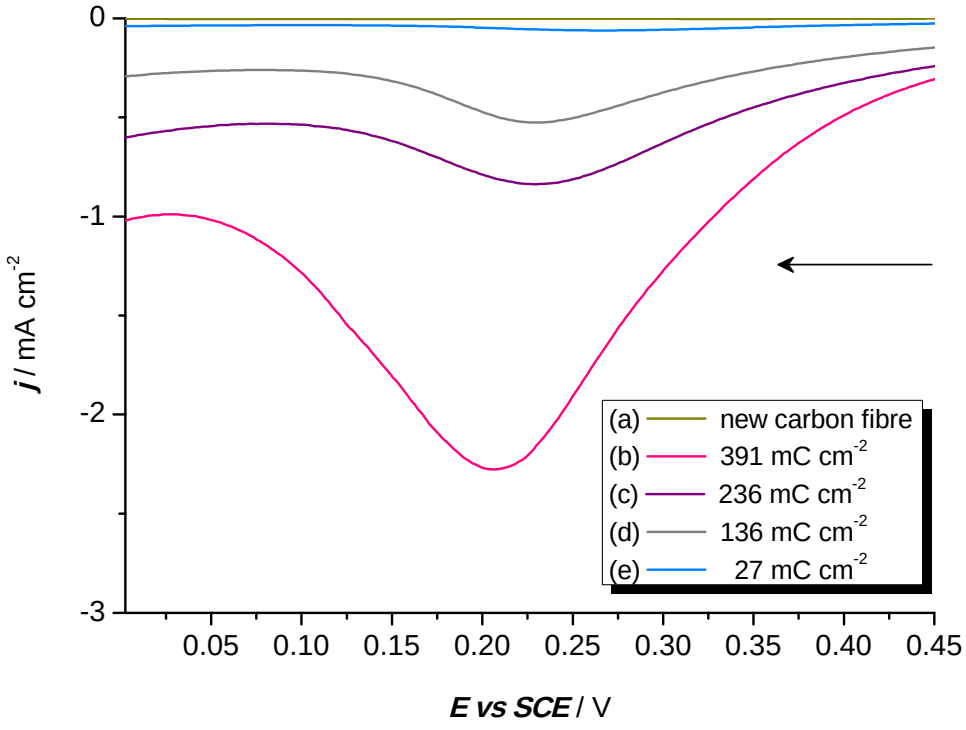

Figure 71. Linear sweep voltammograms for the reduction of platinum oxide recorded at platinum coated carbon fibre wire electrode in 1 M sulphuric acid. Scan rate 100 mV s^{-1}. The fibres were prepared as shown in Figure 70.

Hydrogen evolution was recorded at all of these platinum coated electrodes, even with a minute amount of platinum loading (2 µg cm^{-2}) as shown in Figure 72. The current densities for the hydrogen evolution recorded at -0.4 V ***versus*** SCE that correspond to the platinum loadings and specific catalyst areas of the platinum deposits are tabulated in Table 6. The platinum loadings range between 1 µg cm^{-2} and 198 µg cm^{-2}. As expected, the current density for the hydrogen evolution increases with the amount of platinum deposited onto the substrate. There is only a small increase in current density for hydrogen evolution when the amount of charge passed is between 136 mC cm^{-2} and 236 mC cm^{-2}. This may be ascribed to the platinum grown to a critical size and arranged closely together to adjacent platinum nuclei. Thus the electroactive area of the platinum loadings are similar, thereby the catalytic response for the hydrogen evolution is about the same.

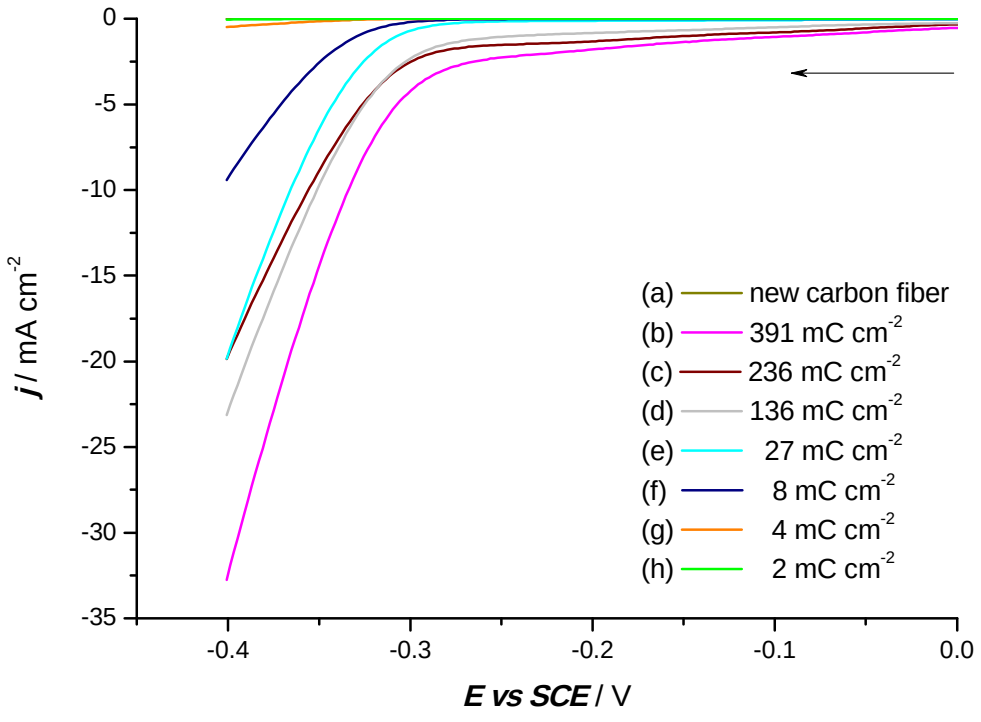

Figure 72. Linear sweep voltammograms for hydrogen evolution recorded at platinum coated carbon fibre wire electrodes in 1 M sulphuric acid. Scan rate 100 mV s^{-1}. The fibres were prepared as shown in Figure 70.

On the other hand, the hydrogen adsorption/desorption peaks are not observed at very low platinum loadings. Thus, it is impossible to determine the specific catalyst area of the platinum deposits. The electrode with highest platinum loadings has a specific catalyst area of 7 m^2 g^{-1}. These values for the specific catalyst area are very low when compared to typical electrocatalyst, 100-200 m^2 g^{-1} Pt [78]. ***Gloaguen et. al.*** [23] reported values for specific catalyst areas of 15-73 m^2 g^{-1} of Pt deposited on three different types of carbon support. It is also reported that the surface area of the carbon support also influences the specific Pt surface area [78].

Table 6. The current densities for the hydrogen evolution at -0.4 V versus SCE and the corresponding platinum loadings, deposition charges passed and specific catalyst areas. Electrodes prepared as in Figure 70.

q_{passed} / mC cm^{-2}	Deposition time / s	Platinum loading, W / μg cm^{-2}	R_f	Specific catalyst area, S / m^2 g^{-1}	$-j$ at -0.4 V / mA cm^{-2}
391	40	198	15	7	32
236	30	119	6	5	20
136	20	69	4	5	23
27	10	14	0.5	4	20
8	5	4	*	*	9
4	2.5	2	*	*	0.5
2	1	1	*	*	0.05

*The grey cells indicate that hydrogen adsorption/desorption peaks were not observed and the electroactive area could not be estimated.

4.4.2. Morphological observations

The morphology of these platinum coated carbon fibre wire electrodes was observed using the scanning electron microscope at high vacuum mode with accelerating

voltage of 10 kV . The SEM images of selected platinum coated carbon fibre electrodes are shown in Figure 73.

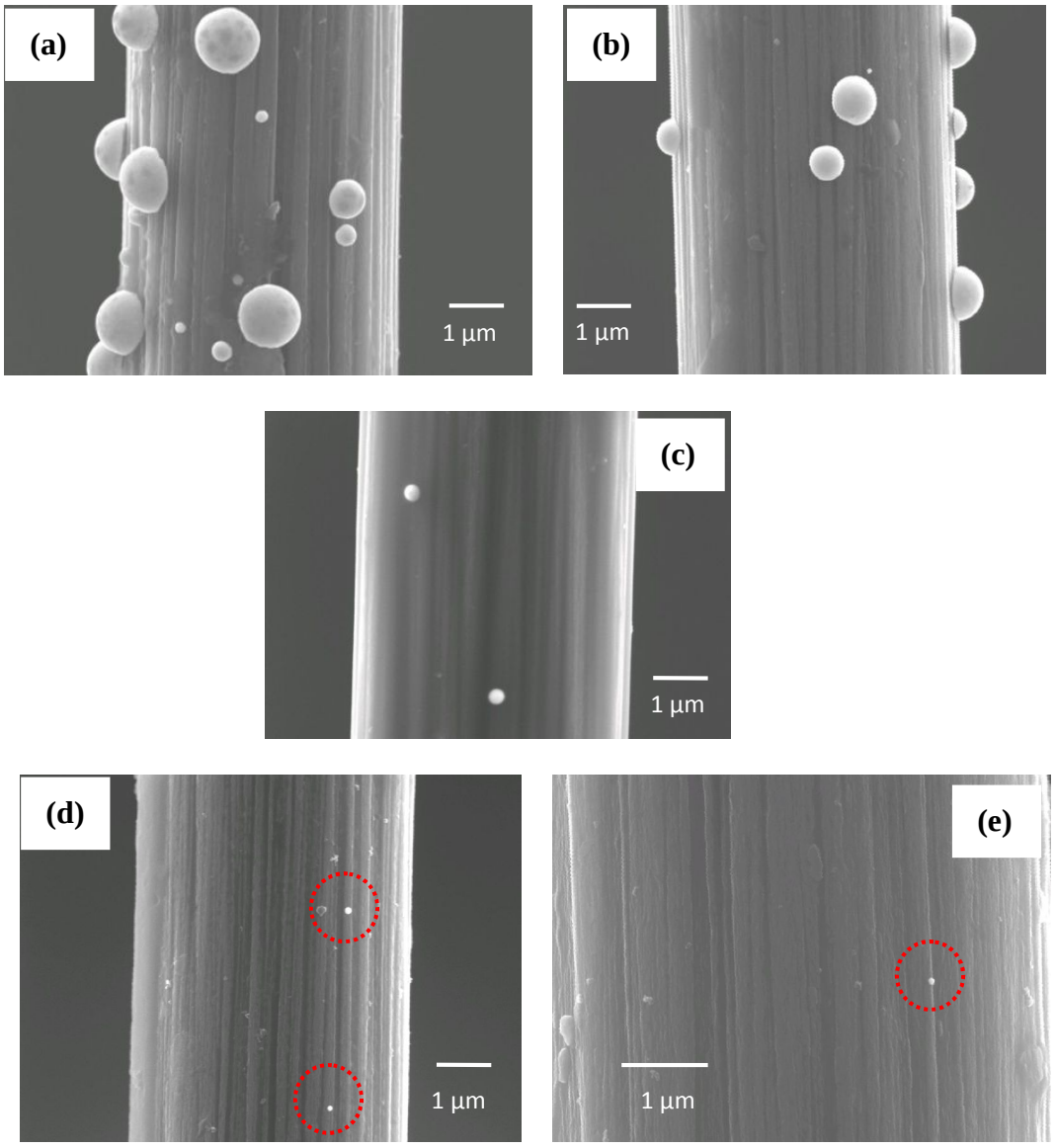

Figure 73. SEM images of platinum coated carbon fibres after electrodeposition in hexachloroplatinic acid at various deposition times; **(a)** *30 s* (236 mC cm^{-2}) **(b)** *10 s* (27 mC cm^{-2}) **(c)** *5 s* (8 mC cm^{-2}) **(d)** *2.5 s* (4 mC cm^{-2}) *[(Images (a-d) have x10,000 magnifications)]* **(e)** *1 s* (2 mC cm^{-2}) *(x20,000 magnifications).*

With longer deposition time, more platinum centres are produced. The size of the nuclei also increases with time. After a deposition time of 30 s, dispersed platinum hemispherical centres with diameters ranging from 150 nm to 1.2 µm can be seen [Figure 73(a)]. After 10 s of deposition at -0.25 V, the diameters of platinum nuclei range 130 nm and 1 µm. Very few platinum deposits are observed with average diameters between 300 nm and 100 nm after the deposition time of 5 s and 2.5 s respectively. Even after a very short time (1 s), very small isolated platinum centres with a diameter of ~70 nm can be seen on the carbon fibre as shown in Figure 73(e). The platinum centres deposited onto the carbon fibre are isolated and hemispherical in shape, and this observation is similar to that observed when deposited on to the vitreous carbon surface. This observation is similar to that reported by ***Duarte et. al***. [76] who observed that the platinum centres deposited on carbon fibres in the presence of sulphate ions electrolyte have wide variation in particle size.

4.4.3. Catalytic activity for oxygen reduction in perchloric acid

These platinum coated carbon fibre electrodes were used to investigate the catalytic activity for the oxygen reduction reactions in 0.5 M $HClO_4$ saturated with oxygen. Figure 74 shows the oxygen reduction waves recorded at these electrodes and the inset shows the magnification on the onset of the oxygen reduction reactions. The platinum nuclei were deposited onto the carbon fibre electrodes via potential step experiments with various deposition charges passed. The platinum loadings range between 1 µg cm^{-2} and 198 µg cm^{-2}. An increase in the electroactive area of platinum on the electrode surface leads to an increase in current density for the oxygen reduction reactions at platinum nuclei. However, the substrate with platinum loadings below 2 µg cm^{-2} does not show catalytic response for the oxygen reduction reaction. Moreover, an increase in the platinum loaded on the carbon fibre helps to reduce the oxygen at a more positive potential. The increase in current density

negative to -0.3 V corresponds to the hydrogen evolution. Even at 2 µg cm^{-2}, a small increase in current density for hydrogen evolution can be observed.

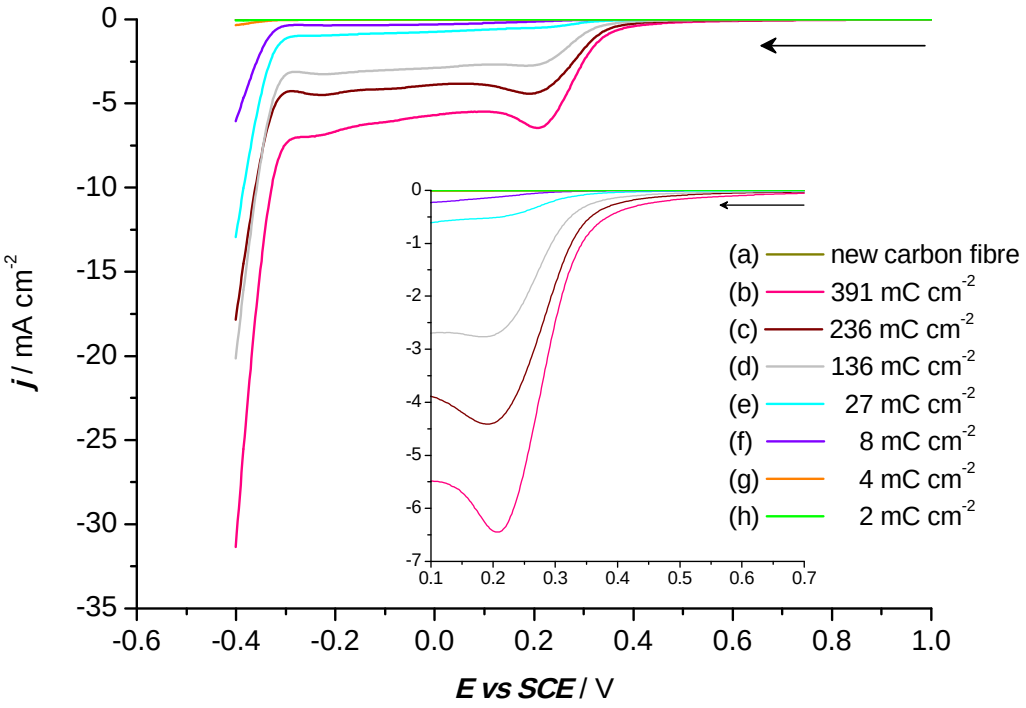

Figure 74. Linear sweep voltammograms for oxygen reduction in 0.5 M $HClO_4$ recorded at platinum coated carbon fibres after passing a range of electrodeposition charges. The inset shows a magnification of the linear voltammograms for selected platinum coated carbon fibres and new carbon fibre. Potential scan rate of 100 mV s^{-1}.

4.5. Distribution of platinum centres onto other carbon substrates

4.5.1. Carbon fibre microdisc electrodes

In this section, the carbon fibre has been fabricated into discs and hence ends rather than sides of the fibre are exposed to the electrolyte. These surfaces are likely to have different structures and properties.

The reduction of platinum(IV) onto a carbon fibre disc electrode of 7 μm diameter was characterised in 1 M sulphuric acid and morphological observation under scanning electron microscope fitted with energy dispersive X-ray spectroscopy (EDXs). The platinum coated carbon fibre disc electrode was prepared by single potential step deposition in the same platinum plating bath solution. The potential was stepped from +0.5 V to -0.2 V ***versus*** SCE until a deposition charge density of 1.5 C cm^{-2} was passed. Figure 75 shows the cyclic voltammogram in 1 M sulphuric acid recorded at a polished carbon fibre disc and the carbon fibre disc with a high charge density coating of platinum.

The cyclic voltammogram recorded at platinum coated carbon fibre electrode shows the presence of oxidation/reduction peaks for platinum oxide and of the hydrogen adsorption/desorption peaks. The hydrogen evolution can also be seen at potential negative to -0.3 V. As expected, the voltammogram recorded at a newly cut carbon fibre electrode shows oxygen evolution and the onset of hydrogen evolution at +1.2 V and negative to -0.4 V respectively.

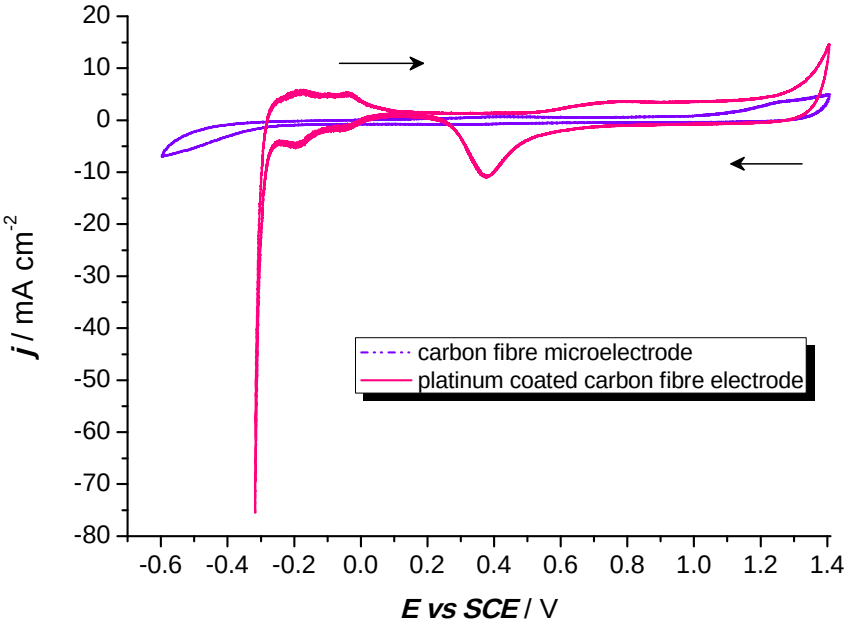

Figure 75. Cyclic voltammetry in 1 M sulphuric acid degassed with argon recorded at a carbon fibre microdisc electrode (Ø = 7 µm diameter) and a platinum coated carbon fibre microdiscc electrode (q = 1.5 C cm^{-2}). Scan rate 50 mV s^{-1}.

The morphology of the platinum deposited onto the carbon fibre microdisc electrode was observed with a scanning electron microscope using secondary electron detector in a wet mode. The SEM image and the energy dispersive X-ray (EDXs) mapping (as shown in Figure 76) show a uniform distribution of platinum except for a small area uncovered on the electrode surface. This might be attributed to an inactive plane of carbon or some other defect on the carbon electrode substrate. The platinum nuclei of sizes ranging from 250 nm to 500 nm appear on the carbon fibre electrode surface with a loading of approximately 760 µg cm^{-2}. The EDXs spectrum recorded at the electrode surface marked as + confirms the presence of platinum on the electrode surface (see Figure 77).

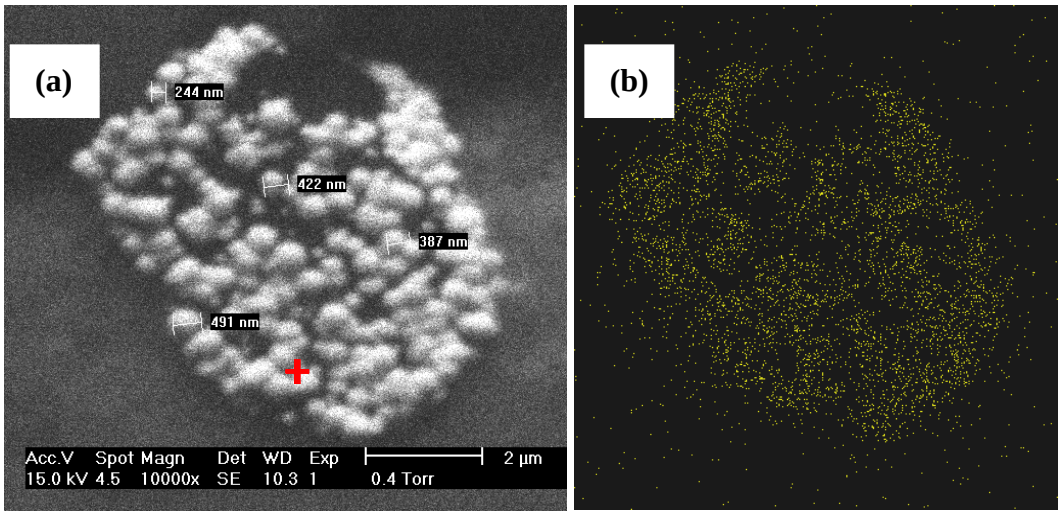

*Figure 76***(a)** *SEM image of platinum nuclei deposited onto a 7 µm diameter carbon microelectrode and* **(b)** *the EDX mapping (the yellow dots indicate the platinum).*

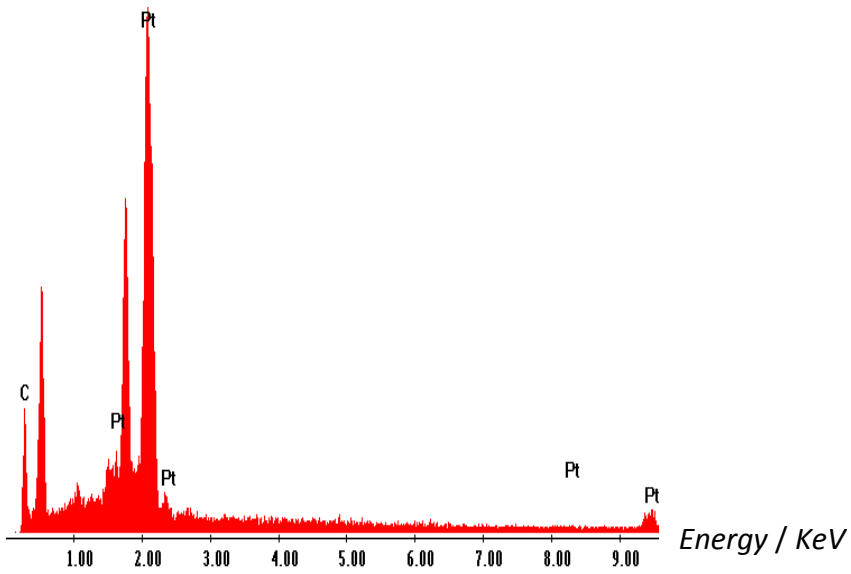

Figure 77. EDXS recorded at the point indicated on the SEM image, by the red cross.

4.5.2. Stationary vitreous carbon disc electrode

Figure 78(a-d) display typical SEM images for platinum deposits onto a vitreous carbon disc electrode. The modified vitreous carbon electrode was prepared by single potential step to -0.16 V ***versus*** SCE, with deposition charge density passed ranging from 33 mC cm^{-2} to 10 mC cm^{-2} (see Figure 78(a)-(c)). Figure 78(d) shows the surface of the platinum coated vitreous carbon electrode after the potential was stepped to -0.25 V with respect to SCE with deposition charge density of 10 mC cm^{-2}.

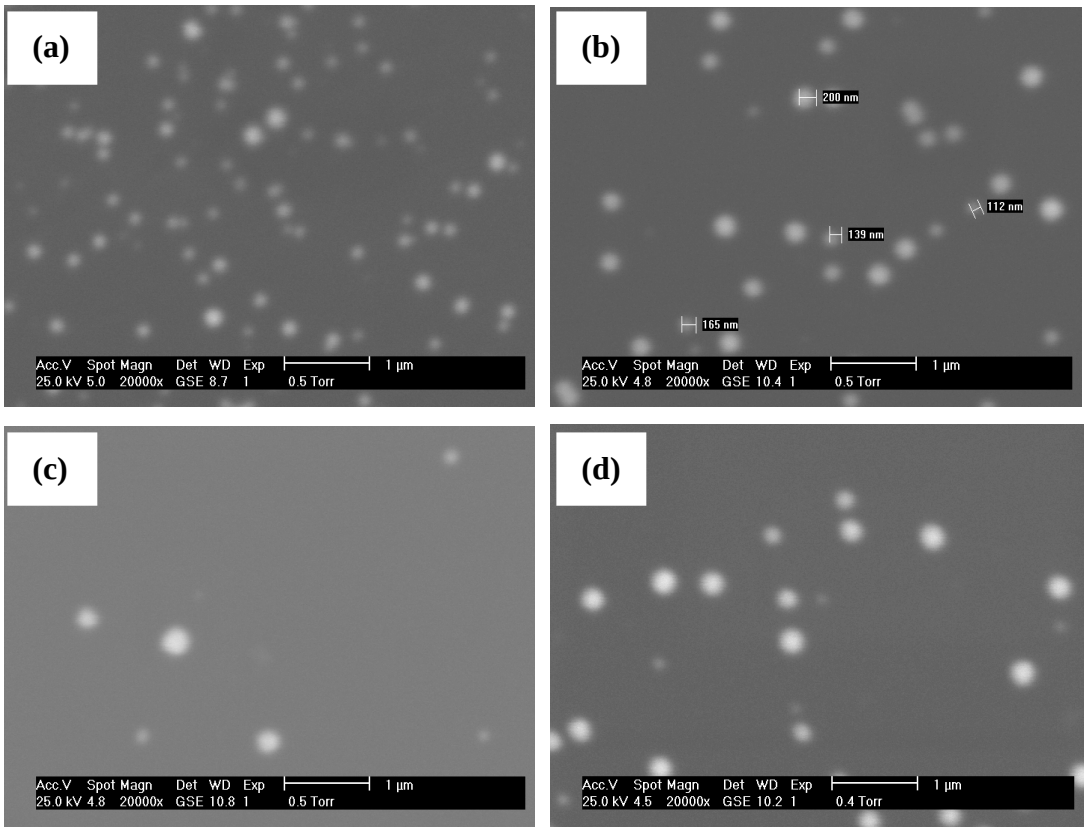

Figure 78. SEM images of platinum centres deposited onto vitreous carbon electrode (3 mm diameter) after undergoing potential step in 5 mM H_2PtCl_6 in 0.1 M HCl from +0.6 V to **(a)** *-0.16 V; 33 mC cm^{-2}* **(b)** *-0.16 V; 20 mC cm^{-2}* **(c)** *-0.16 V; 10 mC cm^{-2} and* **(d)** *-0.25 V; 10 mC cm^{-2}.*

The platinum centres deposited onto the substrate are isolated and well dispersed. The distribution of platinum centres on both forms of carbon substrate; carbon fibre and vitreous carbon electrodes are very comparable. Similar observations of platinum deposits on glassy carbon have been reported [76, 193]. The platinum deposits exhibit uniform size and are widely distributed over the electrode surface [193]. In addition, their electrode surface appears to have more active nucleation sites than those reported here.

Figure 79 demonstrates the size distribution of platinum centres grown on the vitreous carbon electrode surface as shown in Figure 78. As expected, the number of platinum centres and the diameter of the nuclei also increase with the length of deposition time. The platinum centres nucleate at available active sites and start to grow up to an average particle diameter of 200 nm. At low overpotential with longer deposition times, a progressive nucleation can be observed: some of the nuclei grow further while at the same time, more small centres start to grow. The smallest platinum centre that was observed with the scanning electron microscope was approximately 78 nm diameter. The platinum centres with diameter less than 50 nm cannot be observed with the scanning electron microscope used. With a deposition charge density of 33 mC cm^{-2}, most of the platinum centres have an average diameter of 150 nm. There is only a few centres that have grown further to a diameter less than 300 nm and at the same time, more smaller nuclei started to appear. The number of centres and the distribution of sizes of platinum centres when deposited at very negative potential (-0.25 V) is also included for comparison. It is clear that at high overpotential, the nucleation process is easier, thus more nuclei centres are observed on the surface. There is an increase in the number of centres with diameter greater than 100 nm when compared to deposition at -0.16 V after passing the same amount of charge. But the inability to see small centres by SEM makes definitive conclusions difficult.

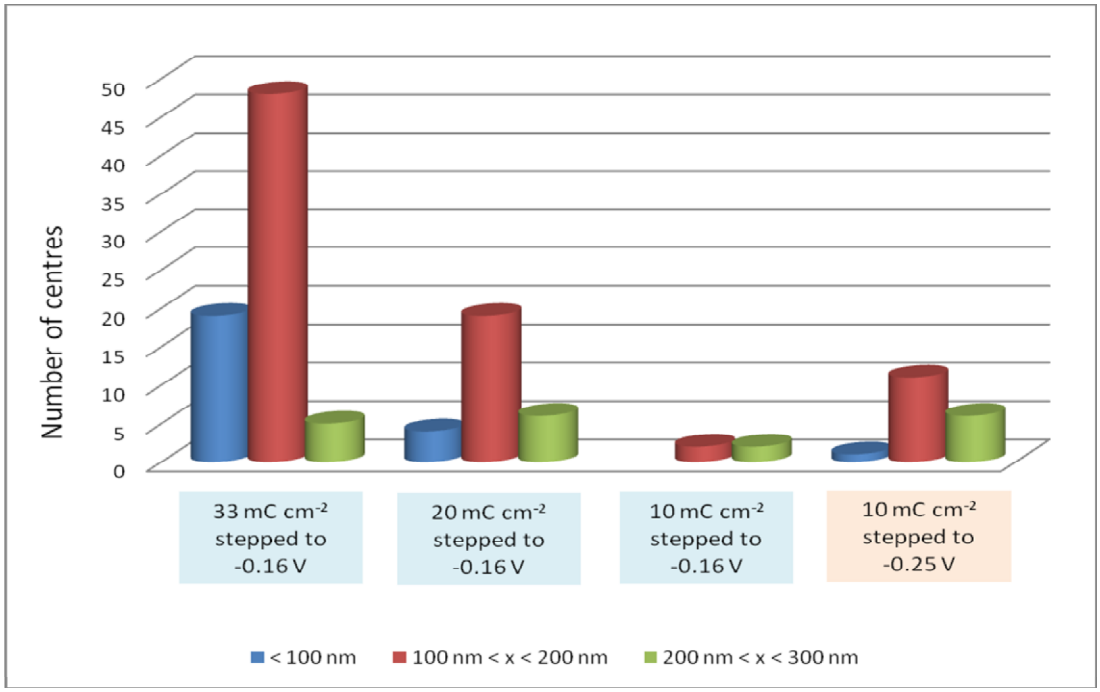

Figure 79. Size distribution of platinum centres deposited at high and low overpotentials with different deposition charge densities. The number of centres is determine from the SEM image of area 2.7 × 10^{-12} m^2 as shown in Figure 78.

4.6. Conclusions

1. All cyclic voltammograms recorded in hexachloroplatinate(IV) acid in acidic media have shown the presence of extended 'nucleation loops', even when the negative potential is limited to allow only the first cathodic wave. This indicates that all the cathodic waves can be associated with the deposition of platinum metal. Moreover, the difference between the first and second cycles of voltammograms strengthens this conclusion.

2. The SEM images after the double potential step experiment have shown strong evidence that deposition of platinum metal occurs at +0.2 V ***versus*** SCE. The nucleation process of the platinum centres on carbon is slow as described by the shape of the voltammogram. The platinum metal is deposited from the reduction of platinum(IV) without having platinum(II) species as a stable intermediate. Thus, the current findings strongly disagree with the earlier literatures suggesting that the reduction of platinum(IV) to platinum(II) occurs in the first reduction wave [187, 189, 191, 192].

3. The chemical species present in hexachloroplatinic acid in aqueous chloride solutions have been studied by ^{195}Pt NMR [164, 172] and UV-visible spectroscopy [174, 175]. The exact ratio of the species depends on the concentrations of $PtCl_6^{2-}$ and Cl^-, pH and temperature. Under the conditions used in this research study, the plating bath solution is expected to contain three kinetically inert platinum(IV) complexes, $PtCl_6^{2-}$, $PtCl_5(H_2O)^-$ and $PtCl_4(H_2O)_2$ resulting from the hydrolysis reactions shown below:

$$PtCl_6^{2-} + H_2O \rightleftharpoons PtCl_5(H_2O)^- + Cl^-$$

$$PtCl_5(H_2O)^- + H_2O \rightleftharpoons PtCl_4(H_2O)_2 + Cl^-$$

It is expected that each complex can be reduced, hence multiple cathodic waves should be produced for the reduction reactions of platinum(IV) to platinum metal took place. The reduction potentials for $PtCl_6^{2-}$, $PtCl_5(H_2O)^-$ and $PtCl_4(H_2O)_2$ will be different. The limiting current densities from the voltammograms would show an approximate ratio of 10:3:7 for $PtCl_4(H_2O)_2$: $PtCl_5(H_2O)^-$: $PtCl_6^{2-}$ in 0.1 M hydrochloric acid.

4. It is possible that platinum(II) species may be formed. However, under the experimental conditions, platinum(II) is not stable and possibly reduced further instantaneously. ***Petrii et. al.*** [194] suggested that the platinum metal is formed by the disproportionation of platinum(II). However the voltammetry observed would require disproportionation for all platinum(II) species resulting from the reduction of the three platinum(IV) complexes. Thus, if platinum(II) is produced in the system, the reduction of platinum(II) to platinum metal is rapid compared to the reduction of platinum(IV) to platinum(II) on the growing platinum nuclei.

5. The morphological observations of the platinum centres deposited onto the carbon fibre wire and vitreous carbon disc electrodes have shown the presence of isolated 'hemispherical' centres. These platinum nuclei are formed at available active sites on the carbon surface. Nevertheless, a large overpotential is still required for the nucleation to occur at these sites. The platinum centres expand until they reach a certain critical size. The slow nucleation of platinum may have been attributed to the adsorption of chloride ion onto the electrode surface as suggested by ***Petrii et. al.*** [194]. The platinum deposit does not dissolve anodically in 0.1 M hydrochloric acid solution.

6. The carbon electrodes modified with platinum centres have shown the expected surface chemistry and high catalytic activity both for the hydrogen evolution and reduction of oxygen reactions.

7. The appropriate use of the parameters, potential and charge density allow control of the morphology of the coated carbon surfaces. Although the small centres (< 50 nm) cannot be confirmed by SEM, it appears that isolated small centres can be produced.

Chapter 5

5 *Electrodeposition of platinum on gold electrode*

Gold is an alternative substrate to carbon at least for fundamental studies. Gold is electroinactive in the potential region for platinum deposition and where platinum shows catalytic activity. It also has a surface structure that is less complex than carbon in its several forms. Recent studies on platinum nanoparticles supported on gold have shown an enhancement of hydrogen related reactions by orders of magnitude. It was reported that the catalytic activity for hydrogen oxidation reaction and hydrogen evolution reaction increased considerably with decreasing amount of catalyst material [7, 9]. ***Van Brussel et al.*** have reported that the electrocatalytic activity for oxygen reduction reaction at polycrystalline gold electrodes modified by platinum was lower than that of the bulk platinum electrode in the negative potential scan, however increased significantly in the positive scan [231]. Moreover, ***Desic et al.*** [217] have also demonstrated that the AuPt electrodes showed higher catalytic activities for oxygen reduction reaction than pure platinum. It is proposed that with AuPt catalyst, the platinum provides the main hydrogenation or dehydrogenation sites, while the gold helps to moderate the poisoning effect of the intermediates by

supplying oxygen atoms to an adjacent surface site of platinum and to facilitate the removal of the poisonous species [252, 253].

In this chapter, an investigation of platinum electrodeposited onto a gold electrodes from hexachloroplatinate(IV) acid in acidic media and aqueous hexachloroplatinate(IV) acid in the presence of surfactant, will be discussed. The surfactant is added to the plating mixture to provide a nanostructure moulds for electrodeposition. The gold electrodes used in this research study are in the form of microdisc electrodes and macrodisc rotating electrodes.

5.1. Reduction of hexachloroplatinate(IV) on gold microelectrodes

The electrodeposition of platinum was recorded at smaller surface area electrodes, with the long term aim to produce low platinum loadings with limited amounts of deposition charge density. 25 µm and 60 µm diameter gold microelectrodes were used as working electrodes. A cyclic voltammogram in 1 M sulphuric acid was initially recorded on a polished gold electrode before proceeding with further measurements. A clean gold electrode surface free of platinum is a vital condition before recording voltammetry if reproducible data relating to the early stages of platinum deposition are to be obtained. Figure 80 shows the cyclic voltammogram of the polished 60 µm diameter gold microdisc electrode in sulphuric acid scanned at 100 mV s^{-1}. The formation of gold oxide appears as a plateau extending from +1.1 V to +1.4 V with respect to SCE. In addition, a sharp cathodic peak for gold oxide reduction is seen between the range +1.0 V and +0.8 V ***versus*** SCE. The double layer region was observed negative to +0.80 V ***versus*** SCE indicating that the electrode surface was free from platinum deposits.

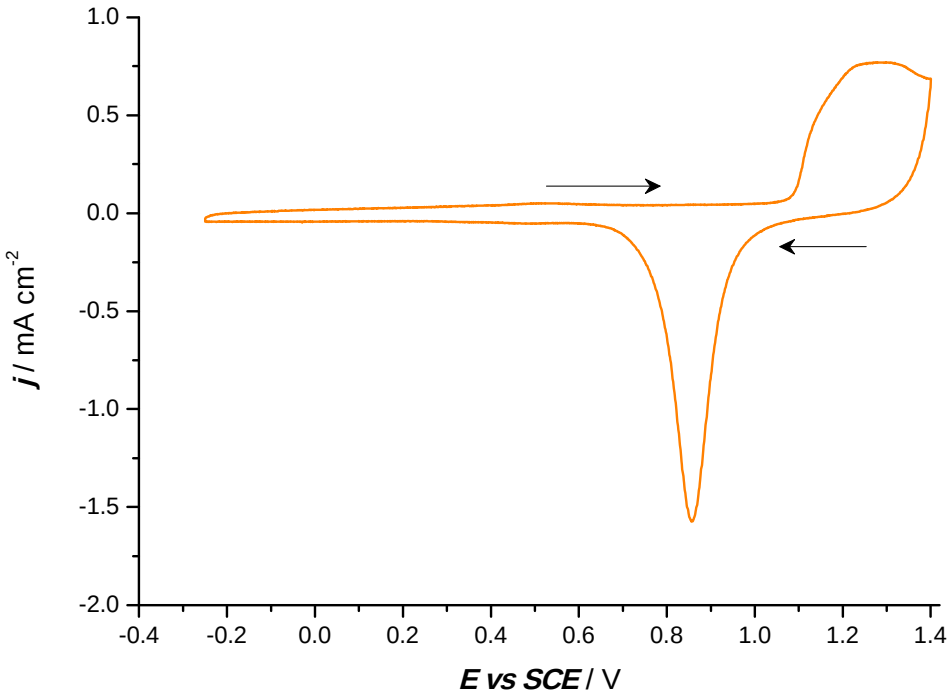

Figure 80. Cyclic voltammogram recorded at a polished gold microdisc electrode (Ø = 60 µm diameter) in 1 M sulphuric acid at a scan rate of 100 mV s^{-1}.

5.1.1. Reduction of platinum(IV) in aqueous solution

As mentioned in the introduction, in Southampton, the electrodeposition of nanostructured platinum has been practised using a plating mixture containing surfactant and aqueous hexachloroplatinate(IV) acid. Thus, in this experiment the reduction of platinum(IV) was investigated using the same concentration of hexachlorplatinate(IV) acid used in the lyotropic liquid crystal plating mixture and without added hydrochloric acid. The electrodeposition of platinum in an aqueous solution containing 0.4 M hexachloroplatinic acid saturated with argon was recorded at a gold microdisc electrode (Ø = 60 µm). The voltammogram was recorded at 10 mV s^{-1}. Figure 81 shows two consecutive cyclic voltammograms in the aqueous platinum plating bath solution, without any additional electrolytes and in absence of surfactant.

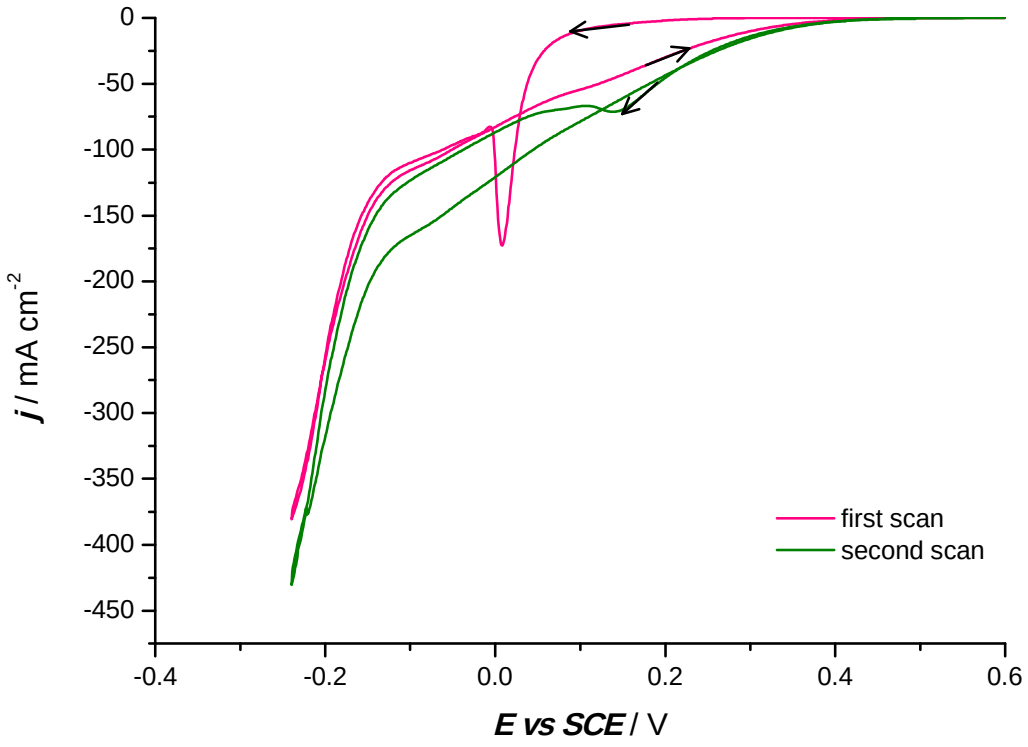

Figure 81. Two consecutive cyclic voltammograms recorded at a 60 µm diameter gold disc electrode at 10 mV s^{-1} in aqueous solution of 0.4 M H_2PtCl_6.

On the forward scan of the first cycle, a very steep reduction peak was observed with an onset of reduction wave at +0.2 V ***versus*** SCE ($E_{½}$ = +0.025 V), followed by a sudden increase in current density at potentials negative to -0.15 V with respect to SCE. A hysteresis is observed in the backward scan at potentials positive to +0.025 V. The characteristic loop observed relates to nucleation and growth. On the backward scan, there is no anodic current observed. This indicates that no dissolution of platinum occurs from the electrode surface. In this experiment, the current densities are large due to the high concentration of hexachloroplatinate(IV) acid.

The forward scan of the second cycle produced a more drawn out reduction wave at potentials negative to +0.4 V with a plateau observed at +0.15 V. This indicates the reduction of platinum(IV) on newly deposited platinum nuclei; hence the reduction of platinum(IV) is much easier to occur. However, a smaller current density was

observed on the second forward scan. This may result from the influence of nucleation effects on the first cycle. The subsequent cathodic current after the plateau is similar to the reduction wave of the first cycle. There is a slight increase in current density on the backward scan with an increase in the amount of platinum deposited.

The reduction waves obtained have similar characteristics when recorded at carbon substrates in aqueous hexachloroplatinate(IV) acid (see Figure 60). In both cyclic voltammograms, a nucleation loop was observed. The potential at which the nucleation of platinum occurs onto polished gold electrode is shifted more positive when compared to nucleation onto carbon fibre wire electrodes. This indicates the nucleation of platinum is easier on a gold surface than on a carbon substrate. Similarly, the reduction of platinum on a newly deposited platinum surface on both gold and carbon substrates occurs at potentials negative to +0.4 V ***versus*** SCE. The cathodic current at very negative potential can be assigned for the onset of hydrogen evolution. Thus, the cathodic current produced at all potentials positive to -0.15 V can be assigned to the reduction of platinum(IV) to platinum(0).

5.1.2. Reduction of platinum(IV) in hydrochloric acid solution

Linear potential sweep voltammograms in a solution containing 5 mM hexachloroplatinate (IV) in 0.1 M hydrochloric acid were recorded at 25 µm and 60 µm diameter microdisc electrodes. For each electrode, Figure 82 shows two reproducible reduction waves. The first reduction wave approximately at +0.1 V is steep indicating the processes of nucleation and growth of platinum nuclei took place. Well-defined second reduction waves with limiting current densities are observed at potentials below -0.25V ***versus*** SCE indicating a mass transport controlled reaction. At potentials negative to -0.35 V, the onset of the hydrogen

evolution is observed. As expected, the current density produced at the 25 µm diameter electrode is 2.5 times higher than that at the 60 µm diameter gold electrodes. The limiting current density produced is inversely proportional to the diameter of the electrode for a mass transport controlled reaction.

Table 7 shows the $E_{½}$ and ($E_{¾}$ - $E_{¼}$) of the reduction waves produced at the gold microelectrodes. The half wave potential of the first reduction wave shifts to a more negative potential as the rate of mass transport increases. The ratios of the limiting currents for the two waves are quite different to those seen at carbon.

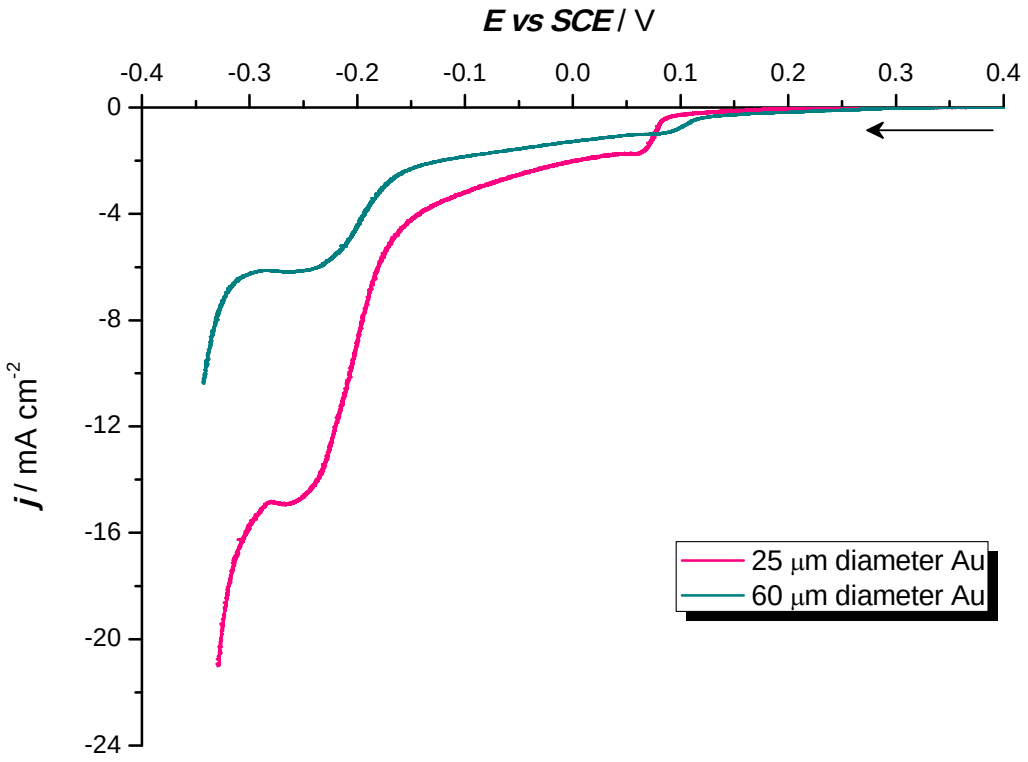

Figure 82. Voltammograms recorded with 25 µm and 60 µm diameter gold microelectrodes in a solution containing 5 mM H_2PtCl_6 in 0.1 M HCl saturated with argon at 5 mV s^{-1}.

Table 7. Data analysis from the linear voltammograms recorded at gold microelectrodes in 5 mM H_2PtCl_6 and 0.1 M HCl.

Diameter of Au electrode	First reduction wave		Second reduction wave	
	($E_{½}$)/ V ***versus*** SCE	($E_{¾} - E_{¼}$)/ V	($E_{½}$)/ V ***versus*** SCE	($E_{¾} - E_{¼}$)/ V
25 µm	+0.075	0.01	-0.2	0.04
60 µm	+0.1	0.02	-0.2	0.04

The electrodeposition of platinum at potentials negative to +0.1 V ***versus*** SCE has been carried out and discussed in the following subsection. After the deposition at very positive potential in the first wave, presence of platinum metal on the microelectrode surface is evidenced by the peaks seen in the cyclic voltammogram in acid solution that are associated with platinum. The deposition of platinum at different potentials are further investigated by potential step experiment and characterised in acid solution and using scanning electron microscope to observe the morphology of the electrode surface. This will be discussed further in the following subsection.

5.1.3. Electrodeposition of platinum at various deposition potentials

The observation of the morphology of the two microelectrodes surfaces at different potentials and charge densites is shown in Figure 83. The EDXS confirms that platinum deposition is occurring but there is no evidence for isolated centres. Complete layers are readily formed. The SEM images in Figure 83 (a-b) emphasize that edge effects appeared on 60 µm and 25 µm diameter gold microelectrodes after

passing a deposition charge density of 4 C cm^{-2} at -0.25 V and -0.3 V ***versus*** SCE, respectively. At 0 V ***versus*** SCE and deposition charge density of 1 C cm^{-2}, edge effects were observed on the two microelectrodes (see Figure 83(c-d)). This indicates a mass transport diffusion controlled reaction has taken place. This may be ascribed to the higher diffusion rate occurring at the edge of the microelectrodes as the rate of deposition increases. At very positive potentials and low charge density [Figure 83(e-f)], no apparent difference can be seen in the SEM images of the gold microelectrode surface after the platinum deposition. Platinum deposition is, however, occurring. This is evidenced by the presence of platinum oxide reduction peak in cyclic voltammogram in acid solution (see Figure 84).

The amount of platinum deposited on the surface of the microelectrodes being used at different potentials and deposition charge densities is displayed in Table 8. The presence of platinum and gold on the surface was confirmed by electron dispersive X-ray spectroscopy (EDXS). The thickness of the platinum layer was estimated using ***Faraday's Law*** assuming that the deposition was 100% efficient. Accordingly, it was expected that a full layer of platinum with an approximate thickness of 1 μm had been deposited onto the surface when a charge density of 4 C cm^{-2} had been passed. However, at low deposition charge density (0.5 C cm^{-2}), gold is the major element detected by EDXS due to the electron beam going through the thin layer of platinum (approximately 0.125 μm thickness for this charge). The cyclic voltammograms in 1 M sulphuric acid solution (not shown) confirm the presence of platinum on both microelectrodes surface even after passing a charge of 0.5 C cm^{-2}. Peaks observed in the cyclic voltammograms in acid solution clearly correspond to the gold oxide formation/reduction and to platinum oxide formation/reduction as well as the hydrogen adsorption/desorption peaks, although the latter are not clearly resolved.

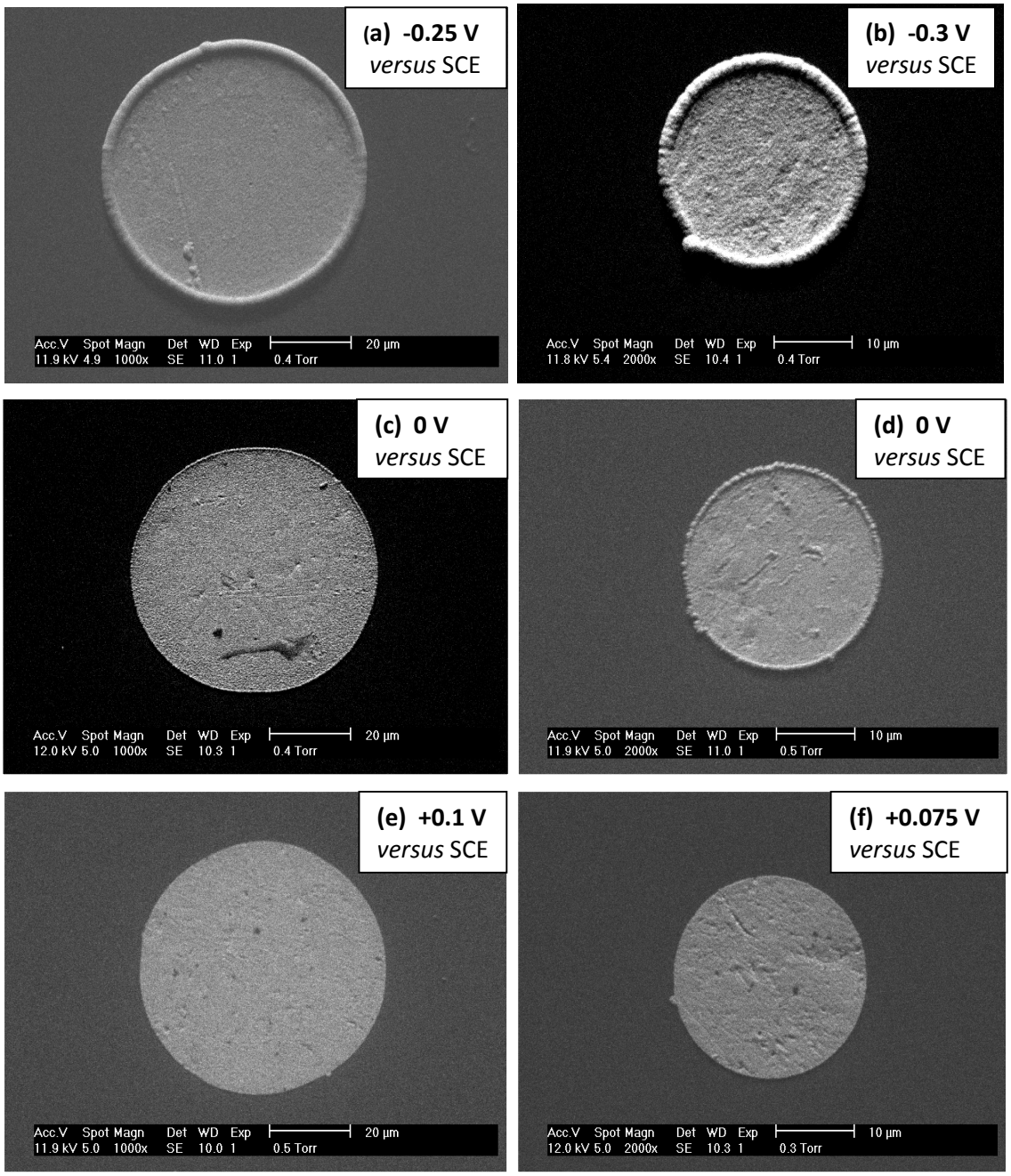

Figure 83. SEM images of the platinised microelectrode (25 µm and 60 µm diameter Au electrodes) after undergoing potential step in 5 mM H_2PtCl_6 + 0.1 M HCl from +0.4 V **(a)** *to -0.25 V; deposition charge 4 C cm^{-2}* **(b)** *to -0.3 V; deposition charge 4 C cm^{-2}* **(c)** *to 0 V; deposition charge 1 C cm^{-2}* **(d)** *to 0 V; deposition charge ~1.2 C cm^{-2}* **(e)** *to +0.1 V; deposition charge 0.5 C cm^{-2}* **(f)** *to +0.075 V; deposition charge 0.5 C cm^{-2}.*

*Table 8. Amounts of platinum deposited onto gold electrode surfaces at different potentials and charge densities. * assuming a uniform layer had been deposited.*

Size of Au microelectrode, µm & potential *versus* SCE	**Charge density, *q* / C cm^{-2}**	**Surface average theoretical thickness* / µm**	**% Pt**	**% Au**
Ø = 60, at +0.1 V	0.5	0.125	38	62
Ø = 60, at -0.25 V	4	1	100	0
Ø = 25, at +0.075 V	0.5	0.125	20	80
Ø = 25, at -0.3 V	4	1	100	0

The deposition of platinum at a much lower charge density at +0.1 V ***versus*** SCE was carried out. The deposition charge of 65 mC cm^{-2} was passed at a 60 µm diameter gold electrode in the same platinum plating bath solution. The microelectrode was removed and transferred into a solution containing 1 M sulphuric acid for characterisation. The cyclic voltammogram in Figure 84 shows that platinum has been deposited onto the gold microelectrode even at this lower charge density: clear platinum oxide formation/reduction peaks and poorly resolved hydrogen adsorption/desorption peaks are observed. Also the gold oxide reduction peak is much diminished.

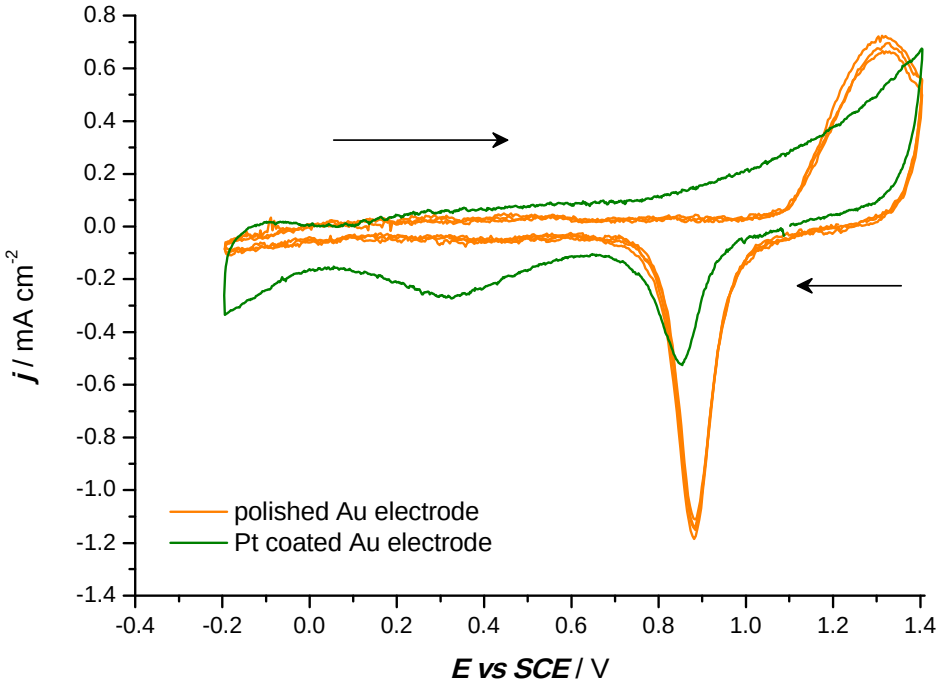

Figure 84. Cyclic voltammograms in 1 M sulphuric acid for a 60 μm diameter polished gold electrode and platinum coated electrode after passing a deposition charge density of 65 mC cm^{-2} at +0.1 V versus SCE. Potential scan rate 100 mV s^{-1}.

With low charge densities, the deposition of platinum onto the gold electrode surface could not be confirmed with the scanning electron microscopy. However, the cyclic voltammogram in acid solution confirmed unambiguously the presence of platinum onto the electrode surface.

5.2. Reduction of hexachloroplatinate(IV) acid on gold RDE

The reduction of platinum(IV) was further studied using a gold rotating disc electrode. The employment of the rotating disc electrode was to investigate if the reaction was mass transport controlled and was carried out by recording voltammograms as a function of rotation rates. Thus the diffusion coefficient of platinum(IV) could be determined.

5.2.1. Reduction waves at variable rotation rates

A series of voltammograms were recorded in 5 mM hexachloroplatinate (IV) in 0.1 M hydrochloric acid for rotation rates ranging from 400 to 2500 rpm at a 5 mm diameter gold rotating disc electrode. The experiments were carried out at room temperature at a scan rate of 50 mV s^{-1}. The solution was saturated with argon before recording each voltammogram. The voltammograms in Figure 85 show that reproducible reduction waves were observed at all rotation rates.

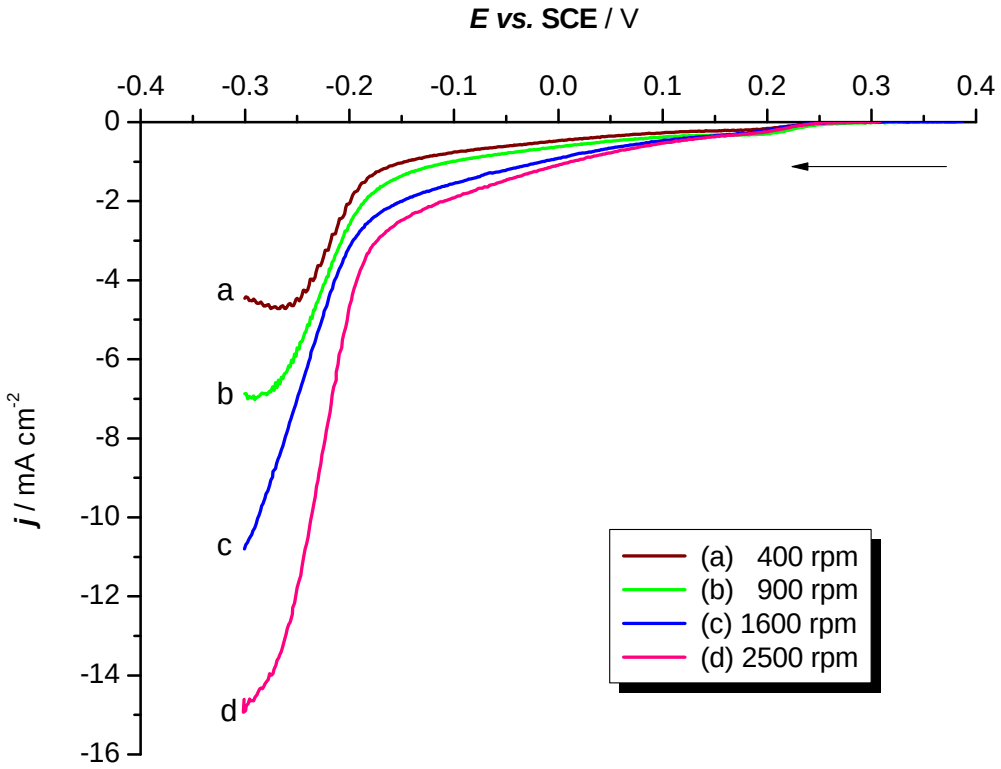

Figure 85. Linear sweep voltammograms at different rotation rates recorded at a 5 mm diameter gold rotating disc electrode in 5 mM hexacloroplatinic acid and 0.1 M hydrochloric acid. Scan rate 50 mV s^{-1}

Similarly to the linear sweep voltammograms recorded at gold microdisc electrodes, two reproducible reduction waves are observed at all rotation rates. A major reduction wave at $E_{½}$ = -0.24 V ***versus*** SCE ($E_{¾} - E_{¼}$ = -0.0625 V) and a much

smaller reduction wave observed with an onset at +0.25 V with half wave potential at +0.225 V ***versus*** SCE. This first reduction wave is followed by a gradual increase in current density, however showing no clear sigmoidal shape. The onset for the first reduction wave on gold electrode is more positive than on vitreous carbon. This observation indicates that the nucleation of platinum(IV) is easier on the gold surface, thus it requires less overpotential. Nonetheless, the second reduction waves are well-defined and occurred at a similar potential when platinum(IV) is reduced on both substrates.

In another sets of experiment, the current density was recorded at -0.35 V ***versus*** SCE at various rotation rates. The graph of current density for the platinum reduction at -0.35 V against the square root of the rotation rates, $\omega^{1/2}$**,** is shown in Figure 86. A linear plot obeying the ***Levich*** equation [19] is obtained. Thus, it is a fully mass transport controlled reaction. The diffusion coefficient was calculated by applying the ***Levich*** equation (3.2), to a set of limiting currents at -0.35 V at different rotation rates:

$$\boldsymbol{j_L} = 0.201\, \boldsymbol{nFD}^{\frac{2}{3}} \upsilon^{-\frac{1}{6}} \boldsymbol{c}^{\infty} \omega^{\frac{1}{2}} \qquad (3.2)$$

taking into account the Faraday constant, $\boldsymbol{F}$ = 96485 C mol^{-1}, a kinematic viscosity, υ = 1 × 10^{-2} cm^2 s^{-1}, four electron exchanged, $\boldsymbol{n}$ = 4 e$^-$, the concentration of hexachloroplatinate(IV), $\boldsymbol{c}^{\infty}$ = 5.0 x 10^{-6} mol cm^{-3} and the angular rotation rate of the disc, ω in rpm. From the slope, the diffusion coefficient of platinum(IV)**,** $\boldsymbol{D}$ was estimated to be 4.7 × 10^{-6} cm^2 s^{-1}. This value is in good agreement with that reported in the literature, 4.5 × 10^{-6} cm^2 s^{-1} [107, 254] and similar to the value found for $AuCl_4^-$ in the same medium. It also suggests that all platinum(IV) complexes in solution are reduced at -0.35 V.

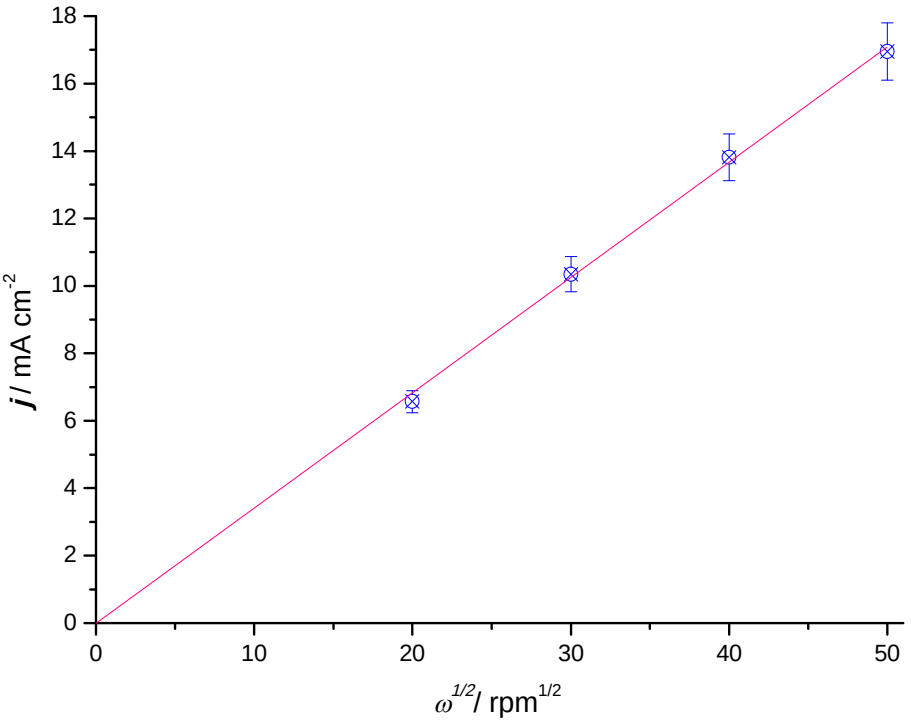

Figure 86. Plot of the current density (j / mA cm^{-2}) versus the square root of the rotation rate. Current density recorded at -0.35 V versus SCE at various rotation rates. Error bars are calculated based on 5 % of each data set value.

5.2.2. Electrodeposition at variable potentials

The formation of a platinum deposits was demonstrated by recording cyclic voltammograms in 1 M sulphuric acid. The polished 5 mm diameter gold rotating disc electrode was modified by a potential step in 5 mM hexachloroplatinate(IV) in 0.1 M hydrochloric acid at 900 rpm at a fixed deposition charge density of 50 mC cm^{-2}. The potential was stepped from +0.4 V to +0.2 V, 0 V and -0.25 V ***versus*** SCE and the modified electrode was removed from the plating solution and rinsed. Cyclic voltammograms of the platinum coated electrode were recorded in 1 M sulphuric acid saturated with argon at a potential scan rate 50 mV s^{-1}. In all of the experiments, shiny silvery appearance on the electrode could be seen instantly after passing 50

mC cm^{-2}. The cyclic voltammograms of a polished gold electrode and platinum coated gold electrode in 1 M sulphuric acid are shown in Figure 87.

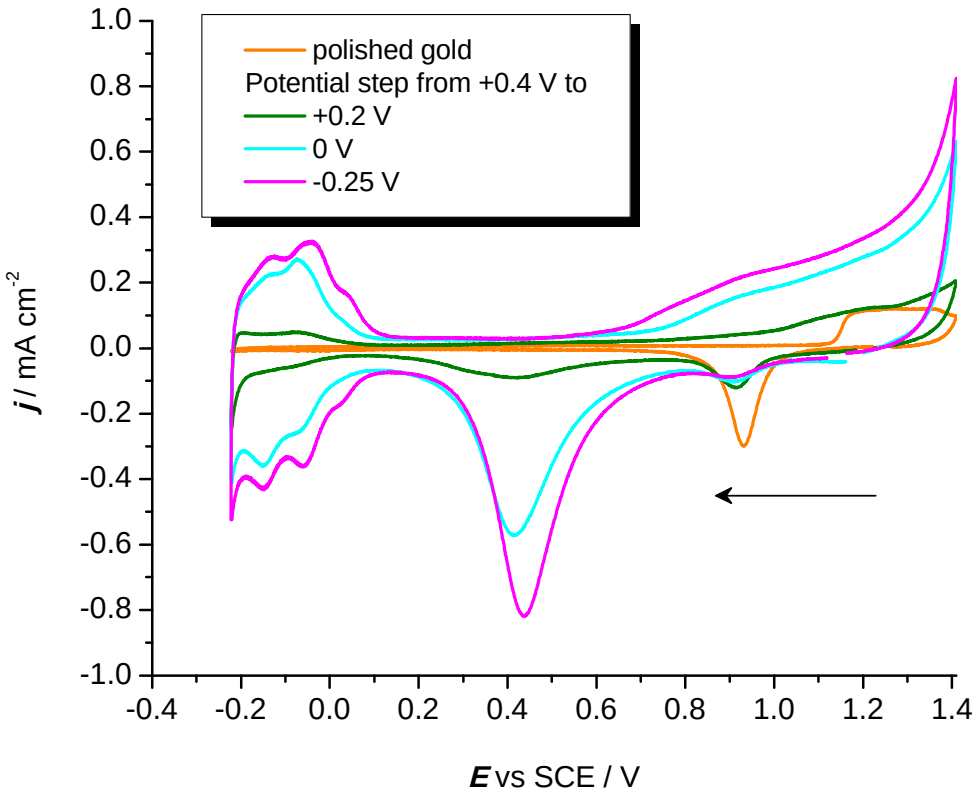

Figure 87. Cyclic voltammograms recorded in 1 M sulphuric acid scanned at 50 mV s^{-1}, with a platinum coated gold rotating disc electrode (diameter = 5 mm), rotated at 900 rpm. The platinum layer was deposited with a fixed deposition charge of 50 mC cm^{-2} but different deposition potentials.

It can be observed that platinum has started to deposit on the gold electrode at +0.2 V ***versus*** SCE as the cyclic voltammetry in acid shows features characteristics of platinum. The platinum oxide formation and reduction peaks appear at +0.7 V and +0.42 V ***versus*** SCE. The hydrogen adsorption and desorption peaks can be seen between the potential range of +0.1 V and -0.24 V with respect to SCE. The charge associated with the hydrogen adsorption/desorption, the platinum oxide reduction peak and the formation of platinum oxide increased as the potential was stepped to a

more negative value at a fixed charge density. After undergoing potential steps to 0 V and -0.25 V ***versus*** SCE, the cyclic voltammogram closely resembles that for a bulk platinum electrode. However, the reduction peak of gold oxide is still visible thus indicating a partial coverage of platinum or lifting of the edge of the platinum deposit. Since the same deposition charge is being used, the different cyclic voltammograms indicate that different morphologies are produced at each potential. The charge under the hydrogen adsorption peak in the cyclic voltammogram reflects the electroactive area of platinum deposited onto the surface. The roughness factor of 1, 7 and 9 was calculated for deposition at +0.2 V, 0 V and -0.25 V ***versus*** SCE respectively, from the charge obtained from the hydrogen adsorption peak after subtraction of the double layer charge. Hence, the specific catalyst area could be determined and was found to be 6.7 m^2 g^{-1}, 26.5 m^2 g^{-1} and 35.2 m^2 g^{-1} with similar amount of deposition charge passed. The roughness factor and the specific catalyst area for the platinum coated gold electrode increase as the deposition potential was made more negative. Assuming the current efficiency is 100 % and all the charge was used for the deposition process, the estimated thickness of a complete layer of platinum was 13 nm. It is more likely the surface still consists of isolated centres. The amount of platinum deposited onto the gold surface was not sufficient to be observed with the scanning electron microscope even at high magnification.

Further investigation on the deposition of platinum was carried out by potential steps from +0.4 V to a range of very positive potentials (+0.275 V, +0.250 V and +0.225 V ***versus*** SCE). A deposition charge density of 50 mC cm^{-2} was passed at a 5 mm diameter gold electrode rotated at 900 rpm. Figure 88 shows the cyclic voltammograms recorded at a polished gold electrode and at a platinum coated gold electrode in 1 M sulphuric acid. The cyclic voltammograms recorded at all three electrodes indicate the presence of platinum on the electrode surface as features characteristic of the formation/reduction peak of platinum oxide and of the hydrogen adsorption/desorption can be observed. In addition, the onset of hydrogen evolution can also seen at -0.22 V. Thus, these observations confirm the reduction of

platinum(IV) on the gold electrode even at very positive potentials. The gold oxide reduction peak is still visible showing that the platinum deposits have not fully covered the gold surface. However, the gold oxide reduction peak reduces with an increase in overpotential. Even after the potential step to +0.275 V, there is clearly substantial platinum deposition, yet less platinum loadings when compared to deposition at more negative potentials. The difference in the cyclic voltammograms are small compared to previous experiment where a wider range of deposition potentials were used.

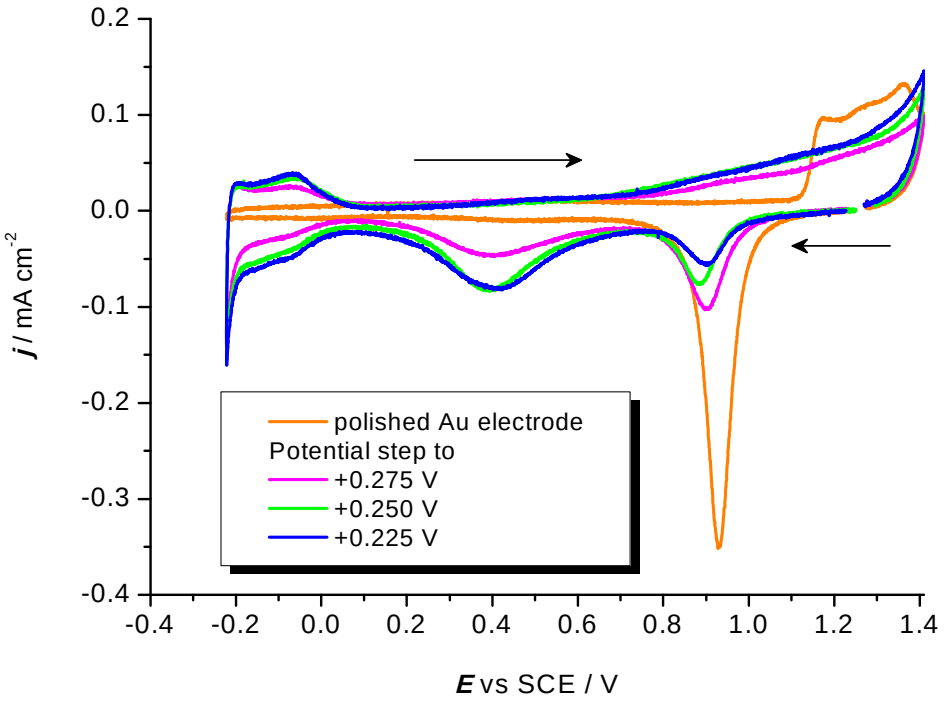

Figure 88. Cyclic voltammograms recorded at 900 rpm and 50 mV s^{-1} in 1 M sulphuric acid with the platinum coated gold electrodes after undergoing potential steps from +0.4 V to various positive deposition potentials.

The average roughness factor for the modified gold electrode is approximately 1.1 as derived from the hydrogen adsorption charge. The specific catalyst areas of the electrodes are found to be in the range between 3.3 and 5.7 m^2 g^{-1}. The thin layer of

platinum deposited is not able distinguish from the gold surface when observed under the scanning electron microscope.

The morphological observations of two electrode surfaces with different thickness as of platinum deposit are shown in Figure 89. The SEM image on the left was captured at a modified gold electrode with platinum loadings of 500 µg cm^{-2} after electrodeposition with a charge density of 1 C cm^{-2} has following a potential step in the same plating bath solution from +0.4 V to +0.2 V ***versus*** SCE. A smooth layer of platinum approximately 0.25 µm thick was deposited; assuming a 100% current efficiency for deposition. The presence of platinum was confirmed with a cyclic voltammogram in acid solution (not shown) and also by observing a silvery reflective appearance on the electrode surface. The platinum deposit was also detected using the electron dispersive X-ray spectroscopy. The EDXS response showed platinum and largely gold, thus reflecting the thinness of the platinum coating. The electron might have gone through the thin layer of platinum, thus it detected mostly the presence of gold. The specific catalyst area and roughness factor for this electrode surface was calculated to be 32.5 m^2 g^{-1} and 165 respectively.

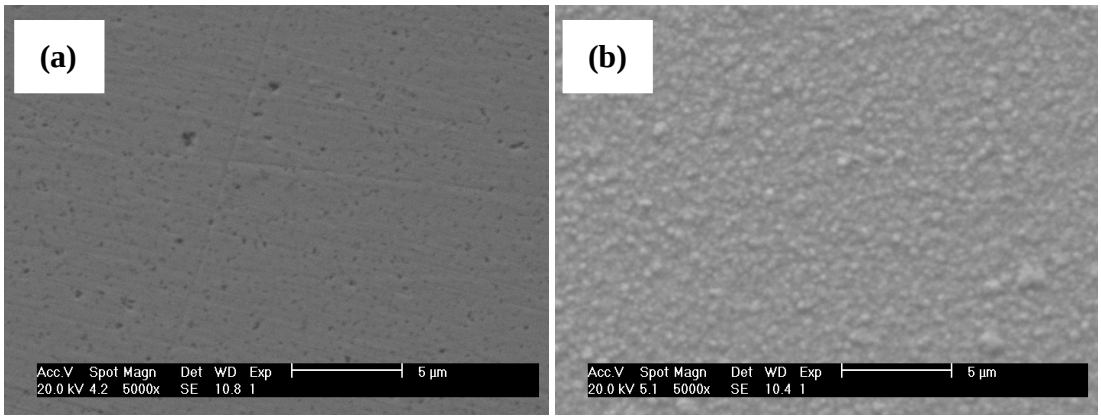

Figure 89. SEM images of modified gold electrode surfaces with platinum loadings of (a) 500 µg cm^{-2} (1 C cm^{-2}) and (b) 2000 µg cm^{-2} (4 C cm^{-2}).

As more platinum has been deposited with loadings of 2000 µg cm^{-2} (4 C cm^{-2}), the gold electrode is fully covered with a layer of platinum approximately 1 µm

thickness. A continuous layer of platinum nuclei was observed on the newly deposited platinum electrode (see Figure 89(b)). The roughness factor for this platinum layered electrode is 368, as determined from the hydrogen adsorption charge. 100 % platinum was detected using the electron dispersive X-ray spectroscopy. Moreover, the cyclic voltammogram in acid solution (not shown) presents the platinum oxide formation/reduction peaks and hydrogen adsorption/desorption peaks without any trace of gold oxide reduction peak that would appear at about +0.9 V ***versus*** SCE. The specific catalyst area of this electrode is 18.2 m^2 g^{-1}. The specific catalyst area was found to be lower with higher deposition charge density passed. The SEM images have shown that a layer of platinum has been deposited onto the gold surface; this contrasts with the isolated platinum nuclei deposited onto carbon substrates even with the same deposition charge density of 1 C cm^{-2} (see Figure 68). ***Plysova et. al.*** [77] also reported the observation of smooth continuous layers of platinum on gold, and suggested that gold substrate has higher number of active nucleation sites.

5.3. Electrodeposition of platinum from lyotropic liquid crystals mixture

The lyotropic liquid crystal mixture, specifically the hexagonal phase, has been widely used to provide a template for electrodeposition, as it self-assembles in the mixture forming a mould with well defined nanostructure. In the earlier studies, the electrodeposition of platinum on gold substrates had always been used to produce a continuous layer of platinum onto the electrode surface. Similar observation of continuous platinum on gold support has been reported by ***Plysova et. al.*** [77]. In this study, the lyotropic liquid crystalline mixture was used with the aim of producing small isolated platinum centres on a gold substrate at low charge density. The reduction of platinum(IV) in the presence of the lyotropic liquid crystal mixture, specifically in micellar and hexagonal phases have been investigated. The surfactant

used in this lyotropic liquid crystal study is octaethyleneglycol monohexadecyl ether ($C_{16}EO_8$), and it is mixed with water and hexachloroplatinate(IV) acid in different ratio in order to obtain the micellar and hexagonal phases. The hexagonal phase of the lyotropic liquid crystal was confirmed by observing the optical texture using a polarising light microscope. The fan-like optical texture confirmed the presence of the hexagonal phase (see Figure 30). On the other hand, the micellar phase is isotropic (and thus non-birefringent) and shows no optical texture when observed under a polarising light microscope.

5.3.1. Voltammetric response in various concentrations of surfactant in lyotropic liquid crystal mixtures

In this set of experiment, the prepared plating mixtures contained different ratio of surfactant to aqueous solution, thus produce different lyotropic liquid crystalline phases. The composition of the ternary plating mixture was chosen to correspond to that for the hexagonal phase ($\boldsymbol{H_1}$) and micellar solutions ($\boldsymbol{L_1}$). This was determined from the ternary phase diagram (see Figure 28) for the system reported previously [143]. The concentration of hexachloroplatinate(IV) acid in the ternary plating mixture was ~0.4 M (derived using the mole fraction of hexachloroplatinate(IV) acid in the ternary mixture). These plating mixtures were prepared by weighing accurately each of the substituents; namely hexachloroplatinate(IV) acid, water and octaethyleneglycol monohexadecyl ether in a small vial. The platinum plating mixture was kept in a sealed vial in the oven at 40 ºC for 30 minutes and later the mixture was stirred using a plastic rod. The sealed vial was kept again in the oven at the same temperature for another 30 minutes. However, the hexagonal phase plating mixture is very viscous, thereby thorough stirring was required. The heating and stirring process was repeated to ensure that the platinum plating mixture was thoroughly mixed. On the other hand, the surfactant dissolved easily as the micellar

solution. Once the resultant mixture was homogeneous, it was left at room temperature to cool before conducting further experiments. The phase structure of the lyotropic liquid crystals were later determined by observing a very small amount of the plating mixture under crossed polarizers in the polarising optical microscope. Table 9 shows the weight percentage of each component in the ternary plating mixture, the resultant texture and observations under the polarizing optical microscope to confirm the phase of the lyotropic liquid crystalline mixture.

Table 9. The compositions (in terms of weight percentage), the resultant texture, optical observations of the ternary plating mixture and the corresponding phase of the lyotropic liquid crystalline mixture.

Weight percentage of compositions in plating mixture (LLC phase)	***Observation under polarizing optical microscope***	***Texture***	***Phase***
0 wt.% $C_{16}EO_8$: 86 wt.% H_2O : 14 wt.% H_2PtCl_6	None	Fluid	Aqueous solutions
2 wt.% $C_{16}EO_8$: 84 wt.% H_2O : 14wt. % H_2PtCl_6	Isotropic (observed blackness)	Slightly viscous	Micellar [145, 247]
10 wt.% $C_{16}EO_8$: 77 wt.% H_2O : 13 wt. % H_2PtCl_6	Isotropic (observed blackness)	Slightly viscous	Micellar
60 wt.% $C_{16}EO_8$: 34 wt.% H_2O : 6 wt.% H_2PtCl_6	Anisotropic (fan-like optical texture) (see Figure 30)	Very viscous	Hexagonal [138, 246]

The cyclic voltammogram recorded in each of the plating mixture with gold microelectrodes is shown in Figure 90. The inset shows the magnified voltammetric response recorded in the hexagonal phase. The two different phases of liquid crystals, the micellar phase (2 wt.% $C_{16}EO_8$: 84 wt.% H_2O : 14 wt.% H_2PtCl_6) and (10 wt.% $C_{16}EO_8$: 77 wt.% H_2O : 13 wt.% H_2PtCl_6), the hexagonal phase (60 wt.% $C_{16}EO_8$: 34 wt.% H_2O : 6 wt.% H_2PtCl_6) and also the aqueous solution of hexachloropltinate(IV) acid (0 wt.% $C_{16}EO_8$: 86 wt.% H_2O : 14 wt.% H_2PtCl_6) were investigated at room temperature. The voltammograms were recorded within the same potential window ranging from +0.6 V to -0.25 V with respect to SCE with a potential scan rate of 10 mV s^{-1}. A platinum mesh and saturated calomel electrode were used as the counter and reference electrodes respectively. Due to the high viscosity, the hexagonal phase plating mixture was placed onto a platinum mesh that acted as the counter electrode. The working and reference electrodes were arranged closely together and immersed into the mixture.

Similar characteristic reduction waves are produced in all the different plating mixtures. On the forward scan, the cathodic wave starts to be observed at +0.2 V with respect to SCE. In all voltammograms, it is followed by a sharp reduction peak that shifts to more negative potentials as the concentration of surfactant increases. Moreover, with the same radius microdisc, the current density measured at the reduction peak decreases as the plating mixture becomes more viscous. The current density observed at the first reduction peak is highest in aqueous hexachloroplatinate(IV) acid solution. Although similar concentrations of hexachloroplatinate(IV) acid were used in each of the plating mixture, the increased amount of surfactant will influence the mass transport of the species reaching the electrode surface; the high viscosity of the plating mixture leads to lower rates of diffusion, thereby smaller current densities. The second reduction wave is followed by an increase in current density that is assigned for the onset of hydrogen evolution. The current density for the hydrogen evolution also increases with the amount of platinum deposited.

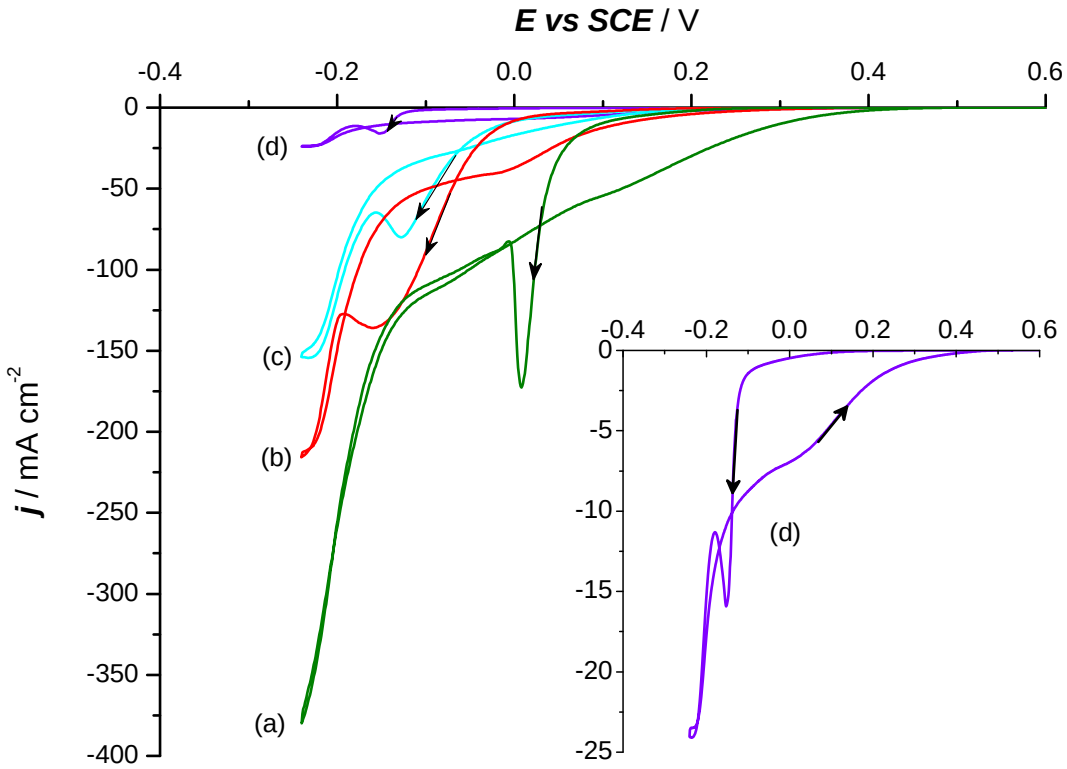

Figure 90. Cyclic voltammograms recorded at gold microelectrodes scanned at 10 mV s^{-1} in different ratios of lyotropic liquid crystals mixture; **(a)** *0 wt.% $C_{16}EO_8$: 86 wt.% H_2O : 14 wt.% H_2PtCl_6* **(b)** *micellar solution (2 wt.% $C_{16}EO_8$: 84 wt.% H_2O : 14 wt.% H_2PtCl_6)* **(c)** *micellar solution (10 wt.% $C_{16}EO_8$: 77 wt.% H_2O : 13 wt.% H_2PtCl_6)* **(d)** *hexagonal phase (60 wt.% $C_{16}EO_8$: 34 wt.% H_2O : 6 wt.% H_2PtCl_6). Voltammograms* ***(b)*** *and* ***(c)*** *are recorded at 50 µm diameter gold electrodes. Voltammograms* ***(a)*** *and* ***(d)*** *recorded at 60 µm and 25 µm diameter respectively.*

On the reverse scan, there are two drawn out reduction waves with the presence of characteristic nucleation loops observed at potentials negative to +0.4 V ***versus*** SCE. Again there is no anodic current observed on the reverse scan. Thus, there is no platinum being removed from the electrode surface. In addition, a background current (not shown) was also recorded at a gold microelectrode in a mixture containing a ratio of 42 wt. % octaethyleneglycol monohexadecylether and 58 wt. %

hydrochloric acid (~ 0.4 M). The background current density recorded at -0.2 V ***versus*** SCE is about -0.15 mA cm^{-2}. Hence, all the cathodic waves produced negative to +0.4 V are attributed only to the reduction of platinum(IV).

5.3.2. Electrodeposition via cyclic voltammetry

In another set of experiments, two consecutive cyclic voltamograms were recorded in each of the plating mixtures over the same potential window, ranging from +0.6 V to -0.25 V ***versus*** SCE. The potential scan rate was 10 mV s^{-1}. The deposition charge densities passed are in the range between 1 and 23 C cm^{-2}. Therefore the deposition layers are relatively thick. The arrangements of the electrodes (working, counter and reference electrodes) were similar to that mentioned earlier. After the electrodeposition in the micellar and hexagonal phases of the plating mixture, the platinum coated gold microelectrode was removed and soaked in copious amount of water to remove the surfactant. The water was replaced at half an hour intervals for the first two hours and later left to soak in stirred water overnight. This was to ensure complete removal of the surfactant from the pores of the nanostructured layer. On the other hand, the electrode used for electrodeposition in aqueous solution only required rinsing with water to remove any excess of plating mixture from the electrode surface.

The deposition of platinum onto the gold microelectrode surface was characterised by recording the cyclic voltammogram in 1 M sulphuric acid. The cyclic voltammogram (not shown) exhibits the characteristic features for polycrystalline platinum with platinum oxide formation/reduction peaks and hydrogen adsorption/desorption peaks. The deposition charge density passed ($\boldsymbol{Q_{passed}}$), the roughness factor ($\boldsymbol{R_f}$), the specific catalyst area ($\boldsymbol{S}$) and the actual measurements and the estimated thickness layer of platinum electrodeposited for each modified gold electrodes after electrodeposition in different compositions of plating mixtures are shown in Table 10. The specific catalyst area of the platinum loadings onto the

electrode surface was determined by applying equation (2.6) using the hydrogen adsorption charge and the amount of charge density passed during the electrodeposition. The actual thickness of the deposit at the edge was recorded using the scanning electron microscope. The estimated thickness was calculated using ***Faraday's law*** (equation 2.3), assuming all the charge is consumed for deposition (100 % efficient).

Table 10. Analysis derived from the cyclic voltammograms in 1 M sulphuric acid solution and the thickness of platinum deposits measured using the SEM and estimated using Faraday's law (assuming 100 % current efficiency). In each case, the concentration of platinum salt is ~0.4 M.

Weight percentage of compositions in plating mixture (LLC phase)	Ø / µm	Q_{passed} /C cm^{-2}	R_f	***S*** /m^2 g^{-1}	***Thickness / µm***	
					Measured by SEM	***Estimated using Faraday's law***
0 wt.% $C_{16}EO_8$: 86 wt.% H_2O : 14 wt.% H_2PtCl_6 (Aqueous solutions)	60	22.9	462	3.9	3.7	5.0
2 wt.% $C_{16}EO_8$: 84 wt.% H_2O : 14wt. % H_2PtCl_6 (Micellar phase)	50	10.8	509	9.3	1.1	2.5
10 wt.% $C_{16}EO_8$: 77 wt.% H_2O : 13 wt. % H_2PtCl_6 (Micellar phase)	50	6.6	485	14.5	1.1	2.0
60 wt.% $C_{16}EO_8$: 34 wt.% H_2O : 6 wt.% H_2PtCl_6 (Hexagonal phase)	50	0.9	83	11.0	0.4	0.39

The morphology of the electrode surface was also observed under a scanning electron microscope. Figure 91 displays the SEM images of the electrode surfaces after the electrodeposition in both the liquid crystal phases as well as in aqueous solution. However, the nanostructured platinum deposit is not observable under the scanning electron microscope scale.

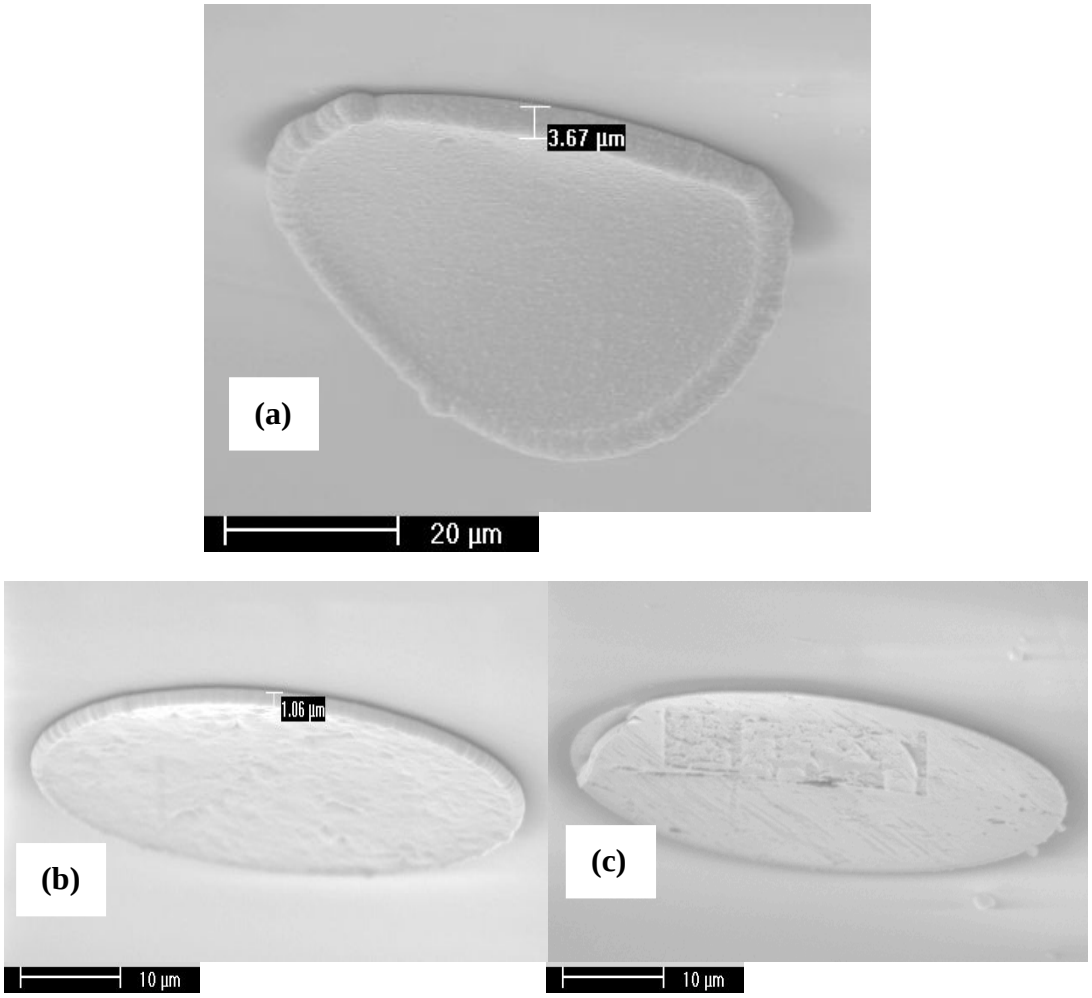

Figure 91. SEM images of the gold coated platinum microelectrode after undergoing two consecutive cyclic voltammograms in **(a)** *hexachloroplatinate (IV) acid aqueous solution (Ø = 60 µm diameter)* **(b)** *micellar phase of LLC mixture (Ø = 50 µm diameter) and* **(c)** *hexagonal phase (Ø = 50 µm diameter).*

The total deposition charge density passed after recording two consecutive cyclic voltammograms in aqueous hexachloroplatinate(IV) acid at 60 µm diameter gold electrode is 22.9 C $cm^{-2.}$. A smooth platinum layer with thickness of 3.67 µm was observed with a roughness factor of 462. The specific catalyst area was found to be 3.9 m^2 g^{-1}. The edge effect of the platinum electrodeposition is clearly enhanced and the layer of platinum deposit started to peel off from the electrode surface (see Figure 91(a)). There is also another thin layer of platinum on the electrode surface underneath the peeled layer. In addition, the platinum deposits have overgrown onto the insulating glass surface. This might contribute to the difference in the actual measurement and the estimated value for the thickness of platinum deposits.

The electrodeposition of platinum in the micellar phase (10 wt.% $C_{16}EO_8$: 77 wt.% H_2O : 13 wt.% H_2PtCl_6) produced a smooth platinum layer of 1.06 µm thickness. The 50 µm diameter platinum coated gold electrode has a roughness factor of 485 (see Figure 91(b)). The calculated specific catalyst area for this electrode is 14.5 m^2 g^{-1} for a total deposition charge density passed 6.6 C cm^{-2}. The electrodeposition in the micellar phase (2 wt.% $C_{16}EO_8$: 84 wt.% H_2O : 14 wt.% H_2PtCl_6) produced a thin platinum layer of 1.08 µm with roughness factor of 509 after deposition charge density of 10.8 C cm^{-2} was passed. The specific catalyst area of the electrode surface is lower than the surface produced in plating mixture with higher percentage weight of surfactant (10 wt.% $C_{16}EO_8$). The discrepancy in the thickness layer of platinum deposits in the micellar phase (2 wt.% $C_{16}EO_8$: 84 wt.% H_2O : 14 wt.% H_2PtCl_6) also attributed to the growth of platinum deposits over the edge of the electrode surface (not shown). Hence, the observed thickness layer is less than the theoretical value.

After recording two cyclic voltammogram in the hexagonal phase with deposition charge density of 0.9 C cm^{-2}, a very thin layer of platinum was obtained on a 50 µm diameter gold electrode (see Figure 91(c)). However the electrode surface is not fully

covered as shown by the presence of cracks within the layer. The roughness factor was found to be 83 with a specific catalyst area of 11 m^2 g^{-1}. The specific catalyst area is low when compared to the literature value reported by ***Bartlett et. al.*** [104, 123]. The specific surface area of the deposited platinum on a 1 cm^2 gold substrate was 22 m^2 g^{-1} after a charge density of 0.66 C cm^{-2} passed.

The specific catalyst area of the modified electrode is higher when the deposition is carried out in the presence of octaethyleneglycol monohexadecyl ether. The roughness factor obtained from the cyclic voltammogram in acid solution is comparable in both micellar phase and aqueous solution, although the charge density passed during electrodeposition in aqueous solution is double the amount in the micellar phase. Therefore, the increase in the electroactive area can be assigned to the presence of nanostructured platinum, however not observable on the scanning electron microscope scale. The calculated roughness factors are surprising. With 0 to 10 wt. % octaethyleneglycol monohexadecylether, the surface is much rougher than when deposition is from the hexagonal phase. This result will be followed up in a project to be commenced soon.

5.3.3. Electrodeposition via chronoamperometry

A set of chronoamperometry experiments have also been investigated in each of the plating mixtures, stepping from zero current (+0.6 V ***versus*** SCE) to the foot of the reduction wave with a fixed deposition charge density of 1 C cm^{-2}. In this experiment, the deposition charge density passed is low, therefore a thin layer of platinum is expected to be observed. In the aqueous hexachloroplatinate(IV) solution, the potential was stepped to +0.05 V ***versus*** SCE. The platinum coated gold microlectrode was rinsed and later characterised in 1 M sulphuric acid solution. The potential was stepped from +0.6 V to 0 V with respect to SCE in both micellar and hexagonal phase of lyotropic liquid crystal mixture. The surfactant was later

removed by soaking the electrode surface in plenty of stirred water overnight. After the complete removal of the surfactant, the platinum deposits on the electrode surface were characterised in the acid solution. Figure 92 shows the cyclic voltammograms recorded at the platinum coated gold microelectrode scanned at 100 mV s^{-1}. Further information of the modified electrode surface analysed from the cyclic voltammogram is tabulated in Table 11.

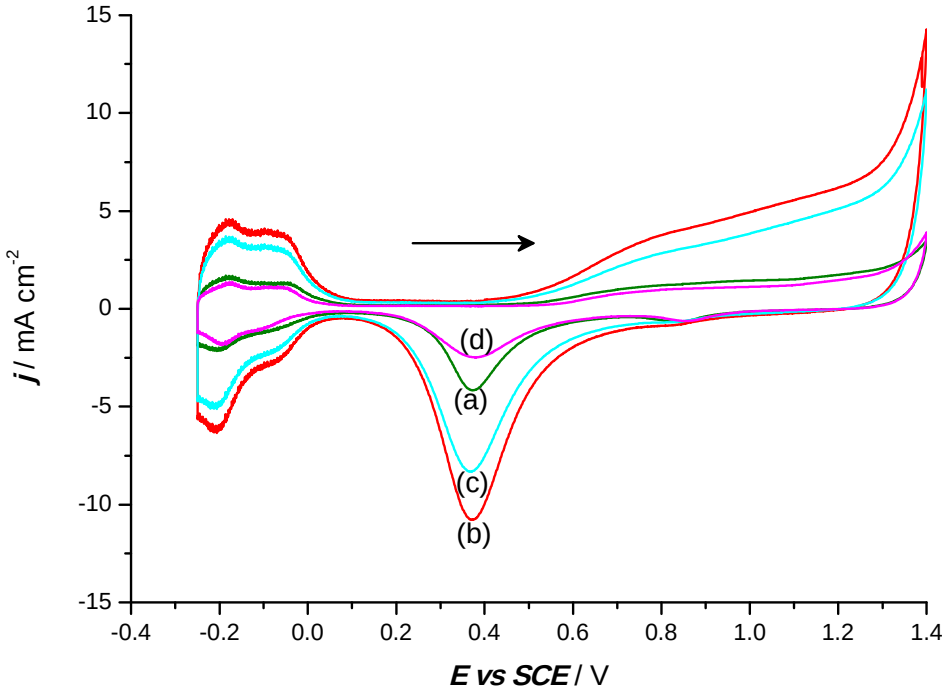

Figure 92. Cyclic voltammograms recorded in 1 M sulphuric acid with a platinum coated gold microelectrode after undergoing potential steps in different compositions of plating mixture.; **(a)** *0 wt.% $C_{16}EO_8$: 86 wt.% H_2O : 14 wt.% H_2PtCl_6* **(b)** *2 wt.% $C_{16}EO_8$: 84 wt.% H_2O : 14 wt.% H_2PtCl_6* **(c)** *10 wt.% $C_{16}EO_8$: 77 wt.% H_2O : 13 wt.% H_2PtCl_6* **(d)** *60 wt.% $C_{16}EO_8$: 34 wt.% H_2O : 6 wt.% H_2PtCl_6. Voltammograms **(a)** and **(d)** are recorded at 50 µm diameter gold electrodes. Voltammograms **(b)** and **(c)** recorded at 60 µm diameter. Scan rate 100 mV s^{-1}.*

Table 11. The charge under hydrogen adsorption peak, roughness factor and the specific catalyst area of the platinum coated gold microelectrode after passing 1 C cm^{-2}.

Weight percentage of compositions in plating mixture (LLC phase)	Q_{ads} / mC cm^{-2}	R_f	S / m^2 g^{-1}
0 wt.% $C_{16}EO_8$: 86 wt.% H_2O : 14 wt.% H_2PtCl_6 Aqueous solutions	3.7	17.6	3.5
2 wt.% $C_{16}EO_8$: 84 wt.% H_2O : 14wt. % H_2PtCl_6 Micellar phase	9.9	47.0	9.3
10 wt.% $C_{16}EO_8$: 77 wt.% H_2O : 13 wt. % H_2PtCl_6 Micellar phase	7.9	37.6	7.4
60 wt.% $C_{16}EO_8$: 34 wt.% H_2O : 6 wt.% H_2PtCl_6 Hexagonal phase	2.9	13.6	2.7

The cyclic voltammetry in acid solution confirmed the presence of platinum on the electrode surface. All the voltammograms present features characteristic of bulk platinum with the presence of platinum oxide formation/reduction peaks and hydrogen adsorption/desorption peaks. However, there is also a small reduction peak that corresponds to the reduction of gold oxide. Hence, there is still some exposed gold electrode surface. The presence of the gold oxide peak might be attributed to the lifting of the platinum layer at the edges, thus the gold surface underneath the deposit layer is exposed. The calculated roughness factor and the specific catalyst area are high for the modified electrodes after electrodeposition in the micellar phase of the lyotropic liquid crystalline mixture. Using ***Faraday***'s law, the estimated thickness of the platinum deposit is 253 nm (assuming 100 % efficient) when 1 C cm^{-2} passed. A smooth surface was observed under scanning electron microscope (not shown). The liquid crystals in the plating mixture could also act as a 'leveler additive', thereby producing smooth platinum deposits. Again, there is an increase in

the roughness factors obtained from the cyclic voltammograms in acid solution, specifically in the micellar phase (see Table 11) when compared to aqueous solutions. Surprisingly, the specific catalyst area of platinum after the deposition in micellar solution is higher than those produced in hexagonal lyotropic phase.

5.3.4. Electrodeposition of platinum in hexagonal lyotropic phase (~2.3 M H_2PtCl_6)

A lyotropic liquid crystal mixture containing 0.42 g surfactant, 0.29 g hexachloroplatinate(IV) acid and 0.29 g water was prepared in a vial. The concentration of hexachloroplatinate(IV) acid was calculated using the mole fraction of hexachloroplatinate(IV) acid in the ternary plating mixture and it is approximately 2.3 M. This is nearly six times larger than the concentration used for the experiments shown in the previous sections. The hexagonal lyotropic phase prepared in this ternary plating mixture contains different percentage weight of each of the compositions with higher concentration of hexachloroplatinate(IV) acid. The procedure in the preparation of the plating mixture (heating and stirring) is similar to that mentioned earlier. The homogeneous mixture is very viscous and orange in colour. Once the mixture is thoroughly mixed, it was left at room temperature before proceeding with further experiment. The hexagonal phase of the lyotropic liquid mixture was confirmed with the appearance of a fan-like optical texture when observed under polarising optical microscope (see Figure 30). A cyclic voltammogram in the hexagonal phase of the lyotropic liquid crystal was recorded with a 25 µm diameter gold disc electrode as displayed in Figure 93.

On the forward scan, the reduction wave started to occur at +0.1 V with a sudden increase in current density observed at -0.175 V with respect to SCE. It is clearly observed that a large overpotential is required for the nucleation to take place on the electrode surface from the lyotropic liquid crystalline mixture when compared to the

reduction of platinum(IV) in aqueous platinum plating solution. This may be ascribed to the adsorption of the lyotropic liquid crystals on the surface that inhibit the nucleation of platinum. The negative potential limit is chosen so that only the first reduction wave is produced. There is a hysteresis observed on the reverse scan with an increase in current density at all potentials positive to -0.25 V. The loop shows feature characteristic of nucleation process taking place. Thus, the cathodic current negative to +0.3 V can be assigned for the reduction of platinum(IV) to platinum(0) from the viscous plating mixture.

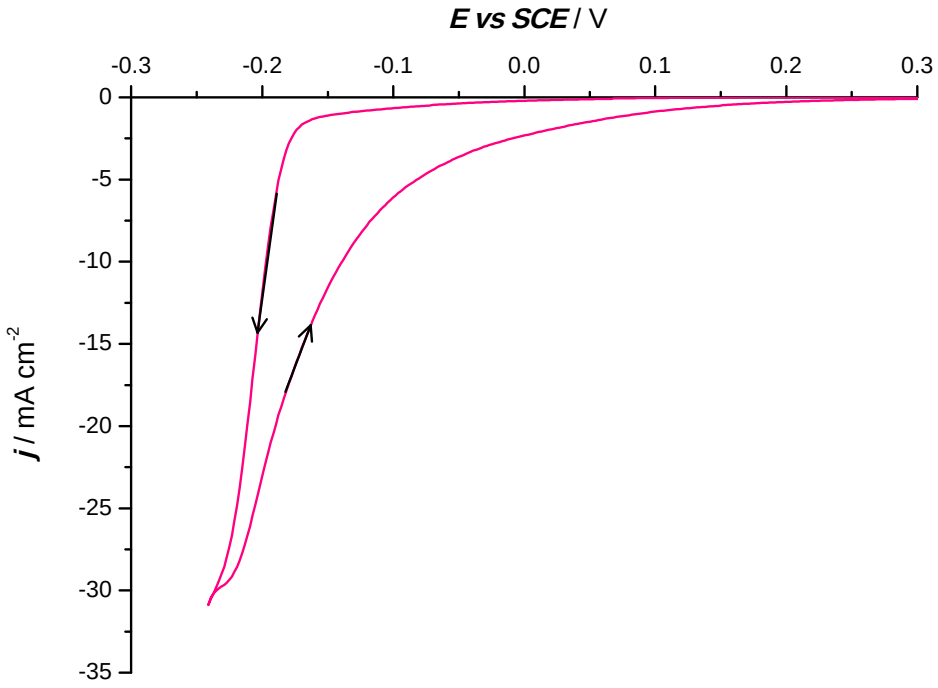

Figure 93. Cyclic voltammogram recorded in the hexagonal phase of the LLC mixture (42 wt.% $C_{16}EO_8$: 29 wt.% H_2O : 29 wt.% H_2PtCl_6) at a scan rate of 10 mV s^{-1} with a 25 µm diameter gold electrode.

The deposition of platinum from the hexagonal phase liquid crystalline mixture was later investigated by single step chronoamperometry within the deposition potential window. The presence of platinum on the electrode surface was confirmed with the cyclic voltammogram in 1 M sulphuric acid. The potential was stepped from +0.6 V to -0.2 V ***versus*** SCE. The 25 µm and 50 µm diameter gold microdisc electrodes

were used as the working electrodes and the deposition charge density of 6 C cm^{-2} and 3 C cm^{-2} were applied. A thick layer of platinum was produced with a thickness of 1.2 µm and 0.6 µm for 25 µm and 50 µm diameter gold electrode respectively. After the single step chronoamperometry, the electrodes were removed from the viscous mixture and soaked in copious amounts of stirred water. The water was changed at 30 minutes intervals except when left overnight. This was to ensure the complete removal of the surfactant from the electrode surface. The cyclic voltammogram in 1 M sulphuric acid was later recorded at the prepared nanostructured platinum on gold electrode surface. The voltammograms were scanned at 100 mV s^{-1}. The cyclic voltammograms in Figure 94 show features that are characteristic of polycrystalline platinum deposits.

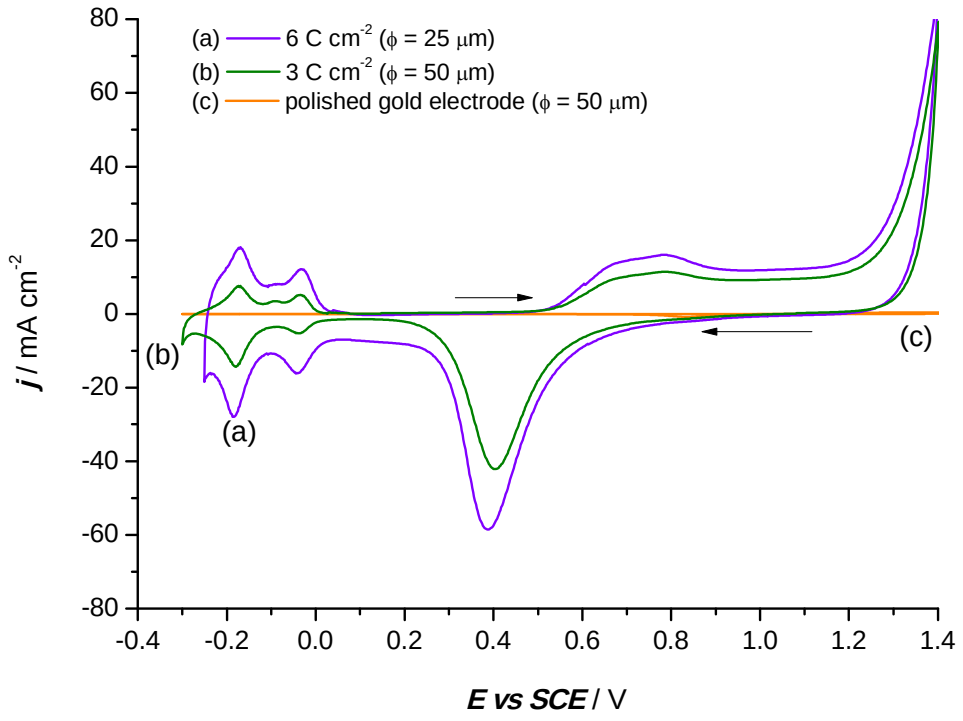

Figure 94. Cyclic voltammograms in 1 M sulphuric acid degassed with argon. Potential scan rate 100 mV s^{-1}. The working electrodes are nanostructured platinum on gold electrodes prepared by potential steps in LLC (42 wt.% $C_{16}EO_8$: 29 wt.% H_2O : 29 wt.% H_2PtCl_6) from +0.6 V to -0.2 V versus SCE with various deposition charge density.

The platinum oxide formation/reduction peaks and hydrogen adsorption/desorption peaks are observed. In addition, the deposition of nanostructured platinum electrode surface produces a much higher current density compared to the polycrystalline platinum electrode (see Figure 94). The increase in the hydrogen adsorption charge reflects an increase in the surface area of the platinum present on the electrode surface. Thus, the roughness factor for the electrodes with 6 C cm^{-2} and 3 C cm^{-2} are 2273 and 983 respectively. The specific catalyst areas of the electrodes are very low (0.74 m^2 g^{-1} and 0.63 m^2 g^{-1}). As expected, the roughness factor is higher with platinum loadings compared to the roughness factor for a polished 50 µm diameter platinum electrode ($\boldsymbol{R_f}$ = 4) (see Figure 95).

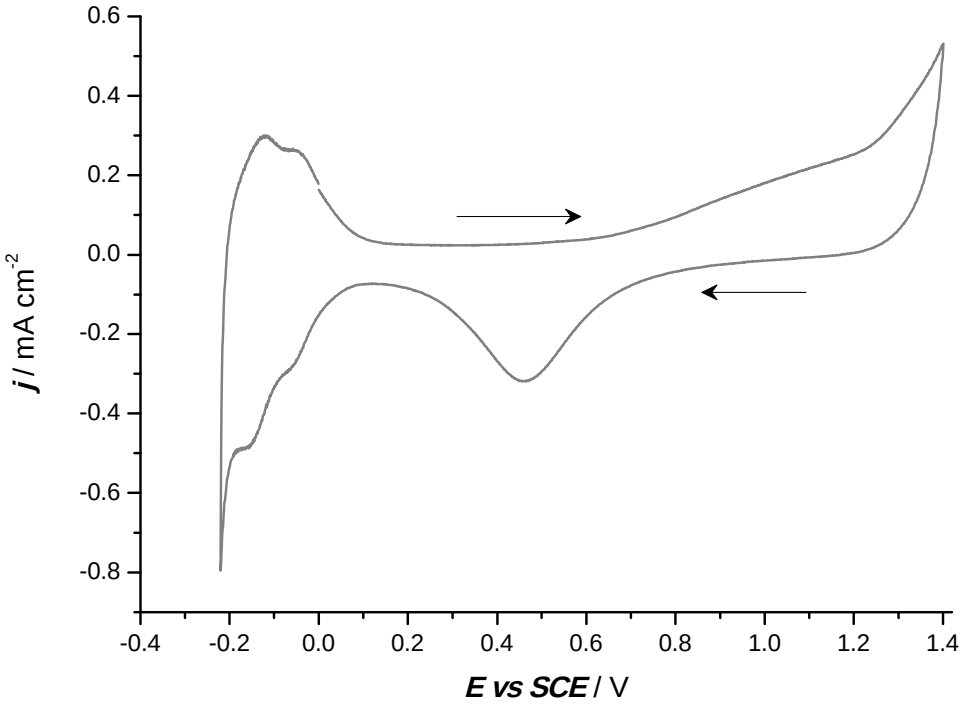

Figure 95. A typical cyclic voltammogram for a 50 µm diameter platinum microdisc electrode in 1 M sulphuric acid at a scan rate of 100 mV s^{-1}.

In another set of experiments, the potential was stepped from +0.6 V to -0.1 V ***versus*** SCE in the same hexagonal phase lyotropic liquid crystalline mixture (42 wt.% $C_{16}EO_8$: 29 wt.% H_2O : 29 wt.% H_2PtCl_6). The deposition potential was chosen to be at the foot of the reduction of platinum(IV). The deposition charged densities applied were intentionally much lower, between 0.3 C cm^{-2} and 0.04 C cm^{-2} to produce a very thin platinum deposit. After the single potential step chronoamperometry, similar procedure was applied for the complete removal of the surfactant by soaking the electrodes in large quantities of stirred water for overnight. The platinum mesoporous gold electrodes were later characterised in 1 M sulphuric acid at a scan rate of 100 mV s^{-1}. Figure 96(a-b, d-e) shows cyclic voltammograms with partial coverage of platinum deposited onto the gold electrode surface.

In all the voltammograms, the gold oxide and platinum oxide reduction peaks can be observed. The hydrogen adsorption/desorption peaks can only be observed when a deposition charge density of 0.3 C cm^{-2} has been passed. Nevertheless there is still visible amount of charge under the gold oxide reduction peak. The hydrogen adsorption/desorption peaks are not resolved when the deposition charge density passed is less than 0.3 C cm^{-2}. Instead, the onset of the hydrogen evolution can be observed at -0.24 V ***versus*** SCE. Even with the deposition for 0.04 C cm^{-2}, there is a hydrogen region with much larger current than for the bare gold electrode. The gold oxide reduction peak is much reduced but a smaller peak corresponding to platinum oxide can be observed. However, the amount of platinum loadings on the electrode surface is still insufficient to produce the hydrogen adsorption/desorption peaks. The roughness factor and the specific catalyst area of the modified electrodes cannot be calculated with the unresolved hydrogen adsorption peaks.

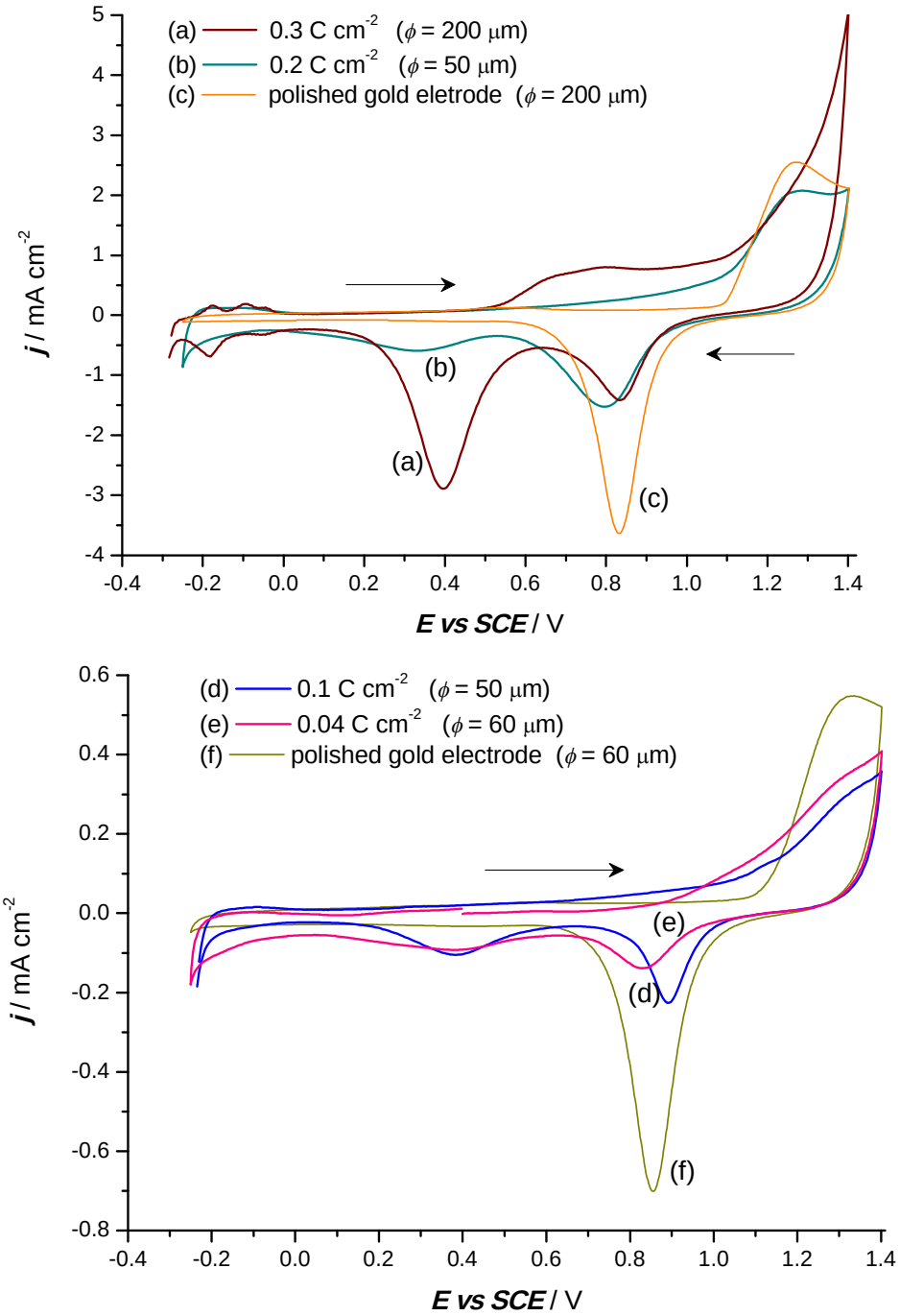

Figure 96. Cyclic voltammograms recorded in 1 M sulphuric acid at 100 mV s^{-1} with nanostructured Pt on Au electrodes with various deposition charge densities applied; **(a)** *0.3 C cm^{-2}* **(b)** *0.2 C cm^{-2}* **(d)** *0.1 C cm^{-2}* **(e)** *0.04 C cm^{-2}. The cyclic voltammogram for polished gold electrodes is included for comparison* **(c)** *Ø = 200 μm* and **(f)** *Ø = 60 μm.*

5.3.5. Electrodeposition of platinum in hexagonal lyotropic phase with ~0.4 M H_2PtCl_6

Another platinum lyotropic liquid crystalline mixture was prepared with a lower concentration of hexachloroplatinate(IV) acid. The ternary mixture contained 0.46 g of surfactant, 0.46 g of water and 0.08 g of hexachloroplatinate(IV) (~0.4 M; one sixth from the previous experiment). The liquid crystalline mixture was similarly prepared by heating and stirring until a homogeneous mixture was obtained. The resultant hexagonal phase liquid crystalline mixture had a pale orange colour with high viscosity.

The nanostructured platinum deposit was prepared by single potential step chronoamperometry in the hexagonal phase liquid crystalline mixture on a 60 µm diameter gold microdisc electrode. The potential was stepped from +0.6 V to +0.15 V, +0.175 V and +0.2 V ***versus*** SCE with fixed deposition times. As expected, the platinum loadings onto the electrode surface increase with overpotential at a fixed deposition time. The deposition charge densities are in the ranged between 2 mC cm^{-2} and 50 mC cm^{-2}. After the electrodeposition experiment, the platinum coated gold electrode was removed and soaked in copious amount of water to remove the surfactant. The cyclic voltammogram in 1 M sulphuric acid (not displayed) exhibited slight platinum oxide reduction peaks with the onset of hydrogen evolution appearing at +0.4 V and -0.24 V respectively even after deposition for 2 mC cm^{-2}. The gold oxide reduction peak was still largely visible yet the presence of platinum was confirmed by the cyclic voltammogram in acid solution. The catalytic response for the hydrogen evolution was investigated in 1 M sulphuric acid at the nanostructured platinum deposit to further confirm the presence of mesoporous platinum. Figure 97 shows the catalytic response for the hydrogen evolution at nanostructured platinum on gold electrodes.

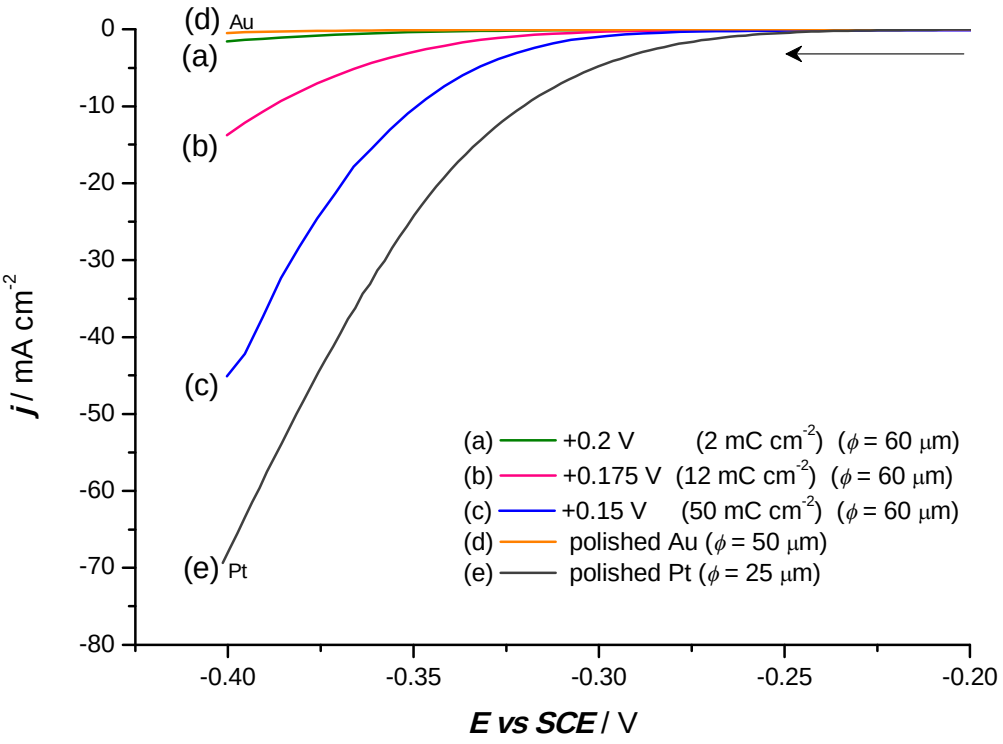

Figure 97. Hydrogen evolution reactions recorded in 1 M H_2SO_4 degassed with argon at H_1e-Pt on Au electrode, prepared by potential step in LLC (46 wt.% $C_{16}EO_8$: 46 wt.% H_2O : 8 wt.% H_2PtCl_6) from +0.3 V to **(a)** *+0.2 V* **(b)** *+0.175 V* **(c)** *+0.15 V. The polished gold and platinum electrode (indicated as* **(d) and (e)**) *was also shown for comparison. Scan rate 100 mV s^{-1}.*

The current density observed at -0.4 V with respect to SCE increases with an increase in deposition charge density. The electrode surface with the deposition charge density of 2 mC cm^{-2} has the least catalytic activity for hydrogen evolution, almost similar to that of a polished gold electrode. With slightly higher charge densities, the modified gold electrodes appear to be good catalyst for the hydrogen evolution reaction. However, even with 50 mC cm^{-2} modified gold electrode has a lower activity than that of a bulk platinum electrode.

In addition, the same nanostructured platinum deposits were also investigated for their catalytic activity towards the oxygen reduction reaction in 0.1 M perchloric

acid saturated with oxygen. Figure 98 shows the catalytic response for the oxygen reduction reaction. The onset of the wave for the oxygen reduction shifted to more positive potentials with an increase in deposition charge density passed. These platinum mesoporous modified gold electrodes show good catalytic response for the oxygen reduction reaction when compared to the gold electrode. However, the catalytic response for the platinum modified gold electrode is still not comparable to that for the bulk platinum electrode. This may be associated with the insufficient amount of platinum loadings onto the electrode surface.

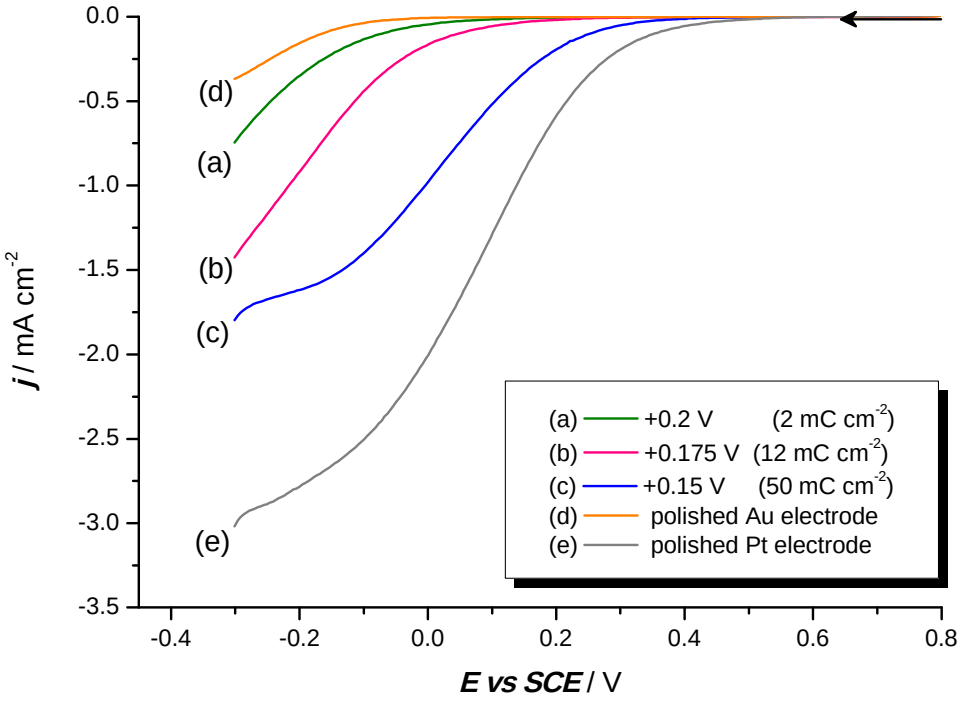

Figure 98. Voltammograms for the oxygen reduction reaction in 0.1 M $HClO_4$ saturated with O_2 recorded at nanostructured Pt on Au electrode, scan rate 10 mV s^{-1}. The modified gold electrodes are prepared by potential steps in LLC (46 wt.% $C_{16}EO_8$: 46 wt.% H_2O : 8 wt.% H_2PtCl_6) from +0.3 V versus SCE for 300 s to **(a)** *+0.2 V* **(b)** *+0.175 V* **(c)** *+0.15 V. The ORR recorded at polished gold and platinum electrodes are also shown, indicated as* **(d)** *and* **(e)** *respectively.*

5.4. Conclusions

1. The voltammetric studies have demonstrated that platinum can be deposited on gold substrates from a solution containing hexachloroplatinate(IV) with and without added electrolyte. Two reduction waves with an increase in current density in between the two waves are produced at gold electrodes. The first reduction wave is always steep and smaller than the second reduction wave. In aqueous solution containing high concentration of hexachloroplatinate (IV) acid (0.4 M), the current density obtained is higher due to the increase in the concentration of hexachloroplatinate(IV) acid in the solution. The ratio of the reduction waves produced at gold substrate is different from those recorded at carbon surface. However, the presence of nucleation loop is similarly observed when recorded on carbon substrate. The differences between carbon and gold substrates are difficult to understand, particularly the second cycles when both surfaces are already platinum.

2. At all potentials negative to +0.25 V (for gold rotating disc electrode) and +0.1 V (for gold microelectrodes), platinum has been successfully electrodeposited onto the electrode surface. The cyclic voltammogram in 1 M sulphuric acid shows features characteristic of platinum even at a charge density as low as 50 mC cm^{-2}.

3. The scanning electron microscopy (SEM) images have shown the presence of platinum deposited onto the electrode surface and been further analysed using the energy dispersive X-ray spectroscopy (EDXS). A thick layer of platinum (approximately 1 μm thick) was obtained with 4 C cm^{-2} on a gold rotating disc electrode at potentials negative to 0 V ***versus*** SCE. However, the platinum nuclei are hardly observed when using lower deposition charge densities, even when using scanning electron microscope at higher magnification. This may be attributed to a continuous thin film deposited on

the gold substrate. Thus isolated nuclei have never been observed. In contrast, the platinum nuclei on carbon substrate produced isolated centres with hemispherical shape. Nevertheless, the morphological observation of the platinum coated gold electrode is in agreement with the observation made by ***Plysova et. al.*** reporting continuous layers of platinum on gold surface [77]. However, the cyclic voltammogram in acid solution shows the platinum oxide reduction peak, thereby confirmed the presence of platinum on the gold surface.

4. The reduction of platinum(IV) at -0.35 V ***versus*** SCE on the gold rotating disc electrode can be concluded as a mass transport controlled reaction. A linear plot of limiting current density against the square root of the rotation rates was obtained that obeys the ***Levich*** equation. Thus the diffusion coefficient of hexachloroplatinate(IV) acid was found to be 4.7×10^{-6} cm^2 s^{-1} assuming that it was reduced by a four-electron step reduction. This value agrees well with the reported literature value, 4.5×10^{-6} cm^2 s^{-1} [254, 255].

5. The voltammetric response for the gold electrodes was investigated in the platinum(IV) plating mixture containing the hexagonal phase and micellar phase of the lyotropic liquid crystalline mixture as well as in aqueous solution. The nucleation of platinum becomes more difficult with an increase in percentage weight of octaethyleneglycol monohexadecyl ether (surfactant) in the plating mixture. There is a possibility of the lyotropic liquid crystals adsorp on the electrode surface, thus inhibiting the nucleation of platinum. Thus, the onset for the first reduction wave shifted to more negative potentials. The platinum electrodeposited from lyotropic liquid crystalline mixture has higher specific catalytic area when compared to electrodeposition in aqueous solution. Surprisingly, the electrodeposition of platinum in micellar solution has produced an electrode surface with highest specific catalytic activity.

6. In acid cyclic voltammetry, presence of platinum was observed after undergoing cyclic voltammetry and potential step experiments at various deposition potentials in the hexagonal phase of liquid crystalline plating mixture (42 wt.% $C_{16}EO_8$: 29 wt.% H_2O : 29 wt.% H_2PtCl_6) at a deposition charge density greater than 0.04 C cm^{-2}. Thus the cathodic current density in the cyclic voltammogram in platinum liquid crystalline mixture can be associated with the reduction reaction of platinum(IV) to platinum(0).

7. The nanostructured platinum onto gold electrode surface have also been prepared from a ternary mixture that contains lower concentration of hexachloroplatinate(IV) acid in a mixture of 46 wt.% $C_{16}EO_8$: 46 wt.% H_2O : 8 wt.% H_2PtCl_6. The modified gold electrodes with nanostructured platinum have shown good catalytic response for the hydrogen evolution and oxygen reduction reactions, however they still produce lower catalytic activity than a polished platinum electrode.

.

Chapter 6

6 Conclusions

This study has confirmed that it is possible to electrodeposit platinum and gold from solutions containing hexachloroplatinate(IV) and tetrachloroaurate(III) respectively, in the presence of hydrochloric acid electrolyte. The voltammetric studies with carbon substrates in hexachloroplatinate(IV) suggest that there are several platinum species present in the solution. They are thought to derive from the following equilibria:

$$PtCl_6^{2-} + H_2O \rightleftharpoons PtCl_5H_2O^- + Cl^-$$

$$PtCl_5H_2O^- + H_2O \rightleftharpoons PtCl_4(H_2O)_2 + Cl^-$$

At sufficiently negative potentials, the platinum deposition reaction becomes diffusion controlled. The platinum centres deposited onto the carbon fibre wire and vitreous carbon disc electrodes are in the form of isolated ‘hemispherical’ nuclei. On carbon surfaces, the platinum centres grow up to a certain critical size without forming a continuous layer of platinum; such layer was never observed even at high deposition charge densities. The nucleation of platinum on carbon is always a slow process even at high overpotentials. The ideal of instantaneous nucleation so that all nuclei have the

same size is not achieved although with some carbon surfaces, e.g. vitreous carbon, the centres appear to have similar sizes at more negative potentials, see Figure 78. The number density of nuclei increases with overpotential. The nucleation of platinum on carbon substrates requires a large overpotential when compared to that on a gold electrode. In contrast to carbon substrates, the electrodeposition of platinum on gold substrates quickly produces a continuous layer of platinum metal deposit. This is clearly observed at even moderate deposition charge densities. On gold surfaces the voltammetric response in hexachloroplatinate(IV) does not confirm the reaction mechanism suggested for carbon substrates. In particular, the ratio of the reduction wave heights produced on the second cycles, that is, for freshly deposited platinum surfaces are different. The reasons for this remain unclear.

The reduction of gold(III) is a much simpler reaction. The voltammetric studies in tetrachloroaurate(III) suggest either that the solution contains only one gold(III) complex or that several species present in the solution are in rapid equilibrium. A mass transport controlled reaction is produced at high overpotentials. The SEM images for the electrodeposition of gold on carbon similarly demonstrate a surface with sparsely distributed hemispherical centres. The gold deposits dissolve anodically in the solution. However, the gold nuclei remain undissolved at very positive potentials. This observation indicates that passivation of gold occurs.

In contrast to real catalysts which typically consist of 2 to 10 nm size platinum centres on rough surfaces, the objective of the project was to electrodeposit uniform platinum sized, well distributed centres on smooth surfaces. The following Table 12 illustrates the influence of charge density and nuclei number density assuming the centres have equal size and all the charge is consumed for metal deposition (100 % efficiency). The table shows the theoretical platinum centre diameters and platinum area per unit electrode area for various charge densities and nuclei number densities.

Table 12. Calculated dependence of the centre diameters and platinum surface area on the deposition charge density and nuclei number density, assuming 100 % current efficiency and equal size nuclei.

Charge density, ***q*** / mC cm^{-2}	Number density, ***N*** / centres cm^{-2}	Diameter, ***Ø*** / nm	Surface area of Pt per unit area / cm^2 cm^{-2}
0.1	10^6	202	0.0006
	10^8	44	0.003
	10^{10}	9	0.013
	10^{12}	2	0.065
1	10^6	439	0.003
	10^8	95	0.014
	10^{10}	20	0.06
	10^{12}	4	0.3
10	10^6	946	0.014
	10^8	204	0.06
	10^{10}	44	0.3
	10^{12}	9	0.22
100	10^6	2038	0.006
	10^8	439	0.3
	10^{10}	95	1.4
	10^{12}	20	6.5

The data in Table 12 shows the possibilities of producing small centres and also the difficulties in achieving the goal of the research. The charge densities considered are based on the wish to form small centres and experience from the project. The number densities tabulated reflect;

(a) With an atomically smooth carbon surface, the number of carbon atoms is approximately 10^{15} cm^{-2} (assuming a graphene sheet).

(b) From the SEM images, the typical number densities observed for platinum on carbon were approximately 10^{8} cm^{-2}.

(c) If nucleation occurs at all possible sites within the lyotropic liquid phase, the number density would be approximately 10^{13} cm^{-2}. This number density is estimated from close packed distribution of rods of liquid crystals structures.

The diameter of the centres increases with the deposition charge density. With a charge density of 10 to 100 mC cm^{-2}, the project goal of centres with diameters in the 2 to 5 nm range is clearly unlikely to be achieved. With the charge densities less than 1 mC cm^{-2}, the size criterion can be met with a high number density. Unfortunately, for the smooth substrates, the active platinum surface area then becomes very low, typically much less than 1 cm^2 of platinum per cm^2 of substrate. Hence, the cyclic voltammograms show very small peaks and the background current density becomes too large. Of course, the experiments are not carried out with atomically smooth carbon surfaces. Hence this increases the number of platinum centres and therefore increases the active surface area of platinum. This sometimes leads to cyclic voltammograms with observable peaks.

It is more useful to vary the number density than the deposition charge density. It is possible to produce small centres with high number densities. Substrates with

smooth surfaces always lead to low number densities and therefore low surface area of the metal; this makes it difficult to study by cyclic voltammetry. In addition, it is not possible to observe any centres with diameter less than 50 nm using scanning electron microscopy. In contrast, real catalyst substrates have high surface areas which present high nuclei number densities and therefore allow the deposition of large areas of platinum.

In this research, the electrodeposition of platinum on carbon substrates has produced a surface with nuclei number density circa 10^8 cm^{-2}. With reference to the data in Table 12, if the charge density is reduced to 0.1 mC cm^{-2}, the centres produced will be small with diameters circa 44 nm. Hence, these small centres will not be observable with the magnification of typical scanning electron microscopes, and the peaks associated with platinum will not be seen in the cyclic voltammogram in acid solution. However, these small centres are believed to be present on the surface. They lead to the centres observed at higher charge densities.

The SEM image in Figure 47 has shown that gold centres deposited on carbon substrates at high overpotential produced a more uniform size than platinum centres. At very negative potentials, these gold centres are believed to be present on the surface, initially in the form of very small centres at low deposition charge densities. However, the centres are too small to be observed using scanning electron microscopy and the surface area of gold per unit area of substrate is expected to be low.

A high surface area of metal catalyst can be achieved when the nuclei number density increases. The metal centres produced will be small. With very low deposition charge densities, the diameters of the metal centres are very small but in the range aimed to be produced in this research. On the other hand, the low surface area of metal centres per unit substrate area makes it difficult to be confirmed with

cyclic voltammetry in acid solution; the centres are definitely not observable with typical scanning electron microscopes.

Hence, the work in this thesis has shown that the formation of efficient catalysts surfaces by electrodeposition should be possible. It would be valuable to extend the work to higher area and rougher substrates where the nuclei number density might be higher. Also it would be interesting to carry out further experiments in the liquid crystal media focusing on both lower charge densities and deposition from the micellar phase.

7 References

[1]. A. Wieckowski, E. R. Savinova and C. G. Vayenas, ***Catalysis and Electrocatalysis at Nanoparticle Surfaces***, Marcel Dekker Ltd, New York, (2003).

[2]. J. Chen, B. Lim, E. P. Lee and Y. Xia, ***Nano Today,*** **4** (***2009***) 81.

[3]. O. V. Cherstiouk, P. A. Simonov and E. R. Savinova, ***Electrochim. Acta,*** **48** (***2003***) 3851.

[4]. H. A. Gasteiger, S. S. Kocha, B. Sompalli and F. T. Wagner, ***Appl. Catal. B,*** **56** (***2005***) 9.

[5]. S. Guerin, B. E. Hayden, C. E. Lee, C. Mormiche, J. R. Owen, A. E. Russell, B. Theobald and D. Thompsett, ***J. Comb. Chem.,*** **6** (***2004***) 149.

[6]. F. Maillard, S. Schreier, M. Hanzlik, E. R. Savinova, S. Weinkauf and U. Stimming, ***Phys. Chem. Chem. Phys.,*** **7** (***2005***) 385.

[7]. S. Pandelov and U. Stimming, ***Electrochim. Acta,*** **52** (***2007***) 5548.

[8]. A. Safavi, N. Maleki, F. Tajabadi and E. Farjami, ***Electrochem. Commun.,*** **9** (***2007***) 1963.

[9]. H. Wolfschmidt, R. Bussar and U. Stimming, ***J. Phys. Condens. Matter,*** **20** (***2008***) 374127.

[10]. Y. Zhu, Y. Kang, Z. Zou, Q. Zhou, J. Zheng, B. Xia and H. Yang, ***Electrochem. Commun.,*** **10** (***2008***) 802.

[11]. D. He, L. Yang, S. Kuang and Q. Cai, ***Electrochem. Commun.,*** **9** (***2007***) 2467.

[12]. P. Sivakumar, R. Ishak and V. Tricoli, ***Electrochim. Acta,*** **50** (***2005***) 3312.

[13]. D. Cameron, R. Holliday and D. Thompson, ***J. Power Sources,*** **118** (***2003***) 298.

[14]. M. Haruta and M. Daté, ***Appl. Catal. A,*** **222** (***2001***) 427.

[15]. Y. D. Jin, Y. Shen and S. J. Dong, ***J. Phys. Chem. B,*** **108** (***2004***) 8142.

[16]. Y. Tian and T. Tatsuma, ***J. Am. Chem. Soc.,*** **127** (***2005***) 7632.

[17]. J. F. Zhai, M. H. Huang and S. J. Dong, ***Electroanalysis,*** **19** (***2007***) 506.

[18]. M. Valden, S. Pak, X. Lai and D. W. Goodman, ***Catal. Lett.,*** **56** (***1998***) 7.

[19]. D. Pletcher, ***A First Course in Electrode Processes***, The Royal Society of Chemistry, Cambridge, UK, 2nd edition (2009).

[20]. M. Haruta, ***Catal. Today,*** **36** (***1997***) 153.

[21]. F. Boccuzzi, A. Chiorino, M. Manzoli, P. Lu, T. Akita, S. Ichikawa and M. Haruta, ***J. Catal.,*** **202** (***2001***) 256.

[22]. M. S. El-Deab and T. Ohsaka, ***Electrochem. Commun.,*** **4** (***2002***) 288.

[23]. F. Gloaguen, J. M. Léger and C. Lamy, ***J. Appl. Electrochem.,*** **27** (***1997***) 1052.

[24]. M. Watanabe, H. Sei and P. Stonehart, ***J. Electroanal. Chem.,*** **261** (***1989***) 375.

[25]. C. R. Raj, T. Okajima and T. Ohsaka, ***J. Electroanal. Chem.,*** **543** (***2003***) 127.

[26]. L. Wang, W. Mao, D. Ni, J. Di, Y. Wu and Y. Tu, ***Electrochem. Commun.,*** **10** (***2008***) 673.

[27]. D. Thompsett, in: G. Hoogers (Ed.), ***Fuel Cell Technology Handbook***, CRC Press, Boca Raton, (2003).

[28]. E. Yeager, ***Electrochim. Acta,*** **29** (***1984***) 1527.

[29]. B. C. Beard and P. N. Ross, ***J. Electrochem. Soc.,*** **137** (***1990***) 221.

[30]. U. A. Paulus, T. J. Schmidt, H. A. Gasteiger and R. J. Behm, ***J. Electroanal. Chem.,*** **2001** (***2001***) 134.

[31]. T. Toda, H. Igarashi and M. Watanabe, ***J. Electroanal. Chem.,*** **460** (***1999***) 258.

[32]. V. S. Bagotzky, ***Fundamentals of Electrochemistry***, John Wiley & Sons, Inc., New Jersey, 2nd edition, (2006).

[33]. K. Kinoshita, ***Electrochemical Oxygen Technology***, Wiley, New York, (1992).

[34]. R. Adžić, in: J. Lipkowski and P. N. Ross (Ed.), ***Electrocatalysis***, Wiley-VCH, New York, (1998), p. 197.

[35]. M. S. Wilson, J. A. Valerio and S. Gottesfeld, ***Electrochim. Acta,*** **40** (***1995***) 355.

[36]. C. A. C. Milhano, ***Electrodeposition of Cu and Cu-Pd alloys from aqueous and liquid crystal media and their activity for nitrate reduction*** PhD thesis, University of Southampton, (2007).

[37]. M. Haruta, S. Tsubota, T. Kobayashi, H. Kageyama, M. J. Genet and B. Delmon, ***J. Catal.,*** **144** (***1993***) 175.

[38]. M. Haruta, N. Yamada, T. Kobayashi and S. Iijima, ***J. Catal.,*** **115** (***1989***) 301.

[39]. M. Valden, X. Lai and D. W. Goodman, ***Science,*** **281** (***1998***) 1647.

[40]. K. Kinoshita, ***J. Electrochem. Soc.,*** **137** (***1990***) 845.

[41]. E.Yeager, ***J. Electrochem. Soc.,*** **128** (***1981***) 160C.

[42]. M. Comotti, W. C. Li, B. Spliethoff and F. Schuth, ***J. Am. Chem. Soc.,*** **128** (***2006***) 917.

[43]. B. E. Hayden, D. Pletcher, M. E. Rendall and J.-P. Suchsland, ***J. Phys. Chem. C,*** **111** (***2007***) 17044.

[44]. B. E. Hayden, D. Pletcher and J.-P. Suchsland, ***Angew. Chemie. Int. Ed.,*** **119** (***2007***) 3600.

[45]. N. Lopez, T. V. W. Janssens, B. S. Clausen, Y. Xu, M. Mavrikakis, T. Bligaard and J. K. Norskov, ***J. Catal.,*** **223** (***2004***) 232.

[46]. M. S. El-Deab and T. Ohsaka, ***Electrochim. Acta,*** **47** (***2002***) 4255.

[47]. Y. Zhang, S. Asahina, S. Yoshihara and T. Shirakashi, ***Electrochim. Acta,*** **48** (***2003***) 741.

[48]. Y. Zhang, V. Suryanarayanan, I. Nakazawa, S. Yoshihara and T. Shirakashi, ***Electrochim. Acta,*** **49** (***2004***) 5235.

[49]. I. Yagi, T. Ishida and K. Uosaki, ***Electrochem. Commun.,*** **6** (***2004***) 773.

[50]. M. S. El-Deab, T. Sotomura and T. Ohsaka, ***J. Electrochem. Soc.,*** **152** (***2005***) C1.

[51]. M. S. El-Deab, T. Sotomura and T. Ohsaka, ***Electrochim. Acta,*** **52** (***2006***) 1792.

[52]. S. Guerin, B. E. Hayden, D. Pletcher, M. E. Rendall and J.-P. Suchsland, ***J. Comb. Chem.,*** **8** (***2006***) 679.

[53]. Y. Guan and E. J. M. Hensen, ***Appl. Catal. A,*** **361** (***2009***) 49.

[54]. Y. Takasu, N. Ohashi, X. G. Zhang, Y. Murakami, H. Minagawa, S. Sato and K. Yahikozawa, ***Electrochim. Acta,*** **41** (***1996***) 2595.

[55]. A. Gamez, D. Richard, P. Gallezot, F. Gloaguen, R. Faure and R. Durand, ***Electrochim. Acta,*** **41** (***1996***) 307.

[56]. Y. Takasu, T. Iwazaki, W. Sugimoto and Y. Murakami, ***Electrochem. Commun.,*** **2** (***2000***) 671.

[57]. K. Yahikozawa, Y. Fujii, Y. Matsuda, K. Nishimura and Y. Takasu, ***Electrochim. Acta,*** **36** (***1991***) 973.

[58]. P. Stonehart, ***Electrochim. Acta,*** **17** (***1972***) 2333.

[59]. E. Higuchi, H. Uchida and M. Watanabe, ***J. Electroanal. Chem.,*** **583** (***2005***) 69.

[60]. M. L. Satter and P. N. Ross, ***Ultramicroscopy,*** **20** (***1986***) 21.

[61]. K. A. Friedrich, F. Henglein, U. Stimming and W. Unkauf, ***Electrochim. Acta,*** **45** (***2003***) 3283.

[62]. F. Maillard, E. R. Savinova and U. Stimming, ***J. Electroanal. Chem.,*** **599** (***2007***) 221.

[63]. H. Zhang, W. Zhou, Y. Du, P. Yang and C. Wang, ***Electrochem. Commun.,*** **12** (***2010***) 882.

[64]. A. Kolics and A. Wieckowski, ***J. Phys. Chem. B,*** **105** (***2001***) 2588.

[65]. Y. Song, Y. Ma, Y. Wang, J. Di and Y. Tu, ***Electrochim. Acta,*** **55** (***2010***) 4909.

[66]. E. Antolini, ***J. Mater. Sci.,*** **38** (***2003***) 2995.

[67]. E. Auer, A. Freund, J. Pietsch and T. Tacke, ***Appl. Catal. A,*** **173** (***1998***) 259.

[68]. K. Honda, M. Yoshimura, T. N. Rao, D. A. Tryk, A. Fujishima, K. Yasui, Y. Sakamoto, K. Nishio and H. Masuda, ***J. Electroanal. Chem.,*** **514** (***2001***) 35.

[69]. J. Lin-Cai and D. Pletcher, ***J. Electroanal. Chem.,*** **149** (***1983***) 237.

[70]. M. Fleischmann and M. Grenness, ***J. Chem. Soc., Faraday Trans I,*** **66** (***1972***) 2305.

[71]. S. Guerin and G. S. Attard, ***Electrochem. Commun.,*** **3** (***2001***) 544.

[72]. F. Gao, M. S. El-Deab, T. Okajima and T. Ohsaka, ***J. Electrochem. Soc.,*** **152** (***2005***) A1226.

[73]. S. Szunerits, M. Manesse, P. Actis, B. Marcus, G. Denuault, C. Jama and R. Boukherroub, ***Electrochem. Solid State Lett.,*** **10** (***2007***) G43.

[74]. W. Ye, D. Wang, H. Zhang, F. Zhou and W. Liu, ***Electrochim. Acta,*** **55** (***2010***) 2004.

[75]. L. Tian, Y. Qi and B. Wang, ***J. Colloid Interface Sci.,*** **333** (***2009***) 249.

[76]. M. M. E. Duarte, A. S. Pilla, J. M. Sieben and C. E. Mayer, ***Electrochem. Commun.,*** **8** (***2006***) 159.

[77]. L. M. Plyasova, I. Y. Molina, A. N. Gavrilov, S. V. Cherepanova, O. V. Cherstiouk, N. A. Rudina, E. R. Savinova and G. A. Tsirlina, ***Electrochim. Acta,*** **51** (***2006***) 4477.

[78]. J. A. Bennett, Y. Show, S. Wang and G. M. Swain, ***J. Electrochem. Soc.,*** **152** (***2005***) E184.

[79]. S. V. Mentus, ***Electrochim. Acta,*** **50** (***2005***) 3609.

[80]. F. Montilla, E. Morallon, I. Duo, C. Comninellis and J. L. Vazquez, ***Electrochim. Acta,*** **48** (***2003***) 3891.

[81]. V. R. Stamenkovic, B. Fowler, B. S. Mun, G. Wang, P. N. Ross, C. A. Lucas and N. M. Marković, ***Science,*** **315** (***2007***) 493.

[82]. B. Fowler, C. A. Lucas, A. Omer, G. Wang, V. R. Stamenkovic and N. M. Markovic, ***Electrochim. Acta,*** **53** (***2008***) 6076.

[83]. U. A. Paulus, A. Wokaun, G. G. Scherer, T. J. Schmidt, V. Stamenkovic, V. Radmilovic, N. M. Markovic and P. N. Ross, ***J. Phys. Chem. B,*** **106** (***2002***) 4181.

[84]. U. A. Paulus, A. Wokaun, G. G. Scherer, T. J. Schmidt, V. Stamenkovic, N. M. Markovic and P. N. Ross, ***Electrochim. Acta,*** **47** (***2002***) 3787.

[85]. S. Mukerjee, S. Srinivasan and M. P. Soriaga, ***J. Phys. Chem. B,*** **99** (***1995***) 4577.

[86]. S. Mukerjee, S. Srinivasan and A. J. Appleby, ***Electrochim. Acta,*** **38** (***1993***) 1661.

[87]. J. Zhang, F. H. B. Lima, M. H. Shao, K. Sasaki, J. X. Wang, J. Hanson and R. R. Adzic, ***J. Phys. Chem. B,*** **109** (***2005***) 22701.

[88]. J. Zhang, Y. Mo, M. B. Vukmirovic, R. Klie, K. Sasaki and R. R. Adzic, ***J. Phys. Chem. B,*** **108** (***2004***) 10955.

[89]. C. R. Henry, ***Surf. Sci. Rep.,*** **31** (***1998***) 231.

[90]. F. Maillard, P. A. Simonov and E. R. Savinova, in: P. Serp and J. L. Figueirdo (Ed.), ***Carbon Materials For Catalysis***, John Wiley & Sons, New Jersey, (2009), p. 429.

[91]. J. Kaiser, P. Simonov, V. Zaikovskii, C. Hartnig, L. Jörissen and E. Savinova, ***J. Appl. Electrochem.,*** **37** (***2007***) 1429.

[92]. A. M. C. Luna, G. A. Camara, V. A. Paganin, E. A. Ticoanelli and E. R. Gonzalez, ***Electrochem. Commun.,*** **2** (***2000***) 222.

[93]. B. Rajesh, K. R. Thampi, J.-M. Bonard, N. Xanthopoulos, H. J. Mathieu and B. Viswanathan, ***J. Phys. Chem. B,*** **107** (***2003***) 2701.

[94]. K. Amine, M. Mizuhata, K. Oguro and H. Takenaka, ***J. Chem. Soc., Faraday Trans.,*** **91** (***1995***) 4451.

[95]. T. J. Schmidt, M. Noeske, H. A. Gasteiger, R. J. Behm, P. Britz, W. Brijoux and H. Bonnemann, ***Langmuir,*** **13** (***1997***) 2591.

[96]. J. Chen, T. Herricks, M. Geissler and Y. Xia, ***J. Am. Chem. Soc.,*** **126** (***2004***) 10854.

[97]. A. Harriman, G. R. Milward, P. Neta, M. C. Richoux and J. M. Thomas, ***J. Phys. Chem.,*** **92** (***1988***) 1286.

[98]. T. Akita, P. Lu, S. Ichikawa and M. Haruta, ***Surf. Interface Anal.,*** **31** (***2001***) 73.

[99]. M. Limat, B. E. Roustom, H. Jotterand, G. Foti and C. Comninellis, ***Electrochim. Acta,*** **54** (***2009***) 2410.

[100]. P. Gorisek, V. Francetic, C. L. Lengauer and J. Macek, ***Acta Chim. Slov.,*** **51** (***2004***) 203.

[101]. M. Aktary, C. E. Lee, Y. Xing, S. H. Bergens and M. T. McDermott, ***Langmuir,*** **16** (***2000***) 5837.

[102]. F. Gloaguen, J. M. Leger, C. Lamy, A. Marmann, U. Stimming and R. Vogel, ***Electrochim. Acta,*** **44** (***1999***) 1805.

[103]. J. Jiang and A. Kucernak, ***J. Electroanal. Chem.,*** **520** (***2002***) 64.

[104]. G. S. Attard, P. N. Bartlett, N. R. B. Coleman, J. M. Elliott, J. R. Owen and J. H. Wang, ***Science,*** **278** (***1997***) 838.

[105]. J. M. Elliott, P. R. Birkin, P. N. Bartlett and G. S. Attard, ***Langmuir,*** **15** (***1999***) 7411.

[106]. X. Zhang, F. Shi, X. Yu, H. Liu, Y. Fu, Z. Wang, L. Jiang and X. Li, ***J. Am. Chem. Soc.,*** **126** (***2004***) 3064.

[107]. J. L. Zubimendi, L. Vazquez, P. Ocon, J. M. Vara, W. E. Triaca, R. C. Salvarezza and A. J. Arvia, ***J. Phys. Chem. ,*** **97** (***1993***) 5095.

[108]. J. V. Zoval, J. Lee, S. Gorer and R. M. Penner, ***J. Phys. Chem. B,*** **102** (***1998***) 1166.

[109]. G. J. Lu and G. Zangari, ***Electrochim. Acta,*** **51** (***2006***) 2531.

[110]. S. D. Thompson, L. R. Jordan, A. K. Shukla and M. Forsyth, ***J. Electroanal. Chem.,*** **515** (***2001***) 61.

[111]. P. He, H. Liu, Z. Li and J. Li, ***J. Electrochem. Soc.,*** **152** (***2005***) E146.

[112]. H. Tang, J. Chen, L. Nie, D. Liu, W. Deng, Y. Kuang and S. Yao, ***J. Colloid Interface Sci.,*** **269** (***2004***) 26.

[113]. J. S. Ye, H. F. Cui, Y. Wen, W. D. Zhang, G. Q. Xu and F. S. Sheu, ***Microchimica Acta,*** **152** (***2006***) 267.

[114]. R. M. Penner, ***J. Phys. Chem. B,*** **106** (***2002***) 3339.

[115]. E. Sheridan, J. Hjelm and R. J. Forster, ***J. Electroanal. Chem.,*** **608** (***2007***) 1.

[116]. H. Liu and Y. Tian, ***Electroanalysis,*** **20** (***2008***) 1227.

[117]. G. S. Attard, J. C. Glyde and C. G. Goltner, ***Nature,*** **378** (***1995***) 366.

[118]. G. S. Attard, C. G. Goltner, J. M. Corker, S. Henke and R. H. Templer, ***Angew. Chem. Int. Ed.,*** **36** (***1997***) 1315.

[119]. J. M. Elliott, G. S. Attard, P. N. Bartlett, N. R. B. Coleman, D. A. S. Merckel and J. R. Owen, ***Chem. Mater.,*** **11** (***1999***) 3602.

[120]. I. S. Nandhakumar, J. M. Elliot and G. S. Attard, ***Chem. Mater.,*** **13** (***2001***) 3840.

[121]. P. A. Nelson, J. M. Elliot, G. S. Attard and J. R. Owen, ***Chem. Mater.,*** **14** (***2002***) 524.

[122]. P. N. Bartlett, P. N. Birkin, M. A. Ghanem, P. d. Groot and M. Sawicki, ***J. Electrochem. Soc.,*** **148** (***2001***) C119.

[123]. P. N. Bartlett, B. Gollas, S. Guerin and J. Marwan, ***Phys. Chem. Chem. Phys.,*** **4** (***2002***) 3835.

[124]. P. N. Bartlett and J. Marwan, ***Chem. Mater.,*** **15** (***2003***) 2962.

[125]. P. N. Bartlett and J. Marwan, ***Microporous Mesoporous Mater.,*** **62** (***2003***) 73.

[126]. S. A. G. Evans, J. M. Elliot, L. M. Andrews, P. N. Bartlett, P. J. Doyle and G. Denuault, ***Anal. Chem.,*** **74** (***2002***) 1322.

[127]. B. Gollas, J. M. Elliott and P. N. Bartlett, ***Electrochim. Acta,*** **45** (***2000***) 3711.

[128]. H. Luo, J. Zhang and Y. Yan, ***Chem. Mater.,*** **15** (***2003***) 3769.

[129]. Y. Yamauchi, M. Komatsu, A. Takai, R. Sebata, M. Sawada, T. Momma, M. Fuziwara, T. Osaka and K. Kuroda, ***Electrochim. Acta,*** **53** (***2007***) 604.

[130]. T. Kijima, T. Yoshimura, M. Uota, T. Ikeda, D. Fujikawa, S. Mouri and S. Uoyama, ***Angew. Chemie. Int. Ed.,*** **43** (***2004***) 228.

[131]. N. R. B. Coleman and G. S. Attard, ***Microporous Mesoporous Mater.,*** **44** (***2001***) 73.

[132]. N. Toshima, T. Takahashi and H. Hirai, ***Chem. Lett.,*** (***1985***) 1245.

[133]. G. S. Attard, N. R. B. Coleman and J. M. Elliott, ***Stud. Surf. Sci. Catal.,*** **117** (***1998***) 89.

[134]. J. M. Elliott, L. M. Cabuche and P. N. Bartlett, ***Anal. Chem.,*** **73** (***2001***) 2855.

[135]. E. B. Priestley, P. J. Wojtowicz and P. Sheng, ***Introduction to Liquid Crystals***, Plenum Press, New York, (1975).

[136]. S. Singh, ***Liquid Crystals Fundamentals***, World Scientific Publishing Co. Pte. Ltd., Singapore, (2002).

[137]. R. G. Laughlin, ***Aqueous Phase Behaviour of Surfactants***, Academic Press, London, (1996).

[138]. P. J. Collings and M. Hird, ***Introduction to Liquid Crystals Chemistry and Physics***, Taylor & Francis Ltd. , London, (1997).

[139]. G. J. T. Tiddy, ***Phys. Rep.,*** **57** (***1980***) 1.

[140]. C. Tanford, ***The Hydrophobic Effect: Formation of Micelles and Biological Membranes***, Wiley Interscience, New York, (1980).

[141]. B. Gollas, ***Coatings for Advanced Technologies***, Habilitation Thesis, Graz University of Technology, (2007).

[142]. K. Fontell, ***Mol. Cryst. Liq. Cryst.,*** **63** (***1981***) 59.

[143]. G. S. Attard, P. N. Bartlett, N. R. B. Coleman, J. M. Elliott and J. R. Owen, ***Langmuir,*** **14** (***1998***) 7340.

[144]. J. J. Eisch, ***J. Am. Chem. Soc.,*** **84** (***1962***) 3830.

[145]. D. J. Mitchell, G. J. T. Tiddy, L. Waring, T. Bostock and M. P. McDonald, ***J. Chem. Soc. ,*** **79** (***1983***) 975.

[146]. S. A. G. Evans, K. Brakha, M. Billon, P. Mailley and G. Denuault, ***Electrochem. Comm.,*** **7** (***2005***) 135.

[147]. F. Leroux, B. E. Koene and L. F. Nazar, ***J. Electrochem. Soc.,*** **143** (***1996***) L181.

[148]. W. G. Pell and B. E. Conway, ***J. Power Sources,*** **63** (***1996***) 255.

[149]. J. Wang and L. Agnes, ***Anal. Chem.,*** **64** (***1992***) 456.

[150]. S. Ye, A. K. Vijh and L. H. Dao, ***J. Electrochem. Soc.,*** **143** (***1996***) L7.

[151]. S. C. Warren, L. C. Messina, L. S. Slaughter, M. Kamperman, Q. Zhou, S. M. Gruner, F. J. Disalvo and U. Weisner, ***Science,*** **320** (***2008***) 1748.

[152]. T. Imokawa, K.-J. Williams and G. Denuault, ***Anal. Chem.,*** **78** (***2005***) 265.

[153]. P. Lozano-Sanchez and J. M. Elliott, ***Analyst,*** **130** (***2005***) 715.

[154]. A. Kucernak and J. Jiang, ***Chem. Eng. J.,*** **93** (***2003***) 81.

[155]. H. Okamoto, W. Kon and Y. Mukouyama, ***J. Phys. Chem. B,*** **108** (***2004***) 4432.

[156]. Z. Wang and K. Qiu, ***Electrochem. Commun.,*** **8** (***2006***) 1075.

[157]. B. M. Babić, I. M. Vraćar, V. Radmilovic and N. V. Krstajić, ***Electrochim. Acta,*** **51** (***2006***) 3820.

[158]. A. N. Golikand, M. G. Maragheh, S. S. Sherehjini, K. M. Taghi-Ganji and M. Yari, ***Electroanalysis,*** **18** (***2006***) 911.

[159]. R. N. Goldberg and L. G. Hepler, ***Chem. Rev.,*** **68** (***1968***) 229.

[160]. F. A. Cotton, G. Wilkinson, C. A. Murillo and M. Bochmann, ***Advanced Inorganic Chemistry***, John Wiley & Sons, Inc., United States of America, Sixth edition, (1999).

[161]. U. Belluco, ***Organometallic and Coordination Chemistry of Platinum***, Academic Press Inc. , London, (1974).

[162]. C. M. Davidson and R. F. Jameson, ***Trans. Faraday Soc.,*** **61** (***1965***) 2462.

[163]. H. M. Yasin, G. Denuault and D. Pletcher, ***J. Electroanal. Chem.,*** **633** (***2009***) 327.

[164]. B. Shelimov, J. F. Lambert, M. Che and B. Didillon, ***J. Am. Chem. Soc.,*** **121** (***1999***) 545.

[165]. J. R. Anderson, ***Structure of Metallic Catalysts***, Academic Press, New York, (1975).

[166]. E. H. Archibald, ***J. Chem. Soc.,*** **117** (***1920***) 1104.

[167]. F. R. Hartley, ***The Chemistry of Platinum and Palladium***, Applied Science Publishers Ltd, London, (1973).

[168]. E. Sonstadt, ***Proc. Chem. Soc.,*** **14** (***1898***) 179.

[169]. A. T. Hubbard and F. C. Anson, ***Anal. Chem.,*** **38** (***1966***) 1887.

[170]. W. A. Spieker, J. Liu, J. T. Miller, A. J. Kropf and J. R. Regalbuto, ***Appl. Catal. A,*** **232** (***2002***) 219.

[171]. E. H. Archibald and W.A.Gale, ***J. Chem. Soc.,*** **121** (***1922***) 2849.

[172]. J. Kramer and K. R. Koch, ***Inorg. Chem.,*** **45** (***2006***) 7843.

[173]. C. Carr, P. L. Goggin and R. J. Goodfellow, ***Inorg. Chim. Acta,*** **81** (***1984***) L25.

[174]. L. E. Cox, D. G. Peters and E. L. Wehry, ***J. Inorg. Nucl. Chem.,*** **34** (***1972***) 297.

[175]. A. B. P. Lever, ***Inorganic Electronic Spectroscopy***, Elsevier, Amsterdam, (1984).

[176]. M. E. Baumgartner and C. J. Raub, ***Plat. Metals Rev.,*** **32** (***1988***) 188.

[177]. K. H. Choi, H. S. Kim and T. H. Lee, ***J. Power Sources,*** **75** (***1998***) 230.

[178]. K. Itaya, H. Takahashi and I. Uchida, ***J. Electroanal. Chem.,*** **208** (***1986***) 373.

[179]. A. A. Mikhaylova, O. A. Khazova and V. S. Bagotzky, ***J. Electroanal. Chem.,*** **480** (***2000***) 225.

[180]. K. Shimazu, K. Uosaki, H. Kita and Y. Nodasaka, ***J. Electroanal. Chem.,*** **256** (***1988***) 481.

[181]. A. J. Gregory, W. Levason, R. E. Noftle, R. Le Penven and D. Pletcher, ***J. Electroanal. Chem.,*** **399** (***1995***) 105.

[182]. R. Le Penven, W. Levason and D. Pletcher, ***J. Appl. Electrochem.,*** **22** (***1992***) 415.

[183]. W. Levason, D. Pletcher, A. M. Smith and A. R. Berzins, ***J. Appl. Electrochem.,*** **28** (***1998***) 18.

[184]. A. J. Gregory, W. Levason and D. Pletcher, ***J. Electroanal. Chem.,*** **348** (***1993***) 211.

[185]. R. H. Atkinson, in: F. A. Lowenheim (Ed.), ***Modern Electroplating***, John Wiley & Sons, New York, 2nd Edition, (1963), p. 310.

[186]. P. E. Skinner, ***Plat. Metals Rev.,*** **33** (***1989***) 102.

[187]. J. J. Whalen, J. D. Weiland and P. C. Searson, ***J. Electrochem. Soc.,*** **152** (***2005***) C738.

[188]. R. H. Atkinsons, ***Trans. Inst. Metal Finishing,*** **36** (***1959***) 7.

[189]. A. M. Feltham and M. Spiro, ***Chem. Rev.,*** **71** (***1971***) 177.

[190]. A. J. Bard, R. Parsons and J. Jordan, ***Standard Potentials in Aqueous Solutions***, Marcel Dekker Inc., New York, (1985).

[191]. K. Shimazu, D. Weisshaar and T. Kuwana, ***J. Electroanal. Chem.,*** **223** (***1987***) 223.

[192]. N. Georgolios, D. Jannakoudakis and P. Karabinas, ***J. Electroanal. Chem.,*** **264** (***1989***) 235.

[193]. O. V. Sherstyuk, S. N. Pron'kin, A. L. Chuvilin, A. N. Salanov, E. R. Savinova, G. A. Tsirlina and O. A. Petrii, ***Russ. J. Electrochem.,*** **36** (***2000***) 741.

[194]. O. A. Petrii, G. A. Tsirlina, S. N. Pron'kin, F. M. Spiridonov and M. L. Khrushcheva, ***Russ. J. Electrochem.,*** **35** (***1999***) 8.

[195]. N. Bartlett, ***Gold Bull.,*** **31** (***1998***) 22.

[196]. P. Pyykko, ***Gold Bull.,*** **37** (***2004***) 136.

[197]. G. C. Bond, C. Louis and D. T. Thompson, ***Catalysis by Gold***, Imperial College Press, London, (2006).

[198]. P. Pyykko, ***Angew. Chemie. Int. Ed.,*** **41** (***2002***) 3573.

[199]. M. Haruta, T. Kobasyahi, H. Sano and N. Yamada, ***Chem. Lett.,*** **16** (***1987***) 405.

[200]. J. H. Gallego, C. E. Castellano, A. J. Calandra and A. J. Arvia, ***J. Electroanal. Chem.,*** **66** (***1975***) 207.

[201]. J. A. Harrison and J. Thompson, ***J. Electroanal. Chem.,*** **59** (***1975***) 273.

[202]. M. A. Diaz, G. H. Kelsall and N. J. Welham, ***J. Electroanal. Chem,*** **361** (***1993***) 25.

[203]. U. Schmidt, M. Donten and J. Osteryoung, ***J. Electrochem. Soc.,*** **144** (***1997***) 2013.

[204]. A. D. Goolsby and D. T. Sawyer, ***Anal. Chem.,*** **40** (***1968***) 1978.

[205]. J. A. Harrison and J. Thompson, ***J. Electroanal. Chem.,*** **40** (***1972***) 113.

[206]. J. N. Gaur and G. M. Schmid, ***J. Electroanal. Chem.,*** **24** (***1970***) 279.

[207]. P. A. Kohl., in: M. Schlesinger and M. Paunovic (Ed.), ***Modern Electroplating***, John Wiley & Sons. Inc., New York, 4th edition, (2000).

[208]. S. A. Losi, F. L. Zuntini and A. R. Meyer, ***Electrodeposition Surf. Treatment,*** **1** (***1972***) 3.

[209]. I. R. Burrows, J. A. Harrison and J. Thompson, ***J. Electroanal. Chem.,*** **53** (***1974***) 283.

[210]. A. M. Sullivan and P. A. Kohl, ***J. Electrochem. Soc.,*** **144** (***1997***) 1686.

[211]. L. Komsiyska and G. Staikov, ***Electrochim. Acta,*** **54** (***2008***) 168.

[212]. A.J.Bard, R.Parsons and J.Jordan, ***Standard Potentials in Aqueous Solutions***, Marcel Dekker Inc., New York, (1985).

[213]. J. E. Anderson and S. M. Sawtelle, ***Inorg. Chim. Acta,*** **194** (***1992***) 171.

[214]. G. M. Schmid and R. N. O'Brien, ***J. Electrochem. Soc.,*** **111** (***1964***) 832.

[215]. A. Kiani and S. Hatami, ***Int. J. Hydrogen Energy,*** **35** (***2010***) 5202.

[216]. M. H. Huang, Y. D. Jin, H. Q. Jiang, X. P. Sun, H. J. Chen and B. F. Liu, ***J. Phys. Chem. B,*** **109** (***2005***) 15264.

[217]. M. N. Dešić, M. M. Popović, M. D. Obradović, L. M. Vračar and B. N. Grgur, ***J. Serb. Chem. Soc.,*** **70** (***2005***) 231.

[218]. N. M. Markovic and P. N. Ross, ***Surf. Sci. Rep.,*** **45** (***2002***) 117.

[219]. A. Sarapuu, K. Tammeveski, T. T. Tenno, V. Sammelselg, K. Kontturi and D. J. Schriffrin, ***Electrochem. Commun.,*** **3** (***2001***) 446.

[220]. M. S. El-Deab, K. Arihara and T. Ohsaka, ***J. Electrochem. Soc.,*** **151** (***2004***) E213.

[221]. A. Sarapuu, N. Nurmik, H. Mandar, A. Rosental, T. Laaksonen, K. Kontturi, D. J. Schiffrin and K. Tammeveski, ***J. Electroanal. Chem.,*** **612** (***2008***) 78.

[222]. S. Strbac and R. R. Adzic, ***Electrochim. Acta,*** **41** (***1996***) 2903.

[223]. J. Kim and A. A. Gewirth, ***J. Phys. Chem. B,*** **110** (***2006***) 2565.

[224]. O. V. Cherstiouk, P. A. Simonov, V. I. Zaikovskii and E. R. Savinova, ***J. Electroanal. Chem.,*** **554** (***2003***) 241.

[225]. E. Antolini, ***Mater. Chem. Phys.,*** **78** (***2003***) 563.

[226]. L. Li and Y. C. Xing, ***J. Phys. Chem.,*** **111** (***2007***) 2803.

[227]. N. T. Napporn, L. Laborde, J. M. Leger and C. Lamy, ***J. Electroanal. Chem.,*** **404** (***1996***) 153.

[228]. M. S. El-Deab and T. Ohsaka, ***J. Electroanal. Chem.,*** **553** (***2003***) 107.

[229]. J. Luo, P. N. Njoki, Y. Lin, L. Wang and C. J. Zhong, ***Electrochem. Commun.,*** **8** (***2006***) 581.

[230]. M. Morita, Y. Iwanaga and Y. Matsuda, ***Electrochim. Acta,*** **36** (***1991***) 947.

[231]. M. Van Brussel, G. Kokkinidis, A. Hubin and C. Buess-Herman, ***Electrochim. Acta,*** **48** (***2003***) 3909.

[232]. J. Zhang, K. Sasaki, E. Sutter and R. R. Adzic, ***Science,*** **315** (***2007***) 220.

[233]. J. Wang, G. Yin, G. Wang, Z. Wang and Y. Gao, ***Electrochem. Commun.,*** **10** (***2008***) 831.

[234]. B. E. Conway, ***Prog. Surf. Sci.,*** **49** (***1995***) 331.

[235]. R. Greef, R. Peat, L. M. Peter, D. Pletcher and J. Robinson, ***Instrumental Methods In Electrochemistry***, Ellis Horwood Limited, England, (1990).

[236]. M. I. Montenegro, M. A. Queiros and J. L. Dschbach, ***Microelectrodes: Theory and Applications***, Kluwer Academic Publishers, Netherlands, (1991).

[237]. B. Scharifker and G. Hills, ***Electrochim. Acta,* 28** (***1983***) 879.

[238]. R.Greef, R.Peat, L.M.Peter, D.Pletcher and J.Robinson, ***Instrumental Methods In Electrochemistry***, Ellis Horwood Limited, England, (1990).

[239]. P. R. Birkin, J. M. Elliott and Y. E. Watson, ***Chem. Commun.,*** (***2000***) 1693.

[240]. M. A. Ghanem and F. Marken, ***Electrochem. Comm.,* 7** (***2005***) 1333.

[241]. P. J. Goodhew, J. Humphreys and R. Beanland, ***Electron Microscopy and Analysis***, Taylor & Francis Inc., London, 3rd edition, (2001).

[242]. J. I. Goldstein, D. E. Newbury, P. Echlin, D. C. Joy, C. Fiori and E. Lifshin, ***Scanning electron microscope and X-ray Analysis***, Plenum Press, New York, (1981).

[243]. M. Bayati, J. M. Abad, C. A. Bridges, M. J. Rosseinsky and D. J. Schiffrin, ***J. Electroanal. Chem.,* 623** (***2008***) 19.

[244]. J. Ustarroz, U. Gupta, A. Hubin, S. Bals and H. Terryn, ***Electrochem. Comm.,* 12** (***2010***) 1706.

[245]. P. N. Bartlett, ***In Biosensors: A Practical Approach***, Oxford University Press, Oxford, (1990).

[246]. Y. Zhong, C.-L. Xu, L.-B. Kong and H.-L. Li, ***Appl. Surf. Sci.,* 255** (***2008***) 3388.

[247]. I. Dierking, ***Textures of Liquid Crystals***, Wiley-VCH, Darmstadt, (2003).

[248]. S. Trassatti and O. A. Petrii, ***J. Electroanal. Chem.,* 327** (***1992***) 353.

[249]. K. Kinoshita, ***CARBON Electrochemical and Physicochemical Properties***, Wiley-Interscience Publication, New York, (1988).

[250]. H. Martın, P. Carro, A. H. Creus, S. Gonzalez, R. C. Salvarezza and A. J. Arvia, ***Langmuir,* 13** (***1997***) 100.

[251]. G. J. Lu and G. Zangari, ***J. Phys. Chem. B,* 109** (***2005***) 7998.

[252]. H. A. Gasteiger, N. Markovic, P. N. Ross and E. J. Cairns, ***J. Phys. Chem.,* 97** (***1993***) 12020.

[253]. J. Luo, M. M. Maye, N. N. Kariuki, L. Wang, P. Njoki, Y. Lin, M. Schadt, H. R. Naslund and C.-J. Zhong, ***Catal. Today,* 99** (***2005***) 291.

[254]. S. Chen and A. Kucernak, ***J. Phys. Chem. B,*** **108** (***2004***) 13984.

[255]. J. L. Zubimendi, L. Vazquez, P. Ocon, J. M. Vara, W. E. Triaca, R. C. Salvarezza and A. J. Arvia, ***J. Phys. Chem.,*** **97** (***1993***) 5095.